Mehmet R. Yuce *Editor*

Ultra-Wideband and 60 GHz Communications for Biomedical Applications

Springer

Ultra-Wideband and 60 GHz Communications for Biomedical Applications

Mehmet R. Yuce
Editor

Ultra-Wideband and 60 GHz Communications for Biomedical Applications

Springer

Editor
Mehmet R. Yuce
Electrical and Computer Systems Engineering
Monash University
Clayton
Victoria
Australia

ISBN 978-1-4614-8895-8 ISBN 978-1-4614-8896-5 (eBook)
DOI 10.1007/978-1-4614-8896-5
Springer New York Heidelberg Dordrecht London

Library of Congress Control Number: 2013948881

Printed on acid-free paper

Springer is part of Springer Science+Business Media (www.springer.com)

Preface

This book covers devices, systems, and circuits that have been proposed for biomedical applications using the two recently established bands: ultra-wideband (3.1–10.6 GHz) and 60 GHz ISM band (57–66 GHz). There has been some recent interest in using ultra-wide band (UWB) and the 60 GHz wireless technology for health care applications because of some important benefits they offer such as low-power design, low radio frequency (RF) and electromagnetic interference (EMI) effects in medical environment, small size antenna, and high-speed communication. The physical size of devices at these frequencies can be extremely small because of the circuit design at gigahertz (GHz) range. These bands are not crowded when compared to the other available bands, and thus have been very attractive for implementation in biomedical environment. Thus far, ultra-wideband has been successfully used for wireless body area network (WBAN) applications, medical imaging, biomedical sensing, and vital signs monitoring.

The unlicensed 60 GHz ISM provides one of the largest bandwidths, making this technology attractive for medical applications. This book investigates some potential applications of this band in the e-health areas. A wireless system based on the 60 GHz ISM band can be deployed in medical centers or homes to initiate fast connectivity at low cost. It can provide video data transmission from one point to another without using wires. The 60-GHz radios can support multi-gigabit per second data communication for body-centric wireless systems with high level of security. It will possibly enable high level of miniaturization for the antennas and transceiver circuits and will have low interference effect on other wireless systems in the same environment.

UWB communication has been used for monitoring continuous medical signals such as EEG (*electroencephalogram*) and ECG (*electrocardiogram*) and high-speed medical monitoring such as electronic pills (i.e., wireless capsules) and multichannel neural recording for brain–computer interfaces. UWB is also attractive for medical gait analysis and tracking due to the highly accurate performance that can be obtained. UWB radar is being used in medicine to detect tumors externally for certain body organs especially for breast cancer detection.

This book contains the current state of art by focusing latest research related to design, development, and circuits for ultra-wide band and the 60 GHz wireless system

technology. The recent technologies and developments proposed or used in medical monitoring systems based on the two bands will be covered. The book will introduce possible solutions and design techniques to implement these systems efficiently in the medical environment.

This book covers topics that will be suitable for a broad range of researchers. The book will be a key resource for the Medical ICT (Information and Communication Technology) professionals, bio-medical engineers, graduate, and senior undergraduate students in computer, electrical, electronic, and biomedical engineering disciplines.

All individual chapters are written by leading experts in their fields. Contributions by authors are on various applications of ultra-wideband and the 60 GHz ISM band including circuit implementation, UWB and 60 GHz signal transmission around and in-body, antenna design solution, hardware implementation of body sensors, UWB transceiver design, 60 GHz transceiver design, UWB Radar for contactless respiratory monitoring, and ultra-wideband based medical imaging.

I hope that this book will be a key resource for researchers and students who are working in these emerging areas of wireless technologies. The rapid progress in these wireless systems will play important roles in the future health care and associated areas. Finally, I would like to thank all the authors for their excellent contributions in helping us develop a key book as we enter the era of wireless e-health. I also thank the publisher for delivering a key book in a timely manner.

Mehmet R. Yuce

Contents

Contributors

Akram Alomainy Antenna & Electromagnetics Research Group, School of Electronic Engineering and Computer Science, Queen Mary, University of London, London, United Kingdom

Qammer H. Abbasi Antenna & Electromagnetics Research Group, School of Electronic Engineering and Computer Science, Queen Mary, University of London, London, United Kingdom

University of Engineering & Technology, Lahore, Pakistan

Hossein Kassiri Bidhendi Department of Electrical and Computer Engineering, University of Toronto, Toronto, Canada

Dajana Cassioli Department of Information Engineering, Computer Science and Mathematics, University of L'Aquila, L'Aquila, Italy

Aye Chan School of Electrical and Electronic Engineering, Nanyang Technological University, Singapore, Republic of Singapore

Shengxi Diao Institute of Microelectronics, A*STAR, Singapore, Rep. of Singapore

Yuan Gao Institute of Microelectronics, A*STAR, Singapore, Rep. of Singapore

Yong-Xin Guo Department of Electrical and Computer Engineering, National University of Singapore, Singapore, Republic of Singapore

Erry Gunawan School of Electrical and Electronic Engineering, Nanyang Technological University, Singapore, Republic of Singapore

Roman Genov Department of Electrical and Computer Engineering, University of Toronto, Toronto, Canada

Chun-Huat Heng Department of Electrical and Computer Engineering, National University of Singapore, Singapore, Rep. of Singapore

Kuo-Ken Huang Electrical Engineering and Computer Science, University of Michigan, Ann Arbor, USA

Yang Hao Antenna & Electromagnetics Research Group, School of Electronic Engineering and Computer Science, Queen Mary, University of London, London, United Kingdom

Minkyu Je Institute of Microelectronics, A*STAR, Singapore, Rep. of Singapore

Hamed Mazhab Jafari Department of Electrical and Computer Engineering, University of Toronto, Toronto, Canada

Xin Liu Institute of Microelectronics, A*STAR, Singapore, Rep. of Singapore

Kay Soon Low School of Electrical and Electronic Engineering, Nanyang Technological University, Singapore, Republic of Singapore

Arash Maskooki School of Electrical and Electronic Engineering, Nanyang Technological University, Singapore, Republic of Singapore

Domenico Pepe Department of Electrical and Electronic Engineering, University College Cork, Cork, Ireland

Tyndall National Institute, "Lee Maltings", Cork, Ireland

Nikola Rendevski Department of Information Engineering, Computer Science and Mathematics, University of L'Aquila, L'Aquila, Italy

Jean-Michel Redouté Biomedical Integrated Circuits and Sensors Laboratory, Department of Electrical and Computer Systems Engineering, Monash University, Melbourne, VIC, Australia

Cheong Boon Soh School of Electrical and Electronic Engineering, Nanyang Technological University, Singapore, Republic of Singapore

Weida Toh Institute of Microelectronics, A*STAR, Singapore, Rep. of Singapore

K. M. S. Thotahewa Biomedical Integrated Circuits and Sensors Laboratory, Department of Electrical and Computer Systems Engineering, Monash University, Melbourne, VIC, Australia

Yisheng Wang School of Electrical and Electronic Engineering, Nanyang Technological University, Singapore, Rep. of Singapore

Xiaoyan Wang Holst Centre, imec-nl, Eindhoven, The Netherlands

David D. Wentzloff Electrical Engineering and Computer Science, University of Michigan, Ann Arbor, USA

Lei Wang Department of Electrical and Computer Engineering, National University of Singapore, Singapore, Republic of Singapore

Mehmet Rasit Yuce Biomedical Integrated Circuits and Sensors Laboratory, Department of Electrical and Computer Systems Engineering, Monash University, Melbourne, VIC, Australia

Yuanjin Zheng School of Electrical and Electronic Engineering, Nanyang Technological University, Singapore, Rep. of Singapore

Bin Zhao Institute of Microelectronics, A*STAR, Singapore, Rep. of Singapore

Domenico Zito Department of Electrical and Electronic Engineering, University College Cork, Cork, Ireland

Tyndall National Institute, “Lee Maltings”, Cork, Ireland

UWB and mmWave Communication Techniques and Systems for Healthcare

Nikola Rendevski and Dajana Cassioli

Abstract Telemedicine has been around for decades, and some apparatuses are currently in operation in few hospitals. Relying on advanced wireless technologies, which enable the use of pervasive communications for a variety of different applications, new-generation systems for healthcare become non-invasive, broadband and mobile. High-data rate wireless systems allow users to share huge amounts of data and multimedia content with other users or with service providers. Consequently, the range of potential applications of healthcare assistance expands to include new scenarios that involve very high data rate wireless transmissions like, for instance, seamless exchange of multimedia content. In this chapter, a survey of new-generation wireless communication techniques and systems based on ultra-wideband technology and millimetre-waves radios is provided, with reference to the modern concepts of patient-centric and hospital-centric application scenarios. The opportunities offered by these two broadband wireless communications technologies beyond basic data transfer are highlighted and discussed in the framework of the new application scenarios that these technologies open.

Keywords mmWave radios · 60-GHz communications · UWB communications · Wireless body area networks · eHealth · Healthcare communication systems · Remote patient monitoring · Pervasive communications · Uncompressed video · Quality of service

Introduction

Innovative data aggregation methods and applications gave a great boost to eHealth services in the recent years such that the users (patients, doctors and formal/informal caregivers) are able to communicate and exchange data as much as possible, anywhere and anytime. Current applications include remote patient monitoring (RPM), ambient assisted living (especially for elderly people) and emergency interventions

D. Cassioli (✉) · N. Rendevski
Department of Information Engineering, Computer Science and Mathematics,
University of L'Aquila, Via Vetoio snc, 67100 L'Aquila, Italy
e-mail: dajana.cassioli@univaq.it

M. R. Yuce (ed.), *Ultra-Wideband and 60 GHz Communications for Biomedical Applications,* DOI 10.1007/978-1-4614-8896-5_1,

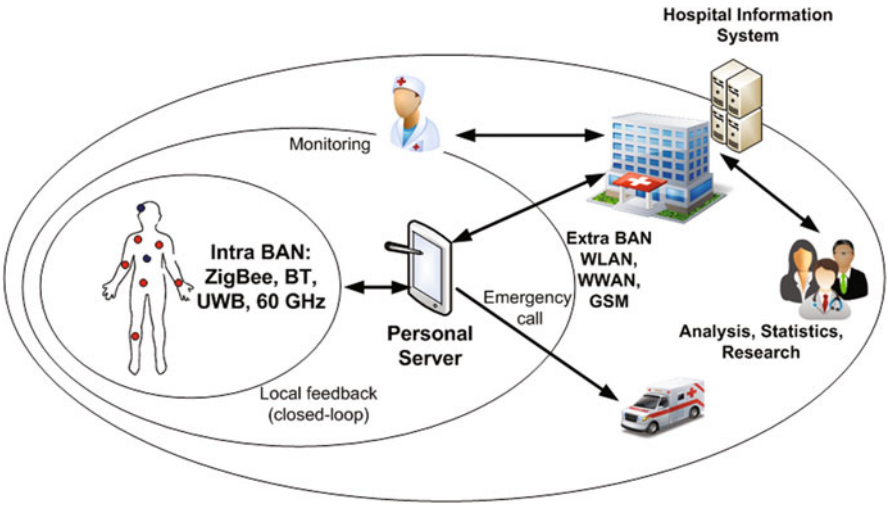

Fig. 1 Patient-centric system

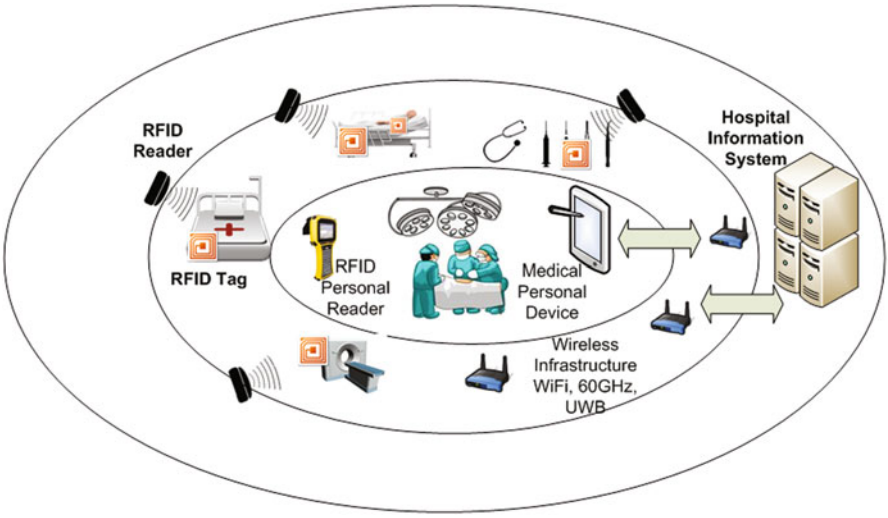

Fig. 2 Hospital-centric system

that fall in the category of the commonly known telemedicine. Nowadays, these kinds of applications have been complemented by applications aimed at improving workflows and productivity of medical personnel in the medical facilities which include tasks like workflow optimization, instruments localization and inventory in the hospital or medical centres. These two concepts are mapped to two different categories of eHealth systems that involve different kinds of users and have different system requirements and architectures [1]: 'patient-centred' and 'hospital-centred' systems, shown in Figs. 1 and 2 respectively.

Both categories strongly benefit by the use of wireless interfaces that enable an easier application and are more cost-efficient. Indeed, recent developments have led to the fabrication of small and intelligent (bio) medical sensors which can be worn on or implanted in the human body, but need to send data to a medical server for further analysis. Wired connections turn out to be too cumbersome, involve high cost for deployment and maintenance and will strongly impact the everyday life of the patient. By the use of wireless, the patient experiences a greater physical mobility and is no longer compelled to stay in a hospital.

While eHealth is defined as the healthcare practice supported by electronic processes and communication, the healthcare is now going a step further by becoming mobile. This is referred to as mHealth. In order to fully exploit the benefits of wireless technologies in telemedicine and mHealth, a new type of wireless network has emerged: a wireless on-body network or a wireless body area network (WBAN). A WBAN consists of small, intelligent devices attached on or implanted in the body, which are capable of establishing a wireless communication link. These devices provide continuous health monitoring and real-time feedback to the user or medical personnel. For instance, small battery-powered biosensors such as an insulin pump with glucometer, wearable fall detector, electrocardiogram monitor and an oximeter can be wirelessly connected through a WBAN to allow an elderly patient to be remotely monitored by a healthcare provider while in his/her home. Furthermore, the measurements can be recorded over a longer period of time, improving the quality of the measured data [1].

In principle, any wireless technology can be used in eHealth and mHealth contexts depending on the specific application, its related data rate and quality of service (QoS) requirements. However in the last few years, high data rate wireless technologies, especially ultra-wideband (UWB) and millimetre-waves (mmWaves), have emerged as the new paradigm for wireless personal area networks (PANs) [2]. Both of them are short-range high-throughput wireless technologies able to provide data rates of several hundred Mbps (and also Gbps in case of 60-GHz mmWaves).

So far, the best candidate technology for WBAN has been the UWB, leading to standardization within, e.g., the IEEE 802.15.6 or 802.15.4a, thanks to its intrinsic characteristics, namely, the good material penetration properties, low power emissions, low-interference operation, robustness against multi-path, radar-like operation and high temporal resolution, enabling accurate sub-centimetres localizations [3, 4].

The new emerging mmWave technology offers very large unlicensed bands available almost worldwide and is nowadays envisaged for very high data rate transmissions, including bulk data transfer and (uncompressed) video streaming over short ranges. Whereas UWB has represented the basis for WBAN standards and imaging sensors, mmWave radios are suitable candidates for hospital-centric systems wherever high data rate diagnostic systems need to be connected to a central server in a cost-effective way that is non-invasive for the patient. Indeed, mmWave signals are mostly reflected by the human body and can be used only to connect wearable devices, not for implantable or endoscopic devices [5, 6].

In this chapter, we propose a survey of UWB and mmWave communication systems and standards for the provision of healthcare services. To the best of our knowledge, currently available solutions for pervasive healthcare are based on UWB, while there is no example of 60-GHz mmWave in this field. Hence, we discuss the

potential of mmWaves for eHealth and mHealth applications, especially for high data rate diagnostic systems. We also propose a specific, assisted-living application for communicative impaired children, which has been conceived within the project VISION [7]. The idea came because cognitive behavioural systems would definitely benefit from a supporting technology able to automatically recognize the context where humans operate, their gestures and even facial expressions. This can be achieved through a supporting infrastructure able to capture a huge amount of information from the environment, much more than humans do, and sending it to a processing unit able to build a representation of the context that would catch all elements necessary to interpret the specific environment. ERC project VISION [8] was started in 2010 with the aim to develop such an innovative infrastructure to support real-time sensing services with particular emphasis on 3D video, with mobile and context-aware operation: 60-GHz UWB radios to enable broadband transmissions in wireless sensor networks, a comprehensive channel model to optimize the radio design, novel techniques to manage the huge number of nodes for ubiquitous sensing, innovative tools to support the development process of intelligent services, full cross-layer adaptability to external conditions to assure the best achievable performance and support of QoS are the main objectives of the project VISION that can concur to the development of future e- and m-Health mmWaves systems.

Architectures

The basic architectures of patient-centric and hospital-centric systems are shown in Figs. 1 and 2, respectively.

Patient-centred systems are generally characterized by a three-tier architecture composed of: (1) body-worn or implanted sensors, with which the patient is equipped for personal monitoring of multiple parameters, (2) a hospital information system (HIS) for storage and management of health data, generally located in the medical facility and (3) a mobile device that generally acts as a personal gateway between the previous two entities. They also act as personal repository to store several users' information (from the usual address book to electronic health records), and use algorithms of data fusion, aggregation and elaboration to give a preliminary interpretation of sensed data, serving as a personal server (PS).

In this case, event-processing middleware and expert systems have been proposed to develop automated decision support systems (DSS) implementing thus a closed-loop approach among the patient, doctors and the PS. The use of this kind of systems allows the reduction of clinical checks and hospitalization costs, and the collection of health data from different patient-centred systems represents a wide and fundamental source of information for the medical research in terms of statistical and epidemiological studies.

Hospital-centred systems are designed to support medical professionals in their activities satisfying different requirements dependent on their role and required interactions. To achieve this objective, these systems have accomplished a longer evolution than patient-centred systems having a far-off origin. Initial solutions have been proposed to solve the problem of electronic storage of medical information to

facilitate information access and organization; they subsequently evolved providing mobile access to those data and connectivity towards patients and other medical staff inside the facility. Then, innovative solutions to improve the workflow have been developed. They involve not only human actors but also the equipment, tagged through electronic devices (e.g. radio frequency identification (RFID) originally used for localization purposes) or able to transmit collected data directly to the medical personal device, like high-resolution images (e.g. computerized axial tomography (CAT) scan, magnetic resonance imaging (MRI)) or videos from implantable devices (e.g. a capsule endoscope with VGA image capabilities). In this way, the system contributes to two main issues: (1) to improve efficiency and productivity of care professionals through increasing data access, and (2) to provide additional instruments that can help reduce the number of medical errors.

Nowadays, hospital-centred systems are evolving in this direction, exploiting current technologies like RFID, sensors, mobile devices and wireless communications; however, a complete and working solution has not been really developed yet. Looking at Fig. 2, we can identify three different subsystems which are strictly connected by multiple information flows: (1) the central subsystem is represented by the personal medical device (generally integrating an RFID reader with the capabilities of a smartphone or a tablet PC), (2) the hospital subsystem identified by the set of wireless devices distributed in the environment (both related to instruments and patient's identifications and the wireless communication infrastructure) and (3) HIS as point of collection, storage and management of health data. The communication flows involve personal medical device in order to communicate with the hospital subsystem and its components, with HIS to access stored data and with the personal devices of other colleagues to exchange data and optimize communications. Thus, the personal medical device must be able to manage different wireless technologies and communication protocols. For further details about the two architectures, we refer the interested reader to the comprehensive survey provided in [1].

UWB Communications for Healthcare

Medical and healthcare solutions can benefit from the low-power spectral density proper of UWB signals. Radiated signal power is low enough to be safe for human tissues, still providing reasonable communication range and data rate. Hence, the UWB becomes by far the best candidate for on-body communications, WBAN standards and also suitable for endoscopic devices [9]. Furthermore, the extremely wide bandwidth of UWB signals provides very accurate positioning capability, which represents a very desirable feature in both endoscopic diagnosis (patient-centric application) and organizational use, e.g. the hospital-centric applications.

Table 1 Examples of medical WBAN applications. [11]

Application	Data rate	Bandwidth (Hz)	Accuracy (bits)
ECG (12 leads)	288 kbps	100–1,000	12
ECG (6 leads)	71 kbps	100–500	12
EMG	320 kbps	0–10,000	16
EEG (12 leads)	43.2 kbps	0–150	12
Blood saturation	16 bps	0–1	8
Glucose monitoring	1,600 bps	0–50	16
Temperature	120 bps	0–1	8
Motion sensor	35 kbps	0–500	12
Cochlear implant	100 kbps	–	–
Artificial retina	50–700 kbps	–	–
Audio	1 Mbps	–	–
Voice	50–100 kbps	–	–

On-Body UWB Communication Systems

WBAN forms a special network structure to implement a small-scale operational environment for medical purposes. Several vital parameters from a human body could be monitored using small on-body sensors, preferably in a non-invasive manner. Moreover, implanted in-body sensors could provide important information on internal changes of organs or implanted devices. A communication from in-body to on-body terminals, and then to a backbone infrastructure, requires effective wireless solutions for WBAN implementation. From a radio link point of view, UWB could be such a solution.

UWB also provides tools to measure the spatial movement or trajectory of an implant after installation. This has a great impact on human healing process because the implant can non-invasively report its conditions and, thus, additional surgical operations are avoided [10].

Finally, UWB is also known in the field of radar techniques that have already been investigated for monitoring vital parameters of a patient (i.e. heart rate, respiration rate, lungs, etc.) in a non-invasive way. In a body area network (BAN), these data are collected by sensors that are communicating wirelessly with an access point placed on the body. Such sensors require two separated units: one unit for sensing and the other for communications purposes. A drastic simplification of this type of sensors could be achieved by signal processing if the signal that propagates through the body (the channel) can provide also such a vital data of interest. UWB can also be exploited for in-body communications, e.g. from an implanted sensor to the access point on a body.

Due to the strong heterogeneity of the applications, data rates will vary strongly, ranging from simple data at a few kilobits per second to video streams of several megabits per second. Data can also be sent in bursts, which means that it is sent at a higher rate during the bursts. The data rates for the different applications are given in and are calculated by means of the sampling rate, the range and the desired accuracy of the measurements [11] (Table 1).

Overall, it can be seen that the application data rates are not high. However, if one has a WBAN with several of these devices (i.e. a dozen motion sensors, ECG,

EMG, glucose monitoring, etc.), the aggregated data rate easily reaches a few Mbps, which is higher than the raw bit rate of most existing low-power radios.

The reliability of the data transmission is provided in terms of the necessary bit error rate (BER) which is used as a measure for the number of lost packets. For a medical device, the reliability depends on the data rate. Low data rate (LDR) devices can cope with a high BER (e.g. 10^{-4}), while devices with a higher data rate require a lower BER (e.g. 10^{-10}). The required BER is also dependent on the criticalness of the data.

UWB, with respect to other wireless technologies, uses a novel approach to emit signals based on the generation of short pulses over a large bandwidth (from 3.1 to 10.6 GHz in US, [3.1, 4.8] GHz and [6, 9] GHz in EU). This not only largely increases the data rate but also reduces the average power output below the threshold defined for noise (-41.3 dBm/MHz). This means that it is not susceptible to noise or jamming and it does not disturb other signals. Two modulation modes are defined for UWB: the impulse radio (IR) and multi-band orthogonal frequency division multiplexing (OFDM). IR mode uses low-power and ultra-short pulses (sub-nanoseconds intervals) while OFDM is based on a multi-banded approach (definition of smaller bands, each greater than 500 MHz) and communications occur inside each band.

The IR-UWB system transmits a train of short-duration pulses through an antenna [12]. A narrow pulse such as the second derivative of the Gaussian pulse is generated by a pulse generator. Then, the generated pulse is reshaped to fit the Federal Communications Commission (FCC) spectral mask before transmitting it through antenna. The other way is to directly generate a precise UWB pulse whose frequency spectrum satisfies the FCC regulation, which makes it easier to design digital-based transmitter systems. In the IR-UWB transmitter, the power amplifier is not needed and a complementary metal-oxide semiconductor (CMOS) output buffer can drive the antenna directly. Therefore, significant power saving can be achieved compared to other wireless transmission systems. Therefore, the IR-UWB technique facilitates carrierless transmission and greatly reduces the system complexity. Typically, pulse-position modulation (PPM) or binary phase shift keying (BPSK) is employed as a simple modulation method. Another important feature of the IR-UWB system is that the intermittent transmission with short-duration pulses enables dynamic power control for significant power reduction. For LDR, the short-duration pulses are not sent for a long time. Hence, the transceiver device can be turned off for most time and activated only when the pulses are sent. With such a low-duty cycled operation, power consumption less than 1 mW is reported for the transmitter system [10].

However, with such a low-duty cycle of the pulsed wavelet sequence, synchronization between the transmitter and the receiver becomes very challenging. Accordingly, having the active receiver window aligned with the short-duration pulses requires a considerable amount of baseband processing, resulting in increased hardware complexity and power consumption. For example, the power consumption of the transmitter in the IR-UWB system is typically less than 5 mW, but the receiver consumes power as high as 100 mW due to complicated synchronization processing with the short duration pulses. The non-coherent, self-correlating receiver is an attractive option because it simplifies the pulse-template synchronization. Unfortunately, BER

will increase as the receiver will not be able to discriminate between noise and transmitted data. In addition, the design of a clock and data recovery loop is still required, as the demodulated data needs to be phase locked with the local receiver clock. From a system's perspective, on–off keying (OOK) modulation formats that operate with more than one pulse per bit can thus be advantageous if they simplify the receiver and reduce its power consumption.

Other important characteristics of UWB are: high precision ranging (at the centimetre level), low electromagnetic radiation and low power consumption. These make it suitable for medical applications. In particular, IR mode has the capability to detect tiny movements inside the human body, in a non-invasive way, and this property can be used to measure a number of physiological signals with a high accuracy (e.g. heart and respiration rate, blood pressure) [13]. To this aim, a UWB transmitter emits discrete pulses to the human body and the reflected pulse from the organ arrives to the receiver where the result of the signal processing is stored. In addition, the low power consumption and the high data rate make an important advance in medical imaging, and one of the most promising applications in this direction is the definition of the capsule endoscope that, with the size and shape of a pill, allows doctors to visualize the digestive and gastrointestinal tract of the patient on a mobile device. All these applications are also possible due to the low electromagnetic radiation generated by the low radio power pulse making this technology safe for the human body and acceptable by patients.

Another modulation mode is emerging as promising for healthcare applications: frequency modulated (FM)-UWB [14]. It uses a double FM modulation: low-modulation index digital frequency shift keying (FSK) followed by high-modulation index analog FM to create a constant-envelope UWB signal. Different from the IR-UWB system, the FM-UWB system generates a constant-envelope UWB signal with wideband FM modulation, featuring a very steep spectral roll-off.

Because the FM-UWB receiver can perform FM demodulation without a local oscillator, carrier synchronization is not needed as in the case of the IR-UWB. As a result, overall system design can be simple and robust.

The FM-UWB can be seen as an analog implementation of a spread-spectrum system with a spreading gain equal to the modulation index, offering a low complexity constant envelope UWB signal. Low-modulation index FSK is followed by high-modulation index analog FM, creating a constant-envelope UWB signal. The receiver demodulates the FM-UWB signal without requiring local oscillator and carrier synchronization, which makes the system simpler and cheaper [9].

It supports low (100 Kbps) and medium (1 Mbps) data rate and provides the possibility to integrate communications and sensing in the same device through radar pulse. It inherits main advantages of UWB, further reducing the power consumption of IR mode. The disadvantage of the FM-UWB system is that the RF oscillator needs to be active all the time. Consequently, low-power system with dynamic power control is difficult. Also, data rate higher than 1 Mbp/s is difficult due to the limited subcarrier frequency. A device implementing this technology has not been developed in pervasive healthcare systems yet.

Finally, a further evolution is represented by UWB-RFID systems [1].

The design of UWB receivers should take into account the other electromagnetic radiations in the vicinity of the transceiver to maximize received signal-to-noise ratio and suppress unwanted signal components to prevent front-end saturation. Indeed, WBAN transmission is usually done over a band already used by other wireless systems. Furthermore, hospital environments host several electrical and electronic equipment, and electrical shot noise interference is a UWB type interference source. Finally, integration of several active BANs in the same environment leads to a considerably high probability that co-channel interference will be present, considering that in a realistic use-case, each UWB BAN typically consists of less than a dozen of nodes in the same network.

Wireless Standards for Body Area Networks

Existing wireless standards have difficulty in meeting low power and low complexity requirements for LDR WBAN devices. For the WBAN and biomedical applications, the following features are desirable:

- Low power and highly energy efficient,
- Coexistence with other wireless standards,
- Robust to multi-path interference,
- Low radiated RF power (less harmful to human body),
- High penetration capability,
- Can provide high resolution sensing network.

The IEEE 802.15 Task Group 6 was established in 2007 to develop a communication standard for BAN applications which is a short-range, low-power and highly reliable wireless communication for use in close proximity to, or inside, a human body [16]. The LDR radio for such applications needs to be of low complexity and yet robust to interference and frequency-selective multi-path and also be able to rapidly join or leave a network. The short physical layer (PHY) synchronization time simplifies the task of the medium access control (MAC), which is similar to the ones used in low power narrowband, but not necessarily robust, radios [9].

The UWB technology has received great attention in recent short-range communication systems and been considered one of the potential candidates for IEEE 802.15.6. This is due to the fact that UWB communications technology may provide robust, easy-to-implement, low-cost and low-power consumption solutions. In particular, high penetration capability and high precision ranging with a wide bandwidth of up to 7.5 GHz (from 3.1 to 10.6 GHz) make it easy to image the organs of human body for medical applications. Furthermore, low electromagnetic radiation less than -41.3 dBm/MHz is safe for human tissue exposure and makes it suitable for hospital and home applications.

UWB Radar for Medical Imaging

With the UWB dielectric properties, the organic motion-related signal is obtained from a UWB radar device aimed at the human body. Especially for heart as a cardiovascular monitor, the UWB radar could detect cardiac contractions, arterial wall

motion and a breath monitor to detect respiratory movements. Because the UWB electromagnetic signal is not influenced by clothes or blankets, and the useful range is in the order of a few metres, the use of the UWB radar in cardiac motion evaluation is a wonderful complement to the electrocardiogram [9].

Having the simple transceiver architecture, the FM-UWB system is considered a good candidate to realize UWB radar.

To achieve finer sensing resolution, multiple-frequency continuous wave radar with the FM-UWB technique is proposed.

To integrate the real-time contact-less healthcare service into the smart phone, the maximum range longer than 1 m is preferred. Another challenging part is to develop a good model of heart movement during breathing. A proper algorithm and signal processing are needed to detect the organic movement during breathing condition. Therefore, a *true* contact-less health monitoring system with the mobile devices such as smart phones needs more innovation in integration of sensing and biomedical technologies.

Even though the heart movement is monitored with the fixed medical equipment with a very short distance, it provides a practical way of contact-less monitoring system where patients do not have to take off their clothes. For high-resolution sensing, multiple FM-UWB radars may be employed. For data transmission from the sensing device to the monitoring equipment, the low power simple S-OOK-based IR-UWB transceiver is considered. By utilizing different UWB technologies for sensing and transmission, crosstalk between two transceivers is minimized. Therefore, non-invasive health monitoring with low radiated power and robust communication can be achieved as a near-term contactless body monitoring solution [9].

Location-Aided Healthcare UWB Systems

UWB indoor positioning systems have gained widespread interest mainly due to their robustness in mitigating multi-path interference and ability to resolve small path delays in the time domain. Current commercial UWB indoor positioning systems are rated at 10–30 cm of 3D real-time accuracy.

A possible application of indoor positioning systems for healthcare is the so-called ‘smart bioinstrumentation’ based on devices that combine biosensors with wireless networking capability.

The integration of the positioning functionality provides connectivity and location of the WBAN-equipped patients while they are outside of their home. In the hospital, overall efficiency can be improved by allowing multiple pieces of medical equipment to be controlled and monitored wirelessly by one single terminal device, while the positioning functionality can provide locating assets and streamlining operation of hospital staff through integrated enterprise architectures [17].

Other medical applications, like e.g., surgical navigation systems [18], typically require 3D real-time tracking capabilities far beyond typical indoor wireless positioning systems. For example, orthopaedic surgical navigation systems require 3D

real-time accuracy of 1–2 mm translational error. Tracking systems used for these applications include infrared tracking systems and magnetic tracking systems, but both have certain drawbacks including only one receiver with line-of-sight (LoS) restrictions for the infrared tracker and susceptibility to metal for the magnetic tracker. Hence, research moved towards alternative systems, like UWB. An energy detection-based UWB positioning system, which is capable of tracking a tag dynamically with 5–10 mm of 3D real-time accuracy, has been proposed in [19–21]and its use for 3D tracking of multiple tags has been discussed in [22].

A more conventional application is the localization of hospital staff, patients and instruments according to the hospital-centric approach. Indeed, in a hospital environment, hospital staff often spend considerable time locating colleagues, patients and patient-related documents. Staff are constantly moving around to perform their daily work, which includes visiting patients, locating resources (e.g. medical records) or consulting with other specialists. On the other hand, patients are also moving within wards. In the event of any emergency, such as falling down, or physiological signal is out of normal range, identifying the patient's location immediately is necessary, seamlessly. In [23, 24] a hand-held mobile device, able to display all location information of the tracked items, has been proposed based on the joint use of UWB sensors and GPS, with the advantage of providing seamless indoor/outdoor location sensing.

60-GHz mmWave Wireless Technology

mmWaves, without any doubts, are the most recent and next-generation emerging wireless communication technology. However, the scientific and industry interests for this part of the radio spectrum have been present for decades mainly by development of communication systems for military purposes (battlefield communications) because of reduced possibility for eavesdropping the low-power mmWave transmissions within given short range [25].

The main reason attracting scientists and engineers for research and development of communication systems in mmWaves is certainly the huge and continuous bandwidth available at this part of the spectrum. Comparing with the contemporary wireless technologies, where the bandwidth is of the size of several tens of megahertz, in mmWaves it can be several hundred times larger. For instance, comparing available at least 3.5-GHz continuous bandwidth at 60-GHz band in all countries with the maximum of 160 MHz in the newest 802.11ac standard, there is more than 20 times available bandwidth at 60 GHz. Figure 3 illustrates the worldwide availability of 60-GHz band.

One can conclude that such a huge bandwidth at this high frequency could produce some processing limitations. However, hardware and DSP constraints for processing such huge bandwidth are today mostly overcome. With the rapid growth and advances of microelectronics and high-density low-cost application specific integrated circuits (ASICs), especially in the last 5 years, tasks like complex signal processing at higher

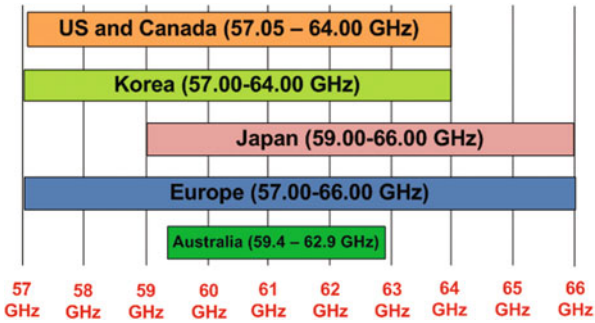

Fig. 3 Worldwide 60-GHz band availability

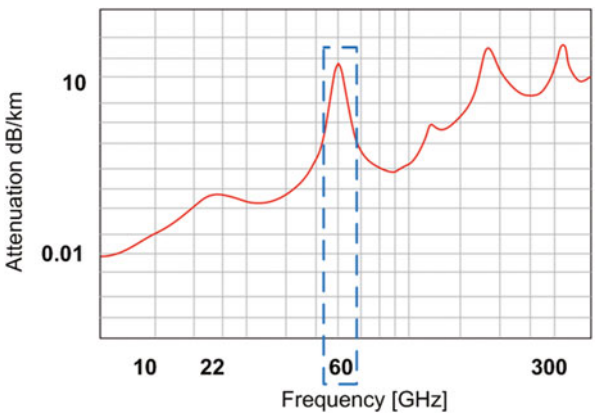

Fig. 4 Attenuation due to oxygen absorption in 60-GHz band

frequencies and wide bandwidth digital processing are achievable at reasonable costs, form factor and energy efficiency. Current solutions are mainly based on CMOS and SiGe IC technology [26]. The wavelength of 5 mm provides perfect conditions for fabrication and integration of on-chip directional antennas. This fact is supporting the consideration of the 60-GHz wireless radios as a valuable candidate for the SoC (system on chip) and NoC (network on chip) concepts for future communication technology.

The fact that radio waves in this band experience high path loss and attenuation due to oxygen limits the operational range of 60-GHz wireless networks within short-range WLAN and PAN applications. The RF absorption peak at 60-GHz band due to atmospheric resonance with oxygen molecules should not be taken as limitation for low-power transmissions as it starts to become significant for range which is greater than 100 m (Fig. 4). It is well known that low-power transmissions do not propagate so far, and this is an advantage for realizing higher frequency reuse density. The free space path loss over 1 m at 60 GHz is around 68 dB which is more than 21 dB worse comparing with the band at 5 GHz.

However, even with those constraints, the application field for 60-GHz wireless networks is still wide, targeting applications from high speed files exchange, multimedia and entertainment systems to security, surveillance and biomedical applications.

Academia, industry and standardization bodies realized an enormous number of scientific research projects and activities for modelling the wireless channels, specifying the potential applications and defining communication standards in a way to integrate this technology as a part in the next-generation heterogeneous networks. At this point, we must clarify that there are still open research challenges in this technology from all aspects, beginning with channel modelling and measurements for the propagation behaviour in different environments, spectrum and carrier allocation techniques, optimal coding and modulation schemes, effective and intelligent antennas to adaptive and performance-aware DSP capable of supporting different QoS requirements and service diversity.

60-GHz Standardization

The first try for standardization of higher frequency bands which also affected the UWB and mmWave radios was 802.16 in 2001 allowing communication links from 2 to 66 GHz. However, the standard was targeting mobile applications and recommendations were to use lower bands which are not unlicensed, most crowded and expensive for allocation.

To overcome the data rate limitations of 802.11 wireless local area networks (LANs) which started facing the future usage models with high demand for multimedia applications, two new IEEE working groups were started: TGac—to specify extensions of 802.11n with challenge to achieve 1 Gbps (802.11ac at 5-GHz band), and TGad which in partnership with WiGig (Wireless Gigabit Alliance) have proposed 802.11ad with target to provide up to 7 Gbps by using 2 GHz of the spectrum at 60 GHz. This standard is expected to arrive in the market in the early days of 2014. 802.11ad is backward compatible with 802.11 management plane including mechanism for very fast session transfer among 2/5/60-GHz infrastructure networks.

In 2005, TG3c group was founded by IEEE with task to provide mmWave PHY specification upgrade for IEEE 802.15.3-2003. In 2006, ECMA TC-48 (TC32-TG20) started the tasks for standardization of PHY and MAC for high data rate 60-GHz multimedia streaming and large data exchange applications. ECMA TC-48 developed the ECMA 387 specifications for high data rate PHY, MAC and HDMI PAL. Interesting point is that in ECMA 387 [27], depending on power constraints and complexity, three types of devices are defined: Type A, B and C, where Type A are the most power-consuming/complex while Type C are least complex and power-consuming devices with lower data rate requirements. The most important goal of this standard was to provide longer operation time on battery-powered devices by implementing two power management modes, active and hibernation, with ability of the devices to select optimal combination of power and transmit rate to reduce BER/FER by allowing the receiving device to recommend data rate and power level based on QoS requirements of the service and the sending device may request feedback for the link quality to finally decide the transmit data rate and power level. Hence, the protocol complexity has increased, especially for Type A devices where by the specification

Table 2 Modulation and coding schemes with respective proposed data rates in 802.11ad specification for single carrier SC and OFDM PHY. [28]

SC PHY				OFDM PHY			
MCS index	Modulation	Code rate	Data rate (Mbps)	MCS index	Modulation	Code rate	Data rate (Mbps)
1	π/2-BPSK	1/2	385	13	SQPSK	1/2	693.00
2	π/2-BPSK	1/2	770	14	SQPSK	5/8	866.25
3	π/2-BPSK	5/8	962.5	15	QPSK	1/2	1,386.0
4	π/2-BPSK	3/4	1,155	16	QPSK	5/8	1,732.5
5	π/2-BPSK	13/16	1,251.2	17	QPSK	3/4	2,079.0
6	π/2-QPSK	1/2	1,540	18	16-QAM	1/2	2,772.0
7	π/2-QPSK	5/8	1,925	19	16-QAM	5/8	3,465.0
8	π/2-QPSK	3/4	2,310	20	16-QAM	3/4	4,158.0
9	π/2-QPSK	13/16	2,502.5	21	16-QAM	13/16	4,504.5
10	π/2-16QAM	1/2	3,080	22	64-QAM	5/8	5,197.5
11	π/2-16QAM	5/8	3,850	23	64-QAM	3/4	6,237.0
12	π/2-16QAM	3/4	4,620	24	64-QAM	13/16	6,756.7

beamforming is mandatory, while Type B devices may receive beamforming training of Type A devices in order to specify optimal antenna weight vector.

In 2006, WirelessHD consortium was founded by a number of key consumer electronics companies with the task of delivering specification for uncompressed audio/video streaming based on 60-GHz radios.

Summarizing, the latest and most advanced development stage in 60-GHz standardization at this moment is 802.11ad with unified specification for 60-GHz wireless radios creating interoperable protocols for wide range of applications and coexisting with other 60-GHz systems: 802.15.3.c and ECMA-387 devices. In the following section, 802.11ad will be summarized from the aspect of the most important PHY and MAC functionalities, data rate transfer speeds and carrier allocation schemes.

The IEEE 802.11ad

The general purpose of the IEEE 802.11ad standards is to improve 802.11 user experiences in drastically higher data rates at UB (ultra band) frequencies from 57 to 66 GHz. The IEEE 802.11ad PHY defines specification for both single-carrier referred to as SC PHY and multi-carrier channel multiplexing referred to as OFDM PHY [28].

Modulation and coding schemes (MCSs) available for usage are represented with indexes from 1 to 24 where MCS indices from 1 to 12 define single-carrier transmission while MCS indexes from 13 to 24 are dedicated to OFDM-based transmissions. Table 2 contains detailed MCSs and recommended modulation and code rates for SC PHY and OFDM PHY with corresponding achievable data rates for different MCSs.

802.11ad also defines optional modulation and coding schemes for low-power transmission based on single-carrier channel with limited data rates up to 2.5 Gbps (low-power SC PHY). This mode can provide drastically lower processing power by

Table 3 Modulation and coding schemes for low-power SC PHY in 802.11ad with corresponding data rates. [28]

MCS	Modulation	Effective code rate	Coding scheme	Rate (Mbps)
25	π/2-BPSK	108/224	RS (224,208) + Block-Code (16,8)	626
26	π/2-BPSK	208/224	RS (224,208)	1,251
27	π/2-QPSK	208/224	RS (224,208)	2,502

mmWave transceivers. MCS indices corresponding to low-power SC PHY are those from 25 to 27 (Table 3).

The control PHY is represented with MCS indice of 0. It defines the minimum data rate that devices use to communicate before high-rate beam-formed link establishment. The modulation of MCS 0 is BPSK with 1/2 coding achieving the necessary minimal required 27.5 Mbps. This PHY mode is used for transmitting and receiving control frames as beacons, management control frames and request-response probes.

Next Generation (5G) Mobile Wireless Technology

The term 5G is used in many research papers and projects to denote the next step of mobile communication standard beyond current 4G/IMT-Advanced and is not still described in any official specification document. However, the scientific debate is going on with daily increased number of scientific papers with proposals for future 5G system architecture and services. One of the main points in next generation 5G networks will be the ability of the devices to have access to different wireless technologies based on OWA (Open Wireless Architecture) by using software-defined radios, and ability to combine different flows from different wireless networks [29, 30].

At the time of writing this text, Samsung announced its own 5G prototype network based on mmWave technology at 28 GHz which can reach 200 m without LoS and 256 Mbps error-free messages, while 512 Mbps can be reached without significant errors [31].

In [32], the authors are summarizing their extensive research in mmWave technology into promising conclusions about future 5G backbone based on mmWaves operating at 28 and 38-GHz band.

mmWaves for Broadband Mobile Biomedical Applications

Biomedical engineering is reducing the gap between engineering and medicine by joint scientific research projects and foundations of research centres as NYU WIRELESS which is the first academic research centre combining wireless technologies computing and medicine [33]. Wireless technologies, however, do not participate yet with significant presence as key communication technology in the healthcare environments and hospitals. eHealth as future healthcare concept requires mobility and reliable communication techniques as it is based on highly integrated heterogeneous networks.

eHealth attracted great scientific interest in the last decade. Several emerging technologies are basically supporting this concept realization:

- Advances in wireless sensor networks (WSN),
- High sophisticated mobile devices with advanced software development platforms for mobile applications,
- Cloud computing.

A first step towards successful eHealth system is RPM , enabling monitoring of patients inside and outside conventional clinical environment. Successful low-power wireless sensor networks implementations for RPM and BANs are reported in the literature, mainly using 802.15.4 radios (ZigBee), and several commercial solutions are available in the market. In any case, mmWave low-power solutions are also considered as they can provide drastically faster transfers and possibility for implementation of more sophisticated sensors capable of real-time capturing of complex signals and body functions.

Several application scenarios, several application scenarios in biomedical engineering can be realized combining different wireless technologies as WSN, 60 GHz, UWB and future 5G. Figure 5 illustrates a possible scenario for RPM based on low-power WSN, 60 GHz and 5G, where multi-interface FFD (fully functional device) is collecting the parameters of BAN and environment, while 60-GHz link is providing high-resolution video monitoring of the patient and allowing the patient to realize high-quality audio/video connections with physician at remote location or to use eHealth services available in the cloud. In a case of critical parameter conditions sensed by the BAN, the intelligent FFD device is able to alarm the remote emergency service and provide further instructions to the patient.

Also, at this point we must emphasize other two emerging technologies as very serious candidates for the future RPM technology: implantable devices and intelligent pills.

In [34], the evolution of implantable devices, such as brain electrodes, neurostimulators, etc., and their wiring problems are emphasized, where low-power mmWaves are considered as key communication technology. The studies conducted in [35] and [36] reported promising results for implementation of BANs based on 60-GHz radios, for off-body and on-body scenarios respectively. In [35], it is shown that in spite of the small distance between the antenna and the body, the impedance matching and antenna gain are almost not affected by the presence of the body.

Scientists from Philips Research are developing intelligent pill named IntelliCap for electronically controlled drug delivery via the intestinal tract where the main challenge is navigating a drug-loaded pill capsule to the right site of the disease [37]. Low-power 60-GHz radios due to small antenna size and possibility for flexible on-chip integration of the antenna arrays are the most serious candidate for those emerging technologies.

Application of 60-GHz wireless technologies is also interesting in hospital environments for realization of medical device networks. Advances in medical devices, such as MRI, tend to provide scans with excellent quality based on several hundred slices in forming the MRI profile. Special designed standard DICOM (digital

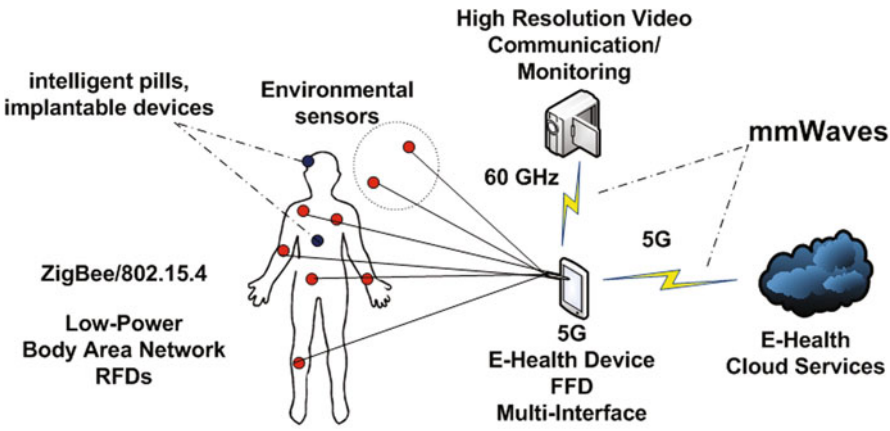

Fig. 5 Remote patient monitoring (RPM)

imaging and communications in medicine) is managing the transfer of those scans (images) to remote locations in special file format for further analyses. The resistance of mmWaves in medical environments to EMI (electromagnetic interference) is a key advantage of 60 GHz as image transfer technology in future medical imaging devices. Today's modern MRI provides high-quality imaging which is drastically increasing the images file size. Multi-gigabit network based on 60 GHz will allow real-time high-speed transfer of the scans to local and remote locations, combining with future mmWave 5G wireless mobile technology.

In Fig. 6, we illustrate a scenario which enables high-speed medical imaging transfers and possibilities for remote medical diagnostics and at the same time has ability to include several parties in the diagnostic procedure.

In Fig. 6, MRI device equipped with 60-GHz wireless interface is performing scans and transferring the DICOM-formatted images to local database and to the radiologist's device. 5G device is providing real-time access to the cloud with possibility to include several remote parties and using cloud services like expert systems, image processing web services, remote storage, etc. Physician on remote location is able to control and monitor the diagnostic procedure receiving the scans/images in real-time. The concept is able to include academia for educational and research purposes (Fig. 6).

VISION as a Support to Cognitive Behavioural Systems

A research supported by VISION ERC project [8] on on its potential application in cognitive behavioural systems was conducted in [7]. The scenario of the system is illustrated in Fig. 7. Heterogeneous network based on 802.15.4, UWB and 60

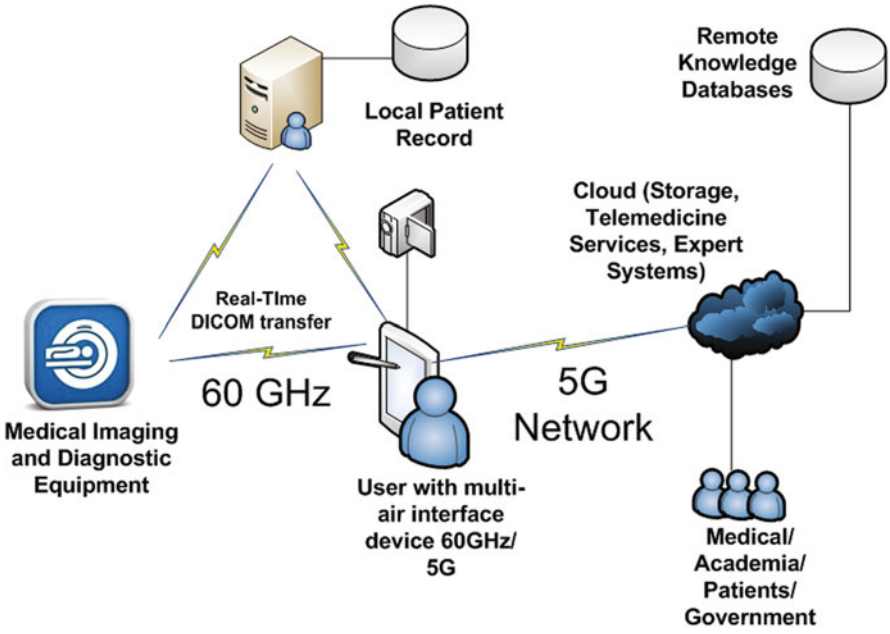

Fig. 6 60-GHz/5G wireless technologies scenario for remote medical diagnostics system realization

GHz is proposed based on VISION infrastructure and HW/SW node model for the realization of a system for impaired children control (Fig. 7).

People who have difficulties in communicating verbally, such as communicative impaired children (i.e. children with aphasia or dyslexia, general speech language impairments), send non-verbal messages that are not immediately captured by caregivers and parents, especially if they are not expert. For example, a child might appear calm and receptive to learning or enjoining in playing a game, while he/she is sad or angry or simply he/she dislikes the activity in which he/she is involved. For this reason, he/she is inattentive or may become aggressive for no reason. This scenario makes useless the attempt to teach or simply entertain the children.

This fundamental communication problem can be addressed by enabling two main functionalities: (1) to collect longitudinal data of emotion-related expressive and physiological signals, in order to reveal the internal state that influence child's behaviour and (2) to provide such information to caregivers to quickly intervene, in order to test the clinical and perceived effectiveness of the applied therapies in the treatments of childhood language disorders. The functionality (1) is enabled if the room is equipped with hidden video sensors, the patient is equipped with physiological sensors analysed in a body area network and hidden microphones are placed around. The functionality (2) is enabled if the above mentioned sensing units can transmit the captured data in real time to a control unit, which forwards global status information, alerts and suggests suitable behaviour and therapies to the

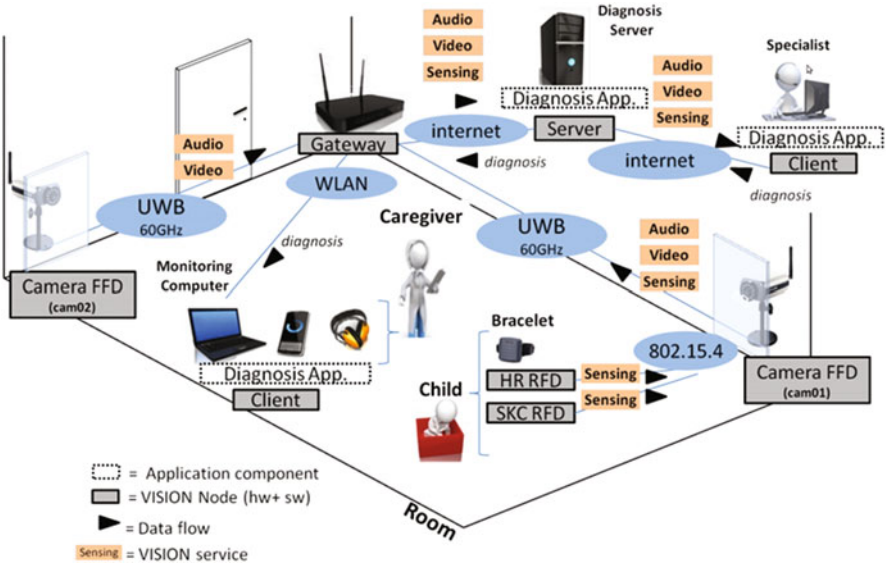

Fig. 7 VISION-based scenario of system for impaired children control

caregiver. This is a typical remote monitoring system, where the 3D-video sensing is fundamental for the success of cares.

VISION infrastructure [38] is able to provide both functionalities in an optimized way because its wireless technology allows the best placement of sensors transparently to the impaired child, even on his/her body; the broadband technology enables the real-time transfer to the control unit and the middleware allows the best reliability of the system and the selection of the relevant data to be collected and transmitted.

VISION can additionally provide artificial tools, such as virtual agents and avatars, that can help in maintaining the attentive focus of the children and enhance the quality of their learning, engaging them in new activities as soon as the monitoring of their involvement in the current activity is understood by the system as degraded or not any more attractive. For further details, we refer the interested reader to [7].

Because this is an indoor scenario, VISION project is focusing on the optimization of the 60-GHz broadband communication system starting from an accurate modelling of the indoor environment. A 60-GHz measurement campaign was performed in a modern building at the University of L'Aquila, Italy. Measurements were realized for two large bands around 60 GHz, i.e. 54–59 and 61–66 GHz. Measurements were done at several different locations, in LoS and non-line-of sight (NLoS) scenarios and using different combinations of transmitting and receiving antennas: either omnidirectional or directional antennas with a beam width of 30 or 9°, respectively. In [39–41], it was shown that the parameters of the path loss models for 60-GHz channels in modern buildings assume values comparable to UWB channels. Another contribution of VISION is the testing of the proposed 802.11ad, 60-GHz standard over a realistic wireless channel, including the presence of human bodies around or in the proximity

of the transmitting and receiving radios, which is typical for the above mentioned scenarios for biomedical applications.

Conclusion

We presented a survey of current research and available results on UWB and mmWave technologies for healthcare applications. UWB has a long story as wireless technology for seamless and non-invasive healthcare services, which also led to the reference standards for WBANs. mmWave radio represents the basic technology for future access and mobile (5G) communications. We proposed some interesting scenarios to show that it is a valuable candidate for all future healthcare systems that may require a very large bandwidth, such as MRI real-time remote diagnostic. UWB provides also additional features like radar for imaging and localization capabilities. We sketched possible scenarios of applications of these additional features. Finally, we provided insights about the VISION project, concerning a healthcare scenario for cognitive applications for impaired children.

Acknowledgments This work was partially supported by the ERC Starting Independent Researcher Grant VISION (Contract n. 240555).

Nikola Rendevski is on leave at the University of L'Aquila through the EUROWEB (Erasmus Mundus) student exchange program from Ss. Cyril and Methodius University in Skopje, Macedonia. He has teaching assistant position at St. Kliment Ohridski University, Bitola, Macedonia, Faculty of Administration and Information Systems Management, Bitola, Macedonia.

References

1. F. Delmastro, Pervasive communications in healthcare. Comput. Commun. **35**, 1284–1295 (2012)
2. C. Park, T. Rappaport, Short-range wireless communications for next-generation networks: UWB, 60 GHz millimeter-wave WPAN, and ZigBee. IEEE Wirel. Commun. **14**(4), 70–78 (2007)
3. D. Cassioli, M.Z. Win, A.F. Molisch, The ultra-wide bandwidth indoor channel: from statistical model to simulations. IEEE J. Sel. Area. Comm. **20**, 1247–1257 (Aug 2002)
4. A.F. Molisch, D. Cassioli, C.-C. Chong, S. Emami, A. Fort, B. Kannan, J. Karedal, J. Kunisch, H.G. Schantz, K. Siwiak, M.Z. Win, A comprehensive standardized model for ultrawideband propagation channels. IEEE T. Antenn. Propag. **54**(11), Part 1, 3151–3166 (Nov 2006)
5. G. Valerio, N. Chahat, M. Zhadobov, R. Sauleau, Theoretical and experimental characterization of on-body propagation at 60 GHz. 7th European Conference on Antennas and Propagation (EUCAP 2013)—Convened Sessions
6. N. Chahat, M. Zhadobov, L. Le Coq, S.I. Alekseev, R. Sauleau, Characterization of the interactions between a 60 GHz antenna and the human body in an off-body scenario. IEEE T. Antenn. Propag. **60**(12) (Dec 2012)
7. L. Berardinelli, D. Cassioli, A. Di Marco, A. Esposito, M.T. Riviello, C. Trubiani, VISION as a support to cognitive behavioural systems. Cognitive Behavioural Systems, EUCogII-SSPnet-COST 2102—Lecture Notes in Computer Science (LNCS, Springer), 2012

8. http://www.vision-ercproject.eu. Accessed 1 July 2013
9. W. Rhee, N. Xu, B. Zhou, Z. Wang, Low power, non invasive UWB systems for WBAN 2 biomedical applications. International Conference on Information and Communication Technology Convergence (ICTC), 35–40, 2010
10. M. Hämäläinen, A. Taparugssanagorn, R. Tesi, J. Iinatti, Wireless Medical Communications Using UWB. ICUWB 2009 (9–11 Sept 2009)
11. B. Latré, B. Braem, I. Moerman, C. Blondia, P. Demeester, A survey on wireless body area networks. Wirel. Netw. **17**, 1–18 (2011)
12. M.Z. Win, R.A. Scholtz, Impulse radio: how it works. IEEE Commun. Lett. **2**(1) (Jan 1998)
13. E. Staderini, UWB radars in medicine. IEEE Aero. El. Sys. Mag. **17**(1), 13–18 (2002)
14. E. Cianca, B. Gupta, FM-UWB for communications and radar in medical applications. Wireless Pers. Commun. **51**(4), 793–809 (2009)
15. F. Delmastro, Pervasive communications in healthcare. Comput. Commun. **35**, 1284–1295 (2012)
16. IEEE 802.15 WPAN^{TM} Task Group 6 Body Area Networks (BAN), website URL: http://www.ieee802.org/15/pub/TG6.html
17. M.R. Mahfouz, G. To, M.J. Kuhn, Smart instruments: wireless technology invades the operating room. IEEE Topical Conference on Biomedical Wireless Technologies, Networks, and Sensing Systems (BioWireleSS 2012), Santa Clara, CA, 33–36 (15–18 Jan 2012)
18. B. Merkl, M. Kuhn, M. Mahfouz, D. DeBoer, Surgical navigation systems: evaluating electromagnetic versus optical technology in the OR. Annual Meeting of American Academy of Orthopaedic Surgeons, San Francisco, CA, 2008.
19. C. Zhang, M. Kuhn, B. Merkl, A. Fathy, M. Mahfouz, Realtime non-coherent UWB positioning radar with millimeter range accuracy: theory and experiment. IEEE T. Microw. Theory **58**(1), 9–20 (2010)
20. M. Kuhn, M. Mahfouz, J. Turnmire, Y. Wang, A. Fathy, A multi-tag access scheme for indoor UWB localization systems used in medical environments. IEEE Topical Conference on Biomedical Wireless Technologies, Networks, and Sensing Systems (BioWireleSS), Phoenix, AZ, 75–78, 2011
21. E. Elkhouly, A. Fathy, M. Kuhn, M. Mahfouz, Investigation of challenges towards achieving sub-millimeter accuracy for UWB localization. IEEE International Symposium on Antennas and Propagation, Spokane, WA (July 2011)
22. M.J. Kuhn, M.R. Mahfouz, N. Rowe, E. Elkhouly, J. Turnmire, A.E. Fathy, Ultra wideband 3-D tracking of multiple tags for indoor positioning in medical applications requiring milimeter accuracy. IEEE Topical Conference on Biomedical Wireless Technologies, Networks, and Sensing Systems (BioWireleSS 2012), Santa Clara, CA, 57–60 (15–18 Jan 2012)
23. L. Jiang, L.N. Hoe, L.L. Loon, Integrated UWB and GPS location sensing system in hospital environment, The 5th IEEE conference on industrial electronics and applications (ICIEA 2010). Taichung, 286–289 (15–17 June 2010)
24. M.R. Mahfouz, M.J. Kuhn, Y. Wang, J. Turnmire, A.E. Fathy, Towards sub-millimeter accuracy in UWB positioning for indoor medical environments. IEEE Topical Conference on Biomedical Wireless Technologies, Networks, and Sensing Systems (BioWireleSS 2011), Phoenix, AZ, 83–86 (16–19 Jan 2011)
25. S.-K. Yong, P. Xia, A. Valdes-Garcia, *60 GHz Technology for Gbps WLAN and WPAN: From Theory to Practice*. (Wiley, 2010)
26. http://cp.literature.agilent.com/litweb/pdf/5990-9697EN.pdf. Accessed 1 July 2013
27. High Rate 60 GHz PHY, MAC and PALs, Standard ECMA-387, ser. 2nd Ed. ECMA, (http://www.ecma-international.org/publications/files/ECMA-ST/ECMA-387.pdf. Accessed 1 July 2010)
28. http://standards.ieee.org/findstds/standard/802.11ad-2012.html. Accessed 1 July 2013
29. T. Janevski, 5G mobile phone concept. Consumer Communications and Networking Conference, 2009. CCNC 2009. 6th IEEE, 1, 2, (10–13 Jan 2009). doi:10.1109/CCNC.2009.4784727
30. A. Gohil, H. Modi, S.K. Patel, 5G technology of mobile communication: a survey. Intelligent Systems and Signal Processing (ISSP), 2013 International Conference on 288, 292, (1–2 Mar 2013). doi:10.1109/ISSP.2013.6526920

31. http://www.technologyreview.com/news/515631/samsung-says-new-superfast-5g-works-with-handsets-in-motion/. Accessed 1 July 2013
32. T.S. Rappaport, S. Sun, R. Mayzus, H. Zhao, Y. Azar, K. Wang, G.N. Wong, J.K. Schulz, M. Samimi, F. Gutierrez, Millimeter wave mobile communications for 5G cellular: it will work! Access IEEE **1**, 335, 349 (2013). doi:10.1109/ACCESS.2013.2260813
33. http://nyuwireless.com. Accessed 1 July 2013
34. http://nyuwireless.com/VTSPlenary.pdf. Accessed 1 July 2013
35. N. Chahat, M. Zhadobov, L.L. Coq, S.I. Alekseev, R. Sauleau, Characterization of the interactions between a 60-GHz antenna and the human body in an off-body scenario. Antennas and Propagation, IEEE Transactions on **60**(12), 5958, 5965 (Dec 2012). doi:10.1109/TAP.2012.2211326
36. G. Valerio, N. Chahat, M. Zhadobov, R. Sauleau, Theoretical and experimental characterization of on-body propagation at 60 GHz. Antennas and Propagation (EuCAP), 2013 7th European Conference on (8–12 Apr 2013), 583, 585
37. http://www.research.philips.com/initiatives/intellicap/index.html. Accessed 1 July 2013
38. D. Cassioli et al., A successful VISION: video-oriented UWB based intelligent ubiquitous sensing. IEEE Consumer Communications and Networking Conference, (CCNC'2011), 963–964, (Las Vegas, NV, Jan 2011)
39. S. Piersanti, L.A. Annoni, D. Cassioli, Millimeter waves channel measurements and path loss models, Communications (ICC), 2012 IEEE International Conference on (10–15 June 2012), 4552, 4556. doi:10.1109/ICC.2012.6363950
40. D. Cassioli, 60 GHz UWB channel measurement and model. Ultra-Wideband (ICUWB), 2012 IEEE International Conference on (17–20 Sept 2012), 145, 149. doi:10.1109/ICUWB.2012.6340429
41. D. Cassioli, L.A. Annoni, S. Piersanti, Characterization of path loss and delay spread of 60 GHz UWB channels vs. frequency. Communications (ICC), 2013 IEEE International Conference on 3746–3750

A Low Power Interference Robust IR-UWB Transceiver SoC for WBAN Applications

Yuan Gao, Xin Liu, Yuanjin Zheng, Shengxi Diao, Weida Toh, Yisheng Wang, Bin Zhao, Minkyu Je and Chun-Huat Heng

Abstract An integrated 3–5 GHz impulse radio ultra-wideband (IR-UWB) transceiver system on chip (SoC) for wireless body area network (WBAN) applications is presented. To enhance system robustness against narrow band interference (NBI) signals, receiver low noise amplifier (LNA) input matching network is optimized to reject out-band NBI. A noncoherent energy detection scheme using analog squarer with band-pass filtering is utilized to increase the rejection to both in-band/out-band NBI. A low-power pulse synchronization algorithm is implemented in the digital baseband. The proposed transceiver achieves energy efficiency of 0.3 and 4.3 nJ/bit for TX and RX respectively and a receiver sensitivity of -92 dBm ($\mathrm{BER} = 10^{-3}$) for UWB on-off keying (OOK) signal at 1 Mb/s pulse rate. The measured maximum in-band/out-band SIR for $\mathrm{BER} = 10^{-3}$ is -33 and -47 dB, respectively.

Keywords Impulse radio ultra-wideband (IRUWB) · Wireless body area network (WBAN) · Transceiver · System on chip (SoC) · Medical monitoring

Introduction

Wireless body area network (WBAN) technology is developing rapidly in recent years as it provides a platform to support various sensors deployment around human body for emerging healthcare applications [1, 2]. Figure 1 illustrates a typical application scenario of WBAN technology in personal healthcare. Different physiological signals such as electrocardiogram (ECG), respiration rate, body temperature,

Y. Gao (✉) · X. Liu · S. Diao · W. Toh · B. Zhao · M. Je
Institute of Microelectronics, A*STAR, Singapore, Rep. of Singapore
e-mail: gaoy@ime.a-star.edu.sg

Y. Zheng · Y. Wang
School of Electrical and Electronic Engineering,
Nanyang Technological University, Singapore, Rep. of Singapore

C.-H. Heng
Department of Electrical and Computer Engineering,
National University of Singapore, Singapore, Rep. of Singapore

M. R. Yuce (ed.), *Ultra-Wideband and 60 GHz Communications for Biomedical Applications,* DOI 10.1007/978-1-4614-8896-5_2,

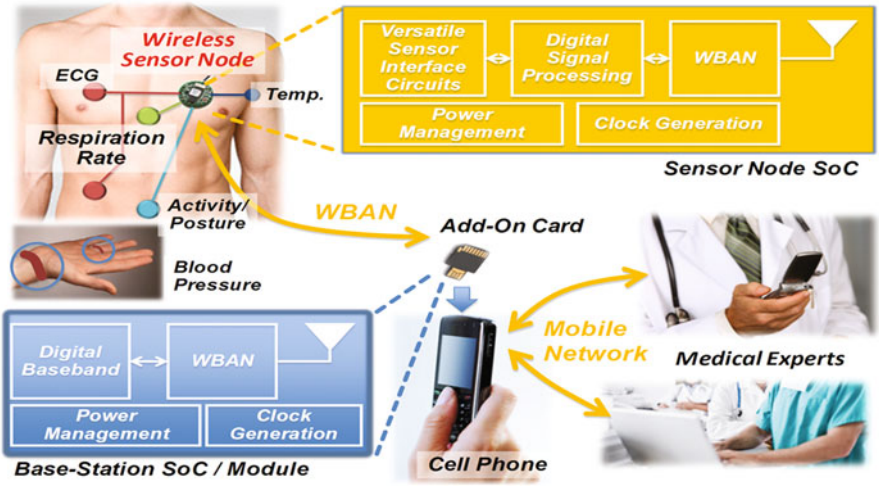

Fig. 1 Application scenario of wireless body area network (WBAN) technology in personal healthcare

etc. are acquired by individual sensors attached to the human body. The data are combined at the wireless sensor node and transmitted through the WBAN wireless link to a portable personal base-station which can be installed in a smart phone. The data can be further transferred to a remote healthcare center for detailed analysis and diagnosis by medical professionals. Benefiting from technology advances in biomedical sensor, wireless communication, and integrated circuits, the WBAN technology helps to develop miniaturized, lightweight, ultra-low power physiological healthcare surveillance and monitoring devices, for the improvement of human lives [3–5].

Among all kinds of wireless communication systems suitable for WBAN applications, impulse radio ultra-wideband (IR-UWB) is well known for its unique low-power and high data-rate merits [6]. In an IR-UWB system, information is encoded in a very narrow pulse of a few nanoseconds, which only occupies a small fraction of the symbol period. Exploiting the low duty cycle of IR-UWB signaling, the transceiver can achieve low power operation with high energy efficiency. Noncoherent energy detector (ED) can be employed in the IR-UWB receiver, which eliminates power consuming local oscillator and carrier synchronization blocks. The simplified receiver architecture also leads to power reduction and faster turn on time. Therefore, IR-UWB has been chosen by IEEE 802.15.6 task group as one of the physical layer solution for high data rate WBAN system [7].

In a noncoherent ED receiver, the energy of the received signal is measured and compared to an appropriately selected threshold to determine the presence of a signal. For an additive white Gaussian noise (AWGN) channel and completely unknown signal parameters, ED provides the optimal detection performance [8]. However, the performance of the conventional ED is sensitive to the narrowband interferences (NBI). The strong signals from other existing narrow-band wireless communication systems can saturate the high-gain IR-UWB RF front-end and ED. The major

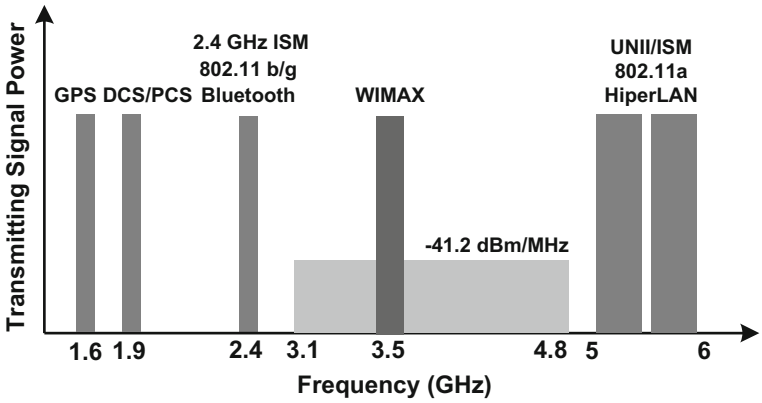

Fig. 2 Major interferers for the 3–5 GHz impulse radio ultra-wideband (IR-UWB) system

interferers to the 3–5 GHz IR-UWB system are illustrated in Fig. 2. The 2.4 GHz industrial science medical (ISM) band is currently adopted by 801.11 b/g WLAN and Bluetooth. The 5 GHz Unlicensed National Information Infrastructure (UNII)/ISM band is divided into two, 5.2–5.8 GHz sub-bands. Besides, in-band interferer such as WiMAX service occupies the 3.4–3.9 GHz bands. Effective suppression of both in-band/out-of-band interference signals is critical for the deployment of IR-UWB communication system for practical applications.

In this chapter, an interference robust single-chip IR-UWB transceiver SoC including RF transceiver and digital baseband for WBAN applications is presented. In-band/out-of-band interference suppression functions are incorporated using notch filter in low noise ampliflier (LNA) matching network and an ED with frequency conversion characteristics. A low-power pulse synchronization algorithm is implemented in the digital baseband. The proposed IR-UWB system on chip (SoC) has been successfully applied in a continuous vital signal monitoring system and the performance is verified with measurement results.

System Architecture

The block diagram of the proposed IR-UWB transceiver SoC is shown in Fig. 3 [9]. A fully differential transceiver radio frequency (RF) front-end architecture is adopted in this design to provide good suppression of common mode noise in power supply and noise through substrate coupling. It also provides direct connection to the external differential antenna, without using bulky and lossy balun circuit. Time-division multiplexing is adopted to activate the TX and RX alternately through the control of on-chip T/R switch.

On the TX side, a fast startup LC voltage-controlled oscillator (VCO) controlled by TX data, generates the UWB pulse and then is amplified by a driving amplifier (DA).

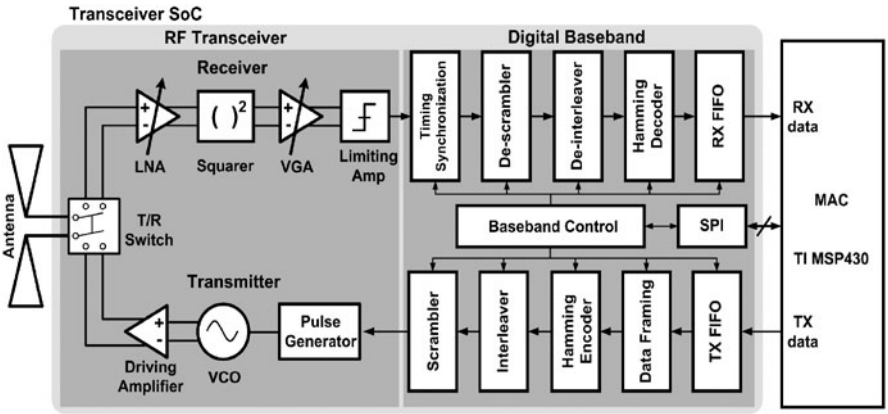

Fig. 3 Block diagram of the impulse radio ultra-wideband (IR-UWB) transceiver system on chip (SoC)

Both VCO and driving amplifier only consume power during the pulse generation. On the RX side, the weak received signal from antenna is amplified by an LNA, followed by a squarer as energy detector to recover the signals. A variable gain amplifier (VGA) further boosts the signal level and finally the analog signal is digitized by a limiting amplifier. Narrow band interference (NBI) is suppressed by embedded notch filter in LNA and the frequency conversion characteristics of energy detector.

Digital baseband (DBB) provides synchronization, forward error correction (FEC) coding/decoding, and data framing/de-framing for the TX and RX data respectively. The media access control (MAC) layer is implemented in a Texas Instrument (TI) low-power microcontroller MSP430 which communicates with transceiver SoC through SPI and dedicated data lines.

In an IR-UWB system, the transmitted signal consists of a sequence of pulses, modulated by information symbols. For the purpose of studying the mechanism of NBI suppression, we focus on the signals in a single period in the interval $(0, t_p)$, where t_p is the pulse period. To simplify the analysis, the multipath effect and circuit noise contribution are neglected. The LNA output signal is expressed as:

$$r(t) = s(t) + i(t) \quad t \in (0, t_p), \tag{1}$$

where *s(t)* is the UWB signal and *i(t)* is the NBI signal.

The carrier-based UWB pulse signal *s(t)* can be approximated as a Gaussian pulse, modulated by a carrier signal, which is expressed as:

$$s(t) = A_s e^{-\pi\left(\frac{t-t_0}{2\tau}\right)^2} \cos(2\pi f_c t), \tag{2}$$

where A_s is the amplitude of the pulse, 2τ represents the duration of the pulse, t_0 is the time delay and f_c is the carrier frequency.

The narrowband interferer is modeled as a single-tone interferer, shown in Eq. (3) for analytical simplicity. However, the results derived for a single-tone interferer also apply for an interferer which can be modeled as a band-limited random process. This will be validated by the measurement results.

$$i(t) = A_i \cos(2\pi f_i t) \tag{3}$$

Based on the input/output relationship of an ideal squarer, the squarer output $V_{out}(t)$ can be written as:

$$\begin{aligned} V_{out}(t) &= K[s(t) + i(t)]^2 = K\left[A_s e^{-\pi\left(\frac{t-t_0}{2\tau}\right)^2} \cos(2\pi f_c t) + A_i \cos(2\pi f_i t)\right]^2 \\ &= K A_s^2 e^{-2\pi\left(\frac{t-t_0}{2\tau}\right)^2} \frac{1+\cos(2\pi f_c t)}{2} + K A_i^2 \frac{1+\cos(2\pi f_i t)}{2} \\ &\quad + K A_s A_i e^{-\pi\left(\frac{t-t_0}{2\tau}\right)^2} \{\cos[2\pi (f_c - f_i) t] + \cos[2\pi (f_c + f_i) t]\} \end{aligned} \tag{4}$$

It can be observed from Eq. (4) that, after squarer operation, *s(t)* would be split into two parts. The first part is a squared Gaussian pulse, down-converted to baseband while the second part is an up-converted squared Gaussian pulse with carrier frequency of $2f_c$. Similarly for NBI *i(t)*, it will generate a DC component and a high-frequency component at $2f_i$. A band-pass filter can filter out the DC NBI signal and the high-frequency components. The low-frequency component of squarer output is used for energy detection because signal amplification in low-frequency region consumes less power and requires simpler circuit implementation. However, there is also a down-converted intermodulation component of *s(t)* and *i(t)* to $f_c - f_i$. This component may fall in the baseband pass-band and affects the receiver performance, depending on the frequency difference between the carrier and the interferer.

Key Circuit Blocks

Transmitter

Figure 4 shows the schematic of the proposed UWB transmitter. The LC VCO core consists of a cross-coupled NMOS pair (NM_{1-2}) and an on-chip LC tank (L_{1-2}, C_{1-2}) [10]. The VCO oscillation frequency can cover the frequency range of 3.5–4.5 GHz by tuning varactor control voltage V_{tune} through SPI. The pulse generator consists of a three-stage delay cell and an edge combiner to convert the standard non-return-to-zero (NRZ) baseband data to return-to-zero (RZ) pulse to control the on/off of the VCO through the tail transistor NM_3. It should be noted that NM_3 does not function exactly as a tail bias current transistor, but rather acts as a control switch to power on/off the VCO. Its sizing is chosen to ensure sufficiently fast turn on time for the pulse generation. Compared to conventional UWB pulse generator with pulse shaping filter [11], high output swing, which is critical for robust communication, can be easily

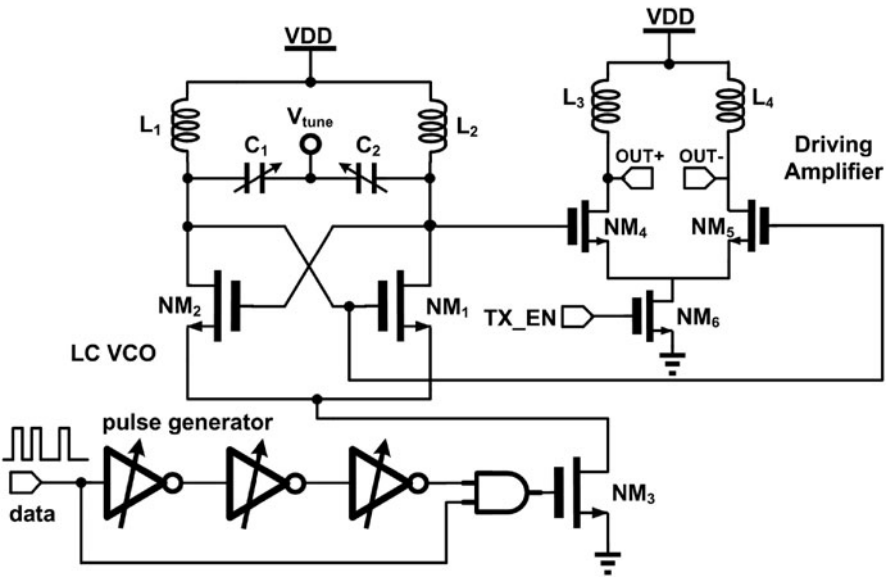

Fig. 4 Schematic of the ultra-wideband (UWB) transmitter

attained due to the positive feedback action of VCO and bandwidth boosting LC components . By turning on the LC VCO only during the pulse generation, transmitter with high energy efficiency can be designed and constant power efficiency can be maintained across a wide range of data rate. Differential DA consists of NM_{4-5} and L_{3-4}, they can further boost the output swing and also isolate the VCO core from the external loading to reduce VCO pulling effect. NM_6 acts as a switch to enable/disable DA, it is controlled by the TX enable signal (TX_EN) from digital baseband.

Low Noise Amplifier

A four-stage fully differential variable gain LNA is designed for the RX front-end. Figure 5 shows the schematic of first two stages. Current reuse topology is utilized to stack the two-stage cascaded amplifiers into one current-reuse cell. Hence, the power consumption is reduced by half while the power gain is maintained. Same architecture is used for the third and fourth stages without the input matching network. Similar current reuse technique has been applied in single-ended LNA [12], however at least four inductors are required in one current-reuse cell, excluding the input matching circuit. Hence, a four-stage differential LNA will require eight inductors in total, occupying a very large area. In this design, the symmetry of the differential LNA is exploited and the single-ended inductors are replaced with differential inductors to save chip area.

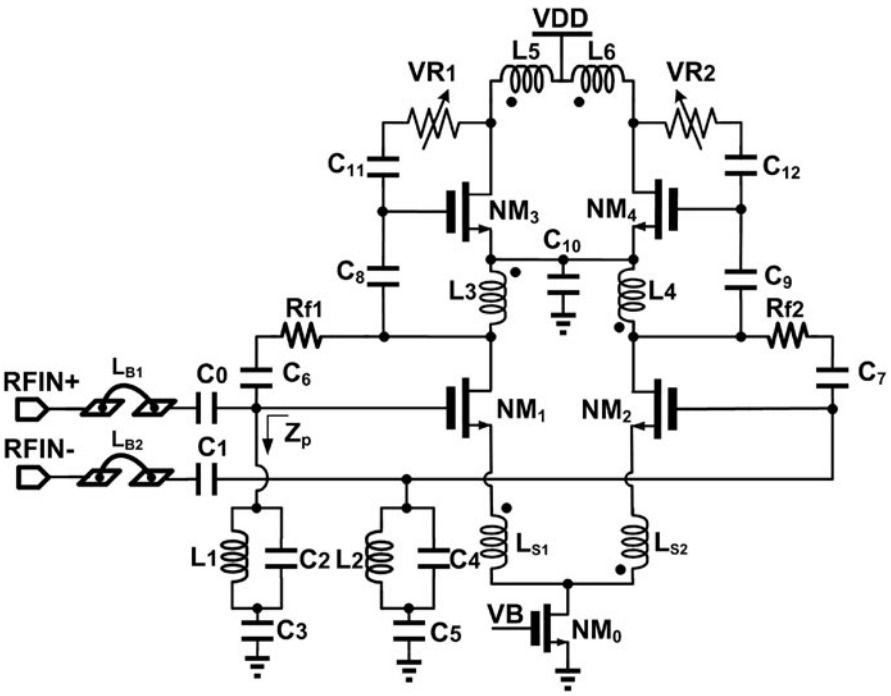

Fig. 5 Schematic of the fully differential low noise amplifier (first and second stages)

A modified LC ladder network input matching network is used for wideband matching. It should be noted that L_{B1} and L_{B2} are implemented with bonding wires, L_1 and L_2 are off-chip high-Q inductors. In addition, the DC decoupling capacitor is optimized to control the transmission zero position to enhance the out-band interference rejection around 2.4 GHz. The shunt LC resonant tank input impedance Z_p can be expressed as:

$$Z_p = \frac{1 - \omega^2 L_1(C_2 + C_3)}{(1 - \omega^2 L_1 C_2) \cdot j\omega C_3} \tag{5}$$

The transmission zero can be calculated as:

$$\omega_p = \frac{1}{\sqrt{L_1(C_2 + C_3)}} \tag{6}$$

By optimizing the value of L_1 and C_2, C_3, the transmission zero can be used to attenuate out-of-band interference at 2.4 GHz while maintaining input matching in 3–5 GHz band. As illustrated in Fig. 6, when C_2 increases from 2 to 4 pF, the notch frequency decreases from 2.48 to 1.9 GHz.

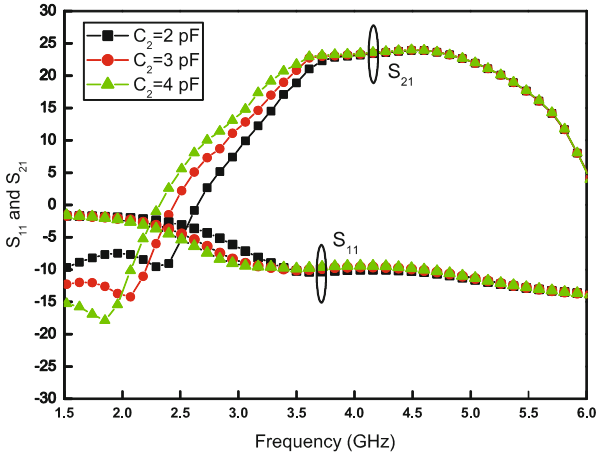

Fig. 6 Simulation results of low noise amplifier (LNA) S_{11} and S_{21} versus C_2 variation

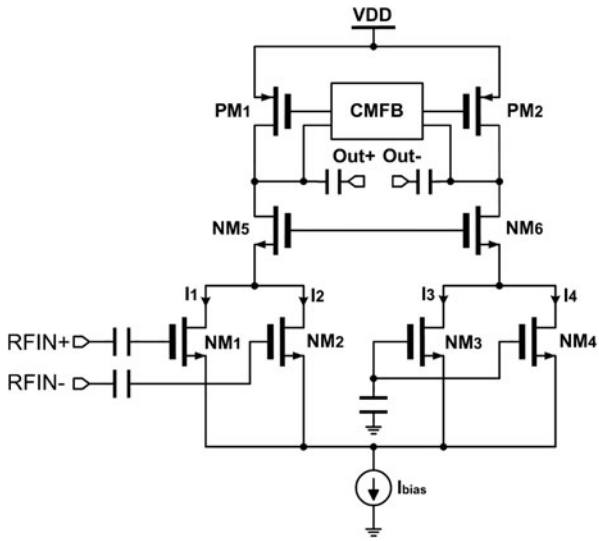

Fig. 7 Schematic of the squarer

Squarer

The schematic of the proposed squarer is shown in Fig. 7 [13]. Transistors NM_{1-4} have the same sizing and the same DC biasing point in saturation region. Differential RF input signals are fed into NM_{1-2} to perform squaring function while NM_{3-4} are AC grounded, so as to cancel the output DC components. The total biasing current is set by the current source I_{bias}. NM_{5-6} are cascode stages to enhance the squarer output impedance. Large output impedance is desired to boost the output voltage swing, hence active load is used here using PMOS transistors PM_{1-2} and they are biased with a common-mode feedback (CMFB) circuit. It is well known that active load value decreases with increasing frequency due to the large parasitic capacitance.

However, since the target signal is in the low frequency range, we can take advantage of this characteristic to implement the embedded band-pass filter function. Ignoring the channel length modulation and transistor body effect, the drain current of NM_{1-4} can be given as:

$$I_1 = \frac{\beta}{2}\frac{W}{L}\left(V_B + \frac{V_{in}}{2} - V_{th}\right)^2 \tag{7}$$

$$I_2 = \frac{\beta}{2}\frac{W}{L}\left(V_B - \frac{V_{in}}{2} - V_{th}\right)^2 \tag{8}$$

$$I_3 = I_4 = \frac{\beta}{2}\frac{W}{L}(V_B - V_{th})^2 \tag{9}$$

The squarer output voltage can be expressed as:

$$V_{out} = I_{out} \cdot R_{load} = (I_1 + I_2 - I_3 - I_4) \cdot R_{load} = \frac{\beta}{4}\frac{W}{L}v_{in}^2 R_{load} \tag{10}$$

where ß is the transistor constant, R_{load} represents the equivalent total loading resistance at the output of the squarer. From (Eq. 10), it can be observed that, besides using larger transistors for the transconductance stage, increasing the squarer load resistance is another efficient way to boost the squarer output voltage. At low frequency, R_{load} is limited by the squarer output resistance, since the squarer output is connected to the gate of next stage which has very high input impedance. The output resistance of proposed squarer can be expressed as:

$$R_{load} \approx r_{o,PM1} || \left[\left(1 + \frac{g_{m,NM5} \cdot r_{o,NM1}}{2}\right) \cdot r_{o,NM5}\right] \tag{11}$$

where r_o is the transistor output resistance and g_m is the transistor transconductance. The large R_{load} together with the parasitic capacitance and the input capacitance of the next stage will form a band-pass filter to suppress the low-frequency and high-frequency NBI components after the squaring operation. The optimized R_{load} should be the one that maximizes the squarer output voltage without significantly filtering the down-converted Gaussian envelope component by the squarer .

Analog Baseband

The block diagram of VGA and comparator is shown in Fig. 8. The VGA consists of a three-stage fixed gain (12 dB) and a variable gain stage (− 15–15 dB). Coarse gain tuning is achieved by selecting the number of fixed gain stages to use. Fine gain tuning is varied by controlling the current ratio in the variable gain stage to achieve resolution of 1 dB/step. The output of the VGA is then connected to a limiting amplifier which output full-swing pulse to the digital baseband. In order to ensure

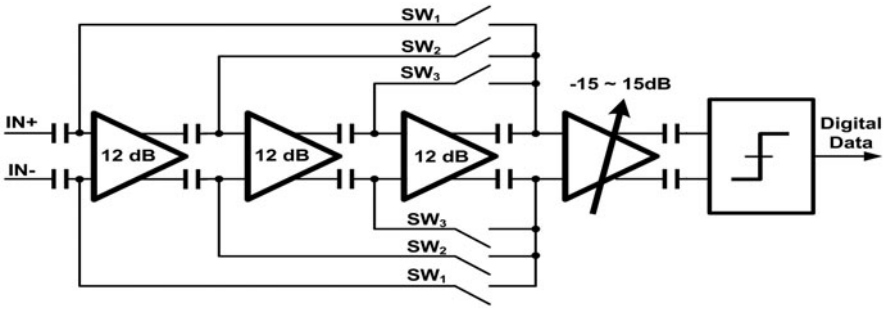

Fig. 8 Schematic of the analog baseband

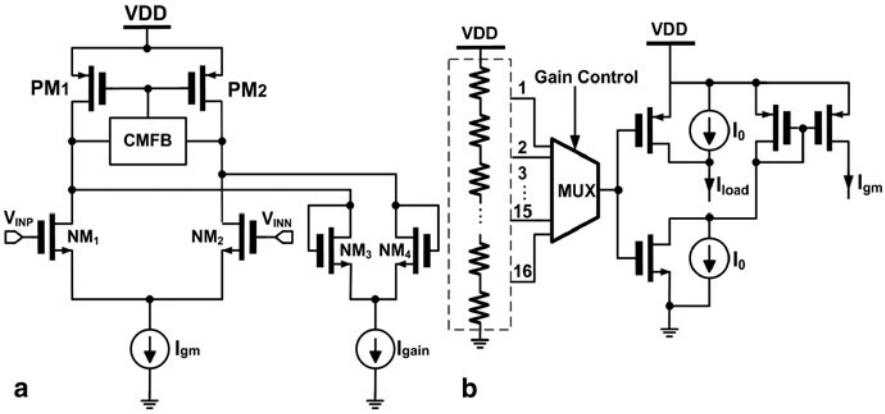

Fig. 9 Schematic of the **a** g_m-cell and **b** fine gain control circuit

accurate gain control, closed-loop amplifiers are typically used [14, 15]. However, a closed-loop amplifier consumes a large amount of current. An alternative way to achieve accurate gain control is to use the g_m-ratioed amplifier as shown in Fig. 9a at low current consumption [16]. The amplifier gain can be approximately expressed as $g_{m,in}/g_{m,load}$, where $g_{m,in} = g_{m1-2}$ and $g_{m,load} = g_{m3-4}$. By proper setting of the size for transistor M_1–M_4, and the current of I_{gm} and I_{load}, the amplifier gain can be accurately controlled.

More importantly, the ratios of transistor size and current deviate very little from the design values in CMOS implementation by proper circuit design and layout techniques. Both the fixed gain and the fine tuning amplifiers are implemented with the g_m-ratioed architecture with different sizes. For the fine tuning amplifier, the accurate gain step is realized by controlling the current ratio of I_{gm} and I_{load} in a logarithmic way. The current steering circuit is depicted in Fig. 9b. The gain control signal is generated using a resistor voltage divider. One of the 16 control references is selected by a MUX, controlled by gain control word from SPI. By a proper selection of transistor M_{7-8} sizes and current I_0, a logarithmic amplifier can be realized based on the g_m-ratioed amplifier [16].

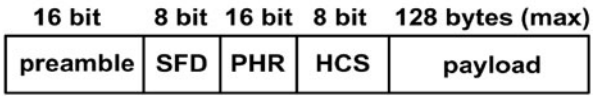

Fig. 10 Data packet format

Digital Baseband

As shown in Fig. 3, the DBB consists of various digital signal processing blocks to support the bidirectional data communication. For TX, the raw data goes through a TX FIFO to separate the data into multiple packets suitable for data packet transmission. The data packet then go through a (8, 4) Hamming encoder which has three parity check bits and one overall parity bit following every four information bits. It can correct 1 bit error and detect 2 bits errors for every codeword. The resulting data packet is then assembled into a packet frame by adding a 16-bit preamble, an 8-bit start frame delimiter (SFD), a 16-bit PHY header (PHR), and a 8-bit header checksum (HCS) in front, the packet format is shown in Fig. 10. The 16-bit preamble pattern consists of 16 consecutive transmitted "1"s to facilitate the identification of received UWB pulse location. The 16-bit PHR sequence defines the size of the data payload. The HCS provides error detection to ensure that the decoded information from PHR is valid. The packet can accommodate a maximum data payload of 128 bytes. In addition, long consecutive 0s of payload are avoided by baseband coding because continuous tracking of pulse location can only occur for received "1"s.

Receiver timing synchronization is the most critical block in the digital baseband. It includes a pulse searcher and a pulse tracker. Given a sequence of pilot signals, pulse searcher would identify the timing location of received UWB pulse within a specific time interval. However, due to clock drift issue between transmitter and receiver, this identified timing location will also drift with time and become inaccurate. To circumvent this problem, pulse tracker module is invoked once pulse searcher successfully identifies received UWB pulse timing location. It will continuously track the location of UWB pulse even in the presence of clock drift. It also recovers the received data into NRZ format and generates the corresponding data clock. Both the period and duty cycle of data clock are adjusted continuously in the presence of clock drift. After synchronization, pulse tracker module also generates enable signal for transceiver's burst mode operation.

A D flip-flop based pulse searching and detection algorithm [17] is developed, instead of the power hungry ADC synchronization approach. As shown in Fig. 11, UWB pulse searching module consists of four D-flip-flop detectors, a sampling controller, ten negative edge-triggered 5-bit registers (NR_0–NR_9), ten positive edge-triggered 5-bit registers (PR_0–PR_9), and a decision finite state machine (FSM). UWB pulses are detected using the D-flip-flop detector shown in Fig. 11. For any given data rate, the system clock is first set to ten times of the data rate through an internal frequency divider. Each symbol period is then divided into ten smaller duration windows by the sampling controller. Therefore, one duration window (T_{dur}) is equivalent to one system clock interval (T_{clk}). Each duration window within the symbol period is then tracked by either positive counter or negative counter. In addition, each duration

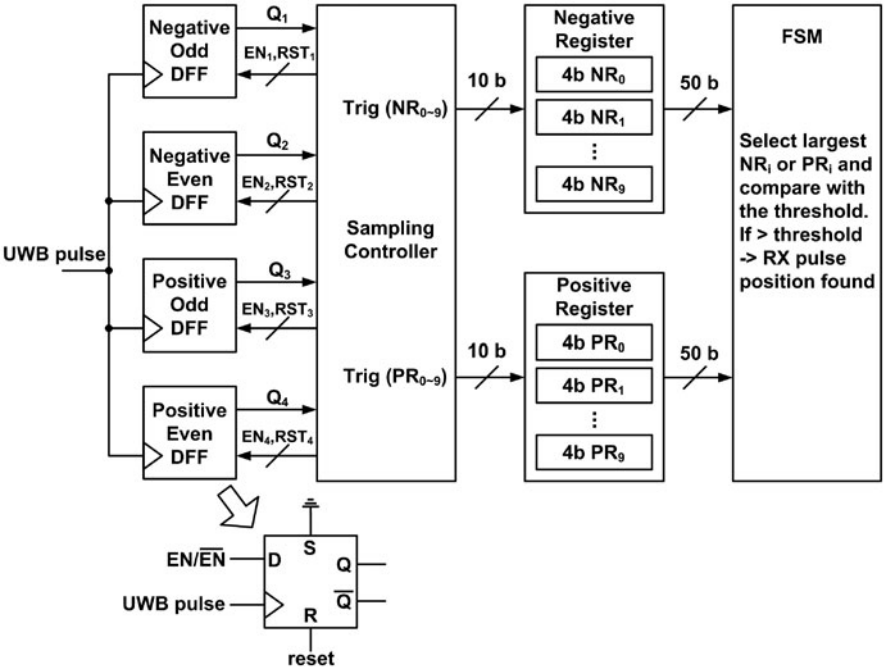

Fig. 11 Ultra-wideband (UWB) pulse searching algorithm block diagram

window will have its corresponding 5-bit register to store the number of UWB pulse detected during that duration window. As an example, NR_1 would be the 5-bit register corresponding to the duration window when the negative counter equals to 1. The sampling controller will generate the control signals (EN_i and RST_i, i = 1–10) for each of the D-flip-flops.

There are three operation phases for D-flip-flop detector. D-flip-flop is first reset during reset phase (RST = 1). After which, D-flip-flop will enter acquisition phase (EN = 1/RST = 0) to detect any incoming pulse for one full duration window. Its output (Q) will then be fed to the controller during sampling phase. Any incoming pulse will set the Q to 1 and increase the count of the corresponding 5-bit register (NR_i or PR_i) by 1 through T_{rig} signal. As the three phases of operation span two duration windows ($2 \times T_{clk}$), both odd and even D-flip-flops are needed to cover ten duration windows alternatively. The sampling controller will generate proper EN_i and RST_i for four flip-flop detectors. It will also produce T_{rig} signals for NR_i and PR_i based on Q outputs from flip-flop detectors. At the end of 16 pilot symbols of transmitted 1s, both the negative and positive edge-triggered registers (NR_i and PR_i) will have statistics which indicate the most likely timing location of incoming UWB pulses. The decision FSM will then determine this timing location based on the collected data from these registers. Its decision will be feedback to sampling controller for proper selection of D-flip-flop detector. Control signals for subsequent detection of incoming UWB pulses will also be generated. As illustrated by the example shown in

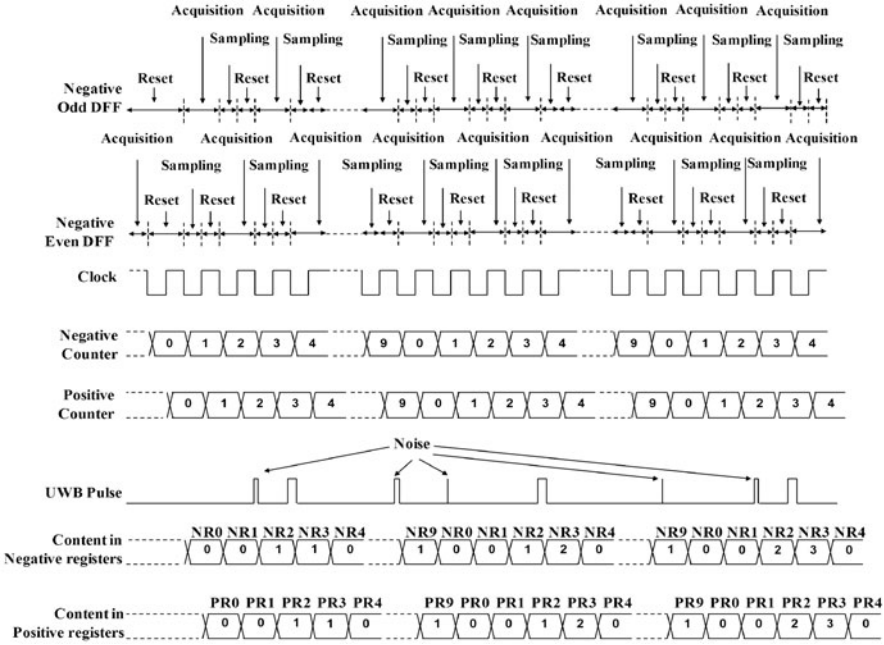

Fig. 12 Ultra-wideband (UWB) pulse searching algorithm timing diagram

Fig. 12, incoming UWB pulses occur at duration window corresponding to NR_3 and PR_3, which have the highest number of count. During detection, noise and glitches could randomly increase the register counts, such as NR_2/PR_2 and NR_9/PR_9. By setting proper threshold in decision FSM (NR_i or $PR_i > 12$), we should be able to mask these detection errors and find the correct timing location for incoming UWB pulses.

The flowchart for pulse detect algorithm is illustrated in Fig. 13a. Most of the time, positive and negative edge-triggered registers will record same number of UWB pulse detection. Therefore, either one can be chosen for subsequent UWB pulse detection. In the proposed algorithm, we choose the duration window corresponding to NR_i, if $NR_i = PR_i$. However, if the incoming pulse is occurring right at the transition edge, the corresponding edge-triggered registers might fail to detect pulses due to metastability issue. Therefore, both positive and negative edge triggered flip-flop and registers are included to overcome the problem. If positive (negative) edge-triggered flip-flop encounters meta-stability issue and fails to detect incoming signal, negative (positive) edge-triggered flip-flop should still be able to detect incoming pulse and result in $NR_i > PR_i$ (or $PR_i > NR_i$).

Once UWB pulse searching algorithm completes, the exact duration window where UWB pulses occur will be known. UWB pulse tracking algorithm as shown in Fig. 13b will begin. Pulse detection will span three consecutive duration windows. The center duration window is determined from pulse searching algorithm. A tracking

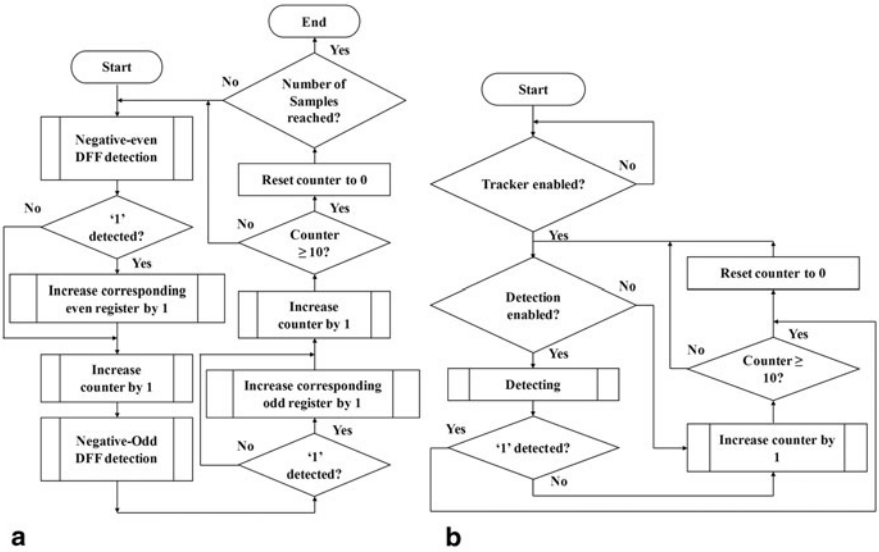

Fig. 13 **a** Ultra-wideband (UWB) pulse searching algorithm flow chart. **b** UWB pulse tracking algorithm flow chart

counter will be used to track UWB pulse. As tracking algorithm only corrects drift upon detection of 1s, slow clock drift coupled with short consecutive transmission of 0s are needed to ensure the proper operation of the algorithm. This is a reasonable assumption given that typical crystal oscillator exhibits frequency stability of ± 50 ppm. When tracking counter value is zero, it indicates the position of duration window where UWB pulse should occur. Under normal condition with no pulse detected, tracking counter would repetitively count to ten cycles and reset, which matches symbol period exactly. The algorithm will reset tracking counter to zero once UWB pulse is detected. If the position of UWB pulse does not change over time, it will be detected when tracking counter value is zero. Therefore, it would not incur any change on tracking counter as well as duration window. However, if clock drift causes the UWB pulse position to change to the adjacent duration window, received UWB pulse will reset the tracking counter to zero instantaneously and the position of the center duration window will now be updated.

The operation status switching of this radio SoC is controlled either by using command strobes or by internal events [18]. There are three main states: IDLE, TRANSMIT, and RECEIVE, and the state machine diagram is presented in Fig. 14. Once the system is powered on or reset, it goes to IDLE state, in which most of the radio modules are inactive. The system calibration and the configuration registers initialization are performed in this state. When the command strobe register of turning on transmitter is set (STXON = 1), and there are valid transmission data in transmitter FIFO (TFIFO = 1), the system goes to TRANSMIT state. On the other hand, when the command strobe register of turning on receiver is set (SRXON = 1), the system goes to RECEIVE state. In TRANSMIT state, if the internal state indicator of transmission completion is on (Trans_complete = 1), and the previous

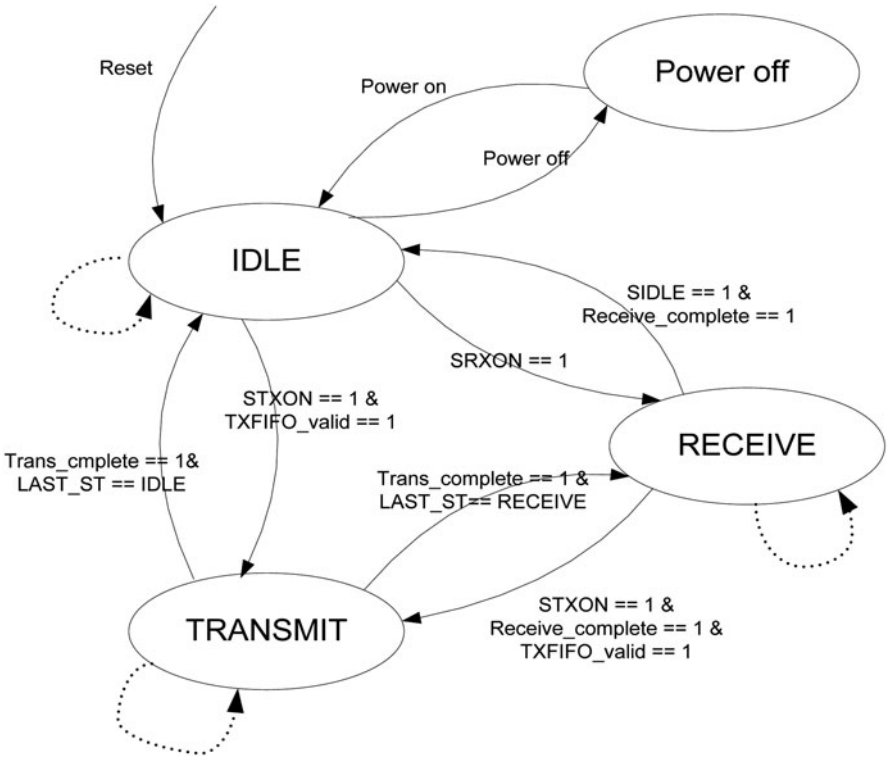

Fig. 14 Baseband control state machine

state is IDLE (LAST_ST = IDLE), the system goes back to IDLE state. On the other hand, if Trans_complete = 1, and the previous state is RECEIVER, the system goes back to RECEIVE state. In RECEIVE state, if the command strobe register of turning on transmitter is set (STXON = 1), the internal state indicator of receive completion is on (Receive_complete = 1), and there are valid transmission data in transmitter FIFO (TFIFO = 1), the system goes to TRANSMIT state. On the other hand, if the command strobe register of switching to IDLE is set (SIDLE = 1), and the internal state indicator of receive completion is on (Receive_complete = 1), the system goes back to IDLE state.

Measurement Results

The proposed IR-UWB transceiver SoC has been implemented in a standard 0.18-μm CMOS process with a die area of 3 × 4 mm as shown in Fig. 15. The whole chip is mounted in a QFN80 package and soldered on a PCB board for performance characterization. Under 1 Mb/s data rate, the transmitter draws an average power of 0.3 mW and the energy efficiency is maintained at 0.3 nJ/bit up to 10 Mb/s. The receiver RF/analog blocks consume 42 mW peak power and digital baseband

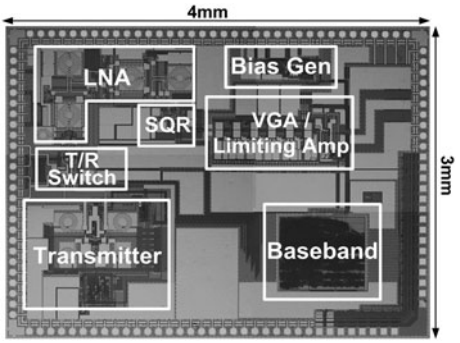

Fig. 15 Transceiver system on chip (SoC) chip photo

consumes 0.5 mW. When TX/RX link is synchronized, the RX duty cycle control signal from DBB will enable the duty cycling of RX, so that RX average power consumption can be reduced significantly. For 1 Mb/s data rate, 10 % duty cycle is achieved given the approximate 90 ns front-end startup time and 2 ns UWB pulse width. The measured RX energy efficiency with duty cycling is 4.5 nJ/bit.

The measured UWB transmitter output time-domain waveform and the corresponding signal spectrum is shown in Fig. 16a and 16b. The UWB pulse width is around 2 ns and the peak-to-peak output amplitude is 4.2 V. The output amplitude can be adjusted by changing the transmitter buffer setting. The signal spectrum is centered at 4.0 GHz and exhibits a 1.68 GHz bandwidth which meets FCC regulation of both the peak and average output power. Figure 17 shows the measured receiver LNA S-parameters and noise figure in high gain/low gain modes. The maximum voltage gain in high/low gain mode is 33 dB/12 dB with a corresponding measured minimum noise figure of 4.7 dB/5.2 dB at 4.0 GHz. The measured LNA IIP3 for high/low gain mode is − 37.8 dBm/20.5 dBm respectively, as shown in Fig. 18. Figure 19 presents the measured squarer output voltage versus RX input UWB pulse power. It can be observed that the squarer RMS output voltage amplitude grows linearly with the increase of input RF power in the range of − 80 dBm to − 70 dBm until it gets saturated at approximately 80 mV when the input power is above − 70 dBm. The usage of cascode stage and active load in squarer limits the output voltage

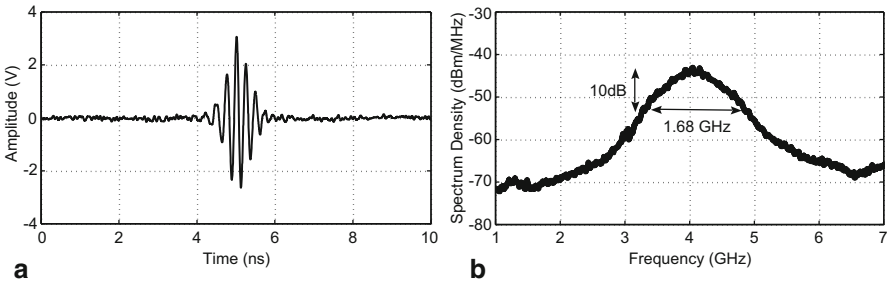

Fig. 16 **a** Measured TX output time domain waveform. **b** Measured TX output spectrum

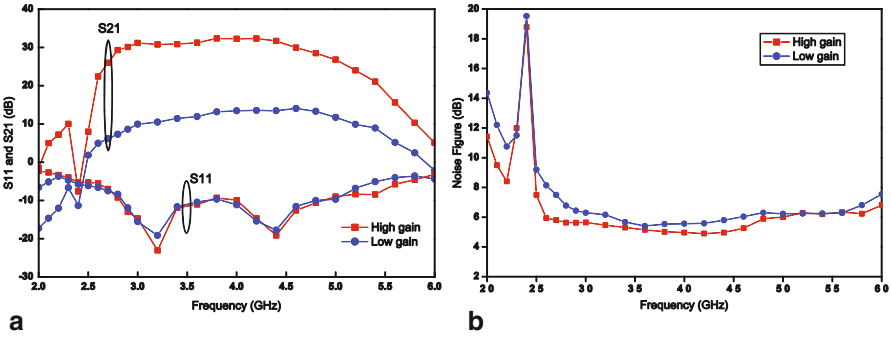

Fig. 17 **a** Measured low noise amplifier (LNA) S_{11} and S_{21} in high/low gain mode. **b** Measured noise figure in high/low gain mode

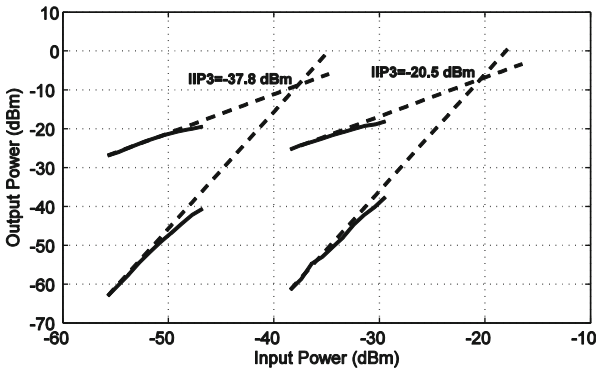

Fig. 18 Measured low noise amplifier (LNA) IIP3 at 4.0 GHz

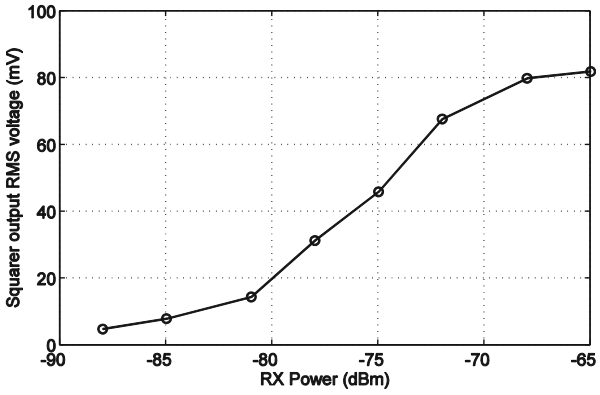

Fig. 19 Measured squarer output voltage versus input power

headroom. Nevertheless, the output saturation can be avoided by switching the gain of LNA to adjust the squarer input power. After 50 dB attenuation, the transmitting pulse is fed into the receiver and Fig. 20a shows the time-domain output signal. Band-pass characteristic of squarer output spectrum is shown in Fig. 20b. The lower 3 dB cut-off frequency is 50 MHz which is sufficient to filter out the down-converted NBI signal.

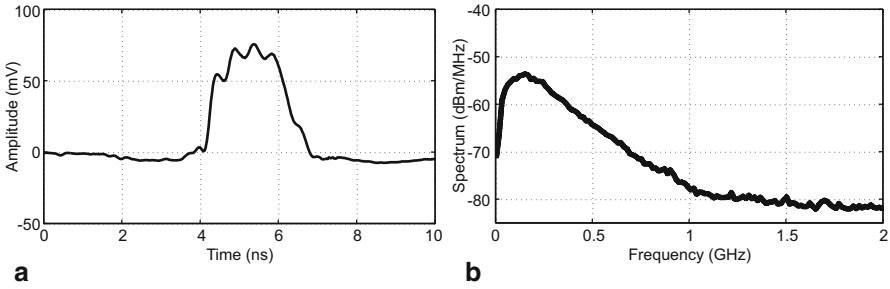

Fig. 20 **a** Measured time domain squarer output waveform, **b** spectrum of squarer output

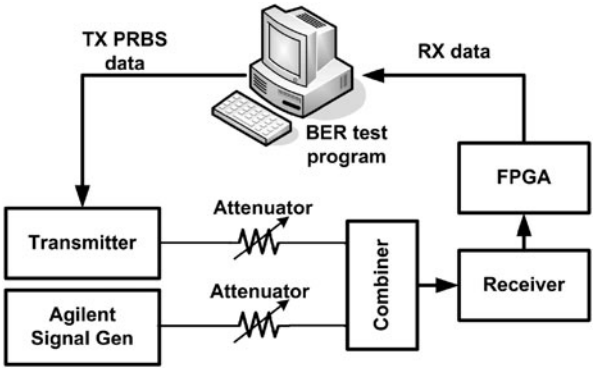

Fig. 21 Measurement setup for bit error rate (BER) and signal-interference-ratio (SIR)

The setup for receiver bit error rate (BER) and signal-interference-ratio (SIR) measurement is shown in Fig. 21. For BER measurement, the randomly generated TX data from the BER software is sent to the UWB transmitter, the TX output is attenuated with a variable attenuator and then fed into the RX. The received data is compared with the TX data by a BER algorithm implemented in FPGA. Figure 22a

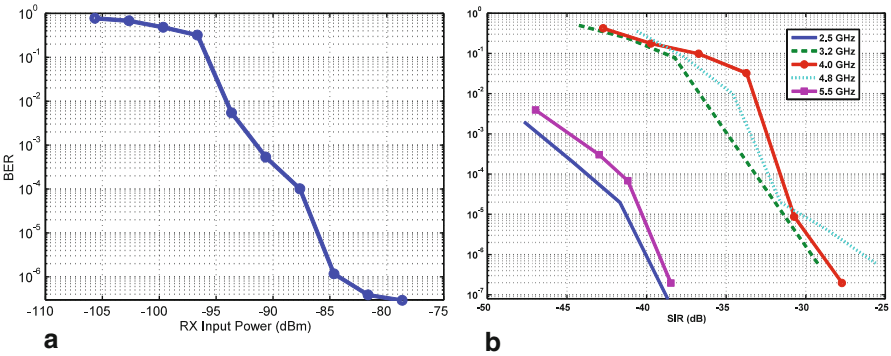

Fig. 22 **a** Measured bit error rate (BER) at 1 Mb/s. **b** Measured receiver signal-interference-ratio (SIR)

Table 1 Performance summary and comparison with state-of-art

Parameters	JSSC 2007 [19]	JSSC 2007 [20]	JSSC 2010 [21]	JSSC 2011 [22]	JSSC 2011 [23]	This work
Modulation scheme	PPM	PPM	Chirp FSK	PPM	S-OOK	OOK
Bit rate (Mb/s)	0.5[a]	0.1	4	5	1	1
TX output swing (V_{p-p})	–	–	0.075	2.2	0.61	4.2
TX power efficiency (nJ/b)	–	–	0.77	0.186	0.258	0.3
Out-of-band SIR at 10^{-3} BER (dB)	− 54	− 46	− 59	− 12 dBm@ 5.4 G	− 11 dBm@ 5.4 G − 21 dBm@ 2.4 G	− 47
In-band SIR at 10^{-3} BER (dB)	− 44	− 15	− 21	–	–	− 33
RX power efficiency (nJ/b)	72	2.5	2.7–4.95	0.84	1.45	4.5
Normalized RX sensitivity at 1Mb/s	− 81	− 80	− 90	− 77	− 65	− 92
Technology	0.18 µm CMOS	90 nm CMOS	0.18 µm CMOS	0.13 µm CMOS	90 nm	0.18 µm

[a] 16 M/s pulse rate, 32 pulses represent 1 bit data

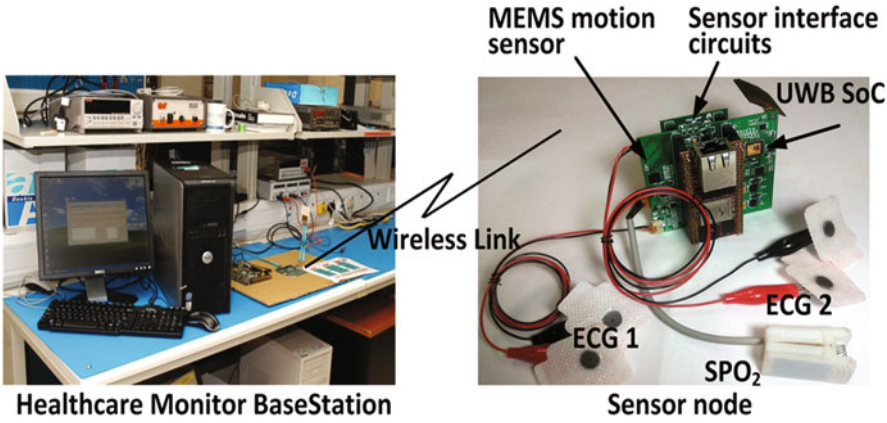

Fig. 23 Picture of wireless sensor node and base station

presents the BER of receiver in high gain modes. The receiver achieves a maximum sensitivity of -92 dBm at a data rate of 1 Mb/s with BER $= 10^{-3}$. For surface insulation resistance (SIR) measurement, another signal generator generates the single tone NBI signal, it is combined with TX data by a wideband balun and fed into the input of receiver. In this measurement, the receiver is first set in the maximum gain mode, and the RX input power is maintained at the level of 10^{-6} BER. Then the interference signal is introduced, its power is increased gradually until the RX BER is degraded to 10^{-2}. The interference signal frequency is swept from 2.0 to 5.5 GHz to test system's performance under in-band/out-band interferences. The receiver (SIR) performance is measured as shown in Fig. 22b. The measured highest in-band/out-of-band SIR is -33 and -47 dB respectively.

The transceiver performance has also been summarized and compared with other state-of-the-art IR-UWB transceivers in Table 1. As shown, our work achieved the highest TX output swing and highest RX sensitivity when normalized to same data rate (1 Mb/s). It also achieved competitive interference mitigation capabilities and provides the added benefit of low system complexity and scalability.

A prototype multichannel vital signal monitoring system has been developed. As shown in Fig. 23, it includes two channels of ECG, one channel of SpO_2, and one channel three-axis motion sensing using microelectromechanical systems (MEMS) accelerometers. Off-the-shelf components are used to construct the sensor readout circuits. The analog signal is digitized at a sampling rate of 1 kHz with 12-bit resolution. A disposable button cell battery (CR2032) is used to power the entire sensor node. The acquired ECG/SpO_2/motion data are transmitted by the sensor node and received by the personal healthcare server for recording and display. The recorded data for a person in motion is shown in Fig. 24. Measurement shows the communication distance is longer than 10 m which is suitable for the in-door health monitoring applications.

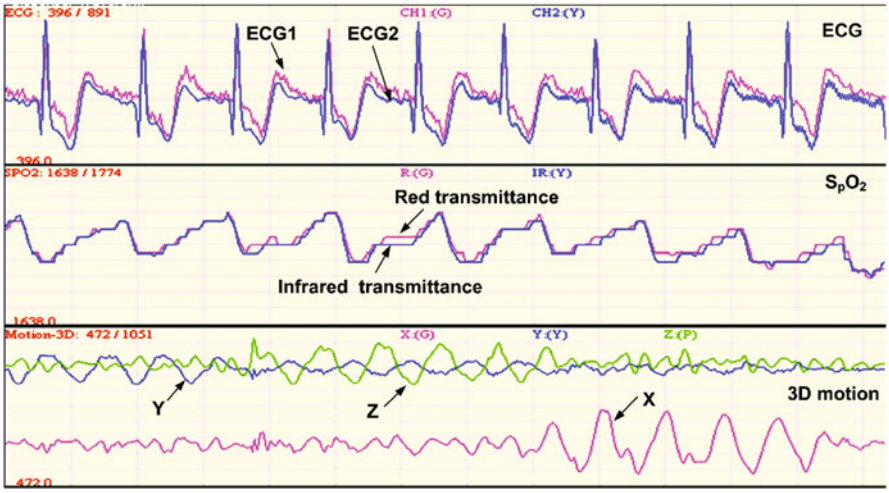

Fig. 24 Recorded ECG, SpO_2 and three axis-accelerator data

Conclusions

An interference robust IR-UWB transceiver SoC for WBAN application is presented in this chapter. Energy efficiency of 0.3 and 4.5 nJ/bit are achieved for TX and RX respectively and the measured receiver sensitivity is − 91.5 dBm at 1 Mb/s data rate. A low-power pulse synchronization algorithm for clock and data recovery is implemented in digital domain without any need for PLL/DLL or ADC. The proposed transceiver SoC has been successfully incorporated into a continuous vital signal monitoring system and the performance is validated by experiments.

References

1. R. Schmidt, T. Norgall, J. Mörsdorf, J. Bernhard, T. Grün, Body area network BAN, a key infrastructure element for patient centered medical applications, Biomed. Tech., **47**, 365–358 (2002)
2. I. Korhonen, J. Parkka, M. Van Gils, Health monitoring in the home of the future, IEEE. Eng. Med. Biol. Mag., **22**, 66–73 (2003)
3. Y. Gao, Y. Zheng, S. Diao, W.D. Toh, C.W. Ang, M. Je, C.H. Heng, Low power ultra-wideband wireless telemetry transceiver for medical sensor applications, IEEE. Trans. Biomed. Eng., **58**, 768–772 (2011)
4. X. Liu, Y. Zheng, M.W. Phyu, B. Zhao, M.K. Je, X.J. Yuan, Multiple functional ECG signal processing for wearable applications of long-term cardiac monitoring, IEEE. Trans. Biomed. Eng., **58**, 380–389 (2011)
5. E.Y. Chow, A.L. Chlebowski, S. Chakraborty, W.J. Chappell, P.P. Irazoqui, Fully wireless implantable cardiovascular pressure monitor integrated with a medical stent, IEEE. Trans. Biomed. Eng., **57**(6), 1487–1496 (2010)

6. A.P. Chandrakasan, F.S. Lee, D.D. Wentzloff, V. Sze, B.P. Mercier, P.P. Daly, D.C. Blazquez, Low-power impulse UWB architectures and circuits, Proc. IEEE., **97**(2), 332–352 (2009)
7. Wireless Body Area Networks (WBAN), IEEE 802.15 Task Group 6, Nov. 2007. http://www.ieee802.org/15/pub/TG6.html
8. S. Gezici, Z. Sahinoglu, V. Poor, On the optimality of equal gain combining for energy detection of unknown signals, IEEE. Commun. Lett., **10**, 772–774 (2006)
9. Y. Gao, X. Liu, Y. Zheng, S. Diao, W. Toh, Y. Wang, B. Zhao, M. Je, C.H. Heng, A low power interference robust IR-UWB transceiver SoC for WBAN applications, Proc. IEEE. Sym. Radio-Frequency Integration Tech., 153–155 (2012)
10. S. Diao, Y. Zheng, C.H. Heng, A CMOS ultra low-power and highly efficient UWB-IR transmitter for WPAN applications. IEEE. Trans. Circuits. Syst., **II 56**, 200–204 (2009)
11. M. Chae, Z. Yang, M. Yuce, L. Hoang, W. Liu, A 128-channel 6 mW wireless neural recording IC with spike feature extraction and UWB transmitter, IEEE. Trans. Neural. Syst. Rehabil. Eng., **17**(4), 312–321 (2009)
12. Y. Gao, Y.J. Zheng, B.L. Ooi, A 0.18-um CMOS dual-band UWB LNA with interference rejection, Electron. Lett., **43**, 1096–1098 (2007)
13. Y. Gao, Y. Zheng, C.H. Heng, Low-Power CMOS RF front-end for noncoherent IR-UWB receiver, in Proc. ESSCIRC., 386–389 (2008)
14. C.-C. Hsu, J.-T. Wu, A highly linear 125 MHz CMOS switches resistor progammable-gain amplifier, IEEE. J. Solid-State. Circuits., **38**(10), 1663–1670 (2003)
15. T.H. Teo, M.A. Arasu, W.G. Yeoh, M. Itoh, A 90 nm CMOS variable gain amplifier with RSSI design for wideband wireless network application, IEEE. Proc. ESSCIRC, 86–89 (2006)
16. Q.-H. Duong, Q. Le, C.-W. Kim, S.-G. Lee, A 95-dB linear lowpower variable gain amplifier, IEEE. Trans. Circuits. System.-I: Regular Papers., **53**, 1648–1657 (2006)
17. W.D. Toh, Y. Zheng, C.H. Heng, Low power digital baseband for impulse radio ultra-wideband transceiver, Circuits. Systems. Signal. Process., **31**, 223–235 (2012)
18. X. Liu, Y. Zheng, B. Zhao, Y. Wang, M.W. Phyu, An ultra low power baseband transceiver IC for wireless body area network in 0.18-μm CMOS technology, IEEE. Trans. Very Large Scale Integr. Syst., **19**, 1418–1428 (2011)
19. J. Ryckaert et al., A CMOS ultra-wideband receiver for low datarate communication, IEEE. J. Solid-State Circuits., **42**, 2515–2527 (2007)
20. F.S. Lee, A.P. Chandrakasan, A 2.5 nJ/bit 0.65 V pulsed UWB receiver in 90 nm CMOS, IEEE. J. Solid-State Circuits., **42**, 2851–2859 (2007)
21. M.U. Nair, Y. Zheng, C.W. Ang, Y. Lian, X. Yuan, C.-H. Heng, A low SIR impulse-UWB transceiver utilizing chirp FSK in 0.18 μm CMOS, IEEE. J. Solid-State Circuits., **45**, 2388–2403 (2010)
22. S. Soldà, M. Caruso, A. Bevilacqua, A. Gerosa, D. Vogrig, A. Neviani, A 5 Mb/s UWB-IR transceiver for wireless sensor networks in 0.13 μm CMOS, IEEE. J. Solid-State Circuits., **46**(7), 1636–1647 (2011)
23. M. Crepaldi, L. Chen, K. Dronson, J. Fernandes, P. Kinget, A ultra-widebandimpulse-radiotransceiverchipsetusingsynchronized-O.O.K. modulation, IEEE. J. Solid-State Circuits., **46**, 2284–2299 (2011)

UWB for Around-the-Body Data Streaming

Xiaoyan Wang

Abstract This chapter presents the first ultra-wide-band (UWB) solution for around-the-body audio streaming. The complete system includes a power-efficient fully integrated transmitter, a receiver front end, an ultra-low-power 500 MHz analog to digital converter (ADC) and a flexible receiver digital baseband mapped on field programmable gate arrays (FPGA). The whole system demonstrates a wireless link upto 12 meters, at a data rate of 0.85 Mbps. Thanks to the inherent nature of the impulse radio, the system is robust to narrowband fades and the average power consumption is brought down to mW range.

Keywords Impulse · Duty-cycle · Ultra-low-power · Ultra-wide-band · Data streaming · Hearing-aid

Introduction

As network and personal mobile gadgets continue to develop, the around-the-body data streaming systems have extended into a large range of applications. More than the conventional devices, such as audio streaming and accessing the internet, edgy demands such as video streaming, data exchanging for EEG/ECG devices for healthcare, one-piece hearing aids, etc. have attracted more and more attention. From the end user point of view, an ideal system is the one which brings all the functions together with smallest form factor and lowest power consumption. From the technical side, however, there are more challenges. Robustness is the first thing to be considered. Resilience to narrowband fades, especially in the indoor environment, needs to be taken care of. The crowded spectrum close to the conventional communication system such as GSM and WLAN should be avoided. Scalability in terms of data rate, power consumption, and link budget are the key components to achieve multi-functions in one device.

Among all the around-the-body wireless applications, the requirements in case of audio streaming around the head, e.g., for wireless audio headsets or hearing

X. Wang (✉)
Holst Centre, imec-nl, Eindhoven, The Netherlands
e-mail: xiaoyan.wang@imec-nl.nl

M. R. Yuce (ed.), *Ultra-Wideband and 60 GHz Communications for Biomedical Applications,* DOI 10.1007/978-1-4614-8896-5_3,

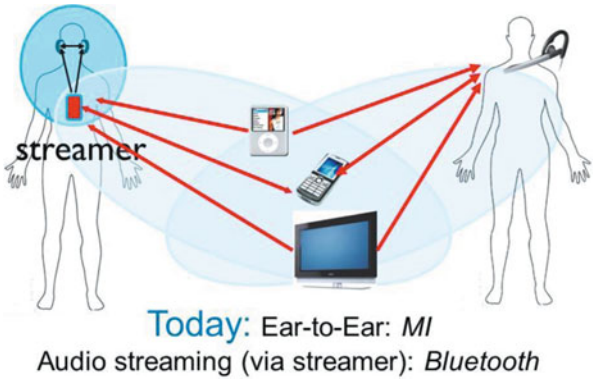

Fig. 1 Today's solution for audio streaming/hearing aids

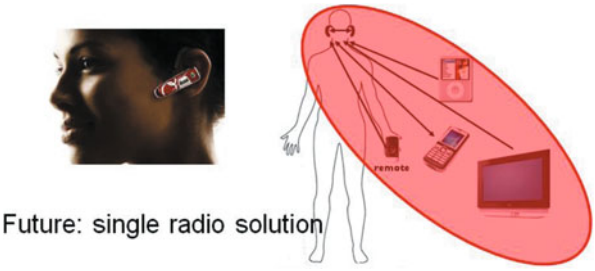

Fig. 2 Integrated solution for behind-the-ear application

aid devices, are particularly tight. Good audio quality is a prerequisite and mW-range power consumption is compulsory in view of battery size. The behind-the-ear device typically serves multiple radio links, e.g., ear-to-ear, ear-to-pocket (a phone or MP3 player), or even a link between the ear and a remote base-station such as a TV. The solution exists today in the market is as shown in Fig. 1. The ear-to-ear link is supported by a magnetic induction system, which needs a streamer to communicate between two ears. The advantage of the magnetic induction system is the low interferences to other users, limited by the coupling distance between the magnetic devices. The second link, ear-to-pocket, or even the ear-to-remote is covered by the radiofrequency (RF) system, for example, Bluetooth radio, for its larger communication distance. The down side of the system for end-users is that an external streamer is always necessary. From the technical side, two transceivers are needed which means more power consumption and larger devices. To tackle that issue, another solution for the behind-the-ear audio streaming is to integrate the two radios into one. For example, as shown in Fig. 2, an RF communication system is chosen to support all the three links.

Apparently, the form factor is reduced in the favor of the end users. However, challenges arise from the technical side. The GHz communication channel is on the top of the candidate list rather than sub-GHz system. The main reason is that the system needs to support a wireless link upto multi-meter range for the ear-to-remote link. There has been published work regarding path loss in the around-the-body ultra-wide-band (UWB) channel. In [1] frequency domain, ear-to-ear channel

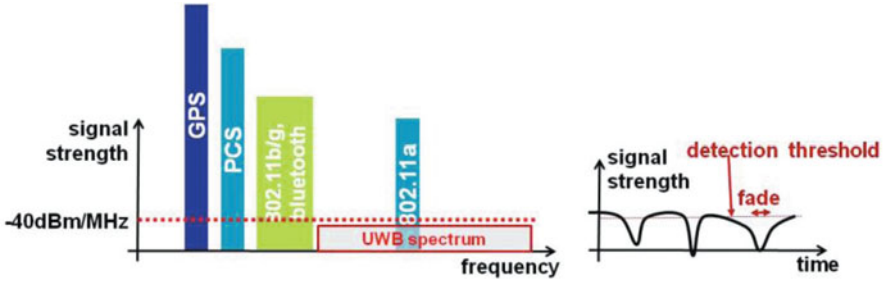

Fig. 3 Challenges for existing hearing-aids radios

measurements have been performed with a vector network analyzer on a Phantom head using single-ended antennas. The reported fading is in excess of 80 dB for some UWB channels. However, in [2] novel time domain ear-to-ear measurements with 7 human subjects using differential antennas are reported with a UWB channel fading of around 60–65 dB. Moreover, in [2], it is shown that by using single-ended antennas it is possible to create deep fades in the measurements due to cable cross talk. The results in [2] also indicate that pocket-to-ear has a slightly larger path loss partially due to the increased distance.

To this point, it seems more reasonable (except the part for the antenna size which decreases as the frequency increases) to opt for a radio system at lowest possible frequency, which can still support a wireless link upto multi-meter. One of the good candidates is the Bluetooth radio, which actually exists in the market. The major challenges for these existing solutions are coexistence and fading. As shown in Fig. 3, the lower GHz band is crowded with different wireless systems, such as GPS, PCS, 802.11.b/g and Bluetooth, and is also extended to 802.11.a at 5 GHz. Strong interferences are the first thing to be tackled if the audio streaming device is chosen to operate at this frequency range. Tighter selectivity, better sensitivity, and larger transmitted power are the common solutions for interference issues, which means larger form factor and higher power consumption, thus stringent but solvable. In contrast, fading is more an inherent issue in the narrowband system. As shown in Fig. 3, in a narrow band system, the path loss of the signal varies with time, position, and frequency. Compensations are usually made in the digital algorithm, again at the expenses of power consumption and the complexity.

Considering all the above challenges, high-band impulse-radio ultra-wide-band (IR-UWB) system tackles the spectrum crowdedness and narrow band fading by nature. The high-band choice offers a frequency range that contains channels for worldwide coverage. Moreover, the high-band system benefits from a smaller form factor due to the smaller antenna size. Due to the ability of larger frequency separation, the high-band IR-UWB is more robust against out-of-band interference, such as WLAN at 5 GHz, ISM at 2.4 GHz, and GSM at 1.8 GHz.

Except for the frequency range and the fading, the IR-UWB system also benefits from several other advantages, due to its fundamental structures, i.e., duty-cycling. In a conventional continuous radio system, the signal is transmitted and received

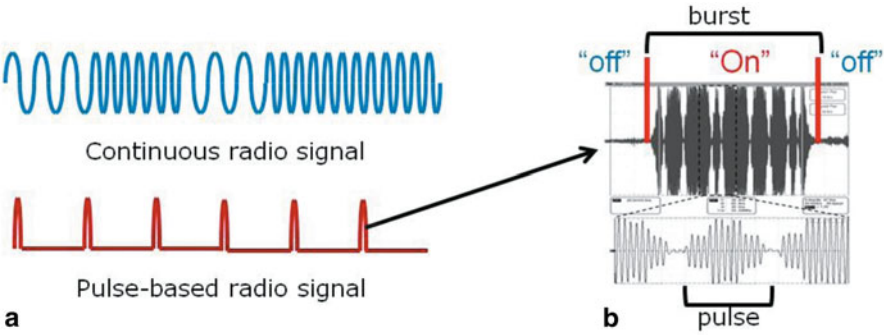

Fig. 4 **a** waveform indication of continuous radio signal and pulse-based radio signal. **b** Real pulse-based signal transmitted by an IR-UWB transmitter

continuously as shown in Fig. 4a. The frequency bandwidth occupied in this case is usually very narrow as compared to the carrier frequency. The system needs to be turned on continuously during the data communication. Very differently in an IR-UWB system, the data is transmitted as very narrow pulses in the time domain, which means the signal occupies a large frequency bandwidth. Since the information is only contained within a small time window, it is possible to turn on the system only during the pulse, while turning off the system otherwise to save the power consumption. Such a behavior is called duty-cycling. In fact, duty-cycling is the essence of such a system in achieving low averaged power consumption. By changing the duty-cycling ratio, variable data-rates can be achieved for different communication systems, such as wireless sensor nodes, WPAN devices, and streaming audio.

An IR-UWB signal transmitted by an IR-UWB transmitter is shown in Fig. 4b. A few terms are defined here to facilitate the reading of the latter part of this chapter. The grouped information is defined as "burst" and each burst consists of a group of "pulses", as shown in Fig. 4b. The pulse (in this system) is defined as a 2-ns wide pulse, with either positive or negative polarity, uploaded to the 6–10 GHz carrier. As seen, signal/information/data is transmitted as a burst of pulses during a short period, and no information is transmitted during the other time. An additional benefit of the narrow pulse feature of IR-UWB is that it allows for precise location systems for low power applications.

In conclusion, as compared to ISM band solutions [3], high band IR-UWB technology (6–10.6 GHz) benefits from small antenna size, resilience to narrowband fades and wider frequency separation from GSM/WLAN bands. Moreover, it allows bit-level duty-cycling enabling low power consumption and flexible data rates. This chapter presents the first complete IR-UWB solution for around-the-head audio streaming.

System Architecture

The application case of the IR-UWB system focused in this chapter is the around-the-body data streaming. In the following part, the system requirements for such application are analyzed, including link budget, transmitted power, receiver sensitivity, and clock scheme.

Link Budget

As mentioned previously, for the around the body data streaming there are three user scenarios: ear-to-ear, pocket-to-ear, and ear-to-remote link. The link budgets for the three scenarios are different due to different path loss. Concluding from the previous work [1, 2], the path loss ranges from 65 dB to maximum 80 dB. Therefore, the UWB system needs to provide enough transmitted power and receiver sensitivity to cover such path loss, as indicated by the following equation:

$$\text{Path loss} = P_{TX} - \text{Sensitivity}_{RX} - \text{IL},$$

where P_{TX} defines the transmitter output power and IL refers to the digital implementation loss. Assuming an output power of −10 dBm, and the rule-of-thumb value for IL of 6 dB, to meet the minimum 65 dB link budget, the receiver sensitivity needs to meet −81 dBm.

Data Structure in IR-UWB System

The IR-UWB system proposed in this chapter is compliant to the IEEE standards 802.15.4a and proprietary standards. The system is designed with certain flexibility so that it can also be adapted to other standards. As background knowledge, the data structure of an IEEE802.15.4a compliant data packet [3] is briefly introduced as shown in Fig. 5a. The data packet can be divided into two parts, the preamble and the payload: preamble consists of isolated 2 ns-wide pulses for synchronization and payload consists of grouped pulses representing data information.

Fig. 5b shows the structure of one preamble symbol, usually there are certain number of preamble symbols within the preamble phase. One preamble symbol consists of a number of N isolated pulses (2 ns-wide), and every two pulses are separated by (L-1) number of "0"s (Fig. 1b). The length of the preamble and L varies for different modes in the 15.4a standard and are designed to meet the spectral mask.

Fig. 5c shows the structure of one payload symbol and the payload consists of a certain number of payload symbols. Each payload symbol (Tsym) is divided into four equal length parts as shown, the data is only transmitted in the first or third quarter, while the second and fourth quarter are defined as guard intervals and are always empty. The first and third quarter are divided into a number of possible burst positions with equal duration. The data is represented by a group of pulses (defined as bursts),

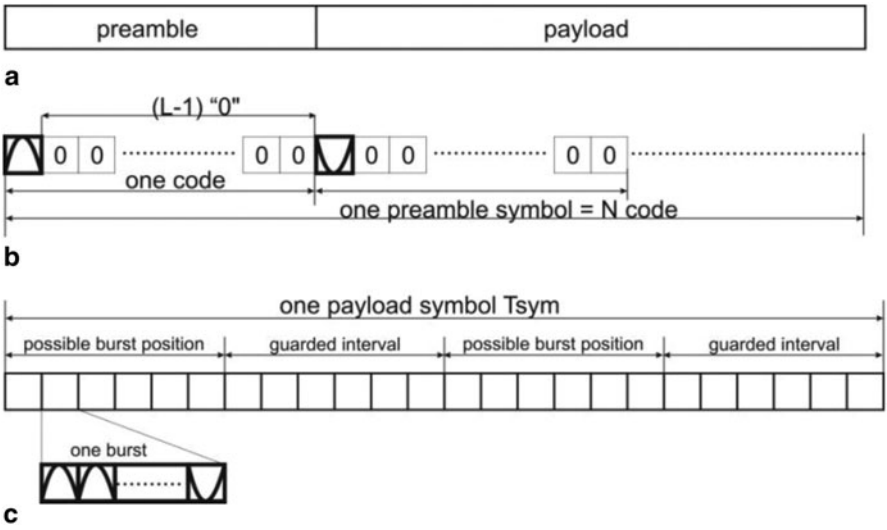

Fig. 5 Structure of **a** 15.4a compliant data, **b** preamble symbol, **c** payload symbol

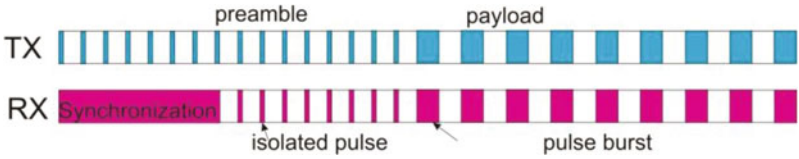

Fig. 6 Transmitted and received enable signal

and can be transmitted in either the first or third quarter. In burst-position-modulation (BPM) scheme, a data in the first quarter represents "0" and in the third quarter "1". The number of pulses per burst (Ncpb) and the duty-cycle ratio determines the data rate.

In both preamble and payload, data information (contained in pulses/bursts) is not transmitted/received continuously. Therefore, it is possible to duty-cycle the system to average down the total power consumption. As shown in Fig. 6, colored blocks indicate that the system is switched on and the white indicates it is off. Obviously, in the transmitter, duty-cycling can be achieved during the whole packet. While the receiver needs to work continuously first to get synchronization, and thereafter is duty-cycled by an enable signal generated by the digital baseband.

In order to apply the duty-cycling in the system, a few clock signals will be needed. A permanent clock will be needed to define the time grid of turning on/off the system, a LO signal is necessary as in any other transceivers to provide the carrier frequency from 6 to 10 GHz with 500 MHz frequency step, and a 499.2 MHz clock to generate the 2-ns wide pulses in the transmitter and to serve as the sampling clock in the receiver. In the proposed system, to minimize the design risk and to reduce the system complexity, the following clock system is chosen. The permanent clock is chosen at 124.8 MHz, and together with the 499.2 MHz clock are generated

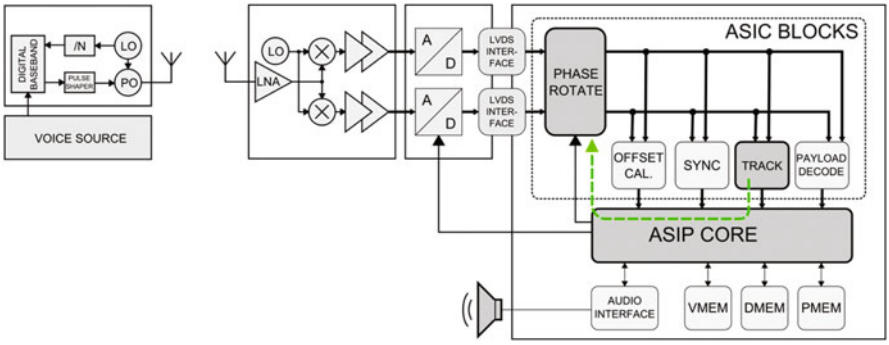

Fig. 7 Behind-the-ear audio streaming

externally. The LO carrier is generated on-chip (as introduced in the following section) and is calibrated for the carrier frequency, while left free running during the operation.

Design of the IR-UWB system

Many previous work about IR-UWB on the lower RF band (3∼5 GHz) or sub-GHz range [4–7] has been published. However, such band selection can't provide worldwide coverage, neither standard compliant. Differently, the work presented here provides the first complete IR-UWB system, including the fully integrated transmitter, a receiver front end, an analog to digital converter (ADC) board [8] and the field programmable gate arrays (FPGA)-based receiver digital baseband for full data synchronization and data processing. The entire system is catered for around-the-body data streaming. However, with minor adaption on the digital baseband, it can also be implemented in accurate localization system (Fig. 7).

The main design challenges for the IR-UWB system (especially the RF frontend) are the low power consumption, large signal bandwidth, and fast startup time. The noise and the linearity requirements are relatively relaxed as compared to the conventional radio systems. Therefore, low power can be achieved partially as a trades-off with noise and linearity performance. Furthermore, the average power consumption can be reduced by duty-cycling the various components. The large signal bandwidth (500 MHz) increases the design difficulties at the input/output matching, and more stringently, at the variable-gain-amplifier (VGA)/analog filters, ADCs, and the digital baseband. Last, the startup time of each block is also a critical design parameter, since the power consumption during this time becomes the overhead of the total power consumption. The RC combination usually implemented in the biasing circuit becomes the bottleneck to shorten the startup time. All these design issues will be addressed in the following sections with details, together with the design choice, circuit techniques, and measurement results.

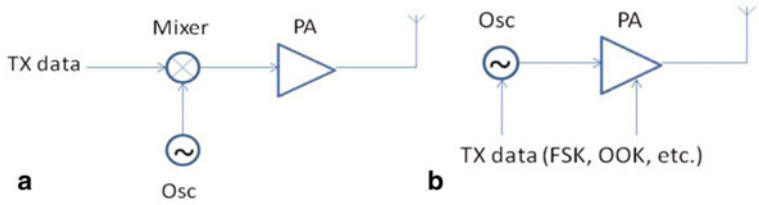

Fig. 8 **a** Conventional up-conversion type transmitter. **b** Direct-conversion transmitter

Transmitter Design

The function of a transmitter is to deliver the modulated RF signal to the air with maximum output power and maximum efficiency. There are different transmitter structures that can be implemented as the IR-UWB transmitter. The advantages and disadvantages of each structure are compared below.

Fig. 8a shows the mixer-based transmitter, which up-converts the baseband data to the LO frequency. The output of the mixer is amplified to a desired power level by a power amplifier (PA), and sent to the antenna. This transmitter architecture can be used with a general purpose modulation scheme in the baseband data, such as Amplitude Shift Keying (ASK), On-Off Keying (OOK), Frequency Shift Keying (FSK), Phase Shift Keying (PSK), etc. The disadvantage of this architecture is that the output power and power efficiency of a mixer are usually relatively low, and this requires a power amplifier with high power gain and large output power. Furthermore, due to the spectrum mask requirement, a linear power amplifier is required in order to preserve the envelope (e.g. triangular or trapezoidal) of the transmitter data. This further reduces the output power and power efficiency of the transmitter, as compared to using a saturated power amplifier.

Instead of using the general purpose up-conversion transmitter, there are other transmitter architectures that can be optimized for the specific modulation scheme, which achieve a higher output power and power efficiency as in Fig. 8b. A direct-conversion transmitter for FSK and OOK modulation in [9–11] is presented. The oscillator and power amplifier can be modulated by the baseband data with FSK or OOK modulation. The power amplifier is directly driven by the oscillator. In comparison with the mixer in Fig. 8a, which uses passive mixer without extra power consumption (therefore the power consumption is equal), the oscillator usually provides a large output signal with high power efficiency thanks to the internal positive feedback. In this way, the input power of the power amplifier is larger as compared to that in Fig. 8a, therefore the output power and power efficiency of the transmitter are increased.

To further improve the output power and efficiency, an injection-locked transmitter [12] can be adopted. As shown in Fig. 9a, the power amplifier in Fig. 8b is replaced by a power oscillator. The reference oscillator provides the LO frequency (with or without a phase-locked loop or frequency-locked loop). The power oscillator can be

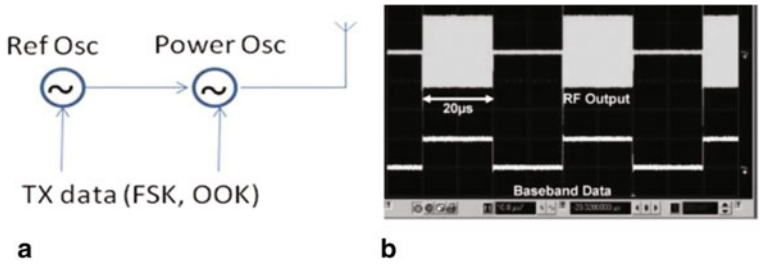

Fig. 9 **a** An injection-locked transmitter. **b** Transient output of the transmitter

frequency-locked to the reference oscillator, and it provides a larger output power to the antenna. The reference oscillator and the power oscillator can be modulated by the baseband data with FSK or OOK modulation. Figure 9b shows the transient output of the transmitter as response to the baseband data with OOK modulation scheme [12]. The rectangular envelope at the output of the transmitter, however, does not meet the IEEE 802.11.15.4a spectrum mask requirements. On the other hand, if the reference oscillator is modulated by the shaped pulse as defined in 15.4a, weak injection locking would be an issue during the ramping up time of the modulated signal. For this reason, the scheme in Fig. 9a doesn't fit the requirement of our system.

In this work, we present an injection locked transmitter with pulse shaping functions as shown in Fig. 10. The baseband data is pulse-shaped and modulates the power oscillator. In this way, the output envelope of the transmitter follows the pulse shape of the baseband data, and meets the spectrum mask requirements. The reference oscillator is not modulated and the output keeps a constant amplitude, which ensures the injection between the reference and the power oscillator. The power oscillator can be modulated by the baseband data with FSK, OOK, PSK, PPM, etc. As compared to the previous architecture, the injection-locked transmitter can achieve larger output power and higher power efficiency at high frequencies (i.e., 10 GHz).

The entire transmitter including the digital baseband is integrated into a single-chip TX-IC. The digital baseband generates data signals for a standard compliant frame; i.e., pre-amble and payload, as well as the control data to duty cycle the front-end blocks. The digital data is converted to pulses by a pulse shaper, which modulates the power oscillator. The local oscillator generates the carrier frequency between 6 and 10 GHz and locks the power.

The schematic of the pulse shaper and the power oscillator are also shown in Fig. 10. In the pulse shaping circuit, the digital baseband data B1P/N is converted to a differential pair of analog signal IF +/- with RC pulse shape. The RC time controls the shape of the pulse and is a trade-off between output power and the 15.4a spectral mask compliancy.

In the power oscillator, transistor M7/8 and the LC tank form a tunable LC-tank oscillator, which can be locked to the injected LO +/- signal from 6 to 9 GHz in measurements. The LO signals (LO +/-) are fed to the power oscillator by transistors M6/M10 and M5/M9 depending on the IF +/- signal on M1-M4. The phase

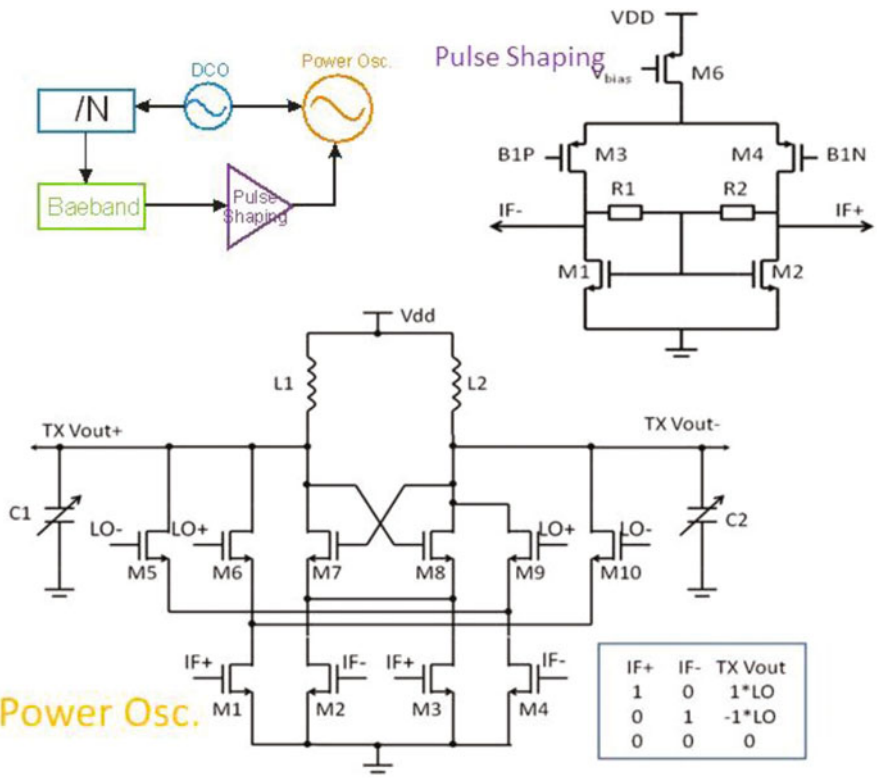

Fig. 10 An injection-locked transmitter with OOK modulation

modulation is realized by swapping the output phase of the transmitter as compared to the LO signals. OOK and position modulation are implemented by turning on/off the power oscillator. In order to keep injection locking effective within such a large tuning frequency (6–10 GHz), a low quality factor inductor is implemented in the power oscillator. The downside is that the output power and power efficiency are reduced to a certain extent.

As compared to the conventional transmitter architecture in [13], the power-oscillator-based transmitter requires less DCO driving capability, thus relaxing the requirement and power consumption of the LO distribution system.

The stand-alone transmitter is evaluated and the measurement results are summarized in Fig. 11. The transmitter data rate is scalable from 0.11 to 27.2 Mbps and both Burst Position Modulation (BPM) and Burst Phase Shift Keying (BPSK) are supported. The transmitted pulse and the baseband data B0/B1 are captured in Fig. 11a. Bit B0 indicates if there is a burst transmitted or not, while Bit B1 indicates the polarity of the pulses in the burst. As can be seen, first the RF output appears where B0 is "1", second, the polarity of the RF output alternates according to the Bit B1. Figure 11b shows the transmitter output spectrum when transmitting a 15.4a packet and the compliancy with the 15.4a spectrum mask.

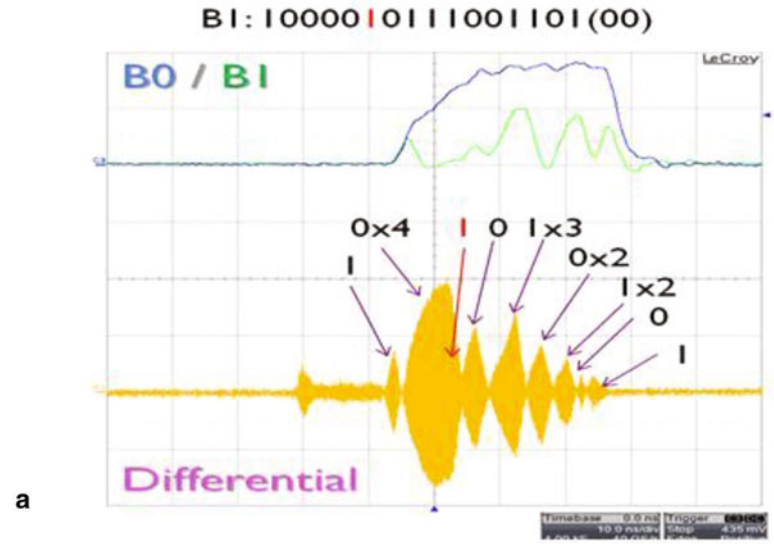

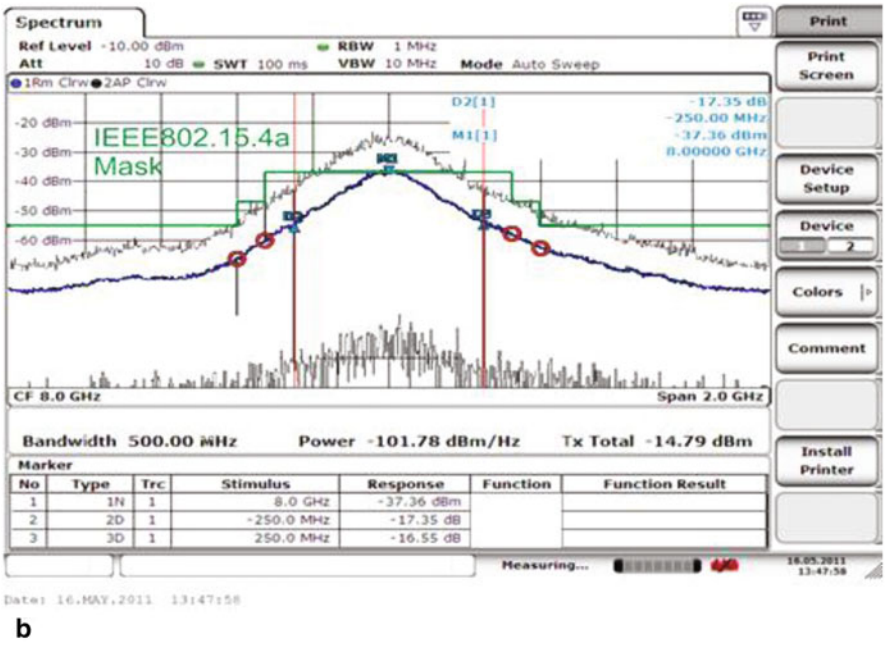

Fig. 11 Transmitter measurement results. **a** The transmitted pulse and the baseband data B0/B1. **b** Transmitter output spectrum when transmitting a 15.4a packet and the compliancy with the 15.4a spectrum mask

When continuously on, the transmitter front-end (excluding the Digitally-Controlled-Oscillator (DCO)) draws 40 mA from a 1 V supply, and delivers a maximum 13 dBm peak output power at the output of the IC, with 50 % power efficiency at 8 GHz. Note that, despite the use of lossy antennas in this application, this high output power maximizes the emission close to the FCC limits. For the wireless link evaluation, it is more important to measure the average output power emitted by the antenna. The average output power obtained at the antenna is −13 dBm assuming 0 dB gain antenna.

DCO Design

A local oscillator (LO) signal from 6 to 10 GHz is needed in both transmitter and receiver, to provide the carrier signal. The generation of a stable LO signal from 6 to 10 GHz is very challenging, mainly because of the large frequency range. The implementation of the oscillation can be chosen between LC-tank based oscillator and ring oscillator, and here the latter option is preferred for the following reason. The ring oscillator avoids the use of large inductance, saving the on-chip area and avoiding the pulling effect in the transmitter. The large frequency bandwidth requires large tuning bank. In an LC-tank oscillator, it means the quality factor of the inductor needs to be largely flattened, which decreases the advantage of using inductors for better phase noise performance. Therefore, a 3-stage ring oscillator is implemented to reach high frequencies (upto 10 GHz), to have a very large tuning range and a settling time of few ns.

The oscillator core consists of three stages of differential inverters in a closed loop, as in Fig. 12a, and each differential pair is as shown in Fig. 12b. The instability created by the odd numbers of stages produces oscillation whose frequency, in the first order, is defined by the product of RC time and the number of stages N. In each differential pair, the input pair M1/M2 are switched on/off alternatively by the input signal IL_1/IR_1. The current from M7 is thus steered between M1 and M2. The output amplitude at OL_1/OR_1 is the voltage drop across the R_{load} by the biasing current. Transistor M5/6 are implemented to enable/disable the oscillator.

The frequency can be tuned by altering the inverter stage load resistance R_{load} or the load capacitance C_{load}. The choice of the RC values is the trade-off between several design parameters. To achieve high oscillator frequency, the RC value needs to be minimized. The swing of the DCO output signal is critical to drive the following stage, and is determined by the product of the biasing current and the R_{load} value. To balance between the power consumption and the output swing, the R_{load} needs to be maximized. To cover the wide tuning range and to achieve the fine tuning step, three tuning banks are implemented. Coarse tuning is based on a 4-bit resistive bank, changing the resistive load in the differential pairs. Medium tuning is based on a 3-bit capacitive bank, which loads at the output of each stage. The capacitive bank is realized by switching on/off the CMIM capacitor.

The fine tuning bank (as in Fig. 13) is also realized by tuning C_{load}. However, the target minimum step of 1 MHz requires very small unit capacitance, down to 0.5

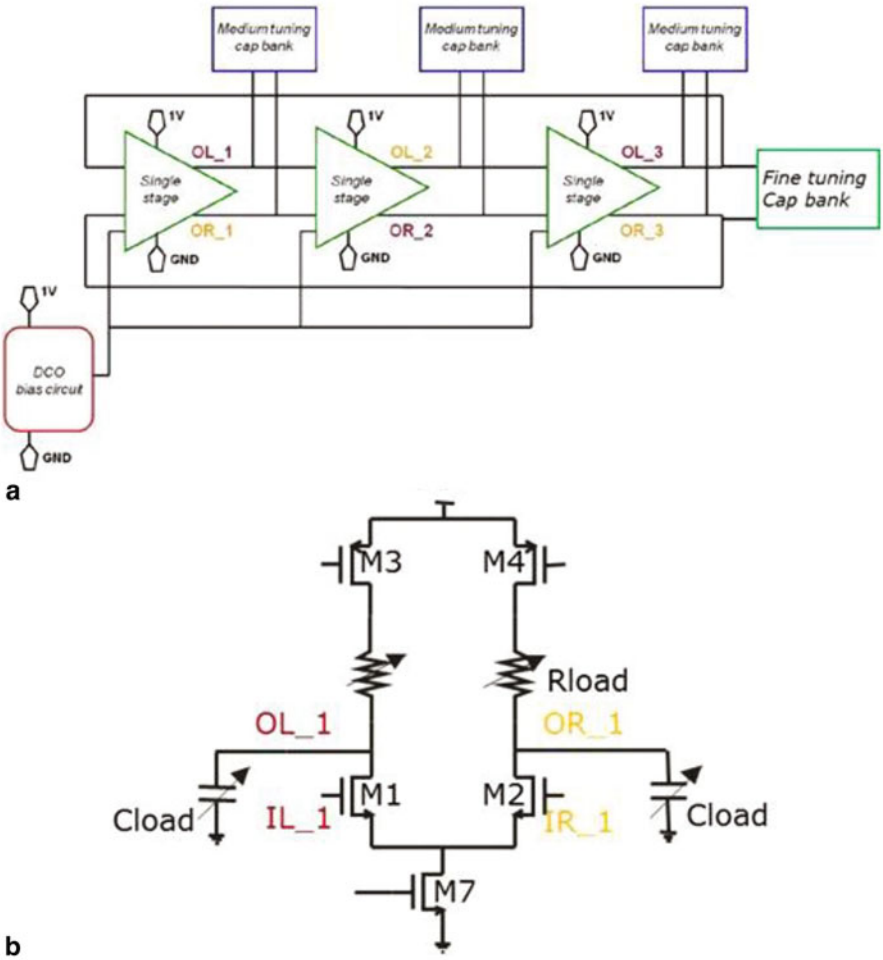

Fig. 12 **a** 3-stage DCO schematic. **b** Schematic of each stage

fF/unit. For such small step values, monotonous behavior needs to be ensured by thermometer encoding. Different from the medium tuning back, digitized MOS varactors are chosen over switched-MIM capacitors, to avoid the effect from the on-resistance of the switches. The 1 MHz tuning step is achieved by connecting the minimum-sized varactor in series with two customized capacitors. The customized capacitor is realized by the fringing capacitor between top metal with a size of 1.4um $\times$ 14um to achieve $<$ 0.5fF/unit capacitance. Each tuning range is required to overlap with the adjacent ones to ensure continuity in the frequency sweep, avoiding gaps created by process variations and inaccuracy of parasitic capacitances estimation.

A phase-aligned technique is implemented by tying one side of the differential output to VDD while the other side to ground using switches as in Fig. 14. Such technique has two advantages. First, the DCO output is ensured to start from a fixed phase each time when the DCO is enabled by the "EN" signal. Second, it avoids

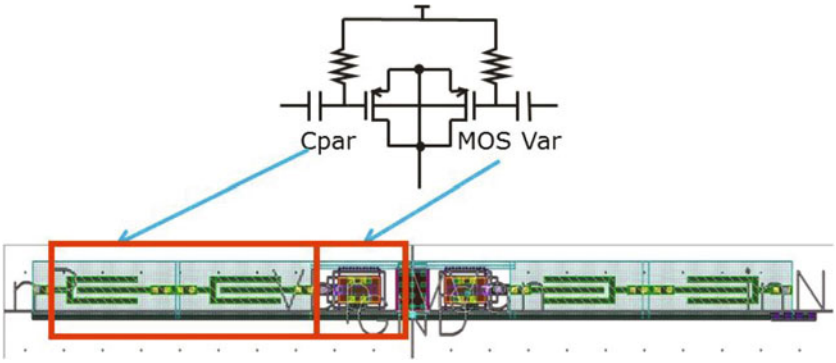

Fig. 13 Fine tuning bank in the 3-stage ring oscillator

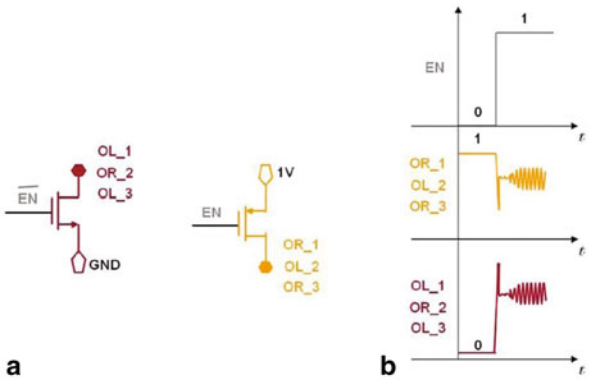

Fig. 14 **a** Implementation of the phase align technique. **b** Start-up behavior at the output of each stage of the DCO

the phase noise accumulation between data bursts. That feature is critical since in the proposed system, the LO carrier frequency is only calibrated, and left free running during the TRX operation. Such choice enables the effective duty-cycling, and thus minimizes the power consumption. On the other hand, the frequency drift that happens in the oscillator are usually low-frequency phenomena. By turning off and on the oscillator at the duty-cycled ratio, the LO signal is effectively high-pass filtered.

The 3-stage DCO provides 3-pair of different output at phases of 0, 60, and 120°, while quadrature signals are needed for the receiver. Therefore, an IQ buffer implemented to generate the IQ signal from the DCO output. The I-branch is a two-stage resistive-loaded buffer to amplify the zero-phase DCO output; in the Q-branch, the 60 and 120° phase DCO outputs are combined to generate the quadrature output Fig. 15. A symmetric loading between the I and Q buffer is necessary to ensure the quadrature output.

The DCO is evaluated with its full tuning range: in total 32,678 tuning steps covered by coarse, medium, and fine steps. A tuning range of 4.7–9.1 GHz with an average tuning step of 1 MHz is measured. Figure 16 [13] illustrates the overall tuning curve, showing that the DCO can be tuned from roughly 5–10 GHz with

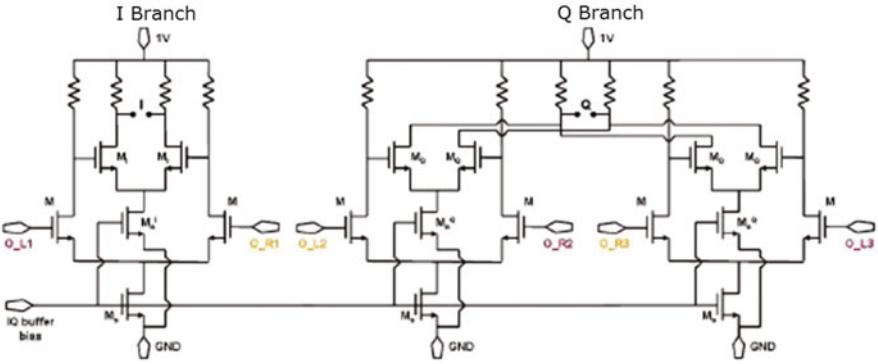

Fig. 15 Schematic of the IQ buffer

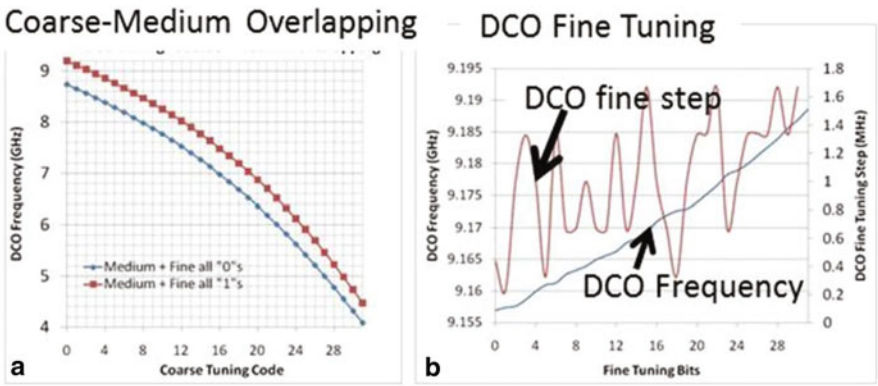

Fig. 16 DCO measurement results. **a** Coarse–Medium overlapping. **b** Fine tuning behavior for fixed coarse and medium codes

sufficient overlap to prevent any gaps in the tuning range. Figure 16b shows the fine tuning behavior for fixed coarse and medium codes. The total power consumption varies from 16 mW to 25mW.

Receiver Design

The IR-UWB receiver consists of three blocks, the front-end IC, a 500 MHz ADC, and the baseband algorithms for synchronization, tracking, and demodulation developed on an FPGA. The FPGA-based digital architecture enables a flexible baseband with advanced algorithms and, thus, better performance.

The receiver front-end consists of a Low-Noise-Amplifier (LNA), a quadrature mixer, and a 5-stage VGA. A differential LNA is chosen for the common mode noise rejection and better gain performance. Moreover, the differential choice is also compatible with the differential transmitter described in the previous section, allowing a direct connection to the differential antenna dedicated to the system.

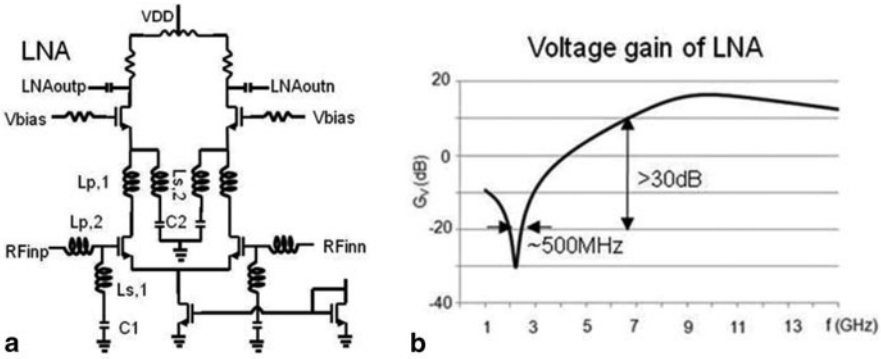

Fig. 17 **a** LNA schematic. **b** Simulated notch effects of the LNA

The LNA employs a dual reactive loop structure as in Fig. 17, which is a differential version from the structure proposed in [14]. The transformer, consisting of Lp1 and Ls1, is used for negative feedback, increasing the bandwidth at the expense of the closed loop gain. The transformer, consisting of Lp2 and Ls2, boosts the gain in the middle of the band. In addition, it provides an opportunity for notch filtering out-of-band blockers and, thus, protecting the following stages from saturation. Here, capacitor C1 is put in series with Ls1 to create a notch, for example, at the 1800 MHz as shown in Fig. 17b, which reduces the need for an external band filter. The above features result in a power-efficient, low-cost, and robust implementation, complying with worldwide regulations and prepared for upcoming standards.

At the mixer stage, an active differential mixer is chosen over the passive mixer. Passive mixers shows typically a higher linearity at the expenses of no gain. Moreover, the down-converted 500 MHz baseband signal is a challenge for the passive mixer. The differential structure is selected for two reasons. First, the receiver is highly differential; i.e., the antenna, LNA, and the quadrature DCO are implemented, fully differential. Second, a double-balanced mixer eliminates the LO-to-IF and RF-to-IF feed through.

The conventional double-balanced switching mixer (shown in Fig. 18a) provides high gain, reduce the noise contributed by subsequent stages and are widely used in RF systems. The transistors in the switching stage (M3, M4, M5, and M6) are stacked on top of the transistors that comprise the transconductor (M1 and M2). Also the load resistor (R) is placed on top of the switching stage. This way of connecting the transconductor, the switching stage and the load resistors is conflicting with operation at low supply voltages. Therefore, at a low voltage supply, the voltages drops across the load resistors, the switching transistors and the transistor in the transconductor become critical. In terms of operation at low supply voltages, several techniques have been proposed to overcome this limitation such as current bleeding, folded mixer and switch-gm mixer. Hence, a folded-switching mixer in Fig. 18b is implemented based on a Gilbert-cell mixer combined with a folded approach.

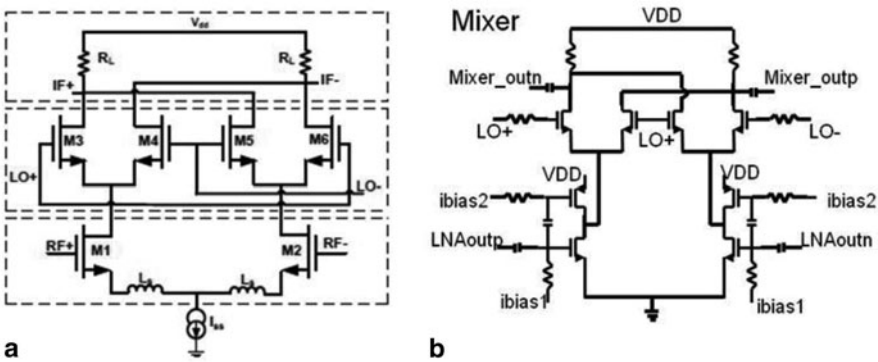

Fig. 18 Conventional **a** double balanced mixer vs., **b** folded mixer

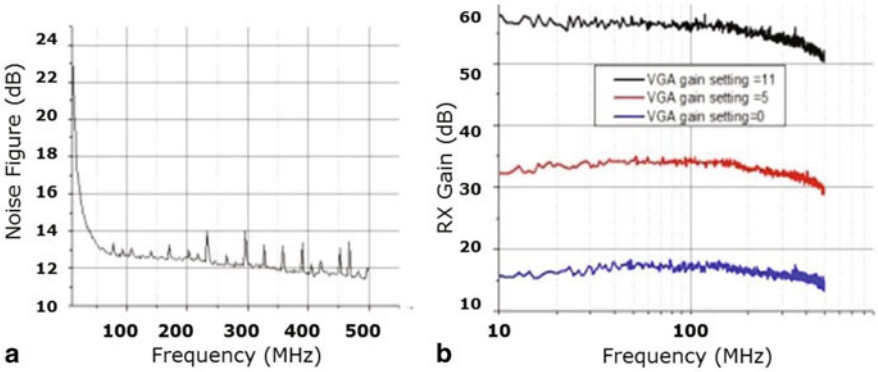

Fig. 19 Receiver measurement results. **a** Noise figure. **b** Conversion gain

This enables operation at a low supply voltage and provides good RF-to-IF and LO-to-IF isolation.

The VGA [15] implemented in this work features low-power consumption, wide-band operating frequency, and fast startup time behavior, dedicated for duty-cycled UWB applications. This is achieved by using DC-coupled open-loop amplifier stages, with fast startup mechanisms in the biasing networks and digitally controlled DC off-set calibration. The measured gain of the VGA is from 0 to 40 dB, in steps of 5 dB and provides 6th order Bessel filtering. The cut-off frequency is programmable between 130 and 350 MHz, depending on the width of the transmitted pulses.

The complete receiver front-end is evaluated in terms of noise figure and gain, with the emphasis of all the measured parameters at the PCB level. This is due to the reason that the de-embedding only reaches the point where the bonding wires touch the PCB board. The loss due to the bonding wires and the contacts between bonding wires and the chip/PCB are difficult to estimate. Besides, for the link evaluation, only the PCB-level results would be relevant. As shown in Fig. 19, the measured noise figure is 12 dB and the maximum conversion gain is 55 dB. The total power consumption in continuous mode is between 46 and 52 mW depending on the different gain mode.

RX Digital Baseband

A digital receiver baseband, currently mapped on a Xilinx Virtex 5 FPGA, processes the 5 bits quantized I and Q baseband signals and controls the receiver frontend. The digital baseband contains an ASIP core in combination with ASIC acceleration blocks. The implemented design is divided into multiple clock domains to reduce the power consumption. The compute intensive operations, i.e., synchronization, Start-of-Frame-Delimiter (SFD) detecting, and payload decoding are hardwired in the ASIC block. The ASIP contains firmware for a lightweight MAC and control algorithms. The combination of ASIP and ASIC allow a flexible but power efficient design. Moreover, wide parallel processing can be implemented to minimize the acquisition time and, consequently, enables a more aggressive duty-cycling of the RF front-end.

During synchronization phase, the frontend is enabled 100 % of the time over a period of multiple preamble symbols. In this time, the incoming samples are correlated against a known sequence, whereby a full-, partial-, or non-coherent correlation can be selected. The pulse position and code phase search are combined in order to reduce the time in the synchronization phase and support full- and partial-coherent synchronization. Once the code phase of the preamble symbols is known, the frontend is duty-cycle between the isolated pulses and the receiver baseband switches into a preamble tracking/SFD detection mode. A hardware implemented correlator is used to search for the SFD. After the SFD has been detected, the frontend is duty-cycled between the burst positions and a hardware supported payload decoding module is used to decode the payload data.

A frequency tracking loop is implemented to compensate the 50 ppm frequency offset between the transmitter and the receiver carriers (Fig. 20). This is essential since the fully-coherent reception outperforms partial/non-coherent receivers when the offset is < 30 ppm. As length of the data symbols is predefined, the frequency offset is measured from the average phase difference between received symbols. The measured frequency offset is low-pass filtered and fed back to control the phase rotator. As such, an offset frequency, equivalent to the measured amount as in Fig. 20, is applied to the received data for compensation. The tracking loop can compensate up to 63 ppm frequency offset and thus ensure the coherent reception with the free-running DCO scheme.

Fast Startup Circuit Techniques

The main power reduction technique for the IR-UWB system is the duty-cycled operation. To fully maximize this property, the system should be strictly turned on only during operation. At the transmitter side, duty-cycle of the RF front-end is achievable during the entire data packet. At the receiver side, duty-cycling is only applicable after the synchronization. Therefore, the RF front-end needs to be turned on continuously until the digital baseband detects the position of the isolated pulses

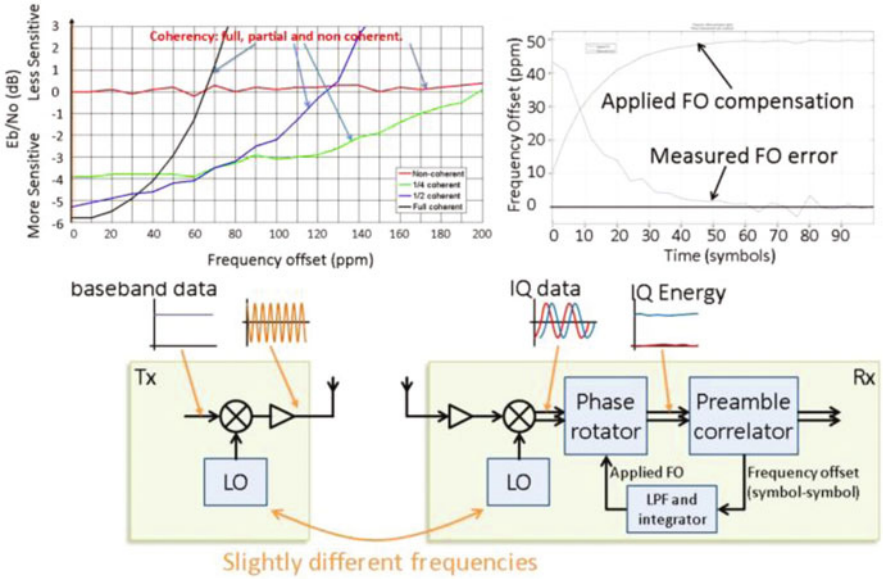

Fig. 20 Closed-loop frequency tracking for coherent reception

and the code phase of the preamble symbols. The longer the synchronization takes, the more power consumption it needs, leading to less duty-cycling efficiency. Another power overhead to reduce the duty-cycling efficiency is the startup behavior of the analog/RF circuit [16]. For efficient duty-cycling, fast start-up is required for each individual block in the receiver. The start-up time is mainly improved by storing the biasing information in large capacitors. For circuit like VGA where the accuracy of the bias current is very critical, the restoring of the biasing information is calibrated, whereas for RF blocks the restoring is noncalibrated. Other than block-level startup optimization, the connections between the blocks are also critical regarding the startup behavior. Obviously, AC coupling becomes less attractive as compared to DC coupling, which however suffers from DC offset. Therefore, offset calibration scheme becomes necessary and critical in the system design, with minimum hardware overhead.

Measurement Results and Conclusions

The complete transmitter, receiver front-end, and ADC are taped out in 90 nm CMOS technology and the die photos are shown in Fig. 21.

The wireless link is evaluated at 8 GHz with a bandwidth of 499.2 MHz and data rate of 0.85 Mbps. The first evaluation is done with the transmitter and the receiver front-end. The down converted baseband data from the receiver front-end

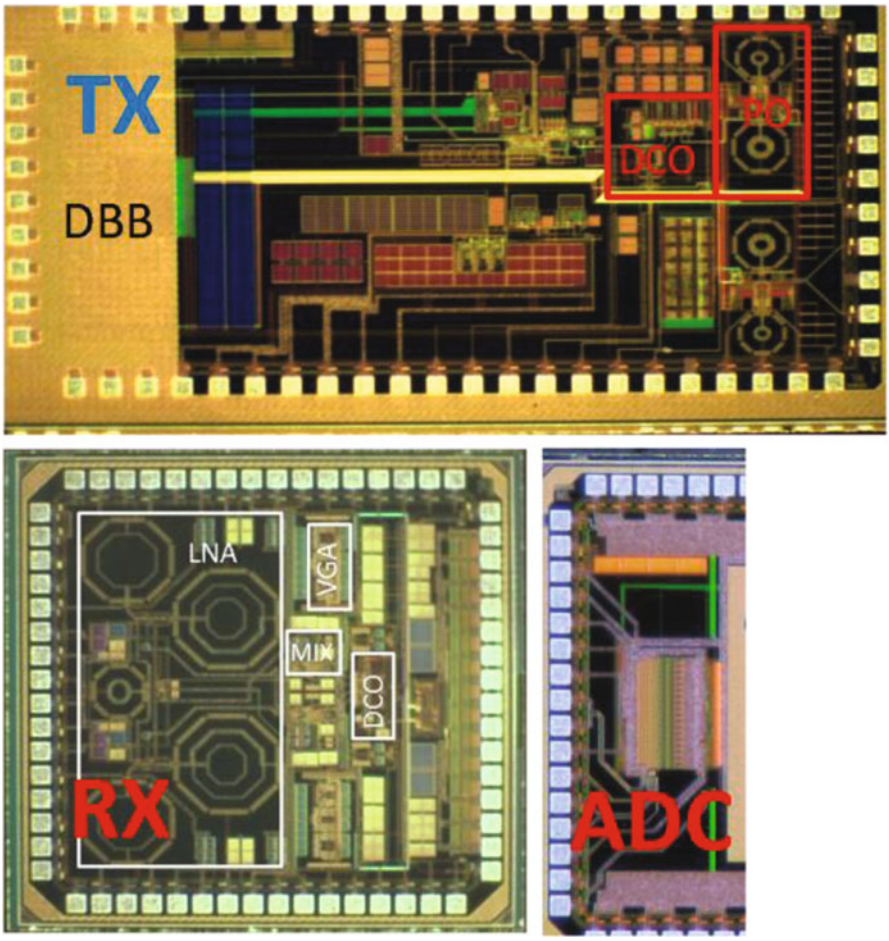

Fig. 21 Die photo of the transmitter, receiver, and ADC

is captured by an oscilloscope in place of an ADC and processed by the baseband algorithm in matlab. The measured receiver sensitivity is − 88 dBm, which matches with theoretical value derived from the noise figure measurement.

In second measurement, as in Fig. 22, the RF FE is evaluated with a 499.2 MHz dual ADC and the DBB mapped on FPGA. Due to the digital implementation loss, the receiver sensitivity is reduced to − 82 dBm. Giving the transmitter output power of − 13 dBm and the non-coherent detection, the − 82 dBm sensitivity enables a link budget of 69 dB. In free space, a wireless link of 16 m can be achieved in principle. The measurement carried out in the lab shows a link distance of 12 m, which is approaching the calculated value. With a more complete clock system in the RF FE, the coherent detection can help to double the link distance to around 30 m.

The overall performance is summarized in Fig. 23. The proposed IR-UWB system is 15.4a standard-compliant and is also easy to adapt to other standards. The complete link works within 6–9 GHz band, and supports a wireless link upto 15 m with − 13

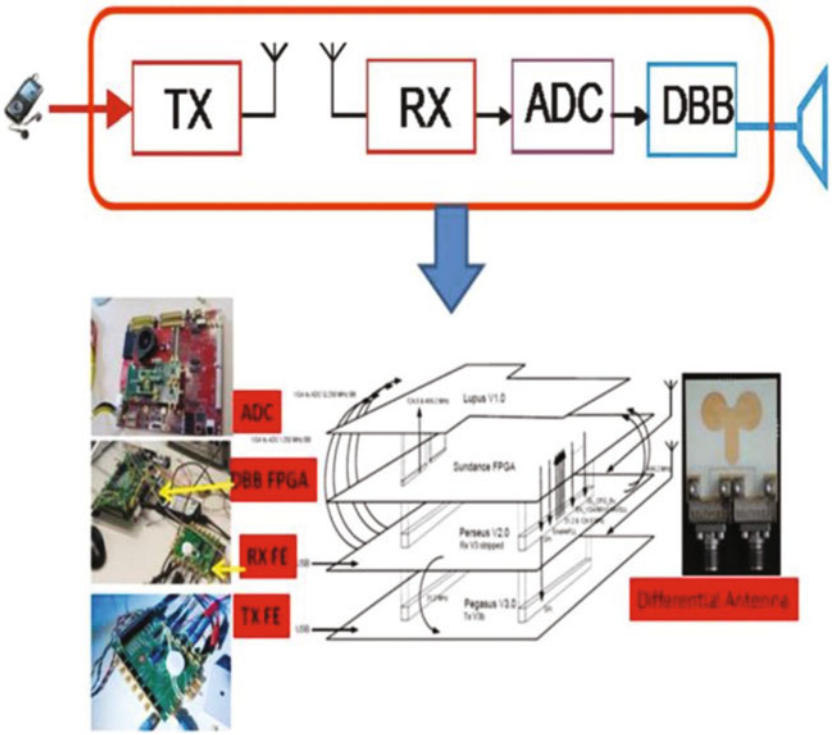

Fig. 22 Measurement setup

	TX	RX
Power consumption	3.5mW (TX FE, DBB,duty-cycled)	46-52mW (RX FE, continuous) 3mW (RX FE, duty-cycled)
Frequency range	6-9GHz	6-9GHz
Pout, peak	13dBm	
Pout,avg	-13dBm (PCB level)	
Sensitivity		-82dBm (PCB level)
Functionality	FE+LO+BB	FE+ADC+BB on FPGA
Data rate	0.85Mbps (upto 27Mbps supported)	
Process	90nm	

Fig. 23 Summary of the measurement results

dBm transmitter output power and − 82 dBm receiver sensitivity. The data rate is variable between 0.85 M and 27 Mbps. The fully integrated transmitter works in the duty-cycled mode and consumes only 3.5 mW with data rate of 0.85 Mbps. The receiver front-end consumes in total 46–52 mW in continuous mode, and 3 mW when being duty-cycled.

References

1. T. Zasowski et al., UWB signal propagation at the human head. IEEE. Trans. MTT. **54**(2), 1836–1845, April 2006
2. C. Roblin, et. al., Antenna design and channel modeling in the BAN context. part II: channel. IEEE. Trans. MTT. **54**(4), 1836–1845, April 2006
3. D. Ruffieux et al., A 2.4 GHz MEMS-based transceiver. ISSCC Dig. Tech. Papers, pp. 522–523, Feb. 2008
4. S. Joo et al., A Fully integrated 802.15.5a IR-UWB transceiver in 0.13 μm CMOS with digital RRC synthesis. ISSCC Dig. Tech. Papers, pp. 228–229, Feb. 2010
5. Y. Zheng et al., A 0.92/5.3nJ/b UWB Impulse Radio SoC for communication and localization. ISSCC Dig. Tech. Papers, pp. 230–231, Feb. 2010
6. D. Lachartre et al., A 1.1nL/b 802.15.4a-compliant fully integrated UWB transceiver in 0.13 μm CMOS. ISSCC Dig. Tech. Papers, pp. 312–313, Feb. 2009
7. M. Verhelst et al., A reconfigurable, 0.13 μm CMOS 110pJ/pulse, fully integrated IR-UWB receiver for communication and sub-cm ranging. ISSCC Dig. Tech. Papers, pp. 250–251, Feb. 2009
8. P. Harpe et al., A 0.47–1.6 mW 5bit 0.5–1GS/s time-interleaved SAR ADC for low-power UWB radios. Proc. ESSCIRC. pp. 147–150, Sep. 2010
9. A. Molnar, B. Lu, S. Lanzisera, B.W. Cook, K.S.J. Pister, An ultra-low power 900 MHz RF transceiver for wireless sensor networks. IEEE Custom Integrated Circuits Conference (CICC), pp. 401–404, 2004
10. B. Otis, Y.H. Chee, J. Rabaey, A 400 μW, 1.6 mW TX superregenerative transceiver for wireless sensor networks. IEEE ISSCC Dig. Tech. Papers, pp. 396–397, 2002
11. B. Otis, Y.H. Chee, R. Lu, N.M. Pletcher, J.M. Rabaey, An ultra-low power MEMS-based two channel transceiver for wireless sensor networks. Symposium on VLSI Circuits, Dig. Tech. Papers, pp. 20–23, 2004
12. Y.H. Chee, A.M. Niknejad, J.M. Rabaey, An ultra-low power injection locked transmitter for 2 sensor networks. IEEE Custom Integrated Circuits Conference (CICC), pp. 797–800, 2006
13. X. Wang et al., A high-band IR-UWB chipset for real-time duty-cycled communication and localization systems. ASSCC Dig. Tech. Papers, pp. 312–313, June 2011
14. S. Bagga, A.L. Mansano, W.A. Serdijn, J.R. Long, K. Philips, J.J. Pekarik, A frequency selective nested dual-loop broadband low-noise amplifier in 90 nm CMOS. ESSCIRC, pp. 121–124, 2012
15. P. Harpe et al., A 1.6 mW 0.5 GHz open-loop VGA with fast startup and offset calibration for UWB radios. Proc. ESSCIRC, pp. 103–106, Sept 2011
16. C. Zhou, P. Harpe, X. Wang, K. Philips. H. de Groot, 10 ns start-up techniques for a duty cycled impulse radio receiver. ESSCIRC, pp. 426–429, 2012

System-on-a-Chip UWB Radar Sensor for Contactless Respiratory Monitoring: Technology and Applications

Domenico Zito and Domenico Pepe

Abstract Thanks to the extremely low level of emitted power, ultra-wideband (UWB) technology is expected to be one of the most important technologies capable of supporting both, the needs of contactless sensing and ultra low-power data communication, opening to interesting opportunities for implementing innovative sensors applied to the continuous monitoring of vital parameters and their communication within wireless body area networks.

In this frame, particularly relevant is the interest in radar sensors for contactless respiratory rate monitoring. Such devices are expected to be the enabling technology for a wide range of continuous bio-monitoring applications, ranging from sleep–wake classifications of drivers in vehicles to respiratory disorder diagnoses (e.g., obstructive apneas) of infants and adults, from fatigue detection for fitness users to health monitoring of patients in hospital and domestic environments. The contribution expected from continuous-time contactless monitoring systems free of any encumbrance will have a pivoting role in tackling respiratory chronic diseases and gaining a better understanding of respiratory rate variability, especially in correlations with other pathological (e.g., cardiovascular, obesity, diabetes, etc.), behavioral, and environmental risk factors.

This chapter reports the key aspects of the research and development of the radar technology carried out by our group. In detail, it focuses on the implementation of a System-on-a-Chip (SoC) UWB pulse radar for respiratory rate monitoring in nano-scale CMOS technology and its experimental tests in the operating scenarios. Paragraph 1 reports an introduction to UWB pulse radar systems for contactless monitoring of vital parameters. Section "SoC CMOS UWB Pulse Radar Sensor" reports the SoC UWB pulse radar system for respiratory monitoring and its operating principle and building blocks. Section "Field Operational Tests" reports the experimental results of the field operational tests, including the detection of the respiratory rate patterns of adults and infants. Finally, the conclusions are drawn in section "Conclusions".

D. Zito (✉) · D. Pepe
Department of Electrical and Electronic Engineering, University College Cork, Cork, Ireland
e-mail: domenico.zito@tyndall.ie

Tyndall National Institute, "Lee Maltings", Dyke Parade, Cork, Ireland

M. R. Yuce (ed.), *Ultra-Wideband and 60 GHz Communications for Biomedical Applications,* DOI 10.1007/978-1-4614-8896-5_4,

Keywords Contactless motion sensing · Respiratory monitoring · Apnea · Adult · Infant · UWB · Radar · System-on-chip · CMOS · Pulse generator · Low noise amplifier · Multiplier · Delay generator · Integrator

Introduction

In February 2002, the Federal Communications Commission (FCC) authorized the marketing and operation of a new class of products incorporating ultra-wideband (UWB) technology [1]. The FCC, by modifying the 47 Code of Federal Regulations (CRF) Part 15 regulations [2] allocated for the UWB systems an unlicensed band 7.5 GHz wide (for the first time, in a nonexclusive way), in the range of the radio-frequency spectrum 3.1–10.6 GHz. The maximum equivalent isotropic radiated power (EIRP) in-band spectral density allowed for UWB devices has been set to − 41.3 dBm/MHz, whereas different out-band restrictions have been set according to the nature of the applications.

Both in-band and out-band restrictions allow the reduction of the interferences with the other wireless communication services already operating in the same region of the frequency spectrum. In the recent years, Asia and Europe adopted similar regulations for the UWB applications in the same frequency band [3, 4].

UWB devices can be exploited for the implementation of several wireless data communication and contactless systems for mass-market applications, such as ground penetrating radars, wall and through wall imaging, surveillance, high data rate communication, and medical imaging. Due to the extremely low level of radiated power spectral density (PSD), significant interests have been focused on medical applications. In this framework, particularly relevant is the opportunity offered by the sensors for contactless respiratory rate monitoring. Such devices are expected to be the enabling technology for a wide range of continuous bio-monitoring applications, ranging from sleep–wake classifications of drivers in vehicles [5] to respiratory disorders monitoring of adults and infants [6], from the fatigue detection for fitness users to monitoring of patients in hospital and domestic environments.

The base concept of UWB devices is to generate, send, and receive extremely short radio-frequency pulses, with time duration in the range of hundreds of picoseconds to few nanoseconds. Very short pulses allow us to achieve a very high spatial resolution. Large pulses allow longer communication ranges; however, their repetition frequency must be kept lower in order to assure the compliance of the EIRP spectral density with the emission mask of the standard regulations. Since pulses and echoes are radiated and captured by means of antennas, it is very important that the antennas transmit and receive the UWB signals without introducing a significant level of distortions. Therefore, the bandwidth of the antennas must be wide enough (a few gigahertz) to transmit and receive the UWB pulses properly.

The market penetration for these emerging devices is related to the opportunity of implementing ultra-miniaturized low-power low-cost transceivers on standard silicon technologies. Complementary metal-oxide semiconductor (CMOS) has emerged

over the last years as the predominant technology of the microelectronics industry [7]. Device scaling results in consistent improvements of the device density and performance, enabling the System-on-a-Chip (SoC) implementation of highly miniaturized and low-cost sensors. Therefore, in addition to the performance requirements, the physical cointegration of radar microchip and antennas has to also consider the manufacturing costs during the design phase [8, 9].

One of the main technical challenges for the SoC CMOS implementation of UWB radars is related with the on-chip generation of extremely short (few hundred picoseconds) radio-frequency pulses with large amplitude and high energy efficiency [10]. Thanks to the successful implementation of the most critical building blocks [11, 12], our research group recently presented the first implementation, including experimental evidence and compliance to FCC UWB spectrum mask, of a SoC UWB pulse radar based on a correlation receiver, in 90 nm CMOS technology by STMicroelectronics [13, 14]. In particular, the work reported by Zito et al. [13] focuses on the technical aspects regarding the SoC implementation of the radar microchip in 90 nm bulk CMOS technology, whereas the work reported by Zito et al. [14] focuses on the extension of the field operational tests for contactless detection of respiratory rate in adults and infants. In the following sections we report the key aspects and main results of this on-going research carried out by our group.

System-on-a-Chip Complementary Metal-Oxide Semiconductor Ultra-Wideband Pulse Radar Sensor

Pulse radars operate by sending short electromagnetic pulses, and by receiving the echoes reflected by the target. The time delay between the transmitted and received pulses is proportional to the distance from the target to the radar. Examples of pulse radars for the detection of vital parameters implemented in hybrid-form circuits by means of discrete components are reported in literature [15, 16]. In this section we report the key aspects of the design of the first implementation, including experimental evidence and FCC UWB mask compliance, of the SoC UWB pulse radar based on a correlation receiver, in 90 nm CMOS technology by STMicroelectronics [13]. In detail, the principle of operation is highlighted in section “Operating Principle”. The design of the building blocks and their experimental results are summarized in section “Building Blocks”. The SoC UWB radar in 90 nm CMOS technology and the results of the experimental characterization of the radar sensor are reported in section “SoC UWB Pulse Radar”.

Operating Principle

The block diagram of the UWB radar sensor is shown in Fig. 1a. The receiver is based on a correlation topology. The operating principle of this radar can be

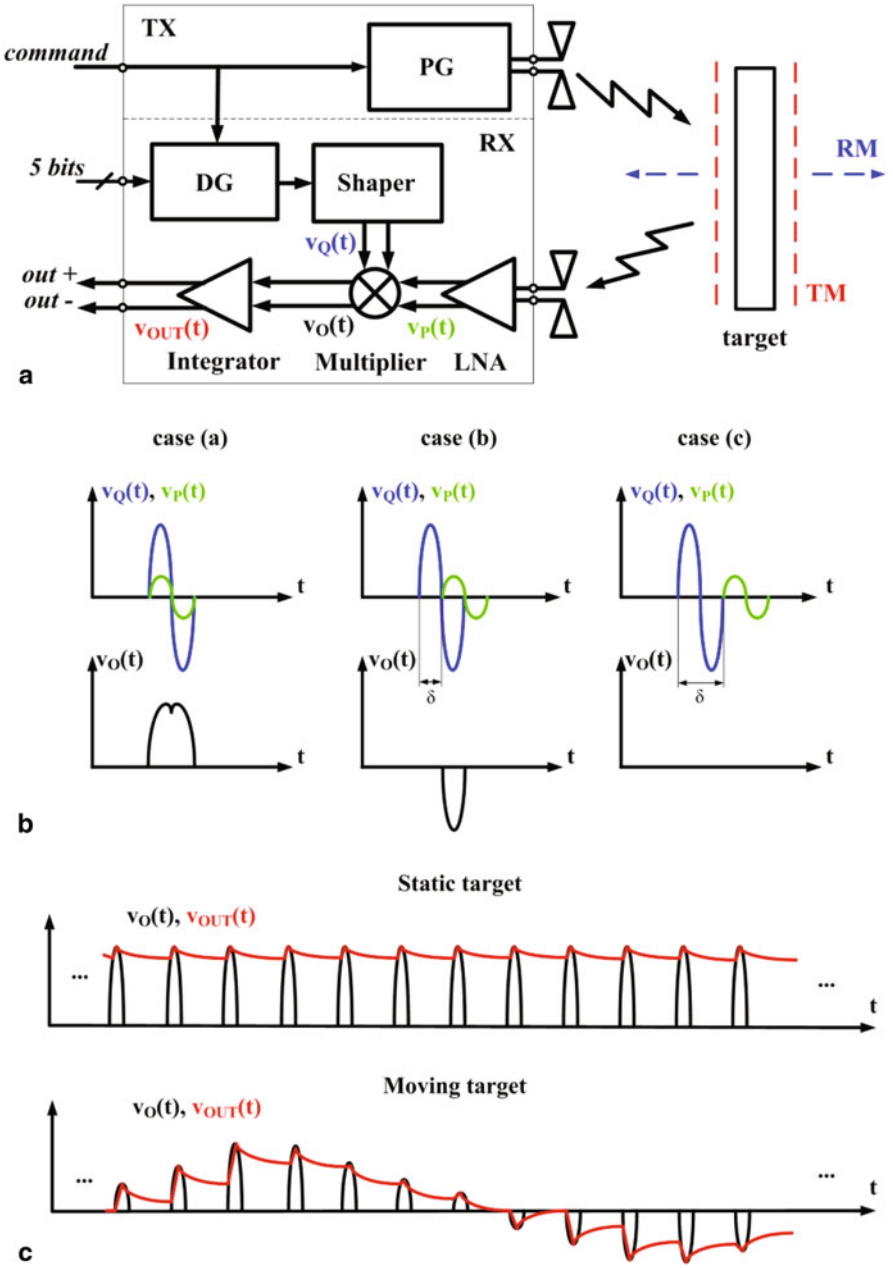

Fig. 1 **a** Block diagram of the System-on-a-Chip (SoC) ultra-wideband (UWB) pulse radar. *PG* is the pulse generator, *LNA* is the low-noise amplifier, *DG* is the delay generator. The *dashed lines* around the target indicate the range spanned by the radar in ranging mode (*RM*) and tracking mode (*TM*). **b** Representation of the pulses at the input and output of the multiplier for three different cases of relative shift (δ) between the input pulses. **c** Representation of the input and output voltages of the integrator for static and moving targets

summarized as follows. The pulse generator (PG) transmits, through the transmitting antenna, electromagnetic pulses with time duration of few hundred picoseconds and a pulse repetition frequency (f_{RP}). After a time delay, approximately equal to the flight time of the pulse from the transmitter to the receiver, the echoes captured by the receiving antenna are amplified by the low-noise amplifier (LNA), and then multiplied with a delayed replica of the transmitted pulse generated locally (i.e., on-chip) by the shaper (see Fig. 1a).

The output of the multiplier is then averaged by a high-gain, low-bandwidth (B) low-pass filter (i.e., integrator, see Fig. 1a), in order to increase the output signal to noise ratio (SNR_{out}) of the receiver and track the envelope of the output voltage of the multiplier [17].

Since vital signs vary within a few hertz, an integrator with a 3-dB band (B_{3dB}) of 100 Hz allows accurate detection of their variations.

To explain intuitively the operating principle, let us assume that the delay generator (DG) provides a delay equal to the entire time-of-flight of the pulses, i.e., round trip, from the transmitter to receiver. If the target is not moving (i.e., static target), the local replica and the amplified echo are timely aligned and the multiplier provides constant amplitude pulses, as shown in Fig. 1b, case (a). Therefore, the signal at the output of the integrator (a high-gain, low-pass filter) is an almost constant envelope, as shown in Fig. 1c.

Note that the integrator will provide an almost constant output voltage envelope regardless of the relative shift (δ) between the local replica and amplified echo, for any other constant δ, assuming δ is lower or equal to the duration time of the pulse. If the target is moving, the movement causes a time-varying δ between the local replica and the eco amplified by the LNA.

Therefore, the multiplier provides an output pulse that may be positive, negative, or zero, depending on the time shift δ caused by time-varying distance between radar and target and due to the target movements around its quiescent position.

In particular, this radar sensor is thought to operate in two operating modes: ranging mode (RM) and tracking mode (TM). In RM, the DG provides a variable delay in order to span the range of interest and identify the target (see Fig. 1a). In RM, the radar sensor allows us to identify the presence of the target and the time of flight. When the target is detected, the radar can be switched to the TM, in which the DG provides a fixed delay (i.e., equal to the time of flight identified in RM) in order to monitor a fixed range gate (see Fig. 1a) and tracking the target motion (displacement) around its quiescent position. Therefore, the output voltage is directly sensitive to the target movements, e.g., the chest movement due to the pulmonary activity in case of respiratory rate monitoring. The output voltage can be expressed approximately as follows:

$$\begin{aligned} v_{OUT}(t) &\approx A\frac{B}{2\pi}\int_{t-\frac{2\pi}{B}}^{t} v_Q(\tau)\times v_P(\tau)d\tau \\ &\approx A\frac{B}{2\pi}\int_{t-\frac{2\pi}{B}}^{t} v_Q(\tau)\times \alpha \times v_Q(\tau-\delta)d\tau \end{aligned} \tag{1}$$

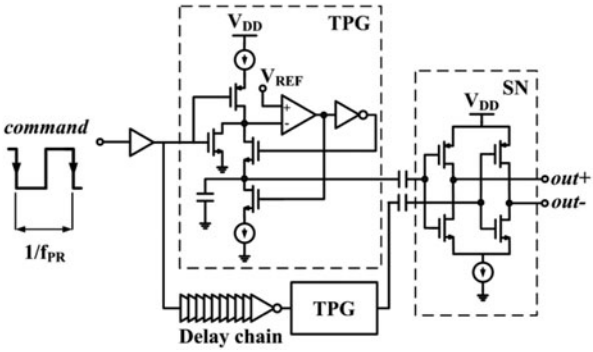

Fig. 2 Schematics of the pulse generator (*TPG* is for 'triangular pulse generator', *SN* is for 'shaping network')

which is obtained assuming that the amplified echo has the same shape of the transmitted pulse (i.e., the same of the local replica), but different amplitude (α is the attenuation factor, A is the correlation voltage gain, B is the bandwidth of the low-pass filter, and δ the relative delay between the input signals of the multiplier).

Building Blocks

The schematic of the building blocks (PG, LNA, multiplier, DG, and integrator) of the SoC UWB pulse radar of Fig. 1a are reported hereinafter, together with a short description of the circuit design and performance. All the circuits are supplied with 1.2 V. Receiver and transmitter have been implemented according to a fully differential topology in order to increase the immunity to common mode noise and interferences.

The schematic of the PG is shown in Fig. 2. The PG has been designed by following the principles reported by Zito et al. [10]. It provides a monocycle pulse on a 100 Ω differential load (i.e., the impedance of the antenna) when activated by the negative edge of the digital signal command occurring at f_{PR}. The measurements show a duration time (t_D) of the pulse of 350 ps and a pulse amplitude of 650 $mV_{pp-diff}$ (including the losses of microprobes and cables) corresponding to about 900 $mV_{pp-diff}$ on chip. The energy consumption (E_C) per transmitted pulse is 19.8 mW $\times$ 350 ps = 6.9 pJ. The measured pulses and its PSD are shown in Fig. 3. The power consumption is equal to 19.8 mW. The circuit schematic of the shaper block follows the same principle of the PG, but it requires a lower bias current (2 mA) for its shaping network since it has a higher load impedance (i.e., the input impedance of the multiplier). The power consumption of the shaper amounts to 13.8 mW.

The schematic of the UWB LNA is shown in Fig. 4. The LNA has been designed according to the design in Pepe and Zito [11]. It consists of a common-gate stage, which realizes a wideband input impedance matching to the 100 Ω differential antenna load, and two subsequent common-source stages which increase the overall gain. The measured performances of the LNA as a stand-alone circuit are shown in Fig. 5. S_{21} is equal to 22.7 dB at 5 GHz, S_{11} is lower than − 10.5 dB and noise

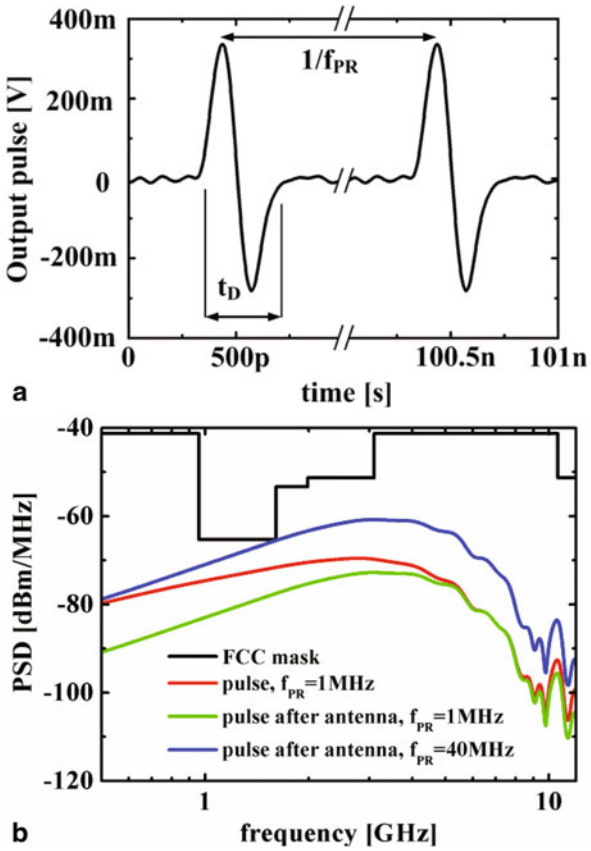

Fig. 3 **a** Output pulses provided by pulse generator (PG) ($f_{PR} = 10$ MHz) captured by means of a two-channel (50 Ω impedance each) real-time digital oscilloscope DSA 91204A (40 GSa/s, 12 GHz bandwidth). **b** Spectrum of the measured pulses before and after the antenna filtering and ultra-wideband (UWB) mask by the Federal Communications Commission (FCC) for biomedical applications

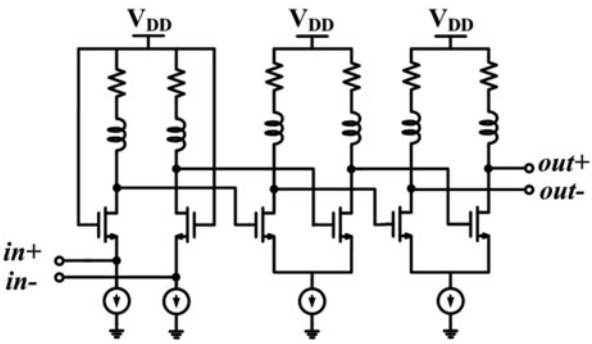

Fig. 4 Schematics of the low noise amplifier

figure (NF) is lower than 6.5 dB (including the noise contributions of UWB baluns, probes, and cables) over the all UWB band. The input-referred 1-dB compression point (iP_{1dB}) is equal to − 19.7 dBm. The LNA power consumption amounts to 34.8 mW.

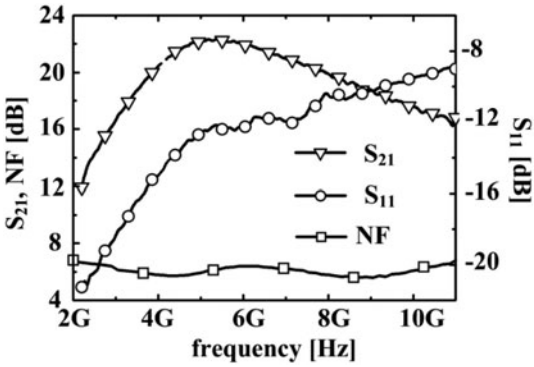

Fig. 5 Low-noise amplifier measurements (S parameters, S_{21} and S_{11}, and noise figure, *NF*)

The schematic of the UWB multiplier is shown in Fig. 6. It has been designed according to the design principle explained by Zito et al. [12]. The multiplier exploits a p-MOSFET (M_P) common-gate pair input stage in order to provide a low-complexity input matching to the LNA output impedance (about 200 Ω differential) over a wide frequency band (Fig. 7).

The multiplier consists of a p-MOSFET (M_Q) Gilbert quad. The common-mode feed-back (CMFB) regulates the common-mode output voltage through V_{CM} and V_C. V_{REF} (0.6 V) is an external DC voltage reference. The multiplier has been tested as a stand-alone circuit by applying two sequences of pseudo-Gaussian monocycle pulses of amplitude 170 $mV_{pp-diff}$ (V_P) and 650 $mV_{pp-diff}$ (V_Q), and time duration (t_D) equal to 700 ps (V_P is expected to be the echo amplified by the LNA, whereas V_Q is the delayed replica generated on-chip by the shaper). The measured output voltage (V_O) for three different delays between the input pulses V_P and V_Q is shown in Fig. 8. The measured NF amounts to 14.4 dB at 4 GHz. The iP_{1dB} is equal to − 3.5 and − 2 dBm for P and Q inputs, respectively. The power consumption is 3.7 mW.

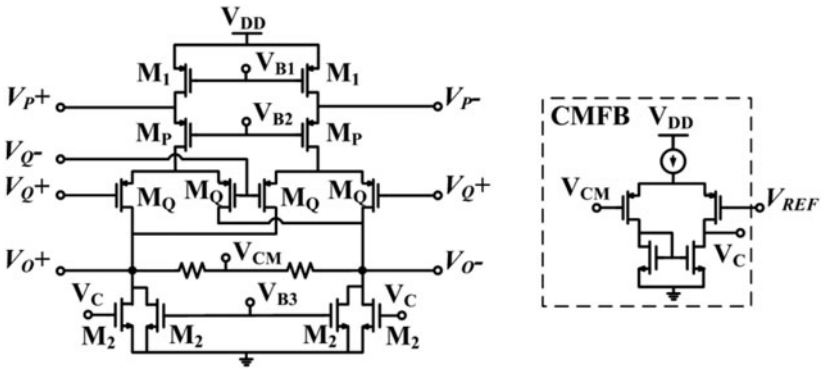

Fig. 6 Schematics of the multiplier including the CMFB sub-circuit

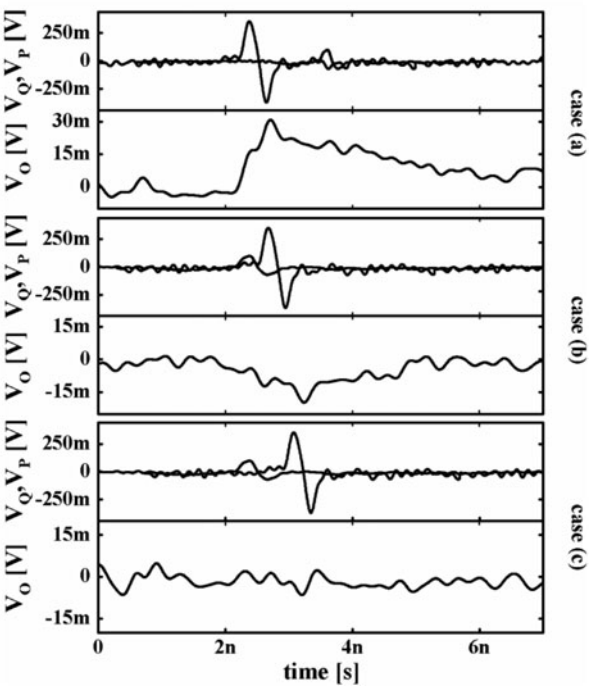

Fig. 7 I/O signals of the multiplier measured in three cases: the input monocycle pulses have **a** no relative delay (i.e., time alignment), **b** a relative delay of half of the time duration, and **c** relative delay equal to the time duration. V_O is captured by means of the probe 1134A (impedance 50 KΩ||0.27 pF) and oscilloscope DSO 54855A

This circuit solution allows us to implement efficiently the multiplication between short pulses.

The schematic of the integrator is shown in Fig. 8a. The integrator consists of a 3-stage amplifier with Resistive-Capacitive (RC) feedback and output buffer. The stages use identical differential pair amplifiers. Details of the devices sizing are reported by Zito et al. [13]. The power consumption is 1.1 mW. The voltage gain is 58 dB and B_{3dB} is equal to 147 Hz.

The schematic of the 5-bit programmable monotonic DG is shown in Fig. 8b. It has been designed following the principle explained by Maymandi-Nejad and Sachdev [18]. Details of the devices sizing are reported by Zito et al. [13]. The 5 bits allow us to select the output current of the inverter (M_8 and M_9) in order to vary the slope of the voltage ramp (high to low) on its load capacitance. By varying the bias current, the DG can provide delays in the range 1–30 ns. The power consumption is lower than 0.1 mW.

System-on-a-Chip Ultra-Wideband Pulse Radar

The micrograph of the radar microchip is shown in Fig. 9. The die area amounts to about 2 mm^2. The overall power consumption amounts to 73.2 mW.

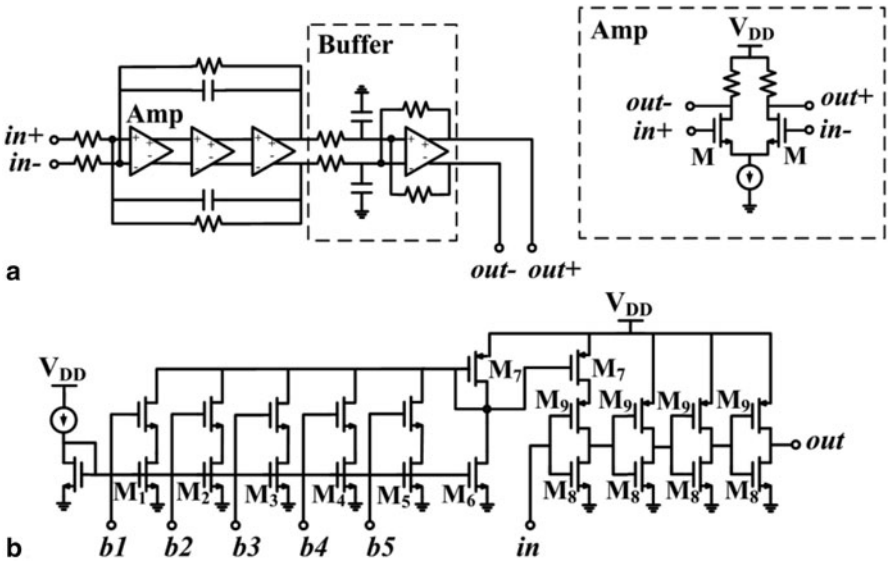

Fig. 8 Schematic of the other building blocks: **a** Integrator. **b** Delay generator

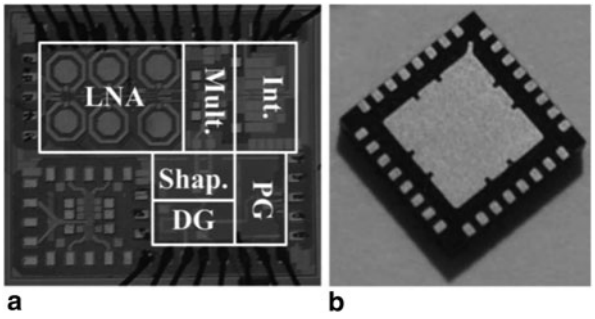

Fig. 9 System-on-a-Chip (SoC) ultra-wideband (UWB) pulse radar. **a** Micrograph of the radar testchip (all pads are ESD protected). The die size is $1.5 \times 1.3\,\text{mm}^2$ (including the multiplier as stand-alone device). **b** Radar testchip packaged in a QFN32 leadless package (*bottom view*) with exposed ground pad (size $5 \times 5\,\text{mm}^2$)

The receiver and transmitter of the SoC UWB pulse radar have been designed in order to have inputs and outputs on the two opposite sides of the die, allowing a straight connection to the input and output pins of the package, and then with the two planar antennas realized on FR4 board as reported hereinafter.

On-chip characterization of the SoC UWB pulse radar has been carried out by means of GSGSG Infinity probes by Cascade®. A test-board in FR4 for supplying DC and control voltages to the radar test-chip has been designed and realized. The testchip has been attached to the board; DC and control voltages have been bonded to the board. The measurement setup is shown in Fig. 10. The PG output is connected to the LNA input by means of microprobes, cables and attenuators. The propagation delay of cables and attenuators has been derived from their measured S-parameters [19] and amounts to about 8 ns.

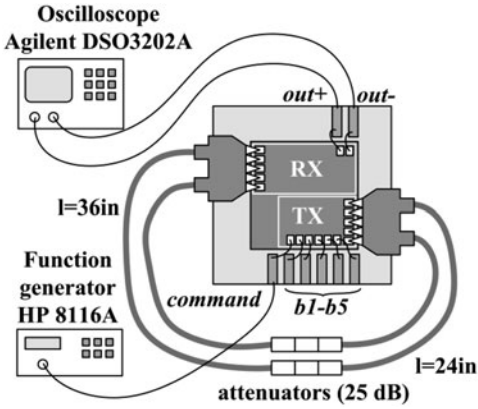

Fig. 10 On-chip measurement setup of the System-on-a-Chip (SoC) ultra-wideband (UWB) pulse radar

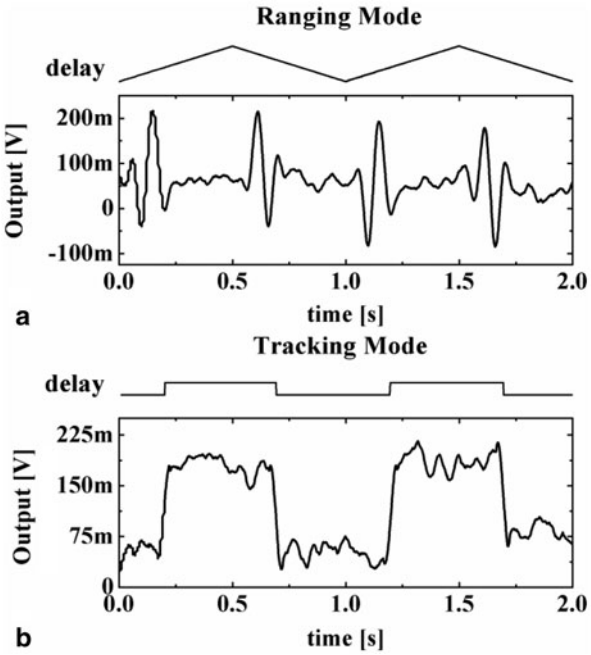

Fig. 11 Measured output of the radar. **a** The delay of the delay generator (DG) is varied as a ramp around the value of the delay of the cables (∼ 8 ns). **b** The delay of the DG is chosen equal to two values, one corresponding to perfect time alignment between output of the shaper and output of the low-noise amplifier (LNA), and one corresponding to the time of total misalignment (i.e., no overlapping)

Since the delay of cables and attenuators is fixed, the simulation of a moving target has been performed by varying the delay of the DG. In the first experiment the DG has been driven by a ramp (with a rise time and a fall time of 0.5 s each) in order to span the range of delays of interest (around 8 ns).The measured output of the radar is shown in Fig. 11a.

Note that the output of the radar is constant when the output of the LNA and the output of the shaper are not time aligned (i.e., the output of the multiplier is zero), and it varies when the two signals overlap themselves in time.

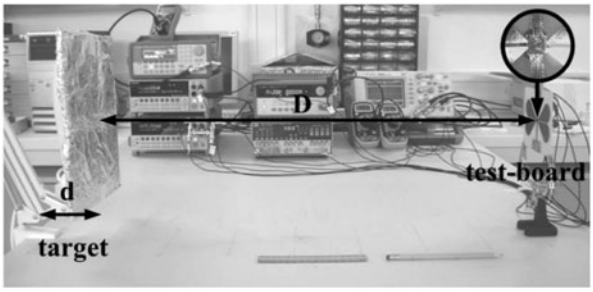

Fig. 12 Experimental setup for the characterization of the ultra-wideband (UWB) pulse radar sensor, including packaged System-on-a-Chip (SoC) pulse radar and on-board antennas. The target is made of a 0.5 cm thick board covered by an aluminum foil. The radar sensor is placed at a distance (D) from the target which may move for a displacement (d). A detail of the packaged radar testchip mounting on test-board is reported in the insert on top right corner

In the second experimental test, the DG has been driven in order to produce only two delays, one corresponding to a perfect time alignment between the two inputs of the multiplier, and one corresponding to a total time misalignment between the two signals. The delay is changed every 0.5 s. The measured output of the radar in this case is shown in Fig. 11b. In both the experiments, f_{RP} was equal to 40 MHz.

Overall, the results of the functional tests demonstrate that the testchip works properly. Note that the DC offset (~ 50 mV), which can be eliminated during the digital processing, is not an issue for this application aimed at detecting the movement rate.

Field Operational Tests

The complete radar sensor consisting of the SoC UWB radar and two identical UWB antennas (one connected to the transmitter output and the other to the receiver input) has been designed and realized on FR4 substrate ($\varepsilon_R = 4.4$, dielectric thickness of 1.6 mm and copper thickness of 0.35 μm).The complete radar sensor has been tested in operational field tests. The complete radar sensor board and the measurement setup for the first operative tests are shown in Fig. 12.

In a first set of operational tests, the target is made by plasterboard covered by aluminum foil and is placed in front of the radar at a distance D. The target may move along the axis radar-target for a displacement d around its quiescent position at a distance D, with a given period (about 0.8 s). The results have shown that the radar sensor is able to detect the three different targets of $26 \times 26\,\text{cm}^2$, $13 \times 26\,\text{cm}^2$, and $13 \times 13\,\text{cm}^2$, for displacement movements $d = 2$ cm around the quiescent position at a distance D up to 70 cm.

The output voltage for the target of area $26 \times 26\,\text{cm}^2$ ($d = 2$ cm, $D = 70$ cm) is shown in Fig. 13. The output voltage swing is about 10 mV. These results demonstrated the radar capability of detecting small variation of the target position.

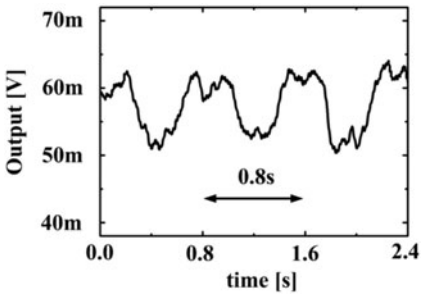

Fig. 13 Output voltages (measured) in tracking mode (TM) ($f_{PR} = 40$ MHz). The target movement rate is 1.25 Hz

Another set of field operational tests has been carried out in order to detect the respiratory activity of a subject under test. Two measurement setups have been adopted as shown in Fig. 14.

In Fig. 14a, an adult person is sitting in front of the radar at a distance of 30 cm. The output of the radar is shown in Fig. 15a. Note that the output voltage swing is about 5 mV during the normal respiratory activity and is almost constant when the person under test stops breathing (i.e., voluntary apnea). A number of additional tests up to a distance of 45 cm and extensive results can be found in Zito et al. [14]. Here it is worth mentioning that tests have been carried out successfully for both genders, with chest displacements of about 1 cm.

In Fig. 14b, an infant (asleep) sitting in a car baby seat placed under the radar sensor at a distance $D = 30$ cm from the chest moving with a displacement of about 2 mm. The output voltage of the radar sensor tracks the respiratory rate profile of the infant, as reported in Fig. 15b. Note the presence of a very short apnea of about 3 s, in which the out voltage remains approximately constant except for small variations (< 2 mV) due to noise.

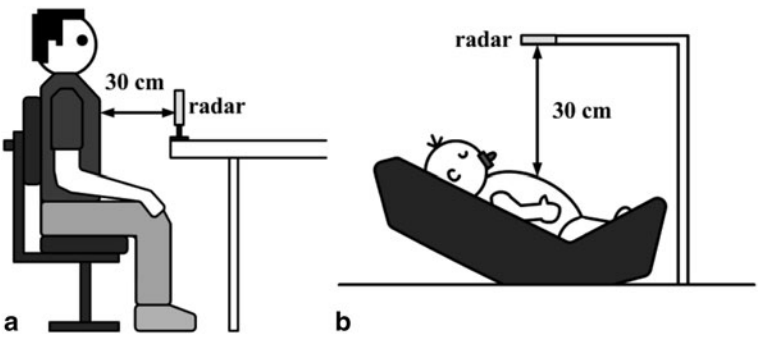

Fig. 14 Measurement of the respiration rate of: **a** an adult person placed at 30 cm from the ultra-wideband (UWB) radar sensor; **b** a baby in a car seat placed at 30 cm from the UWB radar sensor

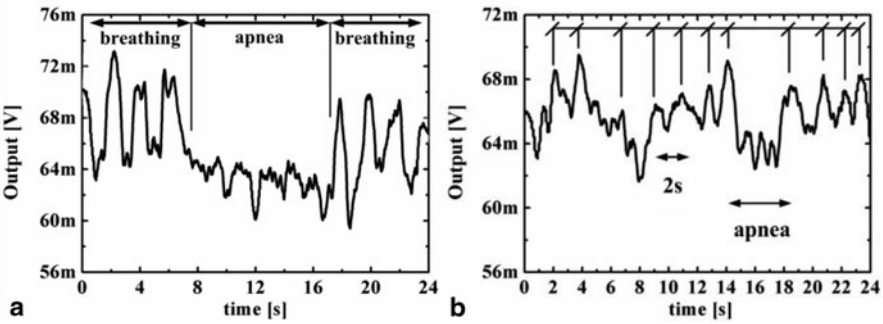

Fig. 15 **a** Output voltage (measured) in tracking mode (TM) ($f_{PR} = 40$ MHz) for the case of an adult person under test (see Fig. 14a). In the first phase of the experiment the person under test is breathing; in the second phase the person under test is holding the breath voluntarily; in the third phase the normal respiration process is restored. **b** Output voltage (measured) in TM ($f_{PR} = 40$ MHz) in the case of a baby under test (see Fig. 14b). The respiratory rate is slightly irregular with an average of 0.5 Hz. Note that the radar detects very short apneas of 3 s

Conclusions

In this chapter, we have introduced the technology and application of UWB radar sensor for the contactless detection of respiratory rate. In particular, we have reported the key aspects and the main results of the on-going research carried out by our group. In detail, we have shown an ultra wideband (UWB) radar sensor for respiratory rate monitoring designed and implemented by integrating a SoC UWB radar realized in 90 nm CMOS technology with a board with two planar antennas, one for the transmitter and one for the receiver. The radar test-chip, packaged in QFN32, was attached to the board and the planar antennas and codesigned accordingly, so achieving a working UWB sensor prototype compliant with the FCC UWB standard regulations, in particular for medical applications.

The operation of the radar sensor was proven by means of functional and field operational tests. The radar was able to track reflective targets for movements (front-back) up to 2 cm around a distance of 70 cm. The UWB sensor was applied to the field operational tests on adult (both gender) and infant volunteers placed at a distance up to 45 cm. The results show that the radar sensor allows the detection of subcentimeter chest movements, allowing the continuous-time monitoring of respiratory rate associated with the normal activity, including apneas.

This UWB sensor could be potentially employed in a number of biomedical applications, such as monitoring babies in cot beds, patients in hospitals, and other people at risk of obstructive apneas. It can be also used for the early detection of sudden sleep of drivers in vehicles. This contactless sensing technology enables also other important applications such as fitness monitoring and personalized healthcare for independent and healthy living. Despite all its potential applications in the biomedical field, it can be also applied to a large number of other civil applications demanding contactless detection of moving objects nontransparent to UWB radiation, opening new and interesting chapters of the long and successful story of the radar technology.

Acknowledgments This work was supported in part by the Science Foundation Ireland (SFI), in part by the UE through the European Project ProeTex (FP6-2004-IST-4-026987), in part by Irish Research Council (IRC), and in part by the Italian Ministry of University and Research (MIUR). The authors are grateful to Prof. Danilo De Rossi, Interdepartmental Research Center "E. Piaggio", University of Pisa, Pisa, Italy, Dr. Martina Mincica, and Dr. Fabio Zito, today with Analog Devices, Limerick, Ireland, and Ansaldo STS SpA, Naples, Italy, respectively, for their contributions to this research.

References

1. New Public Safety Applications and Broadband Internet Access Among Uses Envisioned by FCC Authorization of Ultra-Wideband Technology Federal Commun. Commission, Washington, DC, 2002 (Online), http://www.fcc.gov/Bureaus/Engineering_Technology/News_Releases/2002/nret0203.html. Accessed 10 March 2013
2. Revision of Part 15 of the Commission's Rules Regarding Ultra-Wideband Transmission Systems, FCC 02-48, February 2002
3. Report summary from UWB radio systems committee, Ministry of Internal Affairs and Communications (MIC), 2006 (Online), http://www.soumu.go.jp/joho tsusin/eng/pdf/060327_UWB_report.pdf. Accessed 10 March 2013
4. ETSI ultra wide band, European Telecommunications Standards Institute (ETSI), 2008. (Online), http://www.etsi.org/WebSite/Technologies/UltraWideBand.aspx. Accessed 10 March 2013
5. W. Karlen, C. Mattiussi, D. Floreano, Sleep and wake classification with ECG and respiratory effort signals. IEEE Trans. Biomed. Circuits Syst. **3**(2), (Apr 2009)
6. S.M. Caples, A.S. Gami, V.K. Somers, Obstructive sleep apnea. Ann. Int. Med. **142**(3), 187–197 (2005) (PMID 15684207, Feb 2005)
7. H.-S.P. Wong, D.J. Frank, P.M. Solomon, C.H.J. Wann, J.J. Welser, Nanoscale CMOS. Proc. IEEE. **87**(4), 537–570 (Apr 1999)
8. S. Bagga, et al., Codesign of an impulse generator and miniaturized antennas for IR-UWB. IEEE Trans. Microw. Theory Tech. **54**(4), 1656–1666 (Apr 2006)
9. A.V. Vorobyov, et al., Integration of a pulse generator on chip into a compact ultrawideband antenna. IEEE Trans. Antenn. Propag. **56**(3), 858–868 (Mar 2008)
10. F. Zito, D. Pepe, D. Zito, UWB CMOS monocycle pulse generator. IEEE Trans. Circuits Syst. I. **57**(10), 2654−2664 (Oct 2010)
11. D. Pepe, D. Zito, 22.7 dB gain − 19.7dBm iCP1dB UWB CMOS LNA. IEEE Trans. Circuits Syst II. **56**(9), 689–693 (Sept 2009)
12. M. Mincica, D. Pepe, D. Zito, CMOS UWB multiplier. IEEE Trans. Circuits Syst II. **58**(9), 570–574 (Sept 2011)
13. D. Zito, D. Pepe, M. Mincica, F. Zito, A 90 nm CMOS SoC UWB pulse radar for respiratory rate monitoring. IEEE ISSCC Dig. Tech. Papers. 41–42 (Feb 2011)
14. D. Zito, et al., SoC UWB pulse radar sensor for contactless respiratory rate monitoring. IEEE Trans. Biomed Circuits Syst. **5**(6), 503–510 (Dec 2011)
15. T.E. McEwan, Body monitoring and imaging apparatus and method. US Patent 5,573,012, 12, Nov 1996
16. I. Immoreev, T.-H. Tao, UWB radar for patient monitoring. IEEE Aerosp. Electron. Syst. Mag. **23**(11), 11–18 (Nov 2008)
17. M.I. Skolnik, *Radar Handbook*, 2nd edn. (McGraw-Hill, USA, 26 Jun 1970)
18. M. Maymandi-Nejad, M. Sachdev, A monotonic digitally controlled delay element. IEEE J. Solid-State Circuits. **40**, 2212–2219 (Nov. 2005)
19. H. Nyquist, S. Brand, Measurement of phase distortion. Bell. Syst. Tech. J. **9**(3), 522–549 (1930)

Ultra-Wideband Imaging Systems for Breast Cancer Detection

Hossein Kassiri Bidhendi, Hamed Mazhab Jafari and Roman Genov

Abstract In this chapter we will begin with an introduction to ultra-wideband (UWB) communication systems and their application in medical imaging. The rest of the chapter will present design of UWB receiver and transmitter blocks (low-noise amplifier (LNA), Multiplier and pulse generator) that are designed, fabricated and tested by authors. The reader will have a good understanding of a UWB transceiver system design and its advantages for breast cancer detection after reading this chapter.

Keywords Breast cancer detection · Breast imaging · Ultra-wideband imaging · UWB transceiver · UWB pulses · UWB transmitter · UWB receiver

Motivation

Worldwide breast cancer is one of the leading causes of death among women. Only in the USA, tens of thousands of deaths are reported yearly because of this type of cancer. 26 percent of all types of cancers among women are breast cancer [1]. It is now well-known that a high percentage of patients with this type of cancer can be cured if diagnosed in the early stages. There are many ongoing research projects to develop and improve imaging systems to help early detection of this type of cancer. This includes works which are concentrated on improvement of image processing or imaging system optimization using new technologies.

Ultra-wideband (UWB) communications is one of the newest technologies employed in imaging systems that are utilized for human's body imaging. The motivation is mainly based on using ultra-narrow pulses in the time domain to detect and contrast between normal and malignant tissues. This has initiated many research projects based on using this technology for imaging of a particular organ of body including heart, lung, breast, and organs involved in breath and speech mechanisms [2].

H. K. Bidhendi (✉) · R. Genov · H. M. Jafari
Department of Electrical and Computer Engineering,
University of Toronto, Toronto, ON M5S 3G4, Canada
e-mail: hkassiri@eecg.utoronto.ca

M. R. Yuce (ed.), *Ultra-Wideband and 60 GHz Communications for Biomedical Applications,* DOI 10.1007/978-1-4614-8896-5_5,

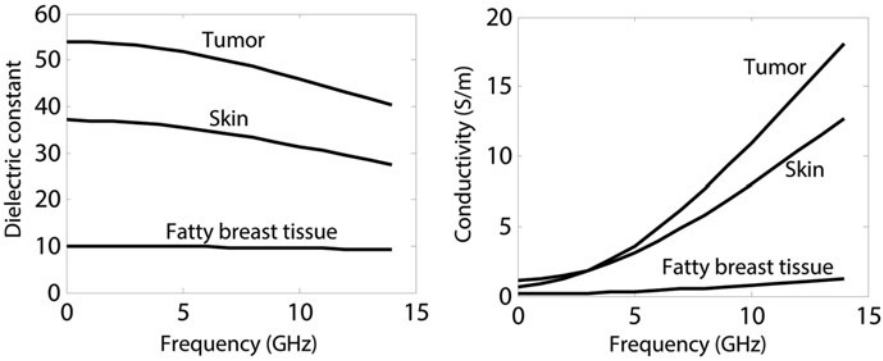

Fig. 1 Frequency dependence of the dielectric constant and conductivity for fatty breast tissue, skin, and tumor. [7]

The main motivation for using ultra-narrow pulses for breast imaging arises from the high contrast between the electrical properties of malignant and normal breast tissues. For instance, this contrast is 5:1 for relative dielectric constant and 10:1 for conductivity at microwave frequencies [3, 4] (see Fig. 1). In addition to contrast, UWB microwave imaging systems are also able to provide both adequate penetration depth and necessary imaging resolution [5, 6].

Medical Imaging for Breast Cancer

Among various types of medical imaging applications of UWB systems, breast cancer detection is one of the most popular fields that has attracted much research interest. In recent years, an increasing number of deaths due to breast cancer are reported. Only in the USA, there is an average of 40,000 deaths a year because of this type of cancer [8]. Since curing this type of cancer or long-term survival of patients are highly dependent on early detection and timely medical intervention, a very precise and dependable imaging system is required in the treatment procedure.

Conventional mammography has been performed using x-ray imaging of a compressed breast for nonpalpable early stage breast cancer [9]. Throughout the time, some technical advancements, such as digital mammography plus radiological expertise, have provided significant improvement of image quality and diagnosis using x-ray. However, due to sensitivity issues of x-ray imaging, there are still many problems with relatively high false-negative rate of detection, and low positive predictive rates resulting in many additional unnecessary biopsies [10]. In addition, in x-ray imaging, patients have to deal with uncomfortable or painful breast compression and exposure to low level ionization.

Usually, magnetic resonance imaging (MRI) and ultrasound are used for verification of mammography detected lesions by x-ray. In these systems, the modalities are not yet sensitive/specific enough or are too operator dependent or too costly to be useful for screening purposes.

All of above limitations have led to efforts to find an alternative to x-ray mammography. One of the most promising alternatives is using microwave imaging with UWB systems. As mentioned before, for the radio frequency (RF) and the microwave range of frequencies, differences in electrical characteristics of malignant and normal tissues are greater than 2:1. Also, dielectric constant, ε_r, and conductivity, σ, change with increasing water content in neoplastic tissues due to increased protein hydration [11]. This fact will result in exploiting strong indicators of malignancy associated with physical or physiological factors of clinical interest such as water content, vascularization, blood flow rate, and temperature.

This advantage over x-ray can compensate for spatial resolution of UWB systems which is not as good as x-ray imaging because of the wavelength difference. In fact, high contrast exists for both high and low frequencies. At lower frequencies, the contrast is due to breakdown of narcotic cell membranes which are being used for electrical impedance topography [12, 13]. On the other hand, at higher frequencies, there will be high contrast due to increase in DNA, protein, and hemoglobin absorption in malignant tissues [14]. Considering the above advantages of working in different frequencies and after studying parameters which are important in an imaging procedure, it has been concluded that the frequency range between 1 and 10 GHz is the optimum band for this application. This band is a range that includes both advantages of having high spatial resolution which is better at higher frequencies and also good penetration depth which is better for lower frequencies.

Today, it is well known that microwave imaging is a promising substitute for conventional mammography. It is also known what frequency range should be used for imaging. From this perspective, there have been two main techniques for active microwave imaging: radar and tomography. Both techniques are based on the dielectric contrast in this range of frequency. In both techniques, low-power microwave signals are transmitted from an array of antennas into the breast. The tomographic image reconstruction technique is the most commonly attempted technique in this frequency range that can be performed using narrowband signals. In this technique, an image reconstruction problem should be solved, which needs regularization to converge and have a meaningful solution. However, many of these concerns are minimized in smaller form-factor cases like that in breast cancer detection. On the other hand, there is UWB radar in which there is no effort to reconstruct the complete profile of dielectric properties of the breast. In fact, in this technique, the goal is to find the presence and location of significant backscattered energy due to difference in dielectric properties of normal and malignant tissues.

In general, the microwave frequency domain for breast imaging is associated with the following features that are expected from a UWB system as an imaging system working in this range of frequency:

1. Significant contrast between dielectric properties of normal and malignant tissues in this frequency range. In normal tissues of the breast, microwave attenuation is low enough that we can image the entire breast.
2. Avoiding breast compression, as well as using low-power signals which result in little health risk.

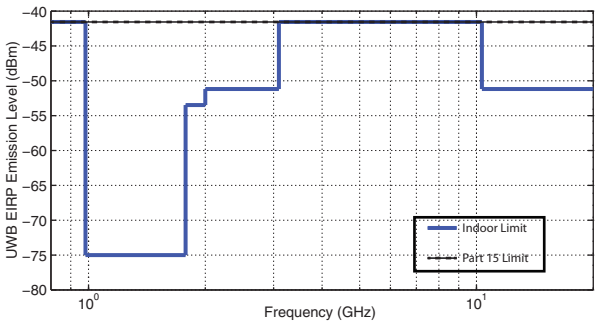

Fig. 2 Ultra-wideband emission limit for indoor systems. [17]

3. Conventional microwave tomography has computational challenges. Using space-time UWB imaging, these problems can be solved and a very good three-dimensional picture of the breast can be obtained.
4. Using space-time UWB imaging systems, a precision of less than 0.5 cm is expected which is good enough for early detection and localization of breast cancer.
5. Finally, UWB microwave imaging is able to detect if the lesion is malignant or benign. For benign lesions, the dielectric properties are not different from normal tissues as much as they are for malignant lesions. As a result, the scattered waves are not as strong as they are for malignant tissues.

Ultra-Wideband Technology for Breast Cancer Detection

UWB is a communication technology that can achieve high data rates of up to 1 Gbps, uses very low power pulses and is suitable for short-distance applications [15, 16].

Due to the use of short pulses which results in high multi-path resolution, UWB systems do not have problems with fading, which is a serious problem in narrowband systems. Furthermore, because of the wideband nature of these systems, power is distributed over a wide range of frequency, which results in a very low power level at each frequency. Consequently, less interference with other RF systems is expected. In 2002, the Federal Communication Commission (FCC) authorized commercial use of the band from 3.1 to 10.6 GHz for research and technology development of new electronic systems. Although different narrowband radio systems operate in this range of frequency, as long as UWB systems satisfy FCC's spectral mask, they can coexist with narrowband systems. For indoor applications, this mask is shown in Fig. 2 and Fig. 3. As shown, maximum equivalent isotropic radiated power (EIRP) spectral density which is allowed by FCC is -41.3 dBm/MHz. This mask suggests interesting short-distance applications for UWB range. On the other hand, high spatial resolution of this technology makes it a promising candidate for medical imaging.

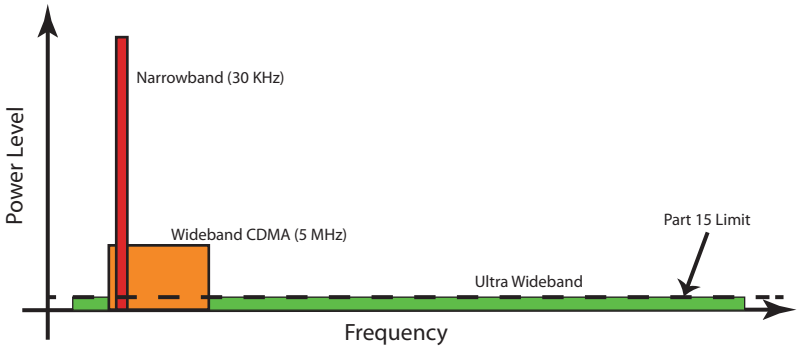

Fig. 3 Power level of ultra-wideband system in comparison with narrowband and wideband systems. [17]

Fig. 4 The hemispherical configuration used for breast cancer detection. [7]

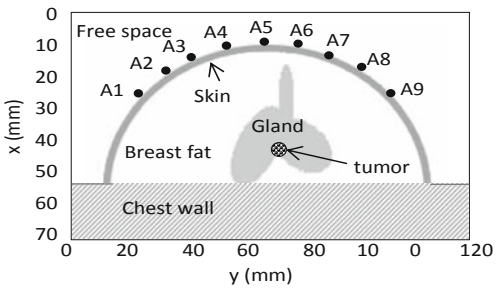

Fig. 5 Detected signal for different positions of tumor. *Thick solid line* is the average of calibration waveform. [7]

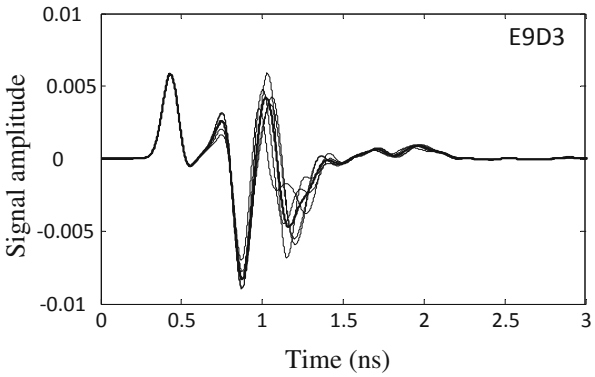

The basic idea of breast cancer detection is to send an ultra-narrow low-power pulses to the patient's body and make a decision based on the received signal by comparing it with a reference signal, average of backscattered signals, or a signal backscattered from normal tissues. Figure 4 shows an example in which nine antennas are positioned on a human's breast in a hemi-spherical configuration. First, as shown in Fig. 5, different pulses will be emitted from each of the antennas and detected by another antenna and location of simulated tumor is being randomly changed. Then,

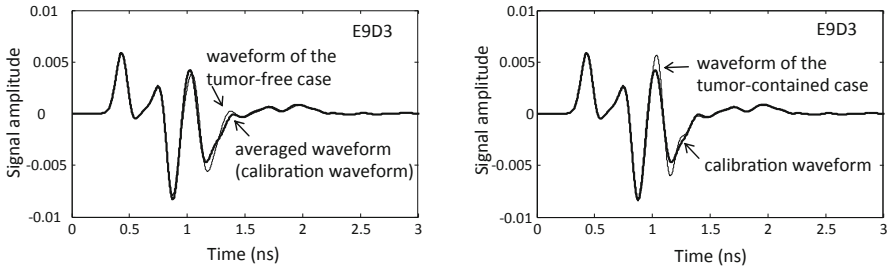

Fig. 6 Received signals compared with average waveform for two cases of normal and malignant tissues. [7]

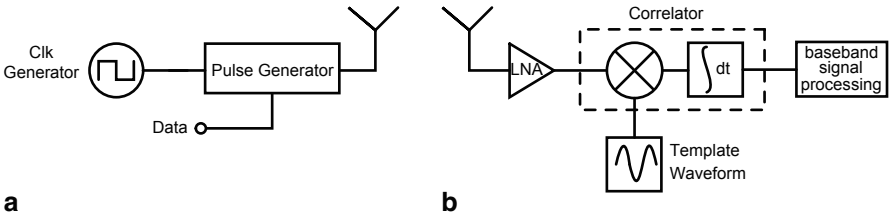

Fig. 7 Typical transceiver of a ultra-wideband system

an average waveform of the received signals is calculated. The next step is comparing the received signals with this waveform, which indicates the probability of a tumor existing in a specific location. Figure 6 shows two cases of normal and malignant tissues. As shown, for the malignant tissue, differences between received signal and the average (calibration) waveform is much higher than for the normal tissue.

Figure 7 shows a symbolic block diagram of UWB medical imaging system for breast cancer detection. As shown, a UWB medical imaging system has major differences when compared with narrowband systems. First, since there is no carrier in this type of communication, there is no need for complicated modulation and demodulation blocks. These are among the most complicated blocks used for conventional continuous wave transmission systems. Not having these complex components makes the transmitter architecture of UWB systems inexpensive, simpler to design, and simpler to implement, when compared to conventional radio systems.

From this point of view, a UWB system's block diagram is much simpler than its narrowband counterparts. As shown in Fig. 7, in UWB systems, time-domain modulation is used for transmitting and receiving data. This makes the correlation and sample waveform generator blocks of this system very important.

According to the work by Proakis et al. [18], the optimal receiver for a signal transmitted in an additive white Gaussian noise (AWGN) channel is a correlation or a matched filter receiver which makes SNR (signal to noise ratio) maximum. Figure 7b shows a receiver architecture that is made of three major blocks: a low-noise amplifier (LNA), a correlation circuitry and a block for providing template waveform for correlation circuit. In addition, there is also the baseband signal processing unit in which the decision making is performed.

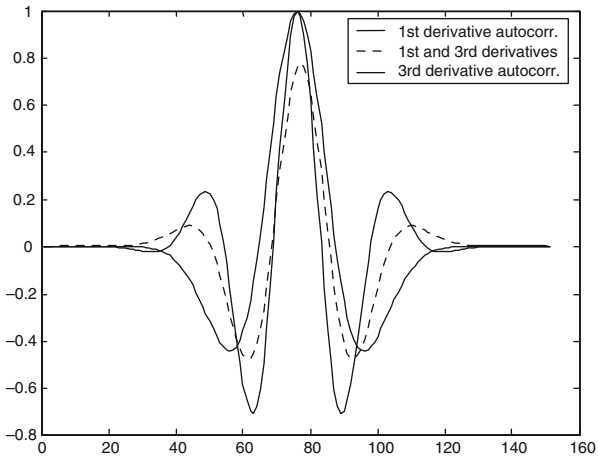

Fig. 8 Correlation results of transmitted and received signals. [20]

The first step in signal detection is to amplify the received signal. If the received signal from the antenna is fairly noisy and weak, then the first stage of the receiver, which is responsible for amplification, must be very low-noise. Also, it should be perfectly matched to the output impedance of the antenna, which is normally 50 Ω.

The next stage is the correlation block in which the amplified signal is compared to the template waveform. Generating a good template waveform is one of the most important issues in UWB receiver design for the correlator block. In fact, this waveform should be as similar to the received signal as possible, to maximize signal-to-noise ratio which is a complicated task. One option is to approximate the received waveform by the transmitted signal. Second way is a coarse approximation such as a rectangular wave, which is very simple to generate but is not very efficient.

Another approach, which is proposed in [19] is to ignore the template waveform and to rely on the finite bandwidth of the transmitting and receiving antennas, which results in a specific pulse shaping. Both transmitting and receiving antennas work as differentiators. As a result, in ideal conditions, the received signal in the receiver must be the second derivative of the transmitted signal. For the UWB pulse, this means the third derivative of a Gaussian pulse. In [20], the autocorrelation of the first and second derivatives of a Gaussian pulse are compared. Also, the crosscorrelation of the first and third derivatives of this pulse are compared to the autocorrelation results. The results in Fig. 8 show that the crosscorrelation results have an almost 80 percent accuracy of the third derivative autocorrelation which means a loss of less than 1 dB, which is quite tolerable for this application.

The template waveform is multiplied by the input signal and gets integrated over the bit duration to maximize the received signal power and minimize the noise component. Consequently, for a pulse train, the integrator's results will be higher than the noise level and the desired signal can be detected and separated from unwanted signals. It should be noted that the architecture introduced above will be different for other types of applications. For example, many UWB systems use time-hopping pulse

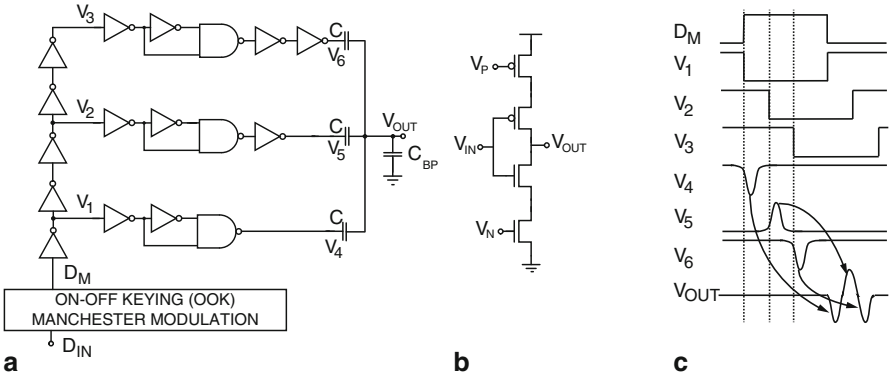

Fig. 9 **a** Ultra-wideband (UWB) transmitter circuit schematic diagram, **b** schematic of one current-starved inverter, and **c** timing diagram of the UWB transmitter

position modulation (TH-PPM) or some other time-domain modulation schemes which should be considered in the transmitter architecture. Also the correlator architecture is not always exactly similar to what was explained here, and it might vary due to the needs of the specific system.

Design Example for Ultra-Wideband Transmitter

The circuit diagram of the all-digital pulsed UWB transmitter is shown in Fig. 9. The input data are modulated using on–off keying (OOK) Manchester modulation. UWB pulses are generated on the rising edge of the modulated data (D_M). A delay line bank is employed together with a capacitively coupled output combiner [21] as shown in Fig. 9a.

The modulated data are passed through a delay line and a delayed version of the data is passed through three pulse generators. The pulse generators shape a first-order Gaussian pulse at the rising edge of the input data. The presented digital UWB transmitter achieves both power efficiency and spectral compliance in a much smaller chip area compared to other designs [22–23]. As illustrated in Fig. 9c, each pulse generator forms pulses that are delayed, and have opposite signs. By capacitively combining the three paths, the opposite signs are canceled, and the zero-DC double differentiated Gaussian pulse propagates to the single-ended antenna. The width of the output pulse depends on the delays in the delay line. The delay cells in all the paths are implemented as current-starved inverters, shown in Fig. 9b, to allow for tuning of the UWB pulse width. The input Manchester-encoded data to the UWB transmitter and its measured output UWB pulses are shown in Fig. 10.

The UWB pulses are measured using custom-built UWB antennas (5 cm spacing between the transmitter and receiver) and a custom-built receiver. A zoomed-in version of one such measured UWB pulse overlayed on a simulated UWB pulse is

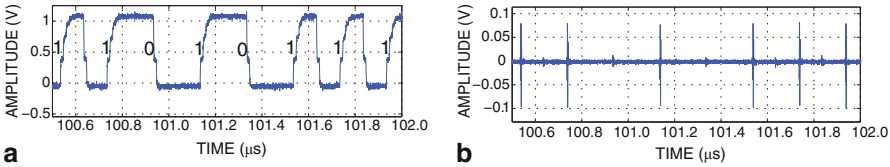

Fig. 10 Experimentally measured **a** Manchester-encoded input data to the ultra-wideband transmitter and **b** the output pulses

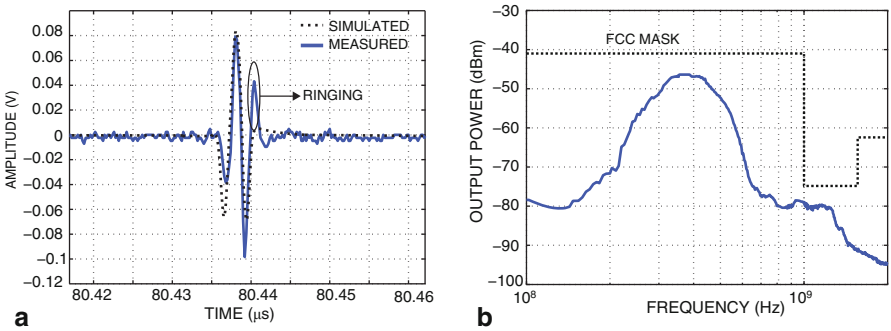

Fig. 11 **a** Wirelessly measured ultra-wideband (UWB) pulse at the distance of 5 cm using a custom-built UWB receiver, and **b** experimentally measured UWB transmitter output spectrum (direct output of the transmitter driving a 50 Ω load). The output spectrum is compliant with the 0–1 GHz Federal Communication Commission (FCC) UWB band output power criteria

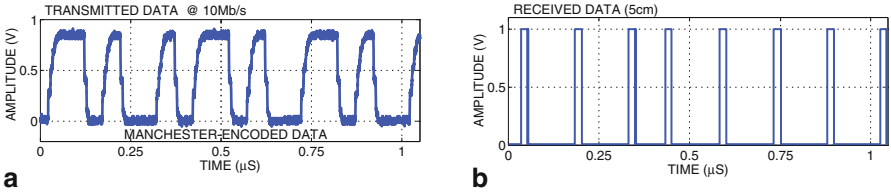

Fig. 12 **a** Manchester-encoded input data to the UWB transmitter and **b** the corresponding data received wirelessly at a 5 cm distance

shown in Fig. 11a. As it can be seen, the measured pulse resembles the expected UWB pulse but includes minor ringing due to the package bondwire inductance. The measured output power spectrum of the UWB transmitter is plotted in Fig. 11b. The power spectrum complies with the FCC-defined 0–1 GHz UWB spectrum (mask) also shown. The same circuit also generates pulses in the 3.1–10.6 GHz range. An example of the input data to the UWB transmitter Manchester-encoded at the rate of 10 Mb/s and the data received at the distance of 5 cm using a custom-built UWB receiver is shown in Fig. 12.

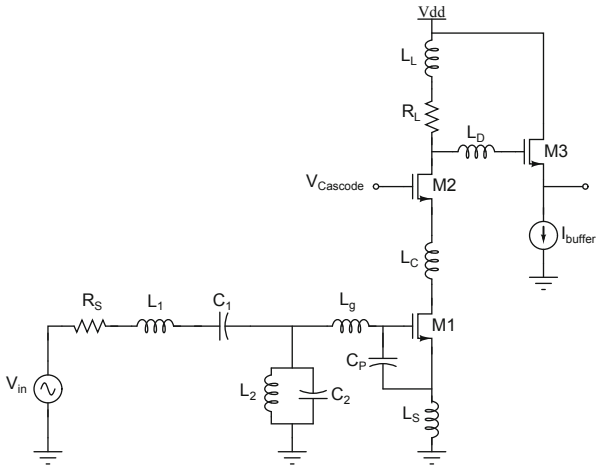

Fig. 13 Low-noise amplifier (LNA) circuit schematic together with the added inductors

Design Example for Ultra-Wideband Receiver

The general block diagram of a UWB receiver was introduced previously in Fig. 7. In this section, an example design and implementation of a UWB LNA and a mixer as two of the most important blocks of the receiver will be presented.

Ultra-Wideband Low-Noise Amplifier

Gain and Bandwidth

In the design presented, a CS (Common Source) configuration with inductive degeneration and a multi-section reactive network for input matching is utilized. The matching network is first proposed in [24]. Also, two auxiliary inductors are added to boost the bandwidth of the amplifier. In the circuit shown in Fig. 13, the drain current i_d can be written as

$$i_d = \frac{V_G g_m}{s(C_p + C_{gs})\omega_t L_s} = \frac{F(s) V_{in} g_m}{s(C_p + C_{gs})\omega_t L_s}, \tag{1}$$

assuming $F(s)$ is the Chebyshev filter transfer function. In the above analysis, C_{gd} is not taken into account. This is mainly because of the very low impedance of the cascode stage seen from drain of M_1. This will result in very weak Miller effect on gate of M_1, so C_M is

$$C_M = C_{gd}\,(1 + g_m(r_o \parallel R_L)). \tag{2}$$

Here, $R_L = 1/g_{m2}$ is small enough to make the Miller capacitance negligible, so the LNA gain without considering L_D and L_C will be

$$\frac{v_{out}}{v_{in}} = \frac{-F(s) g_m}{s(C_p + C_{gs})\omega_t L_s} * \frac{(sL_L + R_L)}{1 + sR_L(C_{db2} + C_{gd3}) + s^2 L_L(C_{db2} + C_{gd3})}. \tag{3}$$

Taking L_D and L_C into account, the gain equation of the LNA becomes

$$\frac{v_{out}}{v_{in}} = \frac{-F(s)g_m}{s(C_p + C_{gs})\omega_t L_s} * \frac{(R_L + sL_L)(1 + s^2 L_D C_{gd3})}{1 + sR_L C_{gd3} + s^2(L_L + L_D)C_{gd3} + C_{gb2}(R_L + sL_L)(s^2 L_D C_{gd3} + 1)}. \quad (4)$$

Comparing two gain equations, it can be concluded that adding the peaking inductors has resulted in removal of one of amplifier's dominant poles which was located at M_2's drain.

This has been done by breaking parasitic capacitance of this node, $(C_{db2} + C_{gd3})$, into two smaller capacitors. From another point of view, if the step response of this circuit is considered, then isolating the buffer stage from the cascode stage and splitting these two capacitors from each other, results in a much smaller capacitance to be charged and discharged every cycle. This means shorter transient time in the time domain or wider bandwidths in the frequency domain.

Figure 14 shows the pole-zero analysis and the effect of adding L_D. Based on this plot, L_D should be designed in a way such that undesired poles and zeros will be removed. In this work, L_D was designed in such a way that the added poles are located at 7.4 and 9.2 GHz and zeros at 5.9 (twin) and 7.6 GHz. The pole at 7.4 GHz and the zero at 7.6 GHz are close enough to approximately cancel each other's effect and consequently would not have any significant effect on the gain curves. In contrast, the zero at 5.9 GHz, which is a twin zero, not only prevents the gain from decreasing at higher frequencies, but it also results in an increase of the gain amplitude for frequencies beyond 5.9 GHz. This increase will continue until the next twin pole at 9.2 GHz, which stops the gain increment and causes a decrease in the gain until the end of bandwidth. Although the gain amplitude and bandwidth is improved significantly, the gain is still not very flat.

Figure 15 shows the gain curves in different stages of design. Figure 15a is the original design without any additional inductances, Fig. 15b shows the effect of adding L_D and Fig. 15c the effect of both L_D and L_C. The problem with flatness is basically due to the parasitics generated by the cascode stage. The addition of an inductor between the gain and cascode stages will help to improve the gain flatness. In fact, L_C, together with C_{gd1} and C_{gs2}, can form a wideband π-section LC network. As a result, it can resonate with the capacitors to produce broadband operation for the LNA. Figure 14b shows that adding L_C has caused three sets of poles to be relocated and also one set of poles to be generated. Among the three poles that have been displaced, two of them do not have a significant effect. The first is a pole at 8.3 GHz which is moved to 8.1 GHz and the other one is the pole which is moved from 7.5 to 7.9 GHz. In contrast, the third pole displacement is moving the undesirable pole out of the band and it is very effective in improving the gain curve. This pole is moved from 8.94 to 10.9 GHz. The most important effect of L_C is the pole which is generated at 6.13 GHz. This pole is designed to be very close to the twin-zero generated due to the addition of L_D, and it can cancel one of the zeros. As a result,

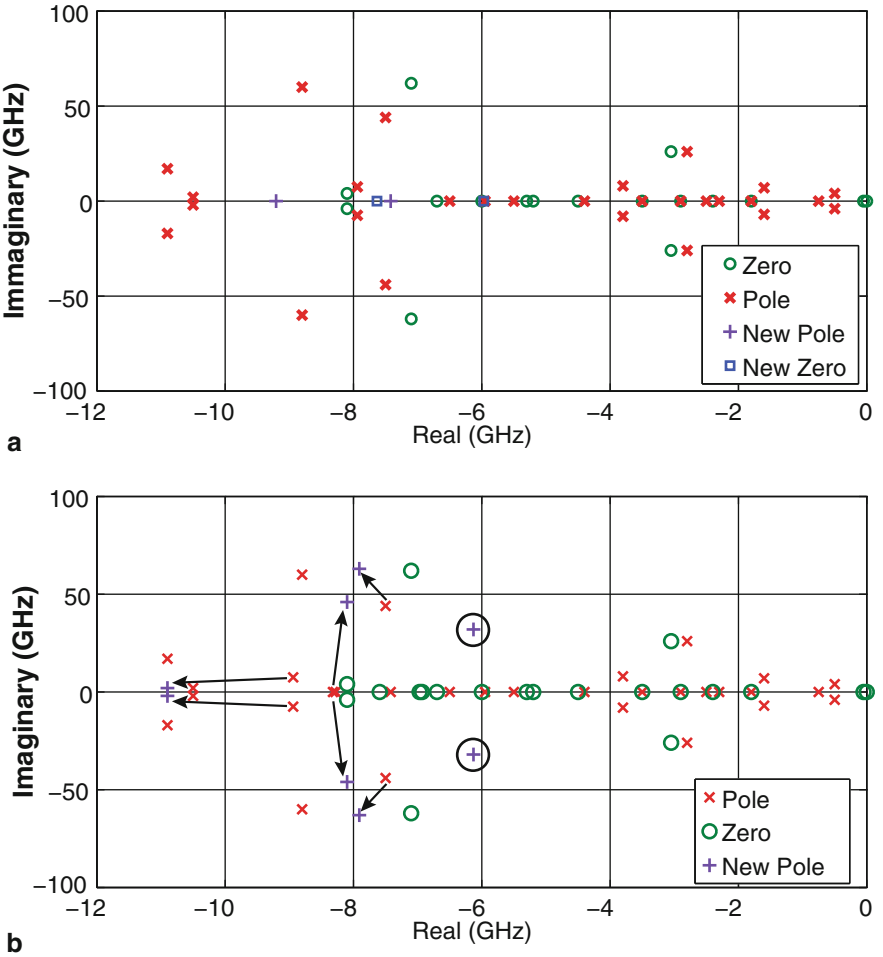

Fig. 14 **a** Pole-Zero analysis results after addition of L_D and **b** after addition of both L_D and L_C

there will be no gain increment from 6.13 GHz, until 9.2 GHz, which is the start of the gain decrease.

Noise Figure

There are two important factors that determine the noise of this low-noise amplifier. First are the losses of input matching network, and second is the input transistor M_1. Generally, the noise of the input matching filter, which is basically due to nonidealities of its reactive components, is negligible in comparison with the noise of the other stages.

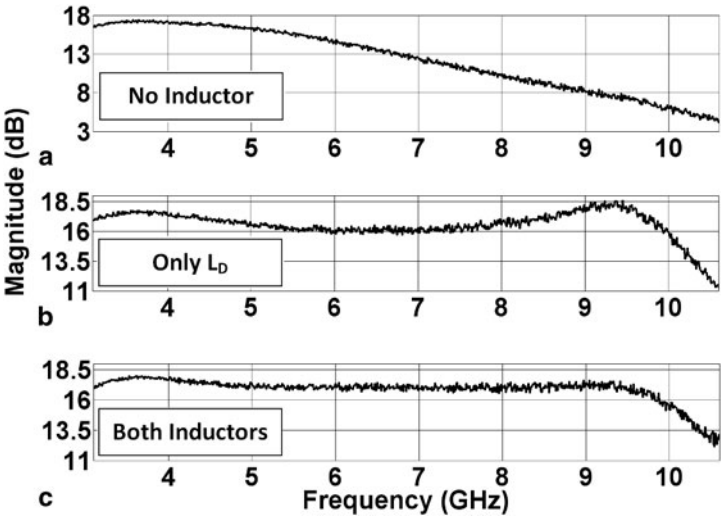

Fig. 15 **a** S_{21} for the original circuit, **b** after addition of L_D, and **c** after addition of both L_D and L_C

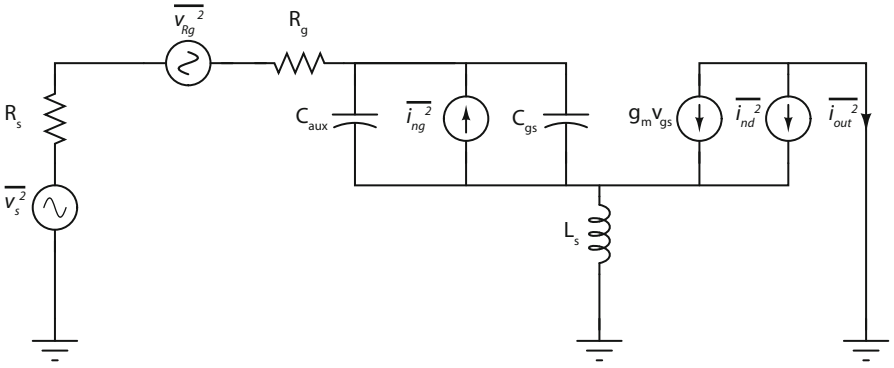

Fig. 16 Noise model for the first stage of designed low-noise amplifier

Furthermore, due to high gain of the first stage, the noise contribution of the cascode and output stages are much smaller than the first stage. As a result, it is assumed that the first stage noise is dominant, and only this noise is considered in calculations. Figure 16 shows a model for the noise of LNA's first stage. Based on this model,

$$F = 1 + \frac{\overline{v_{\mathrm{R_g}}^2}|G_{\mathrm{m}}(j\omega)|^2 + \overline{l_{\mathrm{ng}}^2}|T(j\omega)|^2 + \overline{l_{\mathrm{nd}}^2}|D(j\omega)|^2}{\overline{v_{\mathrm{g}}^2}|G_{\mathrm{m}}(j\omega)|^2} + \frac{\overline{l_{\mathrm{ng}}l_{\mathrm{nd}}^*}T(j\omega)D^*(j\omega) + \overline{l_{\mathrm{nd}}l_{\mathrm{ng}}^*}D(j\omega)T^*(j\omega)}{\overline{v_{\mathrm{s}}^2}|G_{\mathrm{m}}(j\omega)|^2} \tag{5}$$

with,

$$|G_{\mathrm{m}}(j\omega_0)|^2 = \frac{g_{\mathrm{m}}^2}{\omega_0^2 C_{\mathrm{t}}^2 \left(R_{\mathrm{s}} + R_{\mathrm{g}} + \frac{g_{\mathrm{m}} L_{\mathrm{s}}}{C_{\mathrm{t}}}\right)^2}, \quad D(j\omega_0) = \frac{R_{\mathrm{s}} + R_{\mathrm{g}}}{R_{\mathrm{s}} + R_{\mathrm{g}} + \frac{g_{\mathrm{m}} L_{\mathrm{s}}}{C_{\mathrm{t}}}}, \tag{6a}$$

$$T(j\omega_0) = \frac{R_{\mathrm{s}} + R_{\mathrm{g}} + j\omega_0(L_{\mathrm{g}} + L_{\mathrm{s}})}{R_{\mathrm{s}} + R_{\mathrm{g}} + \frac{g_{\mathrm{m}} L_{\mathrm{s}}}{C_{\mathrm{t}}}} \times \frac{g_{\mathrm{m}}}{j\omega_0 C_{\mathrm{t}}}. \tag{6b}$$

Replacing these terms in (5) and with some simplifications, F will be

$$F = \frac{R}{R_{\mathrm{s}}}\left(1 + R\frac{\gamma\omega_0^2 C_{\mathrm{t}}^2}{\alpha^2 g_{\mathrm{d0}}} x\right), \tag{7}$$

where

$$\begin{aligned} x &= \frac{\alpha^2\delta}{5\gamma}(1 + Q_{\mathrm{s}}^2)\frac{C_{\mathrm{gs}}^2}{C_{\mathrm{t}}^2} + 1 - 2|c|\frac{C_{\mathrm{gs}}}{C_{\mathrm{t}}}\sqrt{\frac{\alpha^2\delta}{5\gamma}}, \quad \alpha = \frac{g_{\mathrm{m}}}{g_{\mathrm{d0}}}, \\ Q_{\mathrm{s0}} &= \frac{1}{\omega_0 C_{\mathrm{gs}} R_{\mathrm{s}}}, \quad \omega_\tau = \omega_{\tau 0}\frac{C_{\mathrm{gs}}}{C_{\mathrm{t}}} = \frac{g_{\mathrm{m}}}{C_{\mathrm{t}}}, \\ Q_{\mathrm{s}} &= Q_{\mathrm{s0}}\frac{C_{\mathrm{gs}} R_{\mathrm{s}}}{C_{\mathrm{t}} R} = \frac{1}{\omega_0 C_{\mathrm{t}} R}, \quad R = R_{\mathrm{s}} + R_{\mathrm{g}}, \\ C_{\mathrm{t}} &= C_{\mathrm{gs}} + C_{\mathrm{aux}}, \quad R = R_{\mathrm{s}} + R_{\mathrm{g}}, \quad \text{and} \quad \omega_{\tau 0} = \frac{g_{\mathrm{m}}}{C_{\mathrm{gs}}}. \end{aligned} \tag{8}$$

Based on above equations, the noise figure is optimized with gain and power considerations.

The testchip is designed, fabricated, and tested in a 0.13 μm complementary metal-oxide semiconductor (CMOS) process. Figure 17 shows the measured S-parameters of this circuit. As shown, excellent input and output matching as well as output-to-input isolation are achieved. Peak value of 18.1 dB is measured for S_{21} with excellent gain flatness. Figure 18a shows the measured group delay of the designed LNA. Figure 18b shows the measured IIP3 of this circuit. The intercept point in − 1 dBm shows very good linearity. Also, Fig. 18c shows the noise figure of this circuit, with a minimum value of 3.12 dB and an average of 3.81 dB.

Ultra-Wideband Mixer

Despite all the advantages of UWB systems, their design is typically very challenging due to the fact that they should demonstrate good performance for the entire bandwidth. Power consumption, conversion gain, linearity, silicon area, and noise figure are major concerns in the design of UWB mixers.

For Gilbert cells, which are the most common topology of mixers, an increase in the bias current of RF stage will typically result in a better noise performance as well

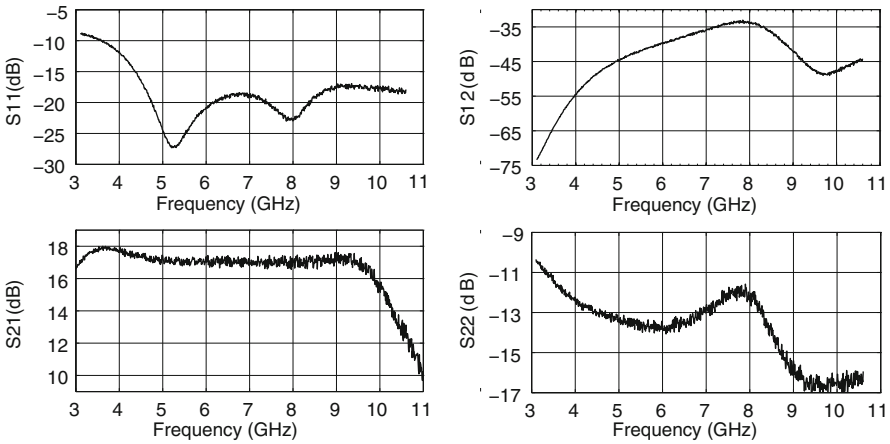

Fig. 17 Measured S-parameters of the designed low-noise amplifier (LNA)

as better linearity and higher transconductance of this stage. Clearly, this will cause a trade-off between power and other performance parameters. One approach that designers took is using current bleeding technique [25, 26] to improve noise, gain, and linearity without dramatic power increase. Using this method is typically limited to narrowband applications; and for UWB, several inductors should be used which results in dramatic area increase. A popular method to overcome this trade-off is to use a folding architecture. There are a number of works [27, 28] that have utilized this topology and achieved good bandwidth without sacrificing area or power. Using a folded architecture, DC current of RF and local oscillator (LO) stages do not have to be equal which results in more degrees of freedom in biasing and consequently a better trade-off. The constraint will be even more relaxed when the biasing of RF and LO stages are isolated.

Figure 19 shows the designed UWB mixer. As shown, a folded architecture with p-type metal-oxide semiconductor (PMOS) LO-stage and inverter RF stage is chosen. In conventional Gilbert cell topology, where RF and LO stages are stacked on top of each other, the bias currents of both stages are tightly correlated which results in a trade-off in performance parameters. For Gilbert cell, the conversion gain can be written

$$CG \propto g_{\mathrm{m,RF}} R_{\mathrm{L}}, \tag{9}$$

where, $g_{\mathrm{m,RF}}$ represents transconductance of the RF stage and R_{L} is the load resistance. Also the input referred intercept point (IIP3) can be expressed as

$$IIP3 = 4\sqrt{\frac{I_{\mathrm{DC,RF}}}{3K_{\mathrm{RF}}}}, \tag{10}$$

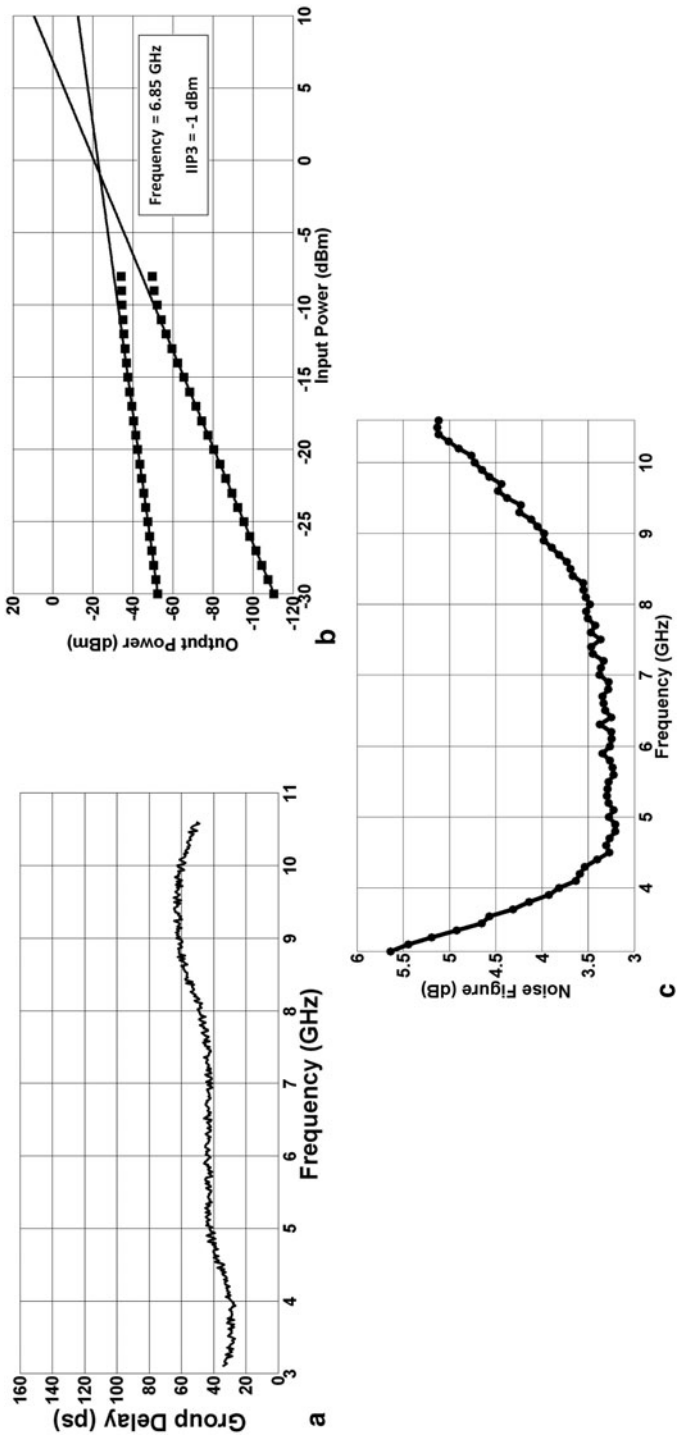

Fig. 18 Measured **a** linearity, **b** group delay, and **c** noise figure of designed low-noise amplifier (LNA)

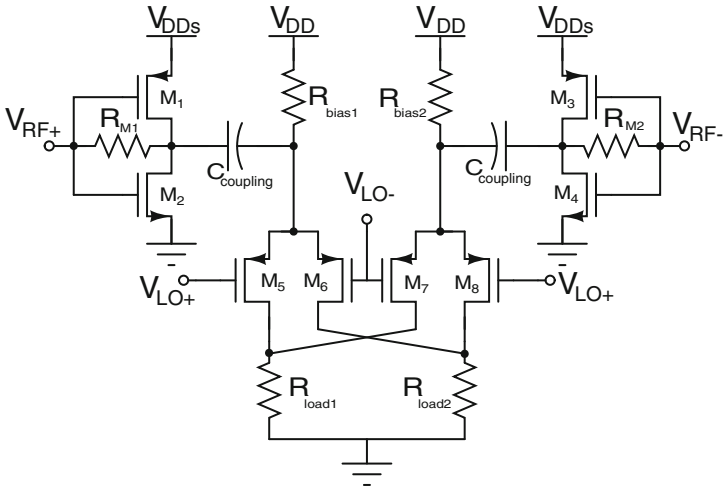

Fig. 19 Circuit schematic of the mixer core. V_{DDs} is the supply voltage of the subthreshold RF stage and is generated by internal biasing circuits

where I_{DC} is the RF stage bias current and $K_{RF} = \mu C_{ox} W/L$ is the process parameter of the RF-stage transistors. Above equations suggest an increase of RF stage biasing current as a way to improve performance of the mixer. However, it is clear that this current increase is confined to the power budget and cannot go above that. Also, despite the fact that increasing current will result in better linearity of the RF stage, for a stacked architecture, increasing the current will result in more voltage drop on load resistances and leaves less voltage swing for LO switches and consequently worse linearity. Considering noise in calculations makes the trade-off even more complicated. Noise of a Gilbert Cell is a combination of four different mechanisms: RF stage white noise, direct switching noise, indirect switching noise, and load thermal noise.

The total noise can be expressed as :

$$\hat{V_{o,n}^2} = 8kTR_L + 8kT\gamma\frac{R_L^2 I}{\pi A} + n\frac{8kT\gamma}{g_m}\left(\frac{2}{\pi}g_m R_L\right)^2, \tag{11}$$

where, the first term expresses the load noise, the second term is the switching noise, and the last term is due to the transconductance (i.e., RF) stage noise. As this equation suggests, reducing bias current of the switches as well as transconductance of the RF stage will result in a total noise reduction. This is in contradiction with the result of equations (8) and (9). It can be concluded that having independent DC currents for the RF and switching stages can relax the trade-off and result in a much more optimized biasing point.

Folded structure, with a decoupling capacitor that is suggested in this work will result in RF and LO stages that have completely independent DC biasing.

Here with the topology that is presented in Fig. 19, the RF stage is optimized to have the maximum conversion gain and linearity while the LO stage's bias is reduced

significantly to keep the power consumption and noise low, and have the minimum voltage drop on load resistances which causes better overall linearity. Also, in this work p-type MOSFETs are used for switches. Having PMOS switches in the LO stage, helps achieve the same overdrive voltage, and consequently similar linearity performance, with lower power consumption compared to the case using n-type metal-oxide semiconductor (NMOS) transistors [29]. In the design of the RF stage, an NMOS–PMOS stacked architecture is used. This will boost up the transconductance and consequently the conversion gain of the mixer. A high conversion gain (CG) for mixers relaxes the gain requirement of the LNA as its previous stage and will result in a better overall receiver design.

Furthermore, we took advantage of DC isolation of RF and LO stages, and designed the RF stage in the subthreshold region. With a good design, the same transconductance can be achieved with a significantly lower power consumption. Of course, this will result in a noise increase in the RF stage, but the switching noise is the dominant contributor in the total noise of the mixer. Our Cadence noise analysis results also show that M_5–M_8 are the main contributors to the total noise with each of them being responsible for 13.4 % of the total noise. In RF stage, $R_{M1,2}$ are placed for input matching of the mixer and stabilize the gate and drain biasing voltage. Although mixer's input is connected to the LNA's output and it does not have to be matched to standard 50 Ω, having these resistors as the parallel feedback for the RF stage will help us match the input resistance to desired value. R_{IN} can be written as

$$R_{IN} \approx \frac{R_M}{1 + (g_{m,n} + g_{m,p})(r_{ds,n} || r_{ds,p})}, \tag{12}$$

and using this equation, and knowing RF stage transistors' transconductance, R_M can be designed to make R_{IN} matched to the output of the previous stage.

Finally, R_{bias} is designed to set the DC voltage on the source of the switches and R_{load} is a passive load made of polysilicon to minimize the flicker noise at the output. In this design, the minimum length of 120 nm is chosen for M_{1-4} while the length of M_{5-8} is chosen to be 300 nm to reduce the flicker noise in the switches. Also, $W_{1-4} = 180$ μm, $W_{5-8} = 200$ μm, $R_{M1,2} = 2.8$ kΩ, $R_{bias1,2} = 600$ Ω, and $R_{load1,2} = 1.2$ kΩ. Finally, $V_{DDs} = 650$ mV is a reduced version of the supply voltage for the subthreshold RF stage, and is provided using internal biasing circuits.

One of the most common problems in UWB transceiver designs is that the LNA (as the first component after antenna) is usually single-ended and the output of this block should be connected to the mixer (multiplier) that has a differential input architecture. One solution to this is to use micro-strip lines and build a balun (balanced to unbalanced converter) to convert the single-ended signal to a differential one right after the antenna. With this solution, two single-ended LNAs can be used, and the output of each LNA can be connected to one input terminal of the mixer.

Although the phase precision of microwave baluns is good, and the differential signals are out-of-phase with a very good precision, having two LNAs that typically have a few inductors, doubles the required silicon area. Also, a passive balun implemented on-board is much bulkier than a circuit that is built on silicon. For these

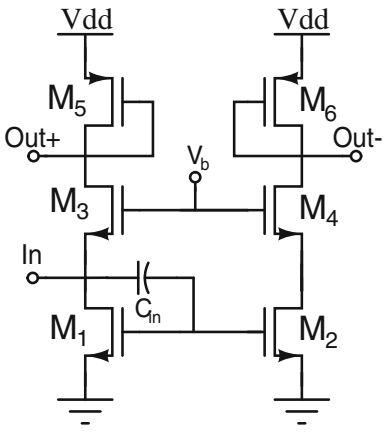

Fig. 20 Circuit schematic of the wideband balun

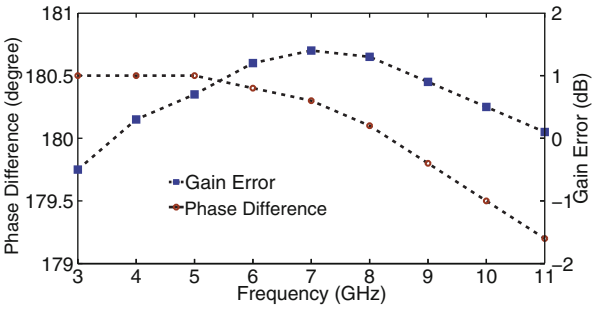

Fig. 21 Gain error and phase difference between the two outputs of the input balun

reasons we have developed a wideband balun, shown in Fig. 20, that converts the single ended input to differential with a high phase precision for the entire band of 3.1–10.6 GHz. In the balun design, we have used a cascode architecture which is to decrease phase error at the differential outputs. In addition to S–D (single to differential) conversion, having a balun at the input of a mixer will result in a reduction of the number of input pads by three (one RF signal and two grounds).

Also, in addition to the balun that is connected to the input of the mixer, another balun is separately laid-out. This helped us to characterize the performance of the balun and to de-embed its effect from core mixer's performance. Figure 21 shows the gain error of the balun as well as the phase difference between the outputs.

As shown, the phase difference between the two outputs is very close to 180° for all the frequencies in the UWB band and the gain error is always less than 1.5 dB. Finally, for the intermediate frequency (IF) outputs of the mixer, a PRODYN balun is used to convert the differential outputs to a single-ended signal that can be connected to lab measurement equipment. Also, at the baseband IF outputs, DC-coupled common source buffers have been used to match to the lab equipment. The buffers are not shown in Fig. 19 and their power consumption is not included in total power consumption of the mixer. Figure 22a shows the measured conversion gain of the mixer for different input RF frequencies as well as different output IF frequencies.

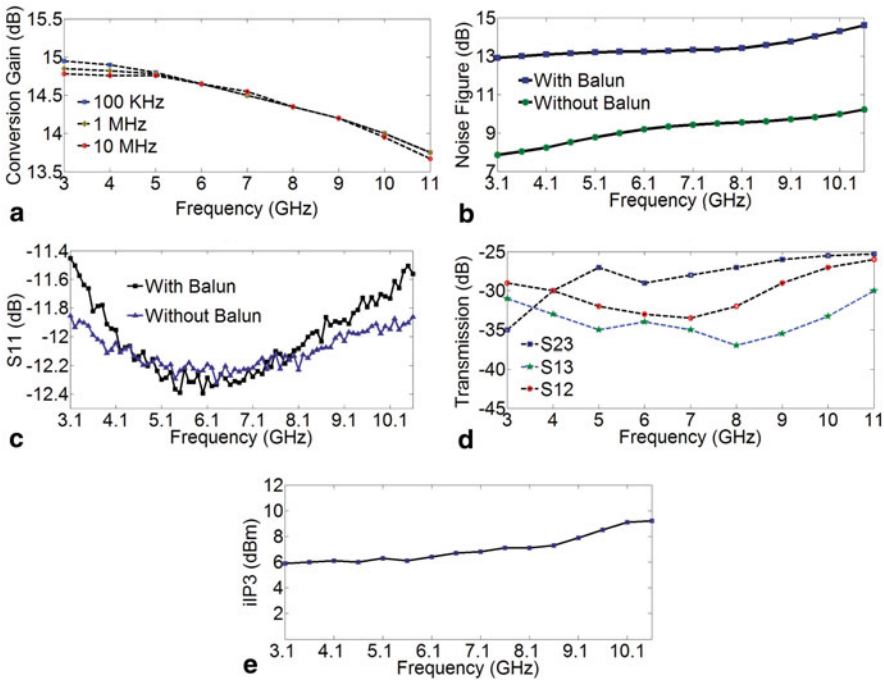

Fig. 22 Measured **a** conversion gain, **b** noise figure with and without the balun, **c** S_{11}, **d** port to port isolation, and **e** IIP3 of the designed mixer

As shown, the gain remains almost constant for various IF frequencies. Also, CG drops less than 3 dB, when the RF frequency is changed from 3 to 11 GHz. Figure 22b shows the noise figure of the designed circuit for both cases of with and without the balun. As shown, the core mixer (without a balun) has a minimum value of 6.9 dB and an average of 9.15 dB over the 7.5 GHz bandwidth. Figure 22c shows the input reflection coefficient for the RF port which shows excellent matching at this port for both cases of with and without the balun. Also, Fig. 22d shows the good performance of this design in terms of the port to port isolation. Finally, Fig. 22e provides IIP3 of the mixer for the whole range of RF frequencies.

References

1. A. Jemal, R. Siegel, E. Ward et al., Cancer statistics. CA. Cancer. J. Clin. **58**(2), 71–96 (2008)
2. E.M. Staderini, UWB radars in medicine. IEEE. Aerosp. Electron. Syst. Mag. **17**(1), 13–18 (2002)
3. E.C. Fear, X. Li, S.C. Hagness, M.A. Stuchly, Confocal microwave imaging for breast cancer detection: localization of tumors in three dimensions. IEEE. Trans. Biomed. Eng. **49**, 48–56 (2002)
4. W.T. Joines, Y. Zhang, C. Li, R.L. Jirtle, The measured electrical properties of normal and malignant human tissues from 50 to 900 MHz. Med. Phys. **21**, 547–550 (1994)

5. Y. Xie, B. Guo, L. Xu, J. Li, P. Stoica, Multistatic adaptive microwave imaging for early breast cancer detection. IEEE Trans. Biomed. Eng. **53**, 1647–1657 (2006)
6. L. Xu, S. Davis, S.C. Hagness, D. Weide, B. Veen, Microwave imaging via space–time beamforming: experimental investigation of tumor detection in multilayer breast phantoms. IEEE Trans. Microwave & Theory Tech. **52**, 1856–1865 (2004)
7. X. Xiao, T. Kikkawa, Study on the breast cancer detection by UWB microwave imaging. IEEE. 2008.
8. M. Patlak, S. Nass, I. Henderson, J. Lashof (eds.), *Mammography and beyond: developing technologies for the early detection of breast cancer*. (The National Academy Press, Washington, DC, 2001)
9. E.J. Bond, X. Li, S.C. Hagness, B.D. Van Veen, Microwave imaging via spacetime beamforming for early detection of breast cancer. IEEE Trans. Antennas Propag. **51**(8), 690–705 (2003).
10. J.G. Elmore, M.B. Barton, V.M. Moceri, et al., Ten-year risk of false positive screening mammograms and clinical breast examinations. N. Engl. J. Med. **338**, 1089–1096 (1998)
11. K.R. Foster, H.P. Schwan, Dielectric properties of tissues and biological materials: a critical review. Crit. Rev. Biomed. Eng. **17**, 25–104 (1989)
12. K.S. Osterman, T.E. Kerner, D.B. Williams, A. Hartov, S. P. Poplack, K. D. Paulsen, Multifrequency electrical impedance imaging: preliminary in vivo experience in breast. Physiol Meas. **21**, 99–109 (1989)
13. J.L. Mueller, S. Siltanen, D. Isaacson, A direct reconstruction algorithm for electrical impedance tomography. IEEE. Trans. Med. Imaging. **216**, 555–559 (1989)
14. T.O. McBride, B.W. Pogue, S.D. Jiang, U.L. Osterberg, K.D. Paulsen, S.P. Poplack, Initial studies of in vivo absorbing and scattering heterogeneity in near-infrared tomographic breast imaging. Opt. Lett. **26**, 822–824 (2001)
15. John McCorkle, Ultra-wide bandwidth (UWB): gigabit wireless communications for battery operated consumer applications. 2005 Symposium on VLSI Circuits Digest of Technical Papers
16. K. Siwiak, Ultra-wide band radio: Introducing a new technology. Proc. IEEE Veh. Technol. Conf. **2**, 1088–1093 (May 2001)
17. Ultra-Wideband First Report and Order. Federal Communication Commision, Tech. Rep., February 2002
18. J.G. Proakis, *Digital Communications*. (McGraw-Hill, New York, 1995)
19. J. Lang, UWB chip design with embedded functionality, UWB Summit, Paris, France, CD Proceedings, (1989)
20. I. Oppermann, M. Hamalainen, J. Iinatti, *UWB Theory and Applications, Chapter 6* (Wiley, Chichester, 2004)
21. P.P. Mercier, D.C. Daly, A.P. Chandrakasan, An energy efficient all-digital UWB transmitter employing dual capacitively-coupled pulse-shaping drivers. IEEE. J. Solid-State Circuits, **44**(6), 1679–1688 (2009)
22. Y. Park, D. Wentzloff, An all-digital 12 pj/pulse ir-uwb transmitter synthesized from a standard cell library. IEEE J. Solid-State Circuits, **46**(5), 1147–1157 (2011)
23. P.P. Mercier, M. Bhardwaj, D.C. Daly, A.P. Chandrakasan, A low-voltage energy-sampling IR-UWB digital baseband employing quadratic correlation. IEEE. J. Solid-State Circuits. **45**(6), 1209–1219 (2010)
24. A. Bevilacqua, A.M. Niknejad, An ultrawideband CMOS low noise amplifier for 3.1–10.6 GHz wireless receivers. IEEE. J. Solid-State Circuits. **39**(12), 2259–2268 (Dec 2004)
25. S.-G. Lee, J.-K. Choi, Current-reuse bleeding mixer. Electron. Lett. **36**(8), 696–697 (Apr 2000)
26. S. Douss, F. Touati, M. Loulou, An RF-LO current-bleeding doubly balanced mixer for IEEE 802.15.3a UWBMB-OFDM standard receivers. Int. J. Electron. Commun. **62**, 490–495 (Jul 2008)
27. F. Mahmoudi, C. Salama, 8 GHz, 1 V, high linearity, low power CMOS active mixer. Proc. IEEE Radio FrEq. Integr. Circuits Symp. Dig. 401–404 (Jun 2004)
28. N. Poobuapheun, W.-H. Chen, Z. Boos, A. Niknejad, A 1.5-V 0.7–2.5-GHz CMOS quadrature demodulator for multiband direct-conversion receivers, IEEE. J. Solid-State Circuits. **42**(8), 1669–1677 (Aug 2007)
29. Y. Ding, R. Harjani, *High-Linearity CMOS RF Front-End Circuits*. (Springer, New York, 2005)

Implementation of Ultra-Wideband (UWB) Sensor Nodes for WBAN Applications

K. M. S. Thotahewa, Jean-Michel Redouté and Mehmet Rasit Yuce

Abstract Wireless body area networks (WBAN) applications benefit extensively from the advantages offered by the unique features of ultra-wideband (UWB) wireless communication. This chapter focuses on the hardware implementation of UWB-based sensor nodes for WBAN applications. Different realizations of UWB sensor node architectures are described and a critical analysis of their suitability for WBAN applications is presented. Implementation of narrowband (NB)-based WBAN systems that can be found in the literature is discussed in order to compare their performance with the UWB systems. The design techniques for the implementation of an impulse radio UWB (IR-UWB) sensor node are presented paying attention to the UWB pulse generation and data modulation.

Keywords Ultra-wideband (UWB) · UWB sensor node · UWB-WBAN · UWB body sensor · UWB pulse generation · UWB medical monitoring · Wireless body area networks · UWB transmitter · UWB receiver

Introduction

The ability to remotely monitor patients has many benefits because it is presenting a solution to the increasing demand for physical infrastructure at hospitals. With the use of mobile health facilities, the requirement of patients being physically present in a care providing environment is eliminated. Vital physiological information can be transferred to a remote database via internet using remote health monitoring [1]. Because the patients are monitored in real time while being involved in their day to day activities, physiological parameters give a more realistic overview of the patient's health status. Consider, as an example, a patient suffering from a high blood pressure. If it is possible to remotely monitor his/her blood pressure throughout the

M. R. Yuce (✉) · K. M. S. Thotahewa · J.-M. Redouté
Biomedical Integrated Circuits and Sensors Laboratory,
Department of Electrical and Computer Systems Engineering,
Monash University, Melbourne,
VIC 3800, Australia
e-mail: mehmet.yuce@monash.edu

M. R. Yuce (ed.), *Ultra-Wideband and 60 GHz Communications for Biomedical Applications,* DOI 10.1007/978-1-4614-8896-5_6,

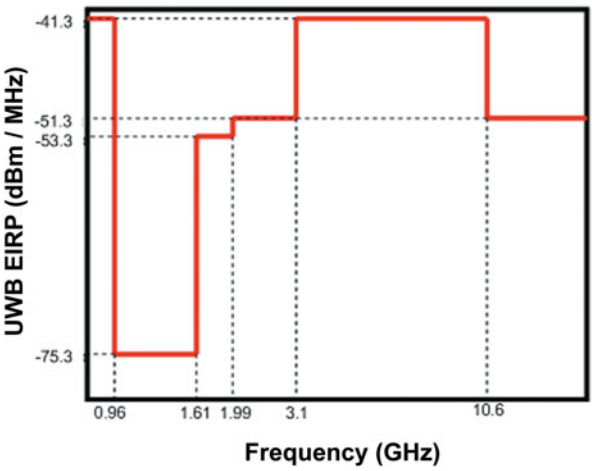

Fig. 1 Federal Communications Commission (FCC)-regulated spectral mask for indoor ultra-wideband (UWB) propagation

day, physicians can get a more realistic idea how the blood pressure built up prior to reaching a certain threshold. Also, it can eliminate inaccurate results caused by changed physical conditions which occur due to travelling to the hospital. It also makes it easy to keep track of the patient's or sportsman's health history. An early health warning system can also be implemented using this technology.

With the recent advancement in wireless sensor networks and miniaturized hardware technologies, it has been possible to implement wireless networks which operate in and around the human body. Wireless body area networks (WBAN) is a networking concept which has evolved with the idea of monitoring vital physiological signals from low-power and miniaturized in-body or on-body sensors [2]. WBANs can be seen as special purpose sensor networks designed to satisfy quality-of-service (QoS) requirements of physiological signals operating in different environments.

Ultra-wideband (UWB) has attracted the attention of the researchers worldwide as a lucrative wireless technology for WBAN applications in recent years [3–6]. The key advantages of the UWB technology, such as low power consumption, high data rate capability, small form factor, and susceptibility to multipath components, provide a significant edge over the existing narrowband (NB) technologies such as medical implant communication system (MICS) [7], Bluetooth [8], ZigBee [9], and wireless local area networks (WLAN) [10].

The UWB frequency spectrum is defined as having a fractional bandwidth larger than 0.2 or at least 500 MHz. The fractional bandwidth is defined as the bandwidth ratio between the − 10 dB lower and upper corner frequency difference and the center frequency of a signal. UWB is allowed to operate in the 0–960 MHz and 3.1–10 GHz bands; however, the effective isotopic radiated power (EIRP) must be kept below − 41 dBm/MHz [11]. The Federal Communications Commission (FCC)-regulated spectral mask for indoor UWB propagation is shown in Fig. 1.

WBAN applications, such as microelectronic arrays, neural recording systems, and wireless capsule endoscopy (WCE) systems, use multichannel monitoring,

Table 1 Different wireless technologies used in WBAN applications

Properties	Wireless technology				
	ZigBee	WLAN	MICS	Bluetooth	UWB
Frequency	2.4 GHz	2.4 GHz	401–406 MHz	2.4 GHz	3.1–10.6 GHz
Transmit power (dBm)	0	10–30	− 16	0	− 41.3
Channel bandwidth	2 MHz	22 MHz	300 kHz	1 MHz	500 MHz
Data rate	250 kbps	11 Mbps	200–800 kbps	1 Mbps	850 kbps up to 20 Mbps
Range (m)	0–10	0–100	0–10	0–10	2

WBAN wireless body area networks, *WLAN* wireless local area networks, *MICS* medical implant communication system, *UWB* ultra-wideband

which drastically increases the amount of data that needs to be transmitted simultaneously. This, in turn, increases the demand for high data rate transmission of physiological data. For example, a 128-channel neural recording system with 8-bit sampling requires a data rate in excess of 10 Mbps [3]. Use of wired media for data transmission is not feasible at all times. It restricts the movement of the patient and involves painful surgical procedures (for example in WCE).

Table 1 shows some of the wireless technologies used in WBANs. Out of the existing wireless physical layer technologies, UWB and WLAN standards are able to cater for the data rate requirement of high data rate applications. The WLAN standard is rarely used in WBAN applications because of its large power consumption. The ZigBee standard defines the network, security, and application layer on top of the IEEE 802.15.4 standard [12] which incorporates the physical and medium access control (MAC) layers [13]. It operates in the 2.4-GHz unlicensed industrial, scientific, and medical (ISM) band, alongside with WLAN and Bluetooth, making the 2.4-GHz band more crowded. In the UWB standard, it is possible to choose the operational bandwidth from a wide spectrum which ranges from 3.1 to 10 GHz. The power consumption in a ZigBee-based sensor node is considerably high compared to a UWB-based transmitter. For example, the Chipcon IC (CC2420), which is a commercially available transceiver, consumes in order of 20 mW [14], even when it is operating at lowest transmit power configuration. The MICS band cannot be used for WBAN applications that require high data rates due to data rate restrictions. UWB stands out from the above technologies for WBAN sensor nodes due to the low power requirements of the UWB transmitter, high data rate capability, and reasonably uncomplicated circuit design.

Table 2 depicts some of the available WBAN platforms that are commonly considered for WBAN applications. These devices operate using a low supply voltage ranging from 2 to 3 V. From the available NB sensor platforms, Microsemi (formerly Zarlink) platform provides the complementary metal oxide semiconductor (CMOS)- based integrated circuit (IC) with the lowest power consumption for WBAN applications. This IC is used in the Given Imaging's PillCam® series WCE devices for low-power NB-based implant communication [19]. The MICA2DOT shown in

Table 2 Sensor platforms for WBAN applications

Sensor	Company	Frequency	Data rate	Physical dimension	Power/current	
					Tx	Rx
UWB-based	Ref1 [5]	3.1–10.6 GHz	10 Mbps	3 × 4 mm^2 (IC), 5 cm (board length)	0.35 mW	62 mW at 10 Mbps
UWB-based	Ref2 [15]	3.1–10.6 GHz	10 Mbps	25 × 27 × 1.5 mm (board)	15 mA	–
Mica2 (MPR400)	Crossbow [16]	868/916 MHz	38.4 kbps	58 × 32 × 7 mm (board)	27 mA	10 mA
MicaZ	Crossbow [17]	2.4 GHz	250 kbps	58 × 32 × 7 mm (board)	17.4 mA	19.7 mA
Mica2DOT	Crossbow [17]	433 MHz	38.4 kbps	25 × 6 mm^2 (board)	25 mA	8 mA
CC1010	TI [17]	300–1,000 MHz	76.8 kbps	12 × 12 mm^2 (IC)	26.6 mA	11.9 mA
C2400	TI [17]	2.4 GHz	1 Mbps	7.1 × 7.1 mm^2 (IC)	19 mA	23 mA
MICS-based	Microsemi-ZL70250 (formerly Zarlink) [18]	402–405 MHz, 433 MHz ISM	800 kbps	7 × 7 mm^2 (IC)	5 mA, continuous Tx/Rx	

WBAN wireless body area networks, *UWB* ultra-wideband, *MICS* medical implant communication system, *IC* integrated circuit, *Tx* transmission, *Rx* reception

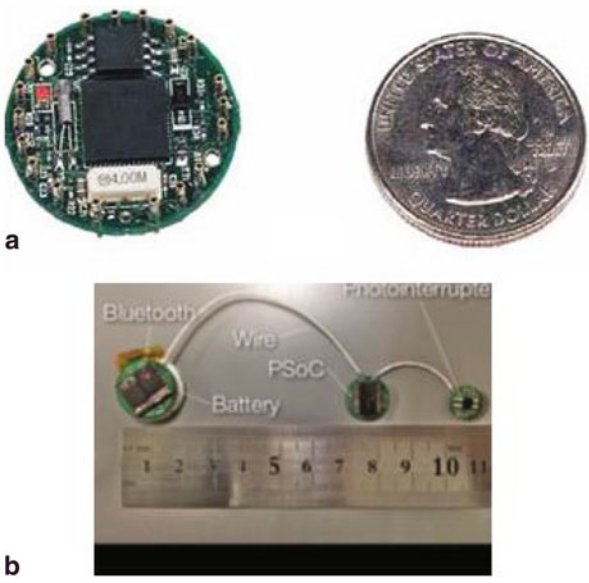

Fig. 2 **a** MICA2DOT sensor platform [16]. **b** Bluetooth-based pulse wave monitoring system [20]

Fig. 2a provides a full sensor implementation on a small sensor platform. However, the power consumption of the transmitter is considerably high compared to that of the Microsemi NB system. An implementation of a small wearable pulse wave monitoring system that uses a Bluetooth-based transceiver is presented in Fig. 2b [20]. The total current consumption of the systems is estimated to be 51 mA, inclusive of the current consumption of the Bluetooth transceiver which is estimated to be 21 mA with an operating voltage of 3.3 V. The comparison in Table 2 shows that the sensor systems based on the UWB transmitters perform better than the NB-based systems in terms of power consumption, form factor, and data rate.

The main drawback of the UWB technology is its receiver complexity. Due to the short pulse width and low-power level of the transmitted signal, the front-end circuitry of a UWB receiver is complex in design and has high power consumption. Synchronization of the IR-UWB (impulse radio UWB) pulses at receive stage using low-power front-end circuitry and controller devices is one of the major problems that restricts the use of UWB receivers for implant applications. For example, an analog-to-digital converter (ADC) to be used in a UWB receiver requires a large input bandwidth and a high sampling rate. ADC12D1800 [21] by National Semiconductor has 3.5 Giga samples per second (Gsps) sampling rate and an input bandwidth of 1.75 GHz, meeting the requirement of digitization at UWB receivers, and consumes 4.4 W of power which is not suitable for battery-powered WBAN sensor design. It is possible to overcome this drawback either by using a transmitter-only method or by using a less complex NB wireless technology for the receiver. This chapter focuses on the implementation of the UWB sensor nodes using these two methods. This chapter investigates the implementation UWB-based wireless sensor nodes for WBAN applications. Different design methodologies reported in the literature for

the implementation of UWB transmitters are discussed. Methods of eradicating the complications introduced by the use of UWB receivers in the power-stringent UWB-based WBAN sensor nodes are discussed herein. The hardware implementation of UWB sensor nodes is described in detail in the latter part of the chapter. Many IC-based implementations of the UWB transmitters can be found in the literature. While this chapter analyzes some of the design techniques used in these IC circuits, we mainly pay our attention toward the full implementation of the UWB sensor nodes, which include the control and interfacing circuits. Because of the factors, such as high power consumption and increased hardware complexity, the use of a UWB receiver in WBAN sensor nodes is disadvantageous. Hence, this chapter mainly focuses on the implementations of UWB sensor node designs that implement UWB transmitter only and eliminate or minimize the use of a receiver.

UWB Transmitter Design Techniques

The UWB transmitter lies at the core of a UWB-based sensor node. UWB transmitters are straightforward in design compared to UWB receivers. Unlike in the case of the NB transmitters, the radio frequency (RF) portion of the UWB transmitters does not dictate the overall power consumption. Hence, care has to be taken in order to minimize the power consumption of the rest of the transmitter circuitry. This section will analyze some common transmitter design techniques that are available in the literature.

A UWB transmitter design starts with a narrow UWB pulse generator. The earlier versions of the UWB pulse generators used step recovery diodes (SRD) in order to generate the pulses and Schottky diodes for pulse shaping. In this technique, the SRD creates a voltage step function with a very short rise time [22, 23]. A delayed version of this step function is also created by making the step function to propagate through a transmission line. The original step function is combined with the delayed version of itself in order to make a narrow UWB pulse. There are several drawbacks in this method of pulse generation which prevents it from using in WBAN applications. The length of the transmission line that is used in order to obtain the delayed version of the pulse is quite large; hence, it results in a large form factor in the circuit design. The pulse generation method is very sensitive to the reflections that may occur in the wave propagation paths; hence, the operation of the circuit can be largely affected even by a small fabrication fault. The amplitudes of the pulses that can be generated by this method are limited to few hundreds of millivolts [22]. Hence, it requires extensive amplification before transmitting through a wireless link. However, this method provides the basis for most of the modern UWB pulse generation techniques: the combining of a waveform and its delayed version in order to generate narrow pulses.

UWB pulse generators can be categorized into three major categories, namely, (1) baseband pulse generators, (2) up-conversion pulse generators, and (3) direct frequency pulse generators. These three pulse generation techniques are further described in the following subsections.

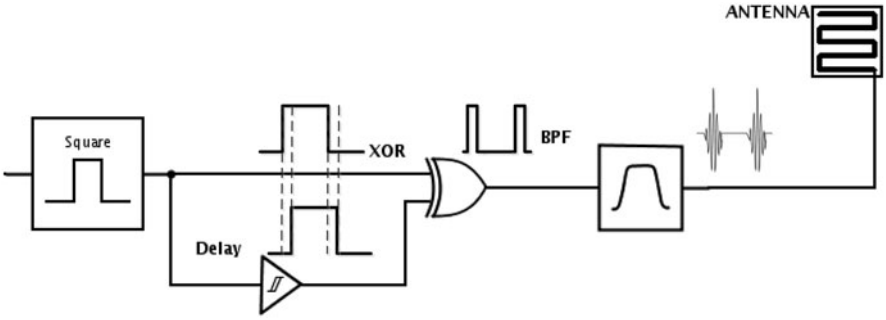

Fig. 3 Baseband pulse generation approach

Baseband UWB Pulse Generators

In this approach, a baseband pulse is generated initially in the form of a rectangular pulse [24–26]. The square baseband pulse provides signal with a wide spectrum. However, initial baseband pulse does not comply with the FCC spectrum requirements. Hence, a filtering stage is used in order to shape the pulse spectrum, such that it complies with the FCC spectral mask. This approach is shown in Fig. 3.

In this approach, the square pulse and its delayed version is passed through a XOR gate, forming an edge combining circuit. The narrow square pulses formed by the XOR output are then filtered using either a passive band pass filter (BPF) [24, 26] or a finite impulse response (FIR)- based filter [27]. The square pulses that form the input to the XOR gate can be obtained either using the input data waveform itself [5], through a flip-flop arrangement [26], or using a separate clock waveform [25].

This method provides advantages in terms of simplicity in design. It avoids the complexities of directly generating the UWB pulses that comply with the FCC spectrum requirements. A significant portion of the power spectrum of the square wave has to be filtered in order to bring the UWB pulse spectrum into the target frequency range. This results in significant power loss. Often, the amplitude of the UWB pulse spectrum after the BPF stage is lower than the FCC spectral mask. Hence, a power amplification stage has to be followed after the BPF in order to use the maximum allowable spectral amplitude. The use of a power amplifier further increases the power consumption of the transmitter.

Up-Conversion UWB Pulse Generators

The difference between the baseband pulse generation technique and the up-conversion method is that the up-conversion method uses a mixer to up-convert the frequency of the baseband pulses into the target frequency range. Both rectangular [28] and triangular [29] pulses can be used as the baseband pulse stream.

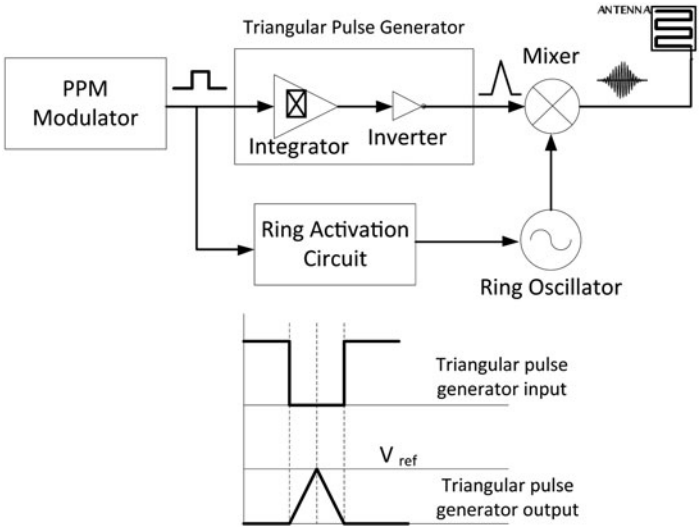

Fig. 4 Triangular pulse-based up-conversion pulse generator

Up-conversion of the pulses eliminates the requirement of a baseband pulse with a wide spectrum as a square pulse in order to generate the final UWB pulse stream. Hence, a triangular pulse stream is more suitable as the basis of the pulse generation. The power spectrum of the triangular pulses has suppressed side lobes, compared to that of the rectangular pulses. Hence, the power loss that might occur by using a square wave pulse as the baseband pulse can be reduced. However, it should be noted that although the triangular pulse generation techniques are easily achievable in CMOS IC-based designs, the rectangular pulse-based approach is the most convenient approach for the development of UWB pulse generators using off-the-shelf components. The up-conversion UWB pulse generation technique described in [29] is shown in Fig. 4.

In this method, the triangular pulse is generated using an integration circuit in combination with an inverter. The triangular pulse generator in fed with a pulse position modulated (PPM) data waveform. The integration happens at the rising and falling edges of the data waveform. The amplitude of the baseband triangular pulse can be determined by the threshold of the integrator. The baseband triangular pulse is then up-converted into the higher frequencies using a mixer. The ring activation circuit activates the oscillator only when a pulse is present, hence, it reduces the overall energy consumption of the circuit.

The use of an integrator for triangular pulse generation increases the power consumption of the circuit. A more efficient triangular pulse generation mechanism using logic gates is described in [30], where the triangular pulse is generated by edge combining the rising and falling edges of a square wave with an inverted version of itself.

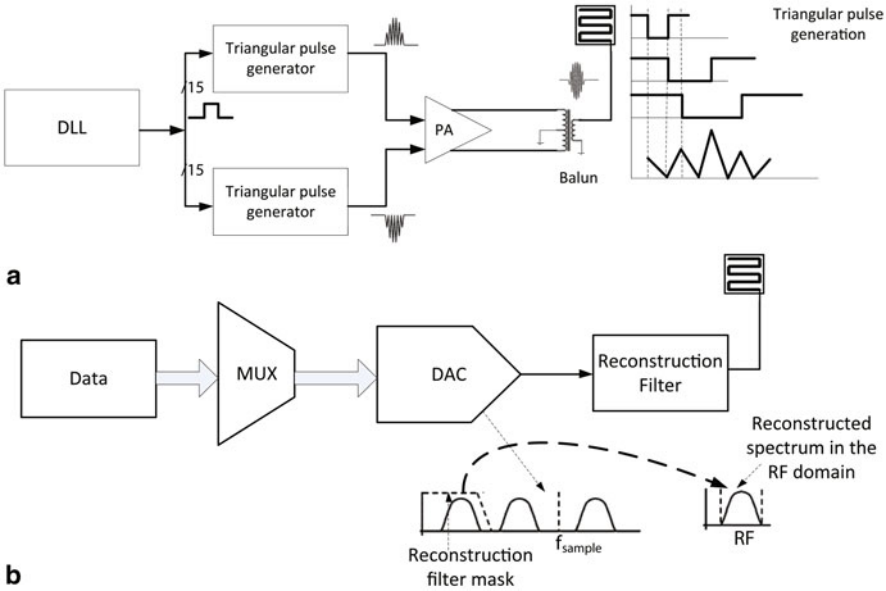

Fig. 5 Direct frequency ultra-wideband (UWB) pulse generators. **a** Triangular pulse synthesis. **b** Digital-to-analog converter (DAC)-based pulse synthesis

The up-conversion pulse generation technique has the same advantages as the baseband pulse generation technique. Additionally, the spectral shape of the final pulse can be determined in the baseband domain in this method. Consequently, baseband pulse-shaping techniques can be applied to this method rather than shaping the pulses at high frequencies. Hence, this approach minimizes the use of the power hungry RF components. However, this method also suffers from the relatively high power consumption in the mixer and the oscillator.

Direct Frequency UWB Pulse Generators

In this method, the UWB pulses are directly synthesized in the targeted frequency range without the use of an intermediate stage. Direct synthesis of the UWB pulses can be realized using several methods. The methods shown in [31, 32] generate triangular pulses in the RF domain. A fully digital implementation of a triangular UWB pulse generator is described in [31]. In this method, the triangular pulses are generated by combining the edges of several square pulses created using a delay locked loop (DLL) (Fig. 5a). The pulse shape can be digitally controlled by varying the delay of the original square pulses; hence, it is preferred over the analog pulse generation techniques for low-power applications. Power amplification is applied for the negative and positive triangular pulses separately. Finally, the pulses are

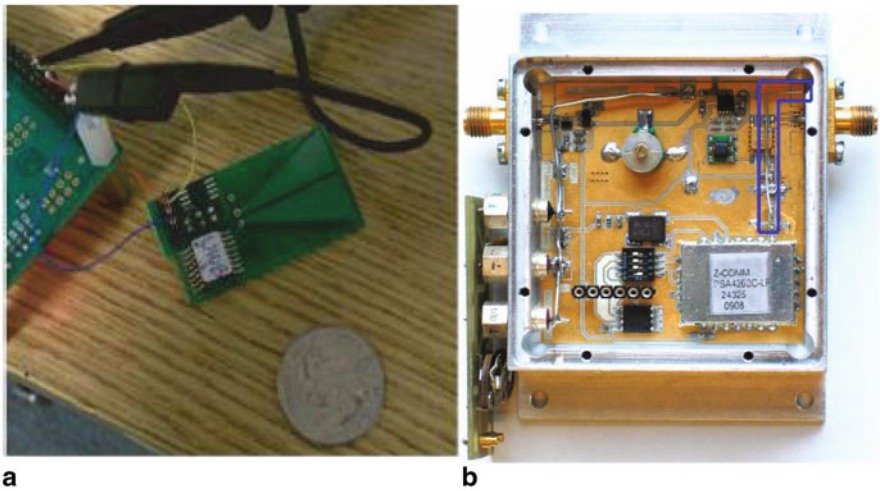

Fig. 6 **a**, **b** UWB sensor implementations**.** (From [34] and [35], respectively)

combined using a balun. This method provides more controllability over the pulse generation at the cost of increased hardware complexity.

A less complex, logic gate-based triangular pulse generation technique is suggested in [32]. In this method, the triangular pulses generated using a combination of XOR gates are used to periodically switch a voltage-controlled ring oscillator. In this manner, it is possible to generate the triangular UWB pulses in the RF domain. Because the oscillator operates only during the presence of a pulse, this method reduces the power wastage due to the continuous operation of local oscillators in the other methods.

A digital-to-analog converter (DAC)- based direct UWB pulse synthesis approach is demonstrated in [33] (Fig. 5b). This technique uses a high-speed DAC in order to synthesize accurate UWB pulse in the RF domain. This method overlooks the precision in pulse generation, hence, the achievable controllability in the pulse spectrum over the hardware complexity. The main drawback of this approach is that the DAC has to operate at very high sampling rates (in the order of 10 Gsps) in order to generate the UWB pulses. This is not only challenging for the implementation of the DAC but also the input data stream has to operate at very high rates; hence, it demands the use of high-speed logic circuits. In general, the direct frequency UWB pulse generation method is suitable for on-chip implementations using advanced technologies such as CMOS due to the requirement of the high precision in circuit implementation.

Implementation of UWB Sensor Nodes

While many publications present the implementation of UWB transmitters in ICs, only few publications present the full implementation of a UWB-based sensor platforms. The work presented in [34] (Fig. 6a) describes the implementation of a UWB

pulse generator using IC technology. A switched-voltage control ring oscillator approach is used in order to generate the UWB pulses. The data is modulated using the pulse stream generated in this pulse generation approach. The data can be fed into the circuit using a field programmable gate array (FPGA). This work also presents the implementation of a UWB antenna on the same printed circuit board (PCB). However, this sensor node is not fully integrated for independent operation as the data and the control signals have to be generated using an external FPGA. A UWB transmitter developed using off-the-shelf components is presented in [35]. In this method, narrow square pulses are generated in the baseband domain using a series of comparators. The RF pulses are generated by mixing these narrow pulses with a high-frequency signal generated using a phase locked loop. The power consumption of this circuit is 660 mW; hence, it is not suitable for power-stringent UWB applications.

This section presents a feasible implementation for the design of UWB sensor nodes that can be used in wearable WBAN applications. Three different sensor node types are discussed herein, namely, a voltage-controlled oscillator (VCO)- based UWB sensor, an amplifier-based UWB sensor, and a VCO-based UWB sensor with integrated NB receiver. These sensor implementations are equipped with interface circuitry in order to monitor both analog and digital signals. A microcontroller operates as the central controlling unit in all three designs. The sensor nodes are intended to operate in the frequency range of 3.5–4.5 GHz. This frequency band is chosen in order to avoid possible interference that can be generated due to the operation of other equipment in RF bands such as 5-GHz WLAN.

IR-UWB sensor nodes can be divided into three major components: the pulse generator, the RF circuit, and the controller. The function of the pulse generator is to generate narrow square pulses which can be modulated with the data bits. The suggested pulse generator in this section is implemented using buffers as the delay element when creating narrow pulses. The RF circuit is responsible for pulse-shaping and amplification. Two design concepts for the RF section of the sensor node are studied in detail herein. Finally, this section describes the overall operation of the sensor node, which includes the operation of a microcontroller that is used to carry out the control operations of the sensor nodes such as sleep mode operation and setting the modulation scheme.

Design of the UWB Pulse Generator

The IR-UWB pulse generator is a common design block in all the three designs. The basic operating principle of the narrow pulse generator is based on the operation of the delay elements. The work presented in [36] shows that the delay between the input and the output of a buffer depends on the applied supply voltage of the buffer. This relationship is given by (1),

$$t_{\mathrm{p}} = \frac{C_{\mathrm{L}}}{2V_{\mathrm{DD}}}\left(\frac{1}{k_1} + \frac{1}{k_2}\right), \tag{1}$$

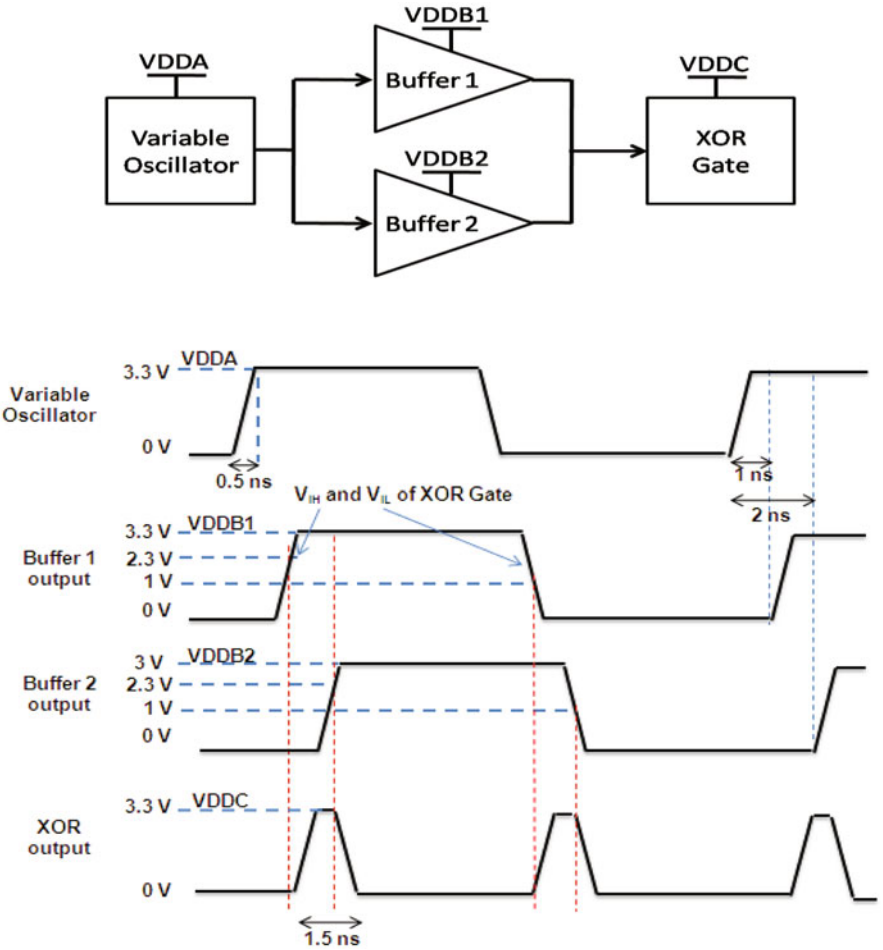

Fig. 7 Delay-based impulse radio ultra-wideband (IR-UWB) pulse generation

where t_p the propagation delay is caused by the buffer, C_L is the load capacitance, V_{DD} is the supply voltage of the buffer, k_1 and k_2 are the gain factors. This narrow pulse generation technique is shown in Fig. 7. Two identical buffers are fed with a resistor set oscillator that generates square pulses. Linear Technology's LT6905 programmable oscillator that generates a variable output frequency from 17 to 170 MHz is used as the reference square pulse generator in this design. Fairchild semiconductor's NC7WZ126 ultra high-speed buffer and NC7SZ86 XOR gate are chosen in this pulse generation mechanism because of their low rise and fall time operations. Identical buffers are chosen to eradicate the delays introduced by external factors other than the operating voltages. Therefore, the only factor that would affect the propagation delay is the modification of the supply voltage (V_{DD}). A narrow pulse is formed by changing the propagation delay on one of the buffers to allow a slightly

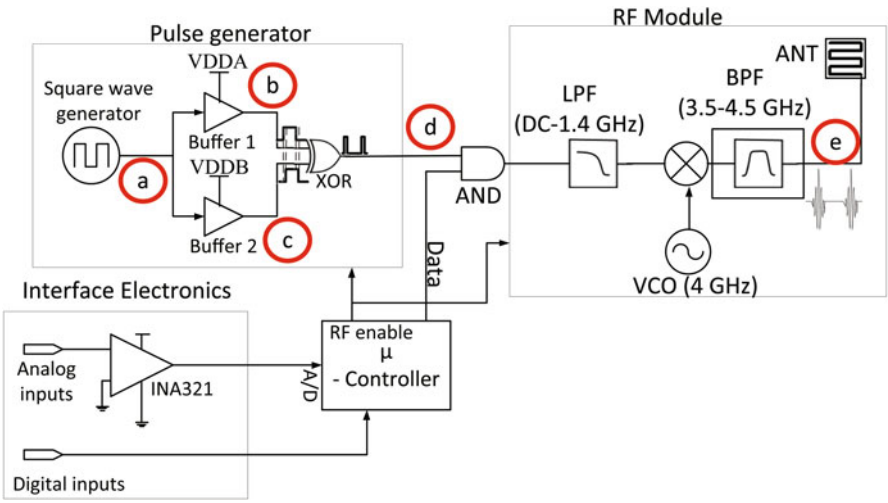

Fig. 8 VCO-based UWB sensor node design

delayed version of the input clock pulse to appear at one of the input port of the XOR gate. Figure 7 illustrates the generation of a 1.5-ns pulse using unequal supply voltages ($V_{DDB1} = 3.3$ V and $V_{DDB2} = 3$ V). Apart from adjustable pulse width, the pulse repetition frequency (PRF) and pulse amplitude can also be varied to meet the different operating requirements. The PRF is varied by changing the oscillator output, while the adjustment of the amplitude is performed by changing V_{DDC}.

The key advantages of the pulse generator mentioned herein are the ability to vary the pulse width, PRF, and pulse amplitude. This allows optimizing the transmitter operation in various environments. It is important to note that the ability to change the PRF in the suggested sensor nodes enables the system to vary the number of UWB pulses that are used to represent a data bit [3, 37].

UWB RF Module

This section analyzes two implementation methods for the UWB RF module converting the baseband pulses into the RF domain.

VCO-Based RF Module

Figure 8 shows the implementation of the VCO-based UWB sensor node design. In this design, the baseband USB pulses are up-converted using a VCO and a mixer. This sensor design uses the higher power contained within the first frequency lobe of the UWB pulse spectrum as an alternative to the amplification of the lower power

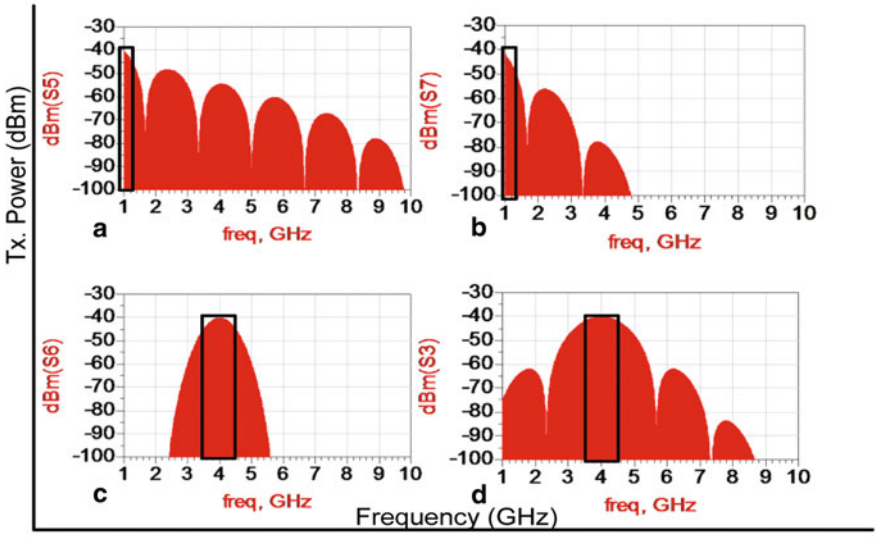

Fig. 9 Frequency spectrum of VCO-based sensor node at **a** UWB pulse generator output, **b** 1.4-GHz low pass filter output, **c** mixer output, and **d** 3.5–4.5-GHz band pass filter output

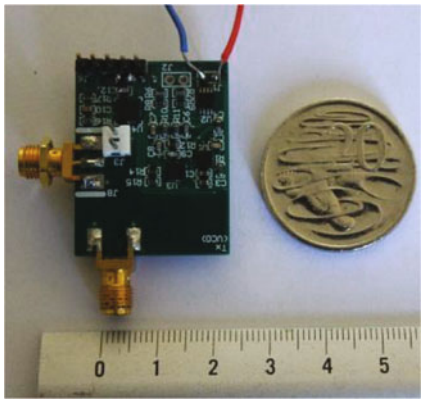

Fig. 10 VCO-based UWB sensor node

frequency lobe used in the amplifier-based design. It employs a low pass filter (LPF) to filter out the 0–1.4-GHz section of the UWB pulse spectrum. As shown in Fig. 9a, 9b, this portion of the spectrum is of the highest power compared to the rest of the spectrum. The filtered spectrum is then shifted using a mixer and a VCO operating at 4 GHz (Fig. 9c). A BPF is used at the output of the mixer in order to contain the UWB signals within the 3.5–4.5-GHz band. The spectrum taken at various points of this process is shown in Fig. 9.

Figure 10 depicts the realization of this design in a PCB. This design is slightly larger in dimension than the amplifier-based design due to the additional space required for the VCO and the mixer. Figure 11 shows the time domain waveforms taken at various sections of the VCO-based design. This sensor node's dimensions are 35 mm (L) $\times$ 27 mm (W) $\times$ 1.5 mm (H).

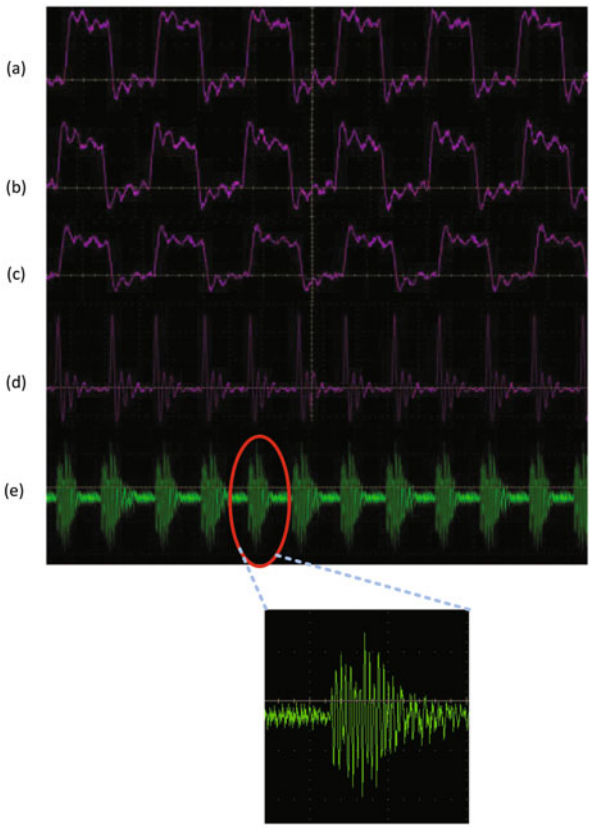

Fig. 11 Waveforms taken at various points of the sensor nodes (the points are marked with reference to the positions marked in Fig. 8)

Amplifier-Based RF Module

Figure 12 depicts the amplifier-based sensor node design. In the amplifier-based implementation, the narrow baseband pulses are filtered using a BPF in the band of 3.5–4.5 GHz. The UWB pulses are then amplified using a wideband low noise amplifier (LNA) to meet the −41.3 dBm transmission power level. This amplifier has been included to guarantee that the amplitudes of the UWB pulses are sufficient enough for the distance targeted by a WBAN application.

The power spectrum of the UWB pulses generated using the UWB pulse generator and the RF module that has a pulse width of 0.5 ns and 20 MHz PRF is shown in Fig. 13. This power spectrum consists of several frequency lobes spread throughout the UWB bandwidth. The amplitudes of these frequency lobes decrease toward the upper part of the UWB spectrum. The UWB sensor node is designed to transmit UWB signals in the band of 3.5 to 4.5 GHz. As shown in Fig. 13a the amplitude of the frequency lobe within the 3.5–4.5-GHz band is well below the maximum allowable power level by the FCC (−41.3 dBm/MHz). The amplifier-based version of the UWB sensor node employs two amplifier stages in order to boost the power

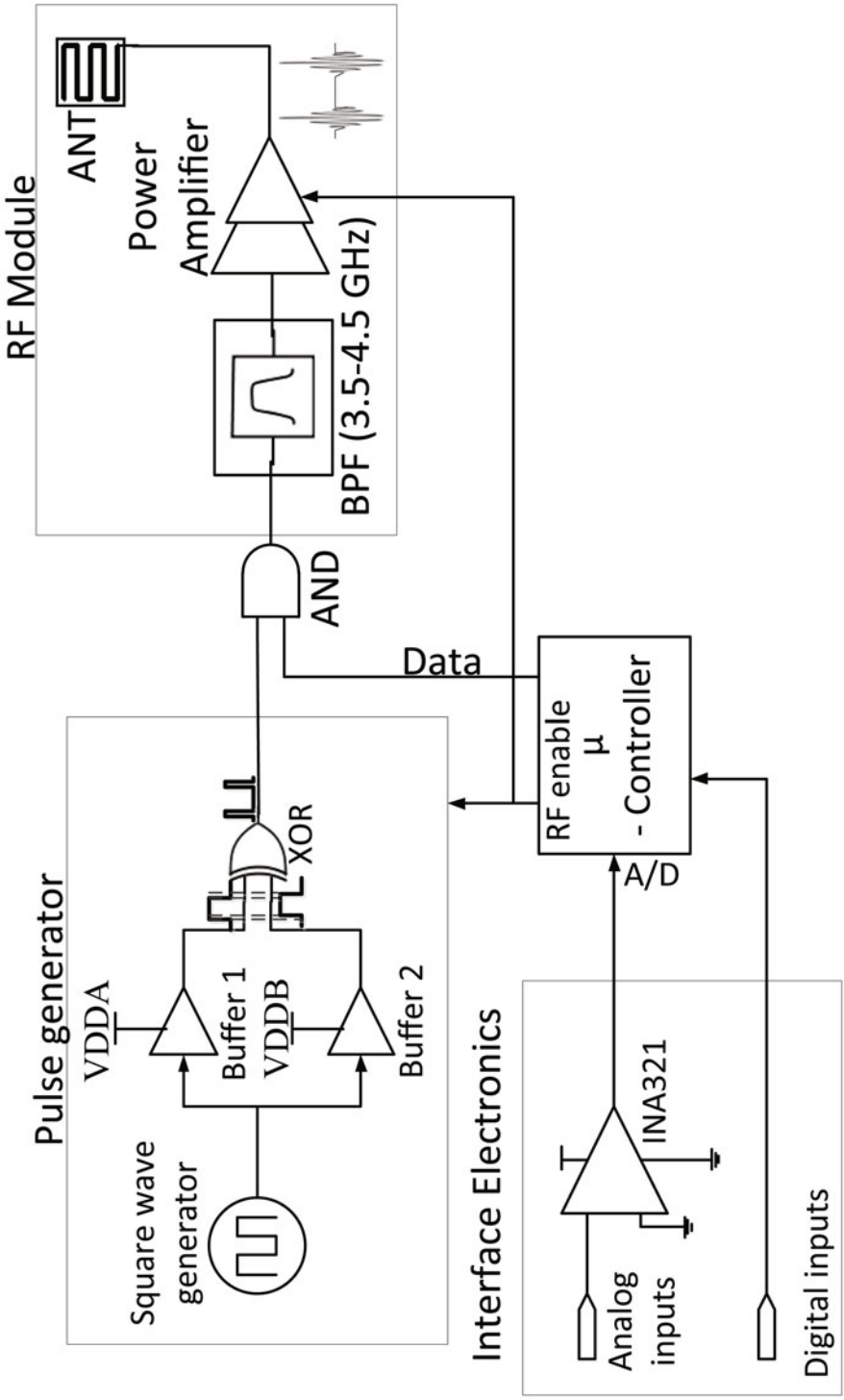

Fig. 12 Amplifier-based UWB sensor node design

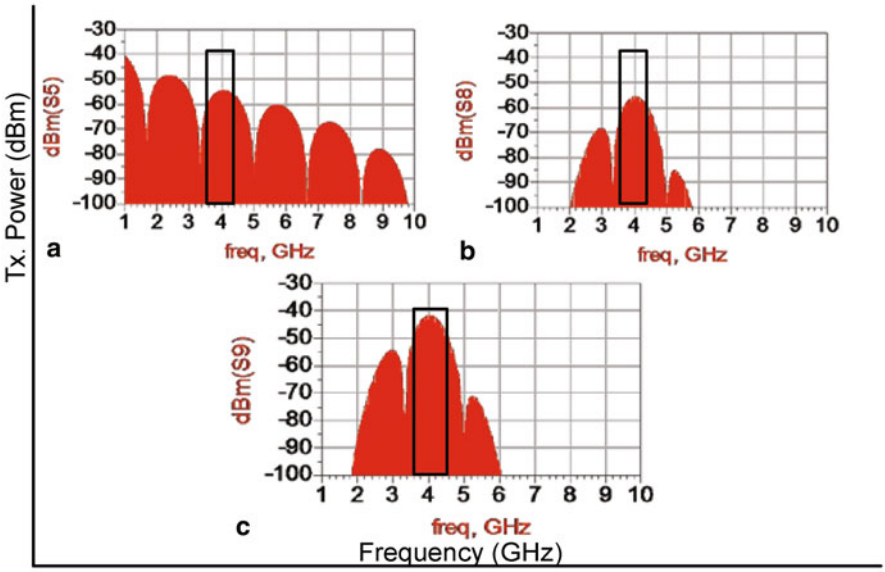

Fig. 13 Frequency spectrum of amplifier-based sensor node at **a** pulse generator output, **b** band pass filter (3.5–4.5 GHz) output, and **c** amplifier output

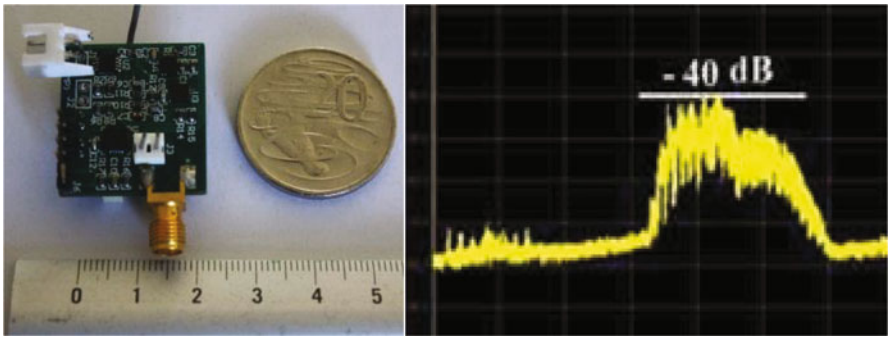

Fig. 14 Amplifier-based UWB sensor node design and transmit spectrum

level of the transmitted UWB signal within the band of 3.5–4.5 GHz (as marked in Fig. 13) while containing the power level within the FCC spectral mask.

Figure 14 shows the UWB sensor node designed based on the amplifier method and its transmit spectrum. The sensor nodes are assembled on a four-layer PCB with dimensions of 27 mm (L) × 25 mm (W) × 1.5 mm (H), which is sufficiently compact for the use in a wearable WBAN node.

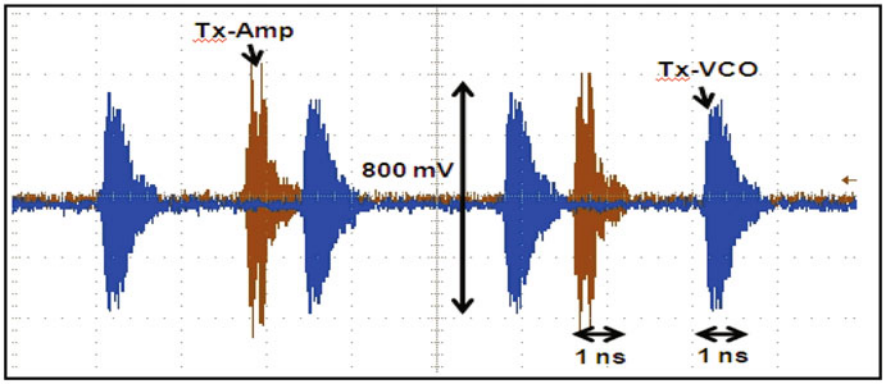

Fig. 15 Comparison of the time domain plot for Tx-Amp and Tx-VCO UWB pulses

Control and Interface Circuitry

The microcontroller acts as the central controlling module of the sensor node (see Fig. 8 and Fig. 12). The microcontroller can control the power to the baseband and RF portions of the circuits. Hence, it can shut down the power-consuming RF and baseband part during an intermittent data transmission situation. The microcontroller also acts as the mediator for analog and digital data inputs. It performs the analog to digital conversion, determines the transmission format and the modulation scheme, and sets the data rate. The UWB pulse rate is independent of the data rate and is arranged by the pulse generator. The generated UWB pulses are multiplied with the binary data bits created by the microcontroller.

The role of the interface electronics is to provide low noise amplification for physiological signals such as electrocardiogram (ECG), electroencephalogram (EEG). A typical ECG/EEG signal has amplitude of less than 500 μV with frequency less than 100 Hz. An instrumentation amplifier (INA321) and an active LPF (LTC6081) is used in this circuit to provide a measurable input to ADC of the microcontroller. The input signals are amplified by 60 dB, with a cutoff frequency at 100 Hz.

Both UWB sensor node designs are powered by a 3.7-V battery. The analog, digital, and pulse generation circuits operate with a supply of 3.3 V while the RF components use a 3-V supply. A National Semiconductor LP5996 linear regulator is selected to power the entire circuit.

Comparison of the Sensor Node Designs

The baseband approach used in the amplifier-based sensor node has advantages over the VCO method in terms of circuit simplicity and the avoidance of the local oscillator leakage. Although the oscillator-based approach is less affected by change of pulse width, it does not require an additional amplifier and has higher flexibility to operate in different frequency bands. The measured time domain plot for the generated UWB pulses of both these sensor types is presented in Fig. 15. Both

transmitters have similar performance because they have the same bandwidth and equal transmission power that is in compliance with the FCC transmission regulation. There is a slight difference between the pulse shapes of amplifier- and VCO-based sensor nodes. The pulse shape of the amplifier-based UWB pulse always contains two spikes as illustrated in Fig. 15 due to the rise and fall time of the narrow rectangular pulse. Because the VCO-based method uses a low pass filtered version of the narrow pulse train for up-conversion, the shape of the pulse is more consistent. The power consumption of the amplifier-based design is 10 nJ per data bit while the VCO-based sensor node operates at slightly low power consumption of 8 nJ per data bit.

UWB Sensor Node Integrated with a Narrowband Receiver

Although the transmit-only based design of the UWB sensor nodes avoids the complexities introduced by the UWB receiver, it lacks the coordination required for upscaling of the network architecture. It cannot reconfigure itself according to the varying data rate requirements of the network. In an IR-UWB network, it is possible to vary the data rate by changing the PRF of UWB pulses. In the previous designs, it was not possible to change the PRF of the UWB pulse generator without manual intervention to the circuit.

A low-power NB receiver circuit can be incorporated into the sensor node to enhance the adaptability of the system. An example of a UWB system transmitter incorporated with a 433-MHz ISM band-based NB feedback is illustrated in Fig. 16.

The typical current consumption of a UWB receiver is around 16 mA, but NB receivers can operate at a current as low as 1.65 mA [38] in a low-current mode. Another advantage of NB receiver is the simplicity of circuit design. Using a feedback path will also reduce the computational complexity at the sensor node end. In a transmit-only system, the position of the receiver has to be fixed and it does not allow for reconfiguration for changing channel conditions. By using an NB receiver, the gateway node can use the NB feedback to reconfigure the system to adapt to the changing channel conditions without the user intervention. It is also important to note that the feedback path does not require high data rate because it will be mostly used for sending acknowledgment and control messages. A simple NB receiver does not consume much of additional design space. It also consumes very small power because it is only powered on when required (sleep mode operation). Compared to the transmit-only method it gives a considerable advantage when scheduling the network and avoiding collisions. It also helps to optimize the power consumption of the sensor node, introducing additional power savings.

As a further improvement to the UWB-based sensor nodes, we have chosen to include an NB receiver operating in the 433-MHz ISM band. We have chosen RX5500 ISM band receiver chip by RFM [38] due to its low operating power. It can operate using both on–off keying (OOK) and amplitude shift keying (ASK) modulation methods. It operates in low-current mode around a power consumption of 5 mW even under the continuous operation. The power overhead introduced by this addition is

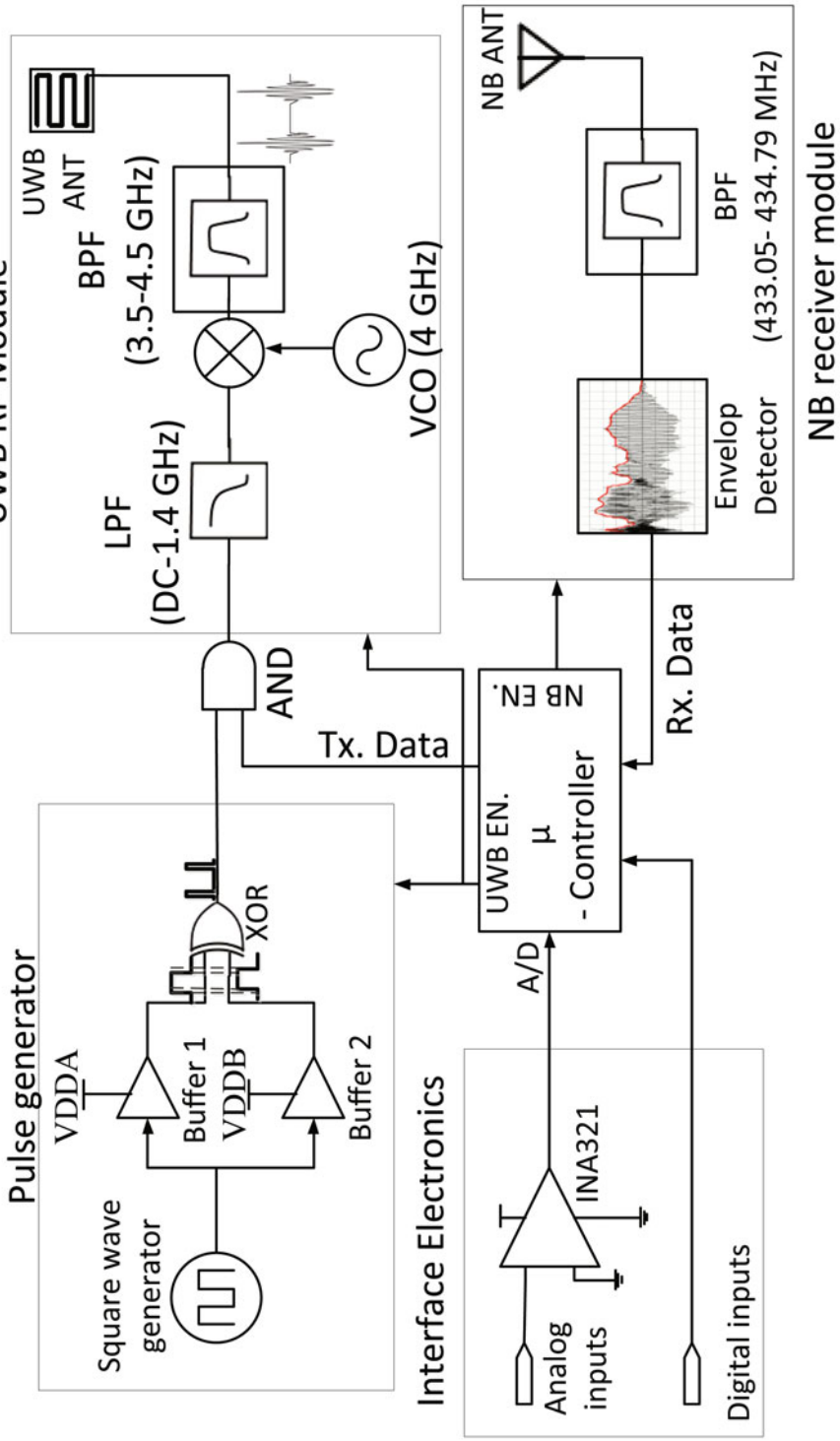

Fig. 16 UWB transmitter integrated with the narrowband (NB) receiver

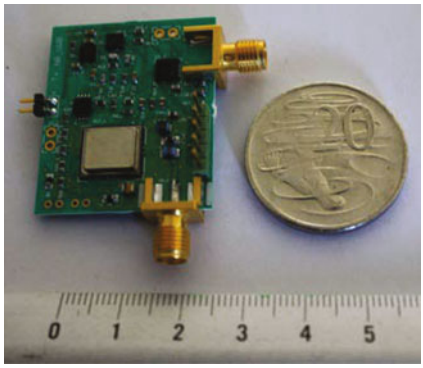

Fig. 17 UWB transmitter integrated with a narrowband (NB) receiver

much lower because it is programmed to operate in sleep mode operation using the control commands by the microcontroller. In this manner, it is possible for the coordinator node of the network to send control commands to the sensor node, allowing several sensor nodes to operate in a coordinated network. The microcontroller will be in charge of the data reception and transmission. It will configure the transmission parameters, such as pulses per bit value and PRF, based on the information received through the NB feedback path. Figure 17 depicts the implementation of the sensor node in a PCB. The board dimensions are 30 mm (L) × 25 mm (W) × 0.5 mm (H).

UWB Reception

The block diagram of the receiver circuit is shown in Fig. 18 [39]. The signal entering the receiver passes through a 3 to 5-GHz BPF to eliminate the unwanted interfering signals. The filtered signal is then amplified by 48 dB using three wideband LNAs before down-converting to a baseband signal using a mixer and a 4-GHz VCO. The

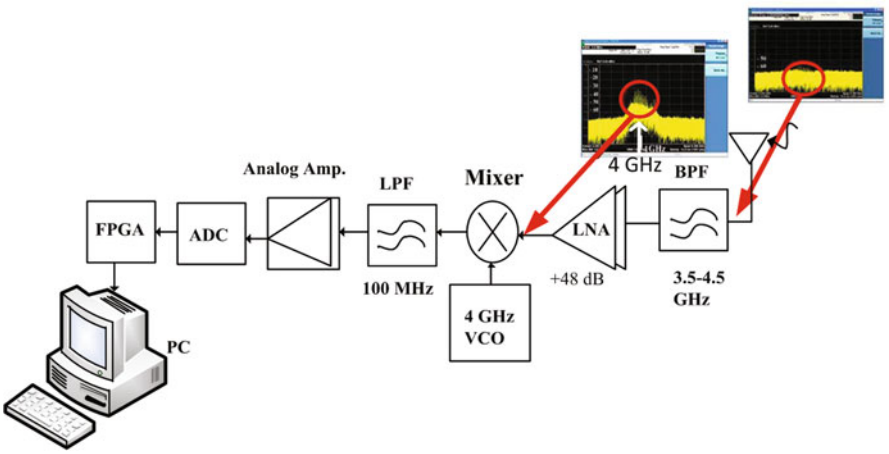

Fig. 18 UWB receiver architecture

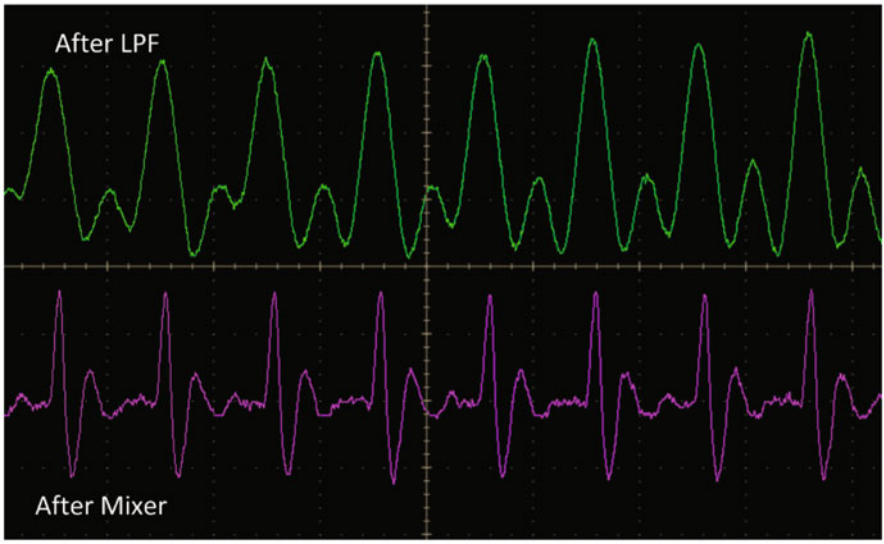

Fig. 19 Received time domain pulses

received signal spectrum after the antenna and after the LNA stage is shown in Fig. 18. The baseband signal is passed through an LPF with 100 MHz bandwidth before going through the analog amplification stage. The LPF acts as an integrator and stretches the pulses so that it is easily detectable using the ADC. The time domain waveforms of the signals after the mixer stage and after the LPF stage are shown in Fig. 19. After the analog amplifier, the transmitted UWB pulses are recovered. The recovered UWB pulses are then digitized using a high-speed ADC and processed by the FPGA before transferring the data to a computer using serial communication. The role of the FPGA is to process the received multiple UWB pulses and determine whether it is bit "1" or bit "0." Because the UWB pulse rate is selected to be much higher than the actual data rate (multiple pulses per bit), it increases the processing gain and, hence, eases the synchronizing process. Figure 20 depicts the recovered data waveform.

The VCO-based UWB sensor node has been evaluated for an on-body application using the bit error rate (BER) performance. The data is transmitted using the transmit-only MAC protocol described in [40]. The sensor was placed on different areas of the human body to represent physiological parameters such as ECG (chest), EEG (head), etc. An energy detection receiver [39], made using off-the-shelf components, is used to receive the UWB data. The receiver has been placed on the waist to configure and study the performance of the sensor node around the human body. The BER is computed using Matlab based on a known pseudorandom data sequence sent by the UWB node placed at various locations on the body. Figure 21 demonstrates the BER performance of the sensor node for various peak transmit powers.

Fig. 20 UWB data recovery

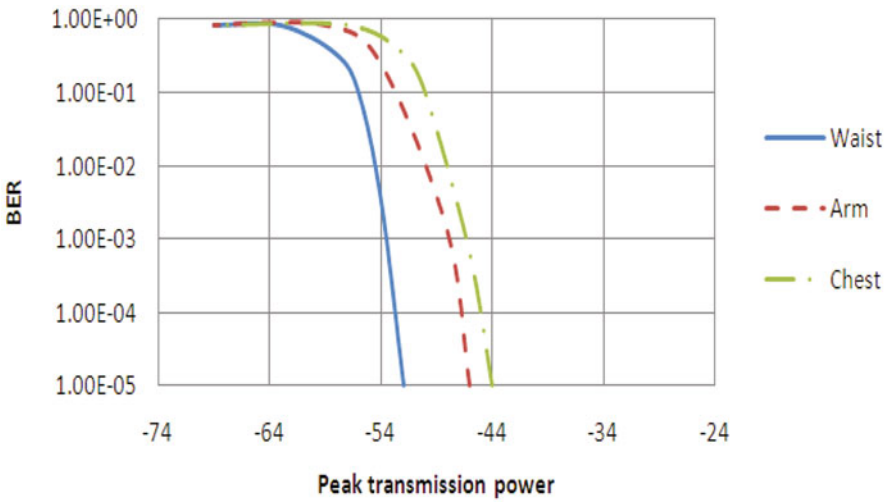

Fig. 21 Bit error rate (BER) performance for various positions of the sensor node [39]

Conclusion

This chapter investigates the design considerations for the implementation of low-power UWB sensor nodes. The common UWB transmitter design techniques are analyzed, while paying attention to their suitability for WBAN applications. Although many IC-based implementations of the UWB pulse generators are reported in the literature, only few studies demonstrate the full implementation of the UWB

sensor nodes. The second half of this chapter describes design techniques that can be used for the implementation of the IR-UWB based sensor nodes for WBAN applications. Three types of sensor node designs are discussed, and the advantages and the disadvantages of each method are presented.

Acknowledgments The authors would like to thank Dr. H. C. Keong for his support in the UWB transmitter-only sensor boards.

References

1. M.R. Yuce, Implementation of wireless body area networks for healthcare systems. Sens. Actuators. A Phys. **162**, 116–129 (July 2010)
2. M.R. Yuce, J. Khan, *Wireless Body Area Networks: Technology, Implementation and Applications*. (Pan Stanford, Singapore, 2011, ISBN 978-981-431-6712)
3. M.R. Yuce, H.C. Keong, M. Chae, Wideband communication for implantable and wearable systems. IEEE Trans. Microw. Theory Tech. **57**(2), 2597–2604 (Oct 2009)
4. M. Chae, Z. Yang, M.R. Yuce, L. Hoang, W. Liu, A 128-Channel 6 mW wireless neural recording IC with spike feature extraction and UWB transmitter. IEEE Trans. Neural Syst. Rehabil. Eng. **17**(4), 312–321 (Aug 2009)
5. Y. Gao, Y. Zheng, S. Diao, W. Toh, C. Ang, M. Je, C. Heng, Low-power ultra-wideband wireless telemetry transceiver for medical sensor applications. IEEE Trans. Biomed. Eng. **58**(3), 768–772 (Mar 2011)
6. M.R. Yuce, T. Dissanayake, Easy-to-swallow wireless telemetry. IEEE Microw. Mag. **13**(6), 90–101 (Sept–Oct 2012)
7. P.D. Bradley, An ultra-low power, high performance medical implant communication system (MICS) transceiver for implantable devices, in *IEEE Biomedical Circuits and Systems Conference*, 2006, pp. 158–161
8. B. Marholev, M. Pan, E. Chien, L. Zhang, R. Roufoogaran, S. Wu, I. Bhatti, T.H. Lin, M. Kappes, S. Khorram, S. Anand, A. Zolfaghari, J. Castaneda, C.M. Chien, B. Ibrahim, H. Jensen, H. Kim, P. Lettieri, S. Mak, J. Lin, Y.C. Wong, R. Lee, M. Syed, M. Rofougaran, A. Rofougaran, A single-chip Bluetooth EDR device in 0.13 μm CMOS, in *IEEE International Solid-State Circuits Conference*, February 2007, pp. 558–759
9. Y. Rui, Y. Theng-Tee, T. Kwang-Hung, M. Shouxian, C. Yike, W. Haifeng, Y. Hwa-Seng, E. Ting, M. Itoh, A 5.5 mA 2.4-GHz two-point modulation ZigBee transmitter with modulation gain calibration, in *IEEE Custom Integrated Circuits Conference*, September 2009, pp. 375–378
10. G. Albasini, L. Mori, I. Bietti, R. Castello, A multi-standard WLAN RF front-end transmitter with single-spiral dual-resonant tank loads, *European Solid-State Circuits Conference*, September 2006, pp. 348–351
11. Federal Communications Commission, FCC 02-48 (First Report and Order), 2002
12. Institute of Electrical and Electronics Engineers, IEEE-802.15.4-2006, Part 15.4: Wireless Medium Access Control (MAC) and Physical Layer (PHY) Specifications for Low-Rate Wireless Personal Area Networks (LR-WPANs). Standard, IEEE
13. http://www.zigbee.org/, 2013
14. http://focus.ti.com/docs/prod/folders/print/cc2420.html, 2013
15. H.C. Keong, M.R. Yuce, UWB-WBAN sensor node design. The *International Conference of the IEEE Engineering in Medicine and Biology Society*, 30 August–3 September 2011, pp. 2176–2179
16. http://www.xbow.com/, 2013
17. http://www.ti.com/, 2013

18. http://www.microsemi.com/, 2013
19. http://www.givenimaging.com/en-us/Innovative-Solutions/Capsule-Endoscopy/Pillcam-SB/Pages/default.aspx, 2013
20. K. Sonoda, Y. Kishida, T. Tanaka, K. Kanda, T. Fujita, K. Maenaka, K. Higuchi, Wearable photoplethysmographic sensor system with PSoC microcontroller. *Fifth International Conference on Emerging Trends in Engineering and Technology (ICETET)*, 2012, pp. 61–65
21. http://www.national.com/pf/DC/ADC12D1800.html#Overview, 2013
22. H. Jeongwoo, N. Cam, A new ultra-wideband, ultra-short monocycle pulse generator with reduced ringing. IEEE Microw. Wirel. Compon. Lett. **12**, 206–208 (2002)
23. L. Jeong-Soo, N. Cam, Novel low-cost ultra-wideband, ultra-short-pulse transmitter with MESFET impulse-shaping circuitry for reduced distortion and improved pulse repetition rate. IEEE Microw. Wirel. Compon. Lett. **11**, 208–210 (2001)
24. S. Bourdel, Y. Bachelet, J. Gaubert, R. Vauche, O. Fourquin, N. Dehaese, H. Barthelemy, A 9-pJ/Pulse 1.42-Vpp OOK CMOS UWB pulse generator for the 3.1–10.6 GHz FCC Band. IEEE Trans. Microw. Theory Tech. **58**, 65–73 (2010)
25. L. Smaini, C. Tinella, D. Helal, C. Stoecklin, L. Chabert, C. Devaucelle, R. Cattenoz, N. Rinaldi, D. Belot, Single-chip CMOS pulse generator for UWB systems. IEEE J. Solid-State Circuits. **41**, 1551–1561 (2006)
26. S. Sanghoon, K. Dong-Wook, H. Songcheol, A CMOS UWB pulse generator for 3–10 GHz applications. IEEE Microw. Wirel. Compon. Lett. **19**, 83–85 (2009)
27. Z. Yunliang, J.D. Zuegel, J.R. Marciante, W. Hui, A 0.18 μm CMOS distributed transversal filter for sub-nanosecond pulse synthesis, in *IEEE Radio and Wireless Symposium*, 2006, pp. 563–566
28. D.D. Wentzloff, A. P. Chandrakasan, Gaussian pulse generators for subbanded ultra-wideband transmitters. IEEE Trans. Microw. Theory Tech. **54**, 1647–1655 (2006)
29. J. Ryckaert, C. Desset, A. Fort, M. Badaroglu, V. De Heyn, P. Wambacq, G. Van der Plas, S. Donnay, B. Van Poucke, B. Gyselinckx, Ultra-wide-band transmitter for low-power wireless body area networks: design and evaluation. IEEE Trans. Circuits Syst. I Regul. Pap. **52**, 2515–2525 (2005)
30. K. Hyunseok, J. YoungJoong, J. Sungying, Digitally controllable bi-phase CMOS UWB pulse generator, in *IEEE International Conference on Ultra-Wideband*, 2005, pp. 442–445
31. T. Norimatsu, R. Fujiwara, M. Kokubo, M. Miyazaki, A. Maeki, Y. Ogata, S. Kobayashi, N. Koshizuka, K. Sakamura, A UWB-IR transmitter with digitally controlled pulse generator. IEEE J. Solid-State Circuits, **42**, 1300–1309 (2007)
32. Z. Ming Jian, L. Bin, W. Zhao Hui, 20-pJ/Pulse 250 Mbps low-complexity CMOS UWB transmitter for 3–5 GHz applications. IEEE Microw. Wirel. Compon. Lett. **23**, 158–160 (2013)
33. D. Baranauskas, D. Zelenin, A 0.36 W up to 20GS/s DAC for UWB wave formation, in *IEEE International Solid-State Circuits Conference*, 2006, pp. 2380–2389
34. T. Wei, E. Culurciello, A low-power high-speed ultra-wideband pulse radio transmission system. IEEE Trans. Biomed. Circuits. Syst. **3**, 286–292 (2009)
35. J. Colli-Vignarelli, C. Dehollain, A discrete-components impulse-radio ultrawide-band (IR-UWB) transmitter. IEEE Trans. Microw. Theory Tech. **59**, 1141–1146 (2011)
36. N.R. Mahapatra, A. Tareen, S.V. Garimella, Comparison and analysis of delay elements, in *IEEE International Midwest Symposium on Circuits and Systems*, August 2002, pp. 473–476
37. H.C. Keong, M.R. Yuce, UWB-WBAN sensor node design, in *the Annual International Conference of the IEEE Engineering in Medicine and Biology Society*, 30 August–3 September 2011, pp. 2176–2179
38. http://www.rfm.com/products/data/rx5500.pdf, 2013
39. H.C. Keong, T.S.P. See, M.R. Yuce, An ultra-wideband wireless body area network: evaluation in static and dynamic channel conditions. Sens. Actuators. A Phys. **180**, 137–147 (June 2012)
40. H.C. Keong, M.R. Yuce, Analysis of a multi-access scheme and asynchronous transmit-only UWB for wireless body area networks, in the *31st Annual International Conference of the IEEE Engineering in Medicine and Biology Society (EMBC'09)*, 2009 pp. 6906–6909

Medium Access Control (MAC) Protocols for Ultra-Wideband (UWB)-Based Wireless Body Area Networks (WBAN)

K. M. S. Thotahewa, Jean-Michel Redouté and Mehmet Rasit Yuce

Abstract A wireless body area network (WBAN) is a dedicated network developed to operate in, on or near the human body. In order to design a power-efficient WBAN, a cross-layer solution is required. The physical layer of a WBAN determines the choice of wireless scheme, modulation scheme, synchronization and data rate. The data-link layer provides medium access control (MAC), which ensures reliable and fair access to the communication channel. Ultra-wideband (UWB) is a suitable wireless technology to achieve high data rates while keeping power consumption and form factors small. Hence, it provides numerous advantages to WBAN applications. This chapter analyzes UWB-based MAC protocols available for WBAN systems in terms of their practicality in design, effectiveness in data delivery and power efficiency. In particular, the application of WBAN in healthcare monitoring environments is considered.

Keywords Medium access control (MAC) · Wireless body area network · Body sensor network · Transmit-only MAC · Sensor node · Body sensors · Wearable sensors · IEEE 802.15.6 standard · IEEE 802.15.4a MAC · Medical sensor network

Introduction to Ultra-Wideband-Based Wireless Body Area Networks

Wireless body area network (WBAN) is a short-range communication scheme, which requires a distance of less than 2 m. It includes a set of inter-communicating sensor nodes operating around the human body. They can either be wearable or implantable. WBANs are used in both medical and non-medical applications [1]. Wireless electrocardiogram (ECG) monitoring systems and wireless neural recording systems are

M. R. Yuce (✉) · K. M. S. Thotahewa · J.-M. Redouté
Biomedical Integrated Circuits and Sensors Laboratory,
Department of Electrical and Computer Systems Engineering,
Monash University, Melbourne, VIC 3800, Australia
e-mail: mehmet.yuce@monash.edu

M. R. Yuce (ed.), *Ultra-Wideband and 60 GHz Communications for Biomedical Applications,* DOI 10.1007/978-1-4614-8896-5_7,

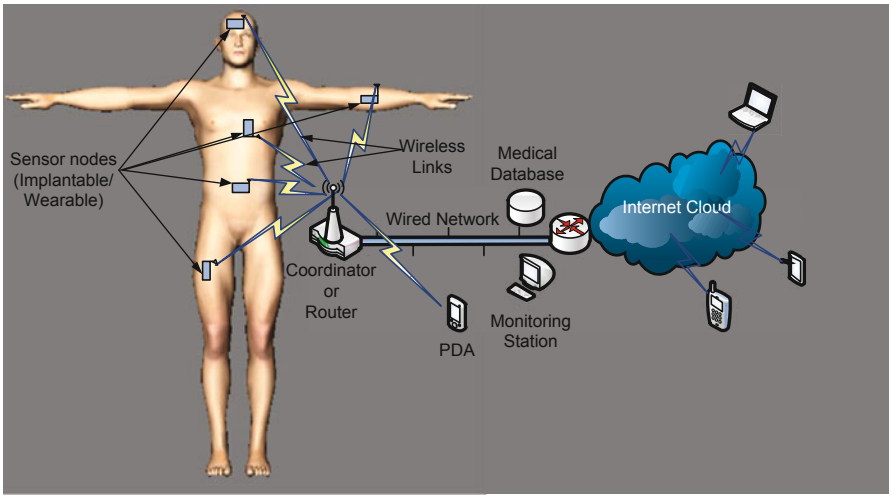

Fig. 1 Key components of a wireless body area network (WBAN)

examples of medical applications that can be implemented using WBAN techniques. WBANs can also be used for non-medical applications such as gaming and smart home control.

Several key components can be identified in a WBAN system for health care monitoring applications. *Sensor nodes* are either implantable or on-body devices that transmit vital physiological information, such as ECG, electroencephalogram (EEG) and body temperature to an outside node.

A *coordinator node* or a *router node* is used to collect and route the information sent by a sensor node and forward that information to a computer-based application for interpretation [2]. Figure 1 illustrates the key components of a WBAN.

A WBAN used for health care monitoring inherits several key requirements. An implanted or on-body sensor node is battery powered. Especially in the implantable case, human intervention in replacing the batteries should be kept at a minimum level, since it might involve surgical procedures. Hence, a WBAN sensor node should consume low power. Low power transmission of signals limits the communication range (usually 0.1–2 m). As a result, an optimized low complexity medium access control (MAC) protocol should be used in WBANs so that it would enhance the low power operation of the sensor node.

A WBAN network structure consists of several tiers of interconnecting networks. This chapter pays attention to the communication between the sensor nodes and an immediate parent node of the sensor nodes, which can either be a central coordinator or a gateway router. This communication is named as sensor tier communication hereafter. Typically, short-range wireless communication of less than 2 m is employed in the sensor tier. This sensor tier is characterized by the following features:

- The sensors are connected to the gateway in a star topology.
- The sensor nodes have limited processing capabilities and very stringent requirements on power consumption.

- Unlike the sensor nodes, the gateway node is allowed to have higher processing power and battery power.
- Communication is mostly one directional from the sensor nodes to the gateway. Communication from the gateway node to the sensor nodes consist mainly of network information and feedback.

A WBAN differs from a wireless sensor network (WSN) because of its specific requirements. Differences between a WBAN and a more generic WSN are listed in Table 1.

Ultra-wideband (UWB) is defined as signals that have a fractional bandwidth larger than 0.2 or at least 500 MHz. It is allowed to operate in the 0–960 MHz and 3.1–10 GHz bands; however, the effective isotopic radiated power (EIRP) must be kept below -41.3 dBm/MHz [4]. UWB technology inherits several key properties that make it a strong candidate for WBAN applications. These properties are briefly discussed below:

1. Low power consumption of UWB transmitters
   WBAN devices are considered as battery-powered devices; hence, the power consumption of the data transmission devices involved in the WBAN should be kept at a minimum in order to elongate the battery life of the devices. This is very critical especially for implantable applications of WBANs, since replacing a device or a battery will involve invasive surgery.
   UWB transmitters use discrete pulses in order to transmit data [5, 6], whereas the traditional narrowband transmitters use data modulated continuous wave signals for wireless transmission [7]. Because of the discrete pulse transmission, a significant portion of the data transmission time for the UWB transmitters consists of a transmitter silent period, where the electronic components involved in pulse generation can be operated at the low power mode. In contrast, traditional narrowband transmitters operate continuously throughout the data transmission period for most of the modulation schemes. This difference in the data mapping principal results in a significant difference in the power consumption between the former and the latter for longer periods of operation.
   The implementation of an UWB transmitter involves very few radio frequency (RF) components compared with the continuous wave transmitters. In fact, all digital realizations of the UWB transmitters are achievable with the aid of state of the art complementary metal-oxide semiconductor (CMOS) technology [5, 8]. In contrast, traditional narrowband transmitters utilize power-consuming RF and analog components, such as RF power amplifiers (PA) and analog phase-locked loops (PLL), extensively because of the nature of the signal generation [9].
   Furthermore, because of the possibility of direct mapping of the data into the UWB pulses, complex modulation schemes are not required for UWB transmitters. This further reduces the data processing requirement at the transmitter end for UWB communication devices. This feature enhances the achievable power savings of the UWB transmitters. Hence, the UWB transmitters hold a significant advantage over the traditional narrowband transmitters for power-intensive WBAN applications.

Table 1 Differences between a WBAN and a WSN

Property	WBAN	WSN
Sensor position	Located in or on a human body or at a close proximity to a human body	Deployed over a large area
Topology	Typically comprises of multiple sensor nodes and one central receiving node (gateway node). All the sensor nodes will communicate directly with the gateway node forming a star topology	Sensors are connected based on mesh topology, where multiple hops are supported. Each sensor in a WSN can act as a router node
Nature of data	Data from physiological signals is periodic and signals are transmitted at a fixed interval. For example, the transmission frequency of a temperature sensor is once every minute [3]	The nature of data depends on the application. The transmission interval for WSN is irregular
Redundancy	Because of the limited space and limited sensor locations for measuring the physiological signals on the human body, only one sensor exists for measuring each physiological signal. There is no redundancy that allows for node failure in WBAN	More than one sensor can be deployed in WSN to allow for redundancy, especially in areas where data is critical or where sensors are inaccessible
Mobility	Human body movement is unpredictable. Body movements such as bending down or swinging arms will affect the channel condition of the nodes. The interference level for WBAN systems is also unpredictable due to mobility. The level of interference will increase, when two or more users move towards each other	Nodes for WSN are typically stationary, making channel conditions more predictable
Data collection	Multiple receivers (e.g. PDAs carried by doctors and nurses) are used in WBAN systems to collect the data from sensor nodes	Focuses on best-effort data collection at the central database

WBAN wireless body area network, *WSN* wireless sensor network, *PDA* personal digital assistant

2. High data rate capability
   UWB radios map the data bits into very short (nanosecond duration) pulses. This method implies a carrier-less data transmission scheme, where the short pulses represent a signal with a signal power that is spread in a large bandwidth in the frequency domain. According to Shannon's capacity theorem, the data rate capacity of a channel is linearly proportional to the channel bandwidth and logarithmically proportional to the increase in the signal-to-noise ratio (SNR) of the channel [10]. This means that the UWB signals are capable of delivering higher data rates, using the high bandwidth property. A continuous wave-based narrowband signal has to operate at much higher frequencies in order to transmit at the same data rates [11]. The use of higher frequencies leads to higher attenuation of the signals, which has to be compensated by increasing the transmit power. Hence, an UWB transmission system is capable of achieving higher data rates while operating at low power, which makes it an ideal candidate for power-intensive WBAN applications that demands high data rates, such as wireless capsule endoscopy systems [12, 13] and neural recording systems [14].
3. Small form factor
   Small size is an essential property for implantable and wearable WBAN sensor nodes. UWB transmitters can be manufactured with only few electronic components, hence the design space required for the latter is minimal. This is an advantageous property that makes UWB a suitable candidate for WBAN sensor nodes.
4. Susceptibility to multipath components
   UWB uses finite resolution pulses in order to represent data bits. Unlike in the case of continuous wave signals where multipath components always overlap with the time domain signal at the receiver end, the multipath arrivals of the UWB signals can be easily resolved and avoided at the receiver end because the probability of a multipath component overlapping with the received narrow pulse in time domain is very low [15, 16]. This is a very useful feature in UWB when it is operating around the body where the presence of multipath components can be high.

Despite the advantages of the UWB technology, there are some drawbacks in UWB systems that have to be overcome in order to extract the advantages provided by the UWB technology for WBAN applications. These disadvantages are listed below:

1. Complexity of the UWB receiver architecture
   UWB signals use narrow pulses in order to transmit data, and the transmitted signal power is regulated to be very low in order to prevent interference to other systems. An UWB receiver has to be capable of detecting these low power narrow pulses. This implies the use of high-speed analog-to-digital (A-to-D) converters and extensive amplification of the received signals at the receiver front end. This makes the UWB receiver to be complex in design and results in increased power consumption. This is a major drawback in UWB systems that has to be overcome using techniques such as transmit only UWB system architectures [17] in order to use UWB for power-intensive WBAN applications.

2. Susceptibility to interference from other wireless transmission systems
   Unlike in the case of a carrier-based systems, the UWB signal power is spread across a wide bandwidth. Hence, it is susceptible to interference from all the systems operating within the UWB signal bandwidth. The signal processing involved in the reception of carrier-based signals has to consider only the interference rejection in that particular carrier frequency, whereas for UWB systems, the signal processing at the receiver end should consider interference mitigation for the whole signal bandwidth.

The MAC protocols for UWB systems govern the multiple access of the UWB channel. The MAC protocols for UWB systems has to be designed in a way such that it enhances the advantages provided by the UWB signals and overcomes the drawbacks such as the high receiver complexity. In general, MAC protocols based on carrier sensing and clear channel assessment (CCA) is not appropriate for UWB-based MAC protocols because it is extremely difficult to assess the channel condition of a wideband UWB channel that uses narrow pulses to transmit data. CCA for impulse radio (IR)-UWB cannot be implemented using a peak detector, matched filter or correlation method [18]. A frequency domain method to implement CCA for IR-UWB signal is proposed in [18]. This method requires a large number of narrowband filters and energy detectors. The proposed circuit is designed for the detection of IR-UWB signals spread across the entire 7.5-GHz band. It is not suitable for channelized UWB systems where only a sub-band of UWB is utilized. In a channelized UWB system, the typical transmission bandwidth is between 500 MHz and 1 GHz. Most of the energy detectors in the CCA circuit will register a false reading when a strong narrowband interferer is present.

The MAC protocols for UWB systems may preferably use a random medium access method or a transmit-only MAC protocol for the multiple access of the UWB channel. The rest of the chapter intends to give a critical analysis of the recently published work on UWB MAC protocols, which has the potential usage for WBAN applications. Given that the IR-UWB is the well-established and better-suited form of UWB signal type for WBAN applications [19], this chapter will analyze only the IR-UWB-based MAC protocols.

UWB-Based MAC Protocols for WBAN Applications

The IEEE802.15.6 Standard

The IEEE802.15.6 standard [20] is the first standard that defines the MAC architecture that can be used for in-body and on-body wireless communications. The standard defines the physical layer communication using UWB and other narrowband technologies. The standard recommends the star topology as network topology for the nodes in a WBAN. Multiple access is achieved in the time domain with the aid of a super frame structure. The super frame is divided into equal-length time slots, which

are allocated to the contending sensor nodes by a central coordinator, which controls the shared access to the wireless medium.

The IEEE802.15.6 standard supports three communication modes [20]:

1. Beacon mode with super frame boundaries:
   The super frame structure is divided by beacons transmitted in the downlink by the coordinator in this communication mode. Several medium access mechanisms are supported for sensor nodes communicating using this mode: exclusive access, managed access, random access and contention access. Exclusive access and managed access periods in the super frame are used to provide guaranteed data transfer for sensor nodes with high priority while other two methods provide data transfer for less-priority sensor nodes.
2. Non-beacon mode with super frame boundaries:
   This communication mode does not use a downlink beacon in order to indicate the super frame boundaries to the sensor nodes. Instead it uses the scheduling of data communication through techniques such as polling. The coordinator schedules the data transmission of each individual sensor node through polling such that the data communication from the sensor nodes falls within a super frame structure. This communication mode falls within the managed access.
3. Non-beacon mode without super frame boundaries:
   In this communication mode a pre-defined super frame structure is not used. The data communication occurs through polling or posted allocation where a certain amount of time slots are allocated by the coordinator node, which can be accessed by any sensor node waiting for data transmission.

The access to the shared medium is provided using various mechanisms [20]:

1. Random access using slotted ALOHA and carrier sense multiple access with collision avoidance (CSMA/CA)
2. Improvised and unscheduled access mechanism, where the coordinator nodes send polling and posting commands without pre-reservation or pre-scheduling in a random manner
3. Scheduled access using polling

The UWB physical layer (PHY) specifications in the IEEE802.15.6 standard is used to provide high data rate and low power consuming data transfer using UWB signals. The UWB spectrum in the range of 3.1–10 GHz is divided into 11 channels with a channel bandwidth of 499.2 MHz for each channel. The PHY specifications support both IR-UWB and frequency modulation-UWB (FM-UWB). This chapter will only discuss the specifications for IR-UWB, as it is better suited for WBAN applications because of the possibility of implementing low complexity hardware for IR-UWB transmitters.

The IEEE802.15.6 standard supports three different modulation schemes for IR-UWB: on–off keying (OOK), differential binary phase shift keying (DBPSK) and differential quadrature phase shift keying (DQPSK). The physical layer protocol data unit (PPDU) for the IR-UWB-based data communication is shown in Fig. 2.

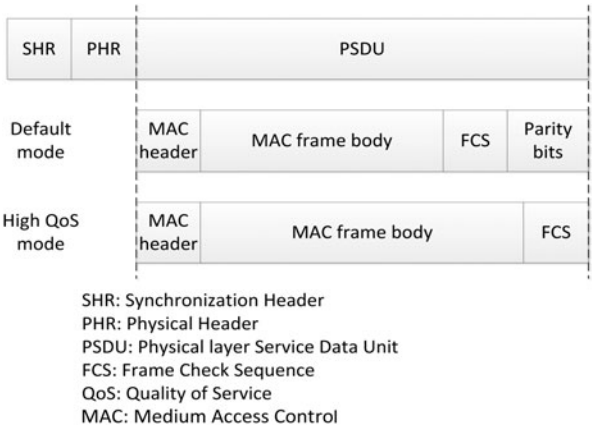

Fig. 2 The IEEE802.15.6 standard physical layer protocol data unit (PPDU) for impulse radio ultra-wideband (IR-UWB) physical layer (PHY) specifications

The synchronization header (SHR) provides a preamble bit pattern (*Kasami* sequence with a length of 63) which is essential part in the narrow pulse-based UWB data transmission. The PHY header (PHR) provides 24 data fields which are used to indicate communication parameters such as data rate, MAC frame body length, pulse type (chirp pulse, chaotic pulse and short pulse) and modulation mode. The IEEE802.15.6 standard also supports bit interleaving using a modulus interleaver in order to provide robust data transmission by avoiding large sequences of consecutive ones and zeros. Because of the difficulty in CCA for UWB, a random access mechanism based on the slotted ALOHA or a polling-based medium access mechanism is recommended for UWB-based WBANS in the IEEE802.15.6 standard.

Drawbacks: Although the IEEE802.15.6 standard defines a robust standard for WBAN applications, it has several drawbacks when it comes to using UWB for WBAN applications. It ignores several key limitations in the implementation of the UWB transceivers. The MAC protocol defined by the IEEE802.15.6 standard assumes the use of a UWB transceiver at the sensor node end. Although the UWB transmitters are relatively less complex, the implementation of the UWB receiver involves power hungry complex hardware designing (refer Sect. "*Introduction* to Ultra-Wideband-Based Wireless Body Area Networks"). Also, it ignores the optimization of the UWB transmit power control through duty cycling and gated pulse transmission techniques [21, 22], which can be used to optimize the power consumption of the transmitter node while controlling the transmit power of the sensor nodes according to the Federal Communications Commission (FCC) regulations for UWB transmission [4].

The IEEE802.15.4a Standard

The IEEE802.15.4a standard [23] is currently the most discussed and adopted standard for UWB applications in the literature. The IEEE802.15.4a standard has been

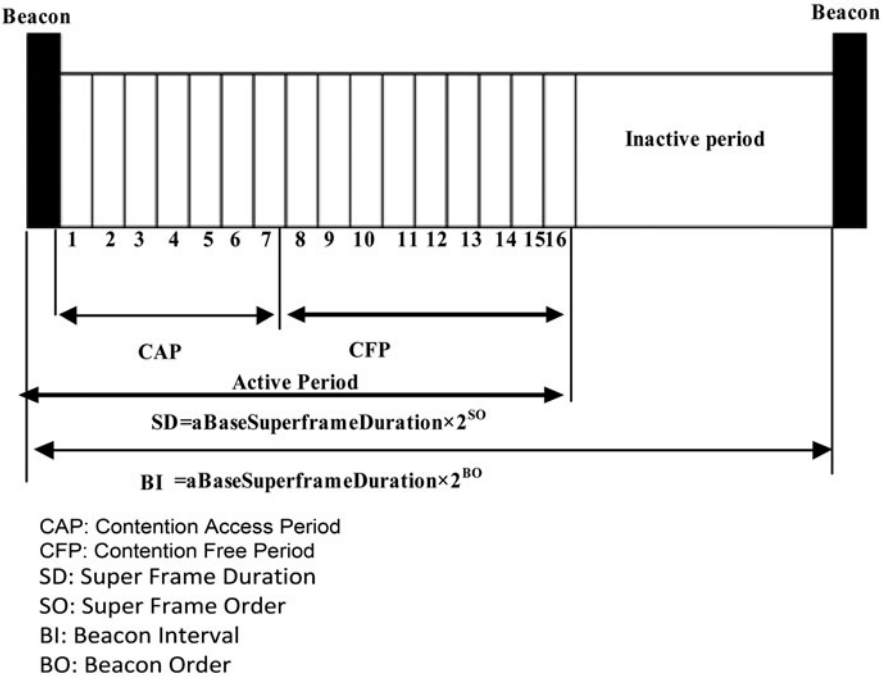

Fig. 3 The IEEE802.15.4a standard super frame structure

the inspiration for many UWB based MAC implementations that can be found in the literature.

The main application of IEEE802.15.4a is for low data rate UWB applications and ranging applications. Similar to the IEEE802.15.6 standard, the IEEE802.15.4a standard also uses a beacon-enabled super frame structure for UWB PHY layer communication. The maximum number of time slots is limited to 16. The super frame is divided into a contention access period (CAP) and a contention free period (CFP). The CAP supports random access using ALOHA, whereas the CFP offers guaranteed time slots (GTS) for high-priority data traffic. The IEEE802.15.4a standard super frame structure is shown in Fig. 3.

The performance of the IEEE802.15.4a standard for WBAN applications has been intensively studied in [24] and [25]. MAC layer for IEEE802.15.4a standard is almost identical to that of IEEE802.15.4. The main difference is that mandatory channel access mechanism is changed to ALOHA or slotted ALOHA rather than CSMA/CA. This amendment is necessary as it is difficult to perform CCA on the low-power UWB signal.

In [24], the delay performance of the IEEE802.15.4a standard for WBAN applications is evaluated on the basis of two categories of physiological signals: continuous and routine signals. Physiological data such as electrocardiography and electroencephalography require continuous monitoring, hence they are considered

as continuous signals. The routine signals include body temperature and blood pressure, which are monitored periodically. The time delay is analyzed on the basis of performance of ALOHA and slotted ALOHA channel access mechanisms on these two types of signals. The results show that the worst-case delay performance for slotted ALOHA is better than that for the ALOHA when continuous signal data is transmitted. The performance further improves for slotted Aloha when the number of GTS increases. The results show that when the number of GTS for slotted ALOHA is increased from 7 to 12, worst-case delay drops from 75 to 25 ms. However, ALOHA has better delay performance as compared with slotted ALOHA for routine data. The results also show that the performance of slotted ALOHA degrades for routine signal as the number of GTS increases. In terms of delay, slotted ALOHA performs better for continuous signal monitoring, but not for routine signal monitoring.

Bit error rate (BER) analysis for on-body WBAN sensor nodes that communicate using IEEE802.15.4a is analyzed in [25]. The results show that the BER increases significantly as the number of on-body sensor nodes increases. The analysis shows that in order to maintain an acceptable BER of 10^{-3}, the maximum number of attached on-body sensor nodes has to be limited to six. The analysis is carried out on the basis of a single user scenario where all the sensor nodes are attached to a single patient. The performance of the WBAN system will significantly degrade if there are other users in the same vicinity.

Drawbacks: The IEEE 802.15.4a standard has similar drawbacks as the IEEE802.15.6 standard, such as the use of a UWB receiver at the sensor nodes and disregarding the dynamic power control achievable through UWB physical layer manipulations. Also, it does not support high data rate communication, hence restricts the extraction of the benefits provided by the UWB communications.

Preamble Sense Multiple Access-Based MAC

The work presented in [26] and [27] analyzes the performance of an IR-UWB MAC protocol for medical data monitoring in terms throughput and the power consumption. It presents a MAC protocol based on a medium access protocol called preamble sense multiple access (PSMA), where the WBAN sensor nodes sense a preamble in order to detect a busy channel or an idle channel condition. Every sensor node attaches a preamble sequence at the beginning of a data packet. The presence of this preamble code in the channel indicates a busy channel condition. The objective of using a preamble sequence is to minimize the false alarms and miss detections that can occur in traditional energy- or feature-based CCA methods [28].

The suggested MAC protocols in [26] and [27] also uses a beacon-enabled super frame structure inspired by the IEEE802.15.4a standard. The operation of the proposed medium access method is depicted in Fig. 4.

The throughput and energy consumption analysis presented in [26] compares the performance of the PSMA-based MAC with the slotted ALOHA-based

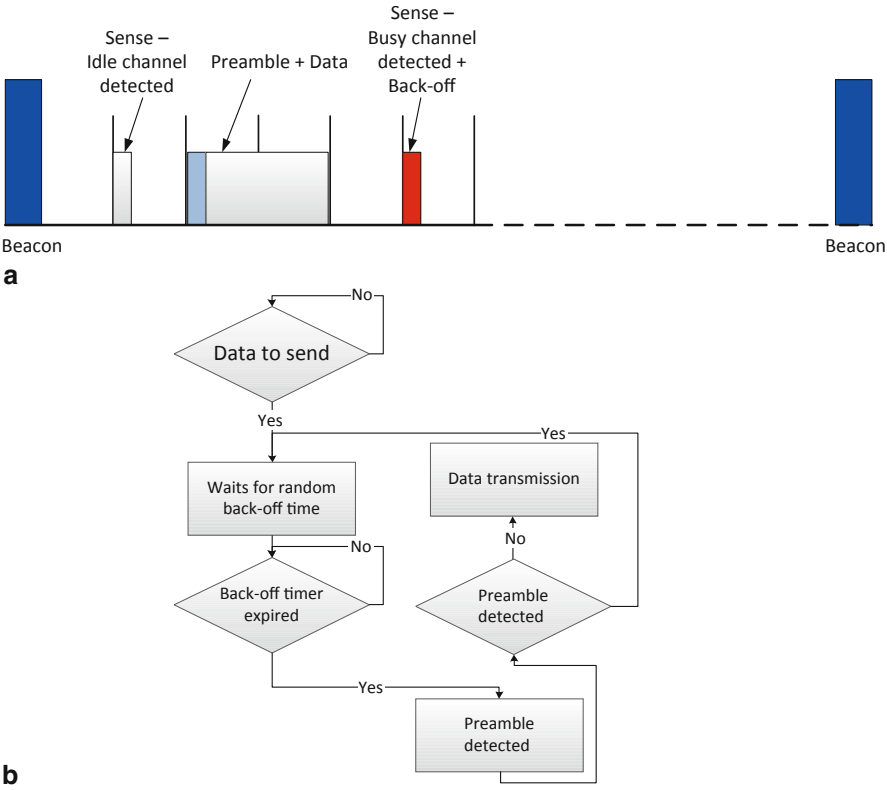

Fig. 4 Preamble sense multiple access (PSMA)-based medium access proposed in [26]. **a** Data transmission using a super frame structure. **b** Channel access mechanism

IEEE802.15.4a standard. The comparison shows that the suggested MAC protocol performs better in terms of throughput and energy consumption for WBANs consisting of large number of sensor nodes.

Drawbacks: The major drawback of this MAC protocol is that it assumes the presence of an IR-UWB-based receiver at the sensor node end in order to sense the channel using PSMA mechanism. Hence, it ignores all the complexities that involve in using an IR-UWB receiver at a WBAN sensor node that are mentioned above. It also does not provide a solution for the case where two or more sensor nodes perform preamble sense simultaneously, which leads to an eminent collision scenario.

MAC Protocol Based on Exclusion Regions

A MAC protocol developed based on transmit and receive antenna patterns and the antenna directionality is proposed in [29]. An exclusion region (ER) is defined as an area surrounding a receiver such that the transmitter sensor nodes within the

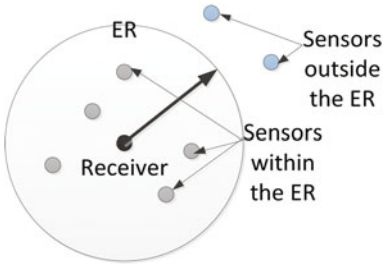

Fig. 5 Exclusion region (ER)-based ultra-wideband (UWB) communication

ER cause interference to each other. However, the transmitter sensor nodes that are not located inside an ER do not cause interference at the targeted receiver. In this MAC protocol, the data communication of sensor nodes within the same ER is resolved temporally using time hopping (TH)-codes, whereas the sensor nodes in different ERs are allowed to transmit data concurrently. All the sensor nodes transmit data asynchronously. The main objective of this MAC protocol is to minimize the interference that can occur in a multiple UWB transmission environment, while optimizing the throughput using concurrent transmissions in mutually exclusive ERs. Figure 5 depicts the sensor communication using the ERs.

Drawbacks: Although this MAC protocol addresses the issue of interference mitigation in UWB multiple access, it does not investigate the efficiency of important factors such as pulse synchronization and multiple access for sensor nodes within the same ER. It also assumes that a sensor node can determine whether it is within the range of a certain ER by accurate ranging capabilities.

Uncoordinated Wireless Baseborn Access for UWB Networks (UWB^2)

The uncoordinated wireless baseborn access for UWB networks (UWB^2) protocol [30, 31] utilizes orthogonal TH-codes in order to achieve multiple access in a shared medium. In this protocol each node is identified using a unique TH-code that is generated using the method provided in [32]. A common TH-code is used in order to communicate control messages and sensor initialization.

At initialization, a sensor node sends a link establishment (LE) frame shown in Fig. 6a, using the common TH-code. In this LE frame, the sensor node proposes a TH-code to be used for communication between the sensor and the coordinator. The coordinator node then replies with a link control (LC) message and listens to the TH-code allocated for the sensor node. The sensor initialization is followed by the data communication using the suggested TH-code and the data frame format shown in Fig. 6b. The UWB^2 MAC protocol supports both acknowledged and unacknowledged data communication. The main advantage of this MAC protocol is that it has avoided the requirement for CCA by using orthogonal TH-codes. Although

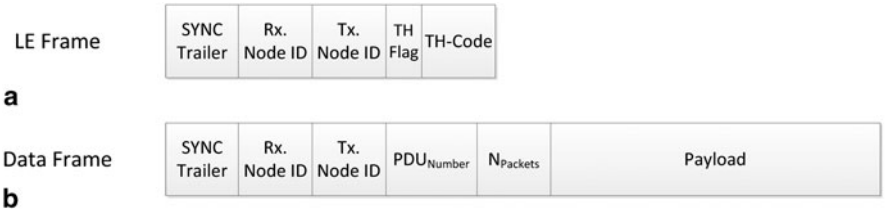

Fig. 6 **a** Link establishment (LE) frame format used for sensor initialization. **b** Data frame format

this MAC protocol assumes the use of a UWB receiver at the sensor node end in order to receive LC messages from the coordinator, a considerable energy saving can be achieved by avoiding the CCA. Reduced energy consumption makes it more suitable for WBAN applications.

Drawbacks: The suggested MAC protocol does not provide a method to re-initialize the data transmission in the case of a lost LC frame. In the case of a lost LC frame, the data transmission from the sensor nodes can be inhibited permanently. Also, collisions can occur while using the common TH-code for control messages. The MAC protocol does not suggest a method to avoid or minimize such collisions.

U-MAC

The U-MAC protocol described in [33] suggests the use of an adaptable pro-active approach for UWB MAC design instead of a re-active approach. It suggests the dynamic allocation of transmit power and data rate at the UWB sensor nodes using *hello* messages that are used by the sensor nodes in order to advertise their local state. These messages are sent at a fixed power level that is known to all the sensor nodes. At the reception of a *hello* message, a sensor node can determine the ranging information of the neighbouring sensor nodes. This information can be used to dynamically adjust the transmit power levels of the senor nodes. This MAC protocol suggests a more sensor centric network organization approach compared with the coordinator centric approach used in other UWB-based MAC protocols. This MAC protocol also supports a prioritized delivery mechanism depending on the quality of sensor (QoS) requirement of the sensor data. Similar to the UWB^2 protocol, U-MAC also uses unique TH-codes in order to provide multiple access to the shared medium, while control messages are sent using a common TH-code. Figure 7 demonstrates the sensor initialization procedure suggested in the MAC protocol.

On the reception of a ready-to- send (RTS) message, the neighbouring sensor nodes will determine whether the new sensor node is transmitting at an admissible data rate and transmit power criteria that are determined by the interference level and SNR at the neighbouring node. A not-clear-to-send (NCTS) message will be sent if a neighbouring sensor node or a coordinator node disagrees with the parameters

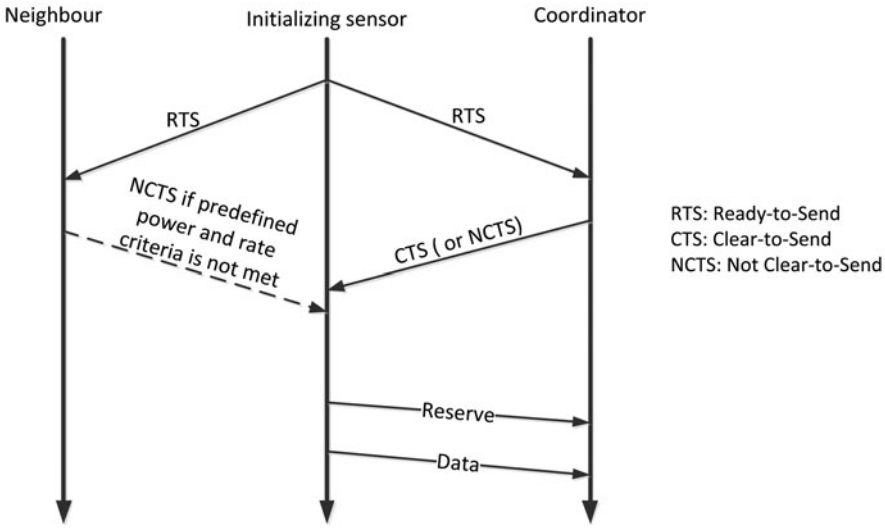

Fig. 7 Sensor initialization in U-MAC

of the new sensor. The reception of a NCTS means that the new sensor node has to reduce its transmitting power or the data rate. If the new sensor parameters are admissible, the coordinator node will reply with a clear-to-send (CTS) message while the neighbouring sensor nodes refrain from sending any messages. The data transmission occurs after the initialization. The link parameters can be dynamically adjusted during the data transmission using the *hello* messages according to the requirement of the sensor nodes.

Drawbacks: While this MAC protocol allows more dynamic usage of the UWB channel resources, it allocates significant processing load to the sensor nodes. In the context of WBANs, it is advisable to minimize the processing at the sensor node end in order to reduce the power consumption. Similar to the UWB^2 MAC protocol, the U-MAC uses a UWB receiver at the sensor node end in order to receive *hello* messages and other control messages, which leads into increased power consumption and complex hardware implementation.

Dynamic Channel Coding-MAC

The DCC-MAC presented in [34] and [35] uses dynamic channel coding (DCC) in order to mitigate the multiple access interference. This MAC protocol assumes that all the sensor nodes transmit at maximum allowable transmit power in contrast to the power control mechanisms used in Sects. “Preamble Sense Multiple Access-Based MAC” and “U-MAC”. A cross layer technique is suggested in this MAC protocol in

order to mitigate the multiple access interference at the PHY layer level. The received UWB pulse amplitude is compared against a predefined threshold at the coordinator end. Since all the sensor nodes transmit using a predefined transmit power, the expected receive power for a particular sensor node can be determined by the coordinator using UWB ranging techniques. If received pulse amplitude exceeds the threshold level, it indicates a collision at the coordinator. This concept is used in the DCC-MAC in order to identify and eliminate erroneous data at the coordinator end.

Rate-compatible punctured convolution (RCPC) [34] codes are used in order to achieve dynamic channel coding. The multiple access to the shared medium is achieved through TH-codes as in the case of UWB^2 and U-MAC. The TH-codes are generated locally at the sensor node using a random number generator.

Drawbacks: This MAC protocol has the same drawbacks as UWB^2 and U-MAC when it comes to the use of a UWB receiver at the sensor node end. Additionally, it tries to mitigate the interference at the expense of physical layer complexity. Also, an extensive amount of processing is allocated to the sensor nodes, which leads into increased power consumption. It also assumes that the sensor nodes always transmit at the maximum allowable transmit power. Although this has some advantages when it comes to interference mitigation and optimizing the throughput [36], a power-controlling approach might be well suited for power-stringent WBAN applications of UWB. It also assumes the presence of resynchronization per every data packet, which results in increased overhead. Instead, synchronization per session is recommended for WBAN applications.

Multiband MAC for IR-UWB

Multiple access through the allocation of a unique frequency band per each sensor-coordinator data communication link is suggested in [37]. A common control channel, which is assigned with a unique frequency band, is used for sensor initialization and control message transfer in this MAC protocol. Both control and data communication bands are allocated with a 500 MHz bandwidth. TH-codes are used in the common control channel in order to share it with multiple users. The main advantage of this MAC protocol is that it can be used for concurrent data transmissions from multiple numbers of sensor nodes, because of the use of different frequency bands. This assists in reducing the probability of collision, hence increases the throughput and results in low latencies that are ideal properties for high data rate WBAN applications.

A super frame structure is used for data and control message transfer. A super frame is divided into 15 sequence frames. Each sequence is used for data transmission in each band. An *availability frame* is used between two super frames in order to indicate the availability of a particular band for data transmissions. If a sensor node intends to continue data transmission in a particular band, it has to send consecutive UWB pulses in the relevant slot allocated to indicate the occupancy of that frequency band.

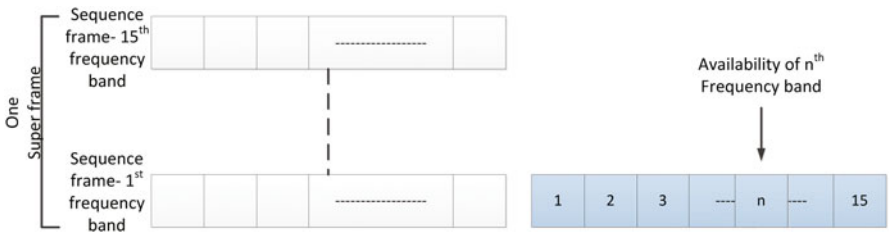

Fig. 8 Super frame structure used in multiband MAC

By sensing those UWB pulses within the corresponding time slots of the *availability frame*, other sensor nodes can determine the availability or occupancy of a particular band for data transmission. This super frame structure is shown in Fig. 8.

Drawbacks: This MAC protocol requires the sensor nodes to operate in multiple frequency modes in order to access different frequency bands. This method increases the hardware complexity of the sensor nodes, which is disadvantageous in WBAN applications. Also, it adds the complexity of modulating the data signals into TH-codes in order to access the common control channel. The sensor nodes have to sense the narrow UWB pulses during the *availability frame.* This implies the use of a UWB receiver at the sensor node and of energy consuming pulse sensing procedures. The authors also have not specified how the node synchronization is achieved in this MAC protocol.

PULSERS

The PULSERS project [38] uses an altered format of the IEEE802.15.4a standard super frame structure in order to provide high guarantee of delivery for sensor nodes with high QoS requirements. It uses an extended CFP that facilitates GTS for priority traffic in the IEEE802.15.4a standard. The CAP is limited to two time slots, where initialization messages and control messages are exchanged. When a sensor node wants to transmit data, it requests the allocation of a GTS in the CFP in the next super frame using the one of the time slots available in CAP. Hence, this MAC protocol follows a time division multiple access (TDMA)-based approach in providing multiple access to the shared UWB channel.

This MAC protocol is well suited for WBAN applications with high data rate requirements. It also proposes a peer-to-peer relay mechanism using a static routing table, which is known to all the sensor nodes during the initialization. This mechanism helps in decentralizing the control of the network, hence reduces the latency. The sensor nodes can be put into inactive mode in between the data transmission slots used in the MAC protocol; hence the power consumption can be reduced.

Drawbacks: This MAC protocol possesses all the drawbacks in the IEEE802.15.4a standard MAC protocol when it comes to WBAN applications. The TDMA-based multiple-access mechanism relies on precise synchronization in timing. However, a synchronization mechanism has not been proposed for the MAC protocol.

Transmit-Only MAC

Most of the MAC protocols discussed above have limitations when it comes to UWB-based WBAN applications. Authors have not paid attention towards the practical constraints that occur in hardware design. Although IR-UWB transmitters consume low power, IR-UWB receiver needs to detect pulses with low power level. This leads to a complex and high power-consuming receiver architecture. For example, the CMOS IR-UWB transmitter discussed in [39] has a power consumption of 2 mW, whereas the IR-UWB receivers consumes up to 32 mW of power [40]. Addition of an IR-UWB receiver in the sensor node will increase its power consumption as well as the design complexity. Implantable or wearable sensor nodes are battery powered. Hence, power consumption in sensor nodes is a critical factor that determines the efficiency of a MAC protocol. The transmit-only MAC protocol suggested in [17] and [21] enables the use of a transmit-only hardware design at the sensor node end.

The suggested transmit-only MAC protocol is of asynchronous nature; hence, it faces several challenges when it comes to collision avoidance and synchronization at the receiver end. It has been designed with following characteristics in order to overcome the challenges:

- Gateway nodes are designed in a way that it is possible to self-synchronize using the received UWB pulses
- Data packets are transmitted at a much higher data rate than the required data rate, so it is possible to get an optimum sleep time for the sensor nodes while it waits for the next set of data
- Each sensor transmits at a pre-allocated unique transmission slot in order to minimize the occurrence of collisions
- A unique pulse rate is assigned for each WBAN in the same region
- Sensor nodes transmit without prior knowledge of the channel condition
- There is no feedback in the network

The frame structure for this WBAN system is shown in Fig. 9.

When a sensor node is first connected to the network, synchronizing frame structure is used in order to assist the self-synchronization at the gateway node end. A guard interval follows immediately after the initial synchronization process to allow the receiver to prepare for the reception of information in the PHR. The PHR contains information on the chirp rate, symbol rate and the timing of the next transmission window. After establishing initial communication with the gateway node, the data frame will be used in the successive transmissions. The data frame has a short preamble, which helps the receiver achieve fine synchronization followed by a

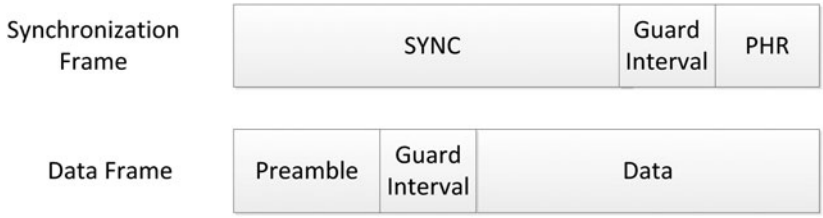

Fig. 9 Frame structure for transmit-only MAC protocol for wireless body area network (WBAN)

guard interval to prepare the receiver for data reception. The data frame overhead is kept to a minimum in order to keep the transmission period short, thus reducing the chances of collision.

Drawbacks: Although the transmit-only MAC protocol addresses the problem of high power consumption that arises because of the use of UWB receiver at the WBAN sensor node, it has several drawbacks.

- When the network traffic increases, the number of collisions that occur owing to asynchronous transmission of pulses adversely affect the data delivery capability in the network.
- There is no feedback path to dynamically adjust the transmit power in accordance with the changing channel conditions.
- Rescheduling of the network requires manual intervention with the sensor nodes.

This MAC protocol can be further improved by the use of a narrowband receiver in order to eliminate the issues regarding the network reconfigurations and network expansion while achieving low power consumption in the sensor nodes. Such a MAC protocol is suggested in [41]. The MAC protocol described in [41] uses a narrowband receiver at the sensor node to receive feedback on properties, such as receive BER.

Comparison of UWB-Based MAC Protocols for WBAN Applications

The MAC protocols discussed above have advantages in different areas when they are used in WBAN applications. A summary of the selected MAC schemes discussed in this section is tabulated in Table 2 on the basis of their performance attributes described below.

- *Energy efficiency*—Factors affecting the energy efficiency of a MAC scheme are energy wastage owing to protocol overhead, idle listening, collisions, overemitting and overhearing.
- *QoS*—QoS is crucial in a WBAN system because of the sensitivity of the data collected by sensor nodes. If the QoS is poor and the data reliability is low, this could lead to a wrong diagnosis and it can be life threatening.

Table 2 Comparison of the medium access control (MAC) protocols

Performance attribute	IEEE 802.15.6	IEEE 802.15.4	PSMA-based MAC	ER-based MAC	UWB^2	U-MAC	DCC-MAC	Multiband MAC	PULSERS	Transmit-only MAC	UWB-Tx and NB-Rx MAC
Energy efficiency	×	×	×	×	✓	✓	×	×	×	✓	✓
QoS	✓	×	×	×	×	✓	×	×	✓	×	✓
Priority traffic	✓	✓	✓	×	×	×	×	×	✓	×	✓
Scalability	✓	×	×	✓	×	✓	×	×	×	✓	✓
Latency	×	×	×	✓	×	×	×	✓	×	✓	×
Interference mitigation	×	×	✓	✓	✓	✓	✓	✓	×	×	✓
Channel access	Random—ALOHA	Random—ALOHA	Random—PSMA	TH-code with spatial reuse	TH-code	TH-code with power management	TH-code	Frequency division	Time division	Random—rate division	Random + TDMA

PSMA preamble sense multiple access, *ER* exclusion region, *UWB*^{2} uncoordinated wireless baseborn access for UWB networks, *DCC-MAC* dynamic channel coding-medium access control, *TH* time hopping, *TDMA* time division multiple access, *NB* Narrow Band

- *Priority traffic*—In a WBAN system, the MAC should be able to support on-demand traffic and provide a method for critical data to be transmitted reliably with minimum latency.
- *Scalability*—Data rates for WBAN range from a few kilobytes to tens of megabytes. The number of nodes in a WBAN system can vary from a single node to tens of nodes. Therefore, scalability is an important factor to be considered in a WBAN MAC scheme.
- *Latency*—WBAN contains time critical data, therefore latency is another important factor to be considered in a WBAN MAC protocol.
- *Interference mitigation*—As the WBAN nodes are mobile, the channel condition is constantly changing. The channel condition deteriorates significantly in areas densely populated with other WBAN users. The MAC scheme should be resilient to multiple network interference.
- *Channel access*—A WBAN constitutes of both implantable and on-body nodes. When selecting a channel access scheme, type of the nodes and the physical layer characteristics should be taken into consideration in order to ensure the reliability of the system.

Conclusion

Low power consumption and reliable operation are the two of the utmost important considerations when developing a WBAN system. In order to develop a platform to satisfy these two requirements, a cross-layer solution that involves both the PHY and MAC layer is required. The IEEE 802.15.6 standard is recently released in order to standardize the WBAN communication. Although the IEEE802.15.6 standard provides a good platform for WBAN applications, it lacks some critical properties when it comes to using the unique feature of the UWB signals for WBAN applications. The IEEE 802.15.4a MAC is commonly used as a reference scheme for developing new MAC protocols for UWB-based WBAN application and as a baseline indicator for performance comparison. Power saving is achieved in a MAC protocol by reducing the need for retransmission and overhearing. A MAC protocol can be used to overcome the hardware limitation of a WBAN platform. For example, the power consumption of a UWB-based WBAN platform can be significantly reduced by using a MAC scheme that minimizes the use of the receiver. Except for the transmit-only MAC, all the other MAC protocols have ignored the complexity that arises by using a UWB receiver at a power critical WBAN sensor node. Although the transmit-only MAC avoids this by using a transmit-only mechanism, it lacks the ability to dynamically adjust the sensor nodes according to the changing network conditions. The use of a simple narrowband receiver instead of an UWB receiver will avoid most of these problems; however, the MAC protocols have to be adjusted in order to achieve optimized data communication using this method.

In conclusion, this chapter has highlighted the requirement and characteristic of UWB-based WBANs. A comparison of the various wireless schemes and MAC protocols for UWB-based WBAN applications is presented.

References

1. M.R. Yuce, J. Khan, *Wireless Body Area Networks: Technology, Implementation and Applications* (Pan Stanford Publishing, Singapore, 2011) (ISBN 978-981-431-6712)
2. M.R. Yuce, Implementation of wireless body area networks for healthcare systems. Sensor Actuat. A-Phys. **162**, 116–129 (2010)
3. K. Takizawa, L. Huan-Bang, K. Hamaguchi, R. Kohno, Wireless patient monitoring using IEEE802.15.4a WPAN. IEEE International Conference on Ultra-Wideband. pp. 235–240 (2007)
4. FCC 02–48 (First Report and Order) (2002)
5. M.R. Yuce, H.C. Keong, M. Chae, Wideband communication for implantable and wearable systems. IEEE Trans. Microwave Theory Tech. **57**, 2597–2604 (2009) (Part 2)
6. H.C. Keong, M.R. Yuce, Low data rate ultra wideband ECG monitoring system. Proceedings of the 30th Annual International Conference of the IEEE Engineering in Medicine and Biology Society (IEEE EMBC08), pp. 3413–3416 (August 2008).
7. A. Tekin, M.R. Yuce, W. Liu, Integrated VCO Design for MICS Transceivers. Proceedings. IEEE Custom Integrated Circuits Conference (CICC'06), pp. 765–768 (Sept 2006)
8. Y. Park, D.D. Wentzloff, An all-digital 12 pJ/Pulse IR-UWB transmitter synthesized from a standard cell library. IEEE J. Solid-State Circuits **46**(5), 1147–1157 (2011)
9. A.C.W. Wong, M. Dawkins, G. Devita, N. Kasparidis, A. Katsiamis, O. King, F. Lauria, J. Schiff, A.J. Burdett, A 1 V 5 mA multimode IEEE 802.15.6/bluetooth low-energy WBAN transceiver for biotelemetry applications. IEEE J. Solid-State Circuits **48**(1), 186–198 (2013)
10. A. Gupta, P. Mohapatra, A survey on ultra wide band medium access control schemes. Comput. Netw. **51**(11), 2976–2993 (2007)
11. K. Okada, N. Li, K. Matsushita, K. Bunsen, R. Murakami, A. Musa, T. Sato, H. Asada, N. Takayama, S. Ito, W. Chaivipas, R. Minami, T. Yamaguchi, Y. Takeuchi, H. Yamagishi, M. Noda, A. Matsuzawa, A 60-GHz 16QAM/8PSK/QPSK/BPSK direct-conversion transceiver for IEEE802.15.3c. IEEE J. Solid-State Circuits **46**(12), 2988–3004 (2011)
12. Y. Gao, Y. Zheng, S. Diao, W. Toh, C. Ang, M. Je, C. Heng, Low-power ultrawideband wireless telemetry transceiver for medical sensor applications. IEEE Trans. Biomed. Eng. **58**(3), 768–772 (2011)
13. M.R. Yuce, T. Dissanayake, Easy-to-swallow wireless telemetry. IEEE Microwave Mag. **13**(6), 90–101 (2012)
14. M. Chae, Z. Yang, M.R. Yuce, L. Hoang, W. Liu, A 128-channel 6 mW wireless neural recording IC with spike feature extraction and UWB transmitter. IEEE Trans. Neural Syst. Rehab. Eng. **17**(4), 312–321 (2009)
15. Y. Zhao, L. Wang, J.-F. Frigon, C. Nerguizian, K. Wu, R.G. Bosisio, UWB positioning using six-port technology and a learning machine. IEEE Mediterranean Electrotechnical Conference, pp. 352–355 (16–19 May 2006)
16. G. Kail, K. Witrisal, F. Hlawatsch, Direction-resolved estimation of multipath parameters for UWB channels: A partially collapsed Gibbs sampler method. IEEE International Conference on Acoustics, Speech and Signal Processing, pp. 3484–3487 (22–27 May 2011)
17. H. C. Keong, K.M.S. Thotahewa, M.R. Yuce, Transmit-only ultra wide band body sensors and collision analysis. IEEE Sens. J. **13**(5), 1949–1958 (2013)
18. N.J. August, H.J. Lee, D.S. Ha, Enabling distributed medium access control for impulse-based ultrawideband radios. IEEE Trans. Veh. Technol. **56**, 1064–1075 (2007)
19. Z. Xiao, D. Jin, L. Su, L. Zeng, Performance superiority of IR-UWB over DS-UWB with finite-resolution matched-filter receivers. IEEE International Conference on Ultra-Wideband, pp. 1–4 (20–23 Sept 2010)
20. http://www.ieee802.org/15/pub/TG6.html. (2013)
21. H.C. Keong, M.R. Yuce, Analysis of a multi-access scheme and asynchronous transmit-only UWB for Wireless Body Area Networks. The 31st Annual International Conference of the IEEE Engineering in Medicine and Biology Society (EMBC'09), pp. 6906–6909 (2009)

22. R.J. Fontana, E.A. Richley, Observations on low data rate, short pulse UWB Systems. IEEE International Conference on Ultra-Wideband, pp. 334–338 (2007)
23. IEEE-802.15.4a-2007. Part 15.4: wireless medium access control (MAC) and physical layer (PHY) specifications for low-rate wireless personal area networks (LR-WPANs): amendment to add alternate PHY. Standard, IEEE
24. K. Takizawa, L. Huan-Bang, K. Hamaguchi, R. Kohno, Wireless patient monitoring using IEEE802.15.4a WPAN. IEEE International Conference on Ultra-Wideband, pp. 235–240 (2007)
25. D. Domenicali, M.G. Di Benedetto, Performance analysis for a body area network composed of IEEE 802.15.4a devices. 4th Workshop on Positioning, Navigation and Communication, pp. 273–276 (2007)
26. L. Kynsijarvi, L. Goratti, R. Tesi, J. Iinatti, M. Hamalainen, Design and performance of contention based MAC protocols in WBAN for medical ICT using IR-UWB. IEEE 21st International Symposium on Personal, Indoor and Mobile Radio Communications Workshops, pp.107–111 (26–30 Sept 2010)
27. J. Haapola, A. Rabbachin, L. Goratti, C. Pomalaza-Raez, I. Oppermann, Effect of impulse radio-ultrawideband based on energy collection on MAC protocol performance. IEEE Trans. Veh. Technol. **58**, 4491–4506 (2009)
28. B. Zhen, H.-B. Li, S. Hara, R. Kohno, Clear channel assessment in 2 medical environments. EURASIP J. Wireless Commun. Netw. **8**(3), 1–8 (2008)
29. L.X. Cai, X. Shen, J. Mark, Efficient MAC protocol for ultra-wideband networks. IEEE Commun. Mag. **47**(6), 179–185 (2009)
30. M.-G.D. Benedetto, L.D. Nardis, G. Giancola, D. Domenicali, The aloha access $(UWB)^2$ protocol revisited for IEEE 802.15.4a. ST J. Res. **4**(1), 131–141 (2006)
31. M.-G. D. Benedetto, L.D. Nardis, M. Junk, G. Giancola, $(UWB)^2$: Uncoordinated, wireless, baseborn medium access for UWB communication networks. Mobile Netw. Appl. **10**(5), 663–674 (2005)
32. M. Iacobucci, M.D. Benedetto, Computer method for pseudorandom codes generation. National Italian Patent RM2001A000592 (Sept 2001)
33. R. Jurdak, P. Baldi, C.V. Lopes, U-MAC: a proactive and adaptive UWB medium access control protocol. Wireless Commun. Mob. Com. **5**(5), 551–566 (2005)
34. R. Merz, J. Widmer, J.-Y.L. Boudec, B. Radunovíc, A joint PHY/MAC architecture for low-radiated power TH-UWB wireless ad hoc networks. Wireless Commun. Mob. Com. **5**(5), 567–580 (2005)
35. J.-Y.L. Boudec, R. Merz, B. Radunovic, J. Widmer, DCC-MAC: a decentralized MAC protocol for 802.15.4a-like UWB mobile ad-hoc networks based on dynamic channel coding. First International Conference on in Broadband Networks, pp. 396–405 (Oct 2004)
36. B. Radunovic, J.-Y.L. Boudec, Optimal power control, scheduling, and routing in UWB networks. IEEE J. Sel. Area Comm. **22**(7), 1252–1270 (2004)
37. I. Broustis, S.V. Krishnamurthy, M. Faloutsos, M. Molle, J.R. Foerster, Multiband media access control in impulse-based UWB ad hoc networks. IEEE Trans. Mobile Comput. **6**(4), 351–366 (2007)
38. I. Bucaille, A. Tonnerre, L. Ouvry, B. Denis, MAC layer design for UWB LDR systems: PULSERS proposal. 4th Workshop in Positioning, Navigation and Communication, pp. 277–283 (Mar 2007)
39. J. Ryckaert, C. Desset, A. Fort, M. Badaroglu, V. De Heyn, P. Wambacq, G. Van der Plas, S. Donnay, B. Van Poucke, B. Gyselinckx, Ultra-wide-band transmitter for low-power wireless body area networks: design and evaluation. IEEE Trans. Circuits Syst. **52**, 2515–2525 (2005)
40. G. Yuan, Z. Yuanjin, H. Chun-Huat, Low-power CMOS RF front-end for non-coherent IR-UWB receiver. European Solid-State Circuits Conference, pp. 386–389 (2008)
41. K.M. Silva, M.R. Yuce, J.Y. Khan, Network topologies for dual band (UWB—transmit and narrow band-receive) wireless body area network. Proceedings of the 4th International Conference on *Body Area* Networks (BodyNets) (7–8 Nov 2011)

Antenna Diversity Techniques for Enhanced Ultra-Wideband Body-Centric Wireless Networks in Healthcare

Qammer H. Abbasi, Akram Alomainy and Yang Hao

Abstract Achieving better system performance and receiving optimum communication link quality with minimum power consumption is the main drive behind the recent surge in interest in diversity-based techniques, whether it is from a spatial, frequency or polarisation perspective. In this chapter, studies for applicability of antenna diversity to be applied in ultra-wideband (UWB) on/off-body channel are carried out. Measurements are performed in both an anechoic chamber (no multi-path reflections) and in a typical indoor environment (dense multi-path surroundings) on a human candidate for various daily life activities including both static and dynamic cases. Various diversity techniques are applied to highlight the benefit of incorporating such methods in enhancing the overall system performance by increasing the reliability of the link and hence, successful reception rate.

Keywords Body-centric wireless network · UWB channel · Diversity · UWB on/off-body diversity · On-body diversity radio channel · UWB antenna · Diversity combining · On-body position

Introduction to Diversity for Body-Centric Wireless Network

Body-centric wireless networks (BCWNs) mainly experience fading due to the following: relative movements of body parts, polarisation mismatch, shadowing and diffraction and scattering from the body parts and surrounding environments [1]. Diversity is a powerful technique to combat fading and multi-path effects [2]. The spatial diversity does not need any additional spectrum and, also, the UWB is inherently a frequency diversity technology. This makes the spatial arrangement of multiple

A. Alomainy (✉) · Q. H. Abbasi · Y. Hao
Antenna & Electromagnetics Research Group,
School of Electronic Engineering and Computer Science,
Queen Mary, University of London, Mile End Road,
E1 4NS London, United Kingdom
e-mail: akram.alomainy@eecs.qmul.ac.uk

Q. H. Abbasi
University of Engineering & Technology, Lahore, KSK, Pakistan

M. R. Yuce (ed.), *Ultra-Wideband and 60 GHz Communications for Biomedical Applications,* DOI 10.1007/978-1-4614-8896-5_8,

antennas a promising technique to enhance the performance of UWB BCWNs [3]. There has been an increasing interest in diversity and multiple-input, multiple-output (MIMO) techniques for enhanced mobile and wireless communications in recent years [4–8]. There are some studies presented in the open literature where the benefits of diversity techniques for body-centric communications in narrow-band systems have been investigated [1, 3, 9–17]. The effect of human body, especially the head and the hand, on the performance of diversity antenna at the mobile handset was discussed in [9] by presenting the change in diversity gain (DG) and envelope correlation with angle of inclination of the antenna and its distance from the head. Introductory studies for on-body diversity measurements at 2.45 GHz were presented in [10].

The diversity performances were evaluated in terms of DG, power imbalance and envelope correlation coefficients between the two receiving channels. A comprehensive study of diversity for an on-body channel at 2.45 GHz was presented in [1], using different antennas and diversity types. A significant gain was observed for non-line of sight (NLOS) channels and dynamic channels involving large body movements. The uplink and downlink diversities were also calculated and found to be similar. A comparison of spatial and pattern diversity was presented in [11]. It was observed that spatial diversity gave a greater improvement than pattern diversity, in terms of DG. Cotton and Scanlon [13, 14] have presented first- and second-order statistics and some diversity results for off-body and on-body channels, at 2.45 GHz and 868 MHz, respectively. On-body diversity at 868 MHz has been thoroughly investigated in [14], with application to medical implants. Off-body spatial diversity and correlation coefficient evaluation was performed in [15, 16] at 868 MHz and 5.8 GHz respectively. Diversity performance using textile antennas for fire-fighters was presented in [17].

Other studies on UWB-MIMO and UWB diversity were presented in [18–27]. Antenna diversity results for the UWB indoor channel are presented in [21], with an emphasis on differences between virtual and real compact arrays, including mutual coupling effects. UWB-MIMO for on-body has been investigated in [19], using frequency space polarisation. The key findings in [19] were that, in BCWN, the MIMO channel capacity is mainly determined by the power imbalance for both spatial arrays and polar arrays. It was also found that the MIMO capacity decreases with the frequency. Roy et al. presented an innovative space–time spatial model for UWB multi-sensor, multi-antenna body area networks (BANs) in [27]. However, to the authors' knowledge, UWB spatial diversity for on/off-body communications has not yet been investigated systematically and thoroughly. In this study, the spatial diversity is investigated for UWB on/off-body communication channels. The improvement due to diversity is often measured in terms of DG; this is basically an improvement in signal strength (or, equivalently, signal-to-noise ratio or bit-error rate) compared with that observed with a single antenna at a certain outage probability [1, 2, 4, 7, 8]. The outage probability is the probability that the system performance falls below a minimum performance threshold (typically defined in terms of signal-to-noise ratio) within a specified time period.

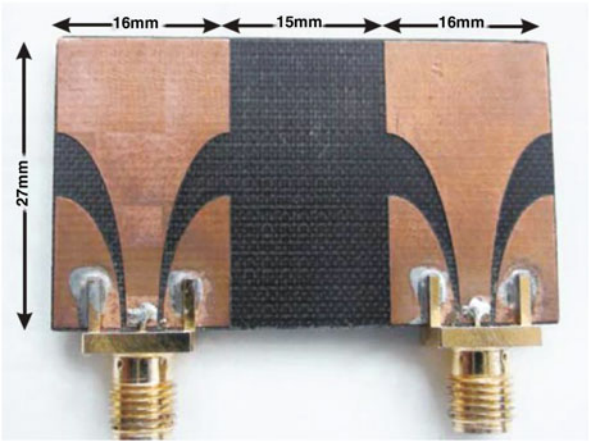

Fig. 1 Two-branch ultra-wideband (UWB) tapered slot antenna (TSA) used in the experimental investigation of spatial diversity for on/off-body radio propagation channels

Measurement Setup for Ultra-Wideband On/Off-Body Diversity

For UWB on/off-body antenna diversity measurements, a two-branch tapered slot antenna (TSA) was used as shown in Fig. 1. The spacing between the two elements shown in Fig. 1 is $0.34\lambda_0$ to keep the mutual coupling well below -15 dB. Diversity antennas with different spacings are fabricated and are used during measurements. A detailed discussion on mutual coupling is presented later in this chapter. For UWB on/off-body diversity channel measurements, an Agilent four-port PNA-X (programmable vector network analyzer), model number N5244A, was used to capture the frequency response of the two diversity branches, as shown in Fig. 2. A single TSA was used as the transmitter (Tx) antenna (connected to port 2 of PNA), while a two-branch diversity TSA antenna, with various spacings, was used for the receiver (Rx) antenna connected to port 1 and port 3 of PNA (as shown in Fig. 2). The PNA was remotely controlled by computer software written in Labview^{TM} version 8.5. The data measured by the PNA was stored in the computer hard disk by the Labview^{TM} software in the form of a.s4p files containing the magnitude (in dB) and phase (in degrees) of all transmission responses. During the measurements, the PNA was always calibrated to exclude the losses that incurred in the cables and thus, the measured data reflects the signal measured at the ports of the antenna. The calibration also ensured that a total power of 0 dBm is transmitted by the transmitting antenna. The PNA was set to capture 3,201 data samples, with a sampling time of 6.6 ms. The sampling time was carefully chosen to capture all variations made by any fast movements of the human subject and to keep the sampling frequency higher (at least double) than the resulting Doppler shift. The Doppler shift is discussed later, in this chapter. The sampling time of 6.6 ms (sampling frequency of 150 Hz) was selected to ensure that all the variations caused by the movement of the body were captured, by making the sampling frequency more than twice the maximum body Doppler shift. The maximum Doppler shift was calculated assuming relative speed of motion

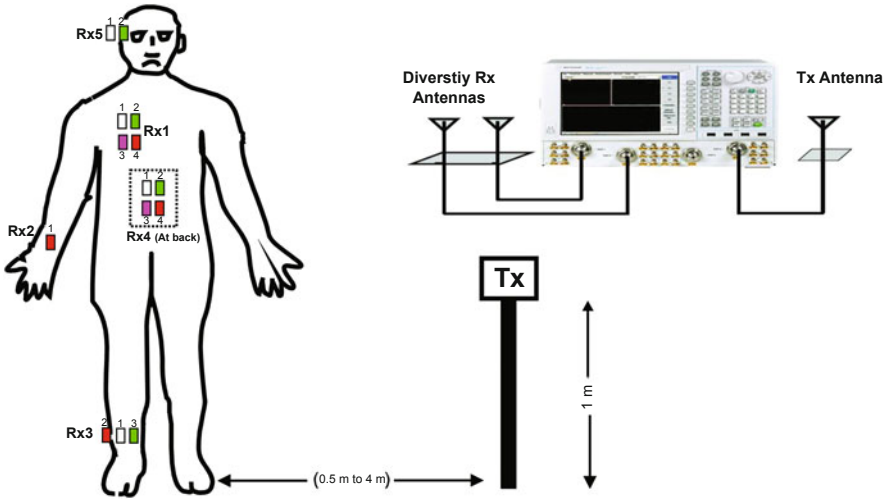

Fig. 2 Measurement setup for ultra-wideband (UWB) on-body and off-body diversity (whereas, for on-body case, transmitter (Tx) was placed at left side of waist instead of away from body as shown here)

of the antennas up to 3 m/s during the movements. These give shifts of about 23.25 Hz with average speed of motion of 1 m/s and about 69.76 Hz with 3 m/s. The noise floor for the measurement was at − 90 dBm.

For on-body case, the position of Tx was fixed at the left side of the waist (belt). The receiving antenna was placed at five different positions: on the right chest (Rx1), right wrist (Rx2), right ankle (Rx3), on the centre of the back (Rx4) and on the right side of the head (Rx5), as shown in Fig. 2. For off-body case, the access point (AP) was fixed at waist height (1 m above the ground). The receiving antenna was placed at same five positions, as for on-body diversity. The distance between the subject carrying diversity branch receivers and AP is varied from 0.5 to 4 m (Tx and Rx locations are as shown in Fig. 2). A number of measurements were made for each Rx position (as shown in Fig. 2), to check the reliability of the measurements with respect to slight variations in the position of the antenna on the body; this was achieved by using a small grid, so that the variation was controlled. Measurements were repeated in three different locations in the indoor environment (denoted in Fig. 3 as Loc. 1, Loc. 4 and Loc. 7, respectively) to highlight the effects of varying multi-path environments on the diversity measurements and results for on-body diversity. For off-body case, measurements were repeated in eight different locations in an indoor environment, each with a step of 0.5 m (denoted in Fig. 3 as Loc. 1 to Loc. 8 respectively). This was done to highlight the effect of varying multi-path environments and the distance between the off-body AP and the human body carrying diversity antennas, on the diversity measurements and results. Measurements for uplink (from Tx on the waist/off-body AP to diversity antenna (Rx) on different locations of the human body) and downlink (from diversity antenna on the waist/off-body AP to Tx antenna on the

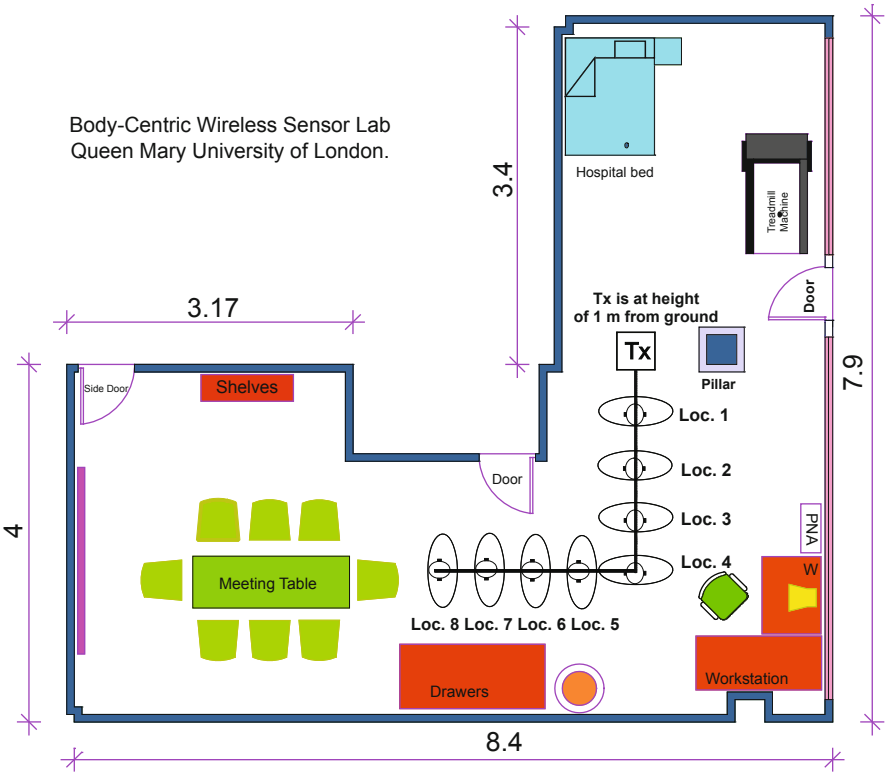

Fig. 3 Indoor environment showing different locations of human subject for on/off-body diversity measurements (access point was at waist height (1 m above ground) for off-body case). *The sensor lab height is 3 m*

different locations of the human body) diversity were also carried out. Moreover, the repeatability of the measurements with respect to time was investigated by repeating the measurement procedures on different days. During the UWB on-body diversity channel characterisation, a variety of daily life movements were included for each channel.

Five sweeps were carried out, thus a total of 16,005 data points were considered during each channel measurement. Measurements were performed in a controlled indoor environment (i.e. not in the real environment) on time-varying human body channel, when the surrounding environment was completely static. Measurements were taken during the evening in the Body-Centric Wireless Sensor Lab at Queen Mary, University of London (Fig. 3), to avoid any variations in the surrounding environment due to moving people. The goal was to investigate the potential improvement achieved by using diversity for BCWN.

Diversity Technique Analysis

Doppler Shift

In mobile communications, a Doppler shift in the signal frequency occurs due to the relative speed of motion between the transmitter and receiver; this is also true for the on-body case.

In order to capture all movements made by the human body during measurements, the sampling frequency of the measurement should be greater than twice the maximum expected Doppler shift. This shift is calculated for all channels using Eq. 1, as given in [28]:

$$f_{\mathrm{m}} = \frac{v}{\lambda_0} \tag{1}$$

where v is the velocity of motion of the human body in metres per second and λ_0 is the wavelength in metres. For the UWB band (3.1–10.6 GHz), with a centre frequency of 6.85 GHz, $f_{\mathrm{m}} = 22.83$ Hz for an average speed of 1 m/s and $f_{\mathrm{m}} = 68.5$ Hz for a speed of 3 m/s. The maximum Doppler shift is observed for the waist-to-wrist channel, compared to the other channels. During measurements, the sampling time was set to 6.6 ms on the PNA, to capture even the fastest movement of 3 m/s by keeping the sampling frequency equal to 150 Hz, which is greater than twice the maximum expected Doppler shift (i.e. 68.5 Hz).

Envelope Correlation Coefficients

For a diversity scheme to be effective, each antenna element should receive statistically independent versions of the transmitted signal reducing the likelihood that all branches are experiencing correlated fading. Two signals are said to be suitably uncorrelated if their correlation is less than 0.7 [2]. Signal decorrelation is usually introduced by multi-path components. The envelope correlation coefficient (ρ_{e}) between the two diversity branches is calculated by the following expression [29]:

$$\rho_{\mathrm{e}} = \frac{\sum_{i=i}^{N} (r_1(i) - \overline{r_1})(r_2(i) - \overline{r_2})}{\sqrt{\sum_{i=i}^{N} (r_1(i) - \overline{r_1})^2} \sqrt{\sum_{i=1}^{N} (r_2(i) - \overline{r_2})^2}} \tag{2}$$

where N is total number of samples and *ri* is the mean value of fast fading envelope *ri* of received diversity branch signal *i*.

Mutual Coupling Between Diversity Branch Antennas

A spacing of $\lambda_0/2$ between diversity branch antennas is considered as sufficient for minimising the effect of mutual coupling [2]. For the five on-body links (i.e. chest-to-waist, back-to-waist, wrist-to-waist, head-to-waist and ankle-to-waist), the spacing between the two branches was varied from 5 mm ($0.11\lambda_0$) to 32 mm ($0.73\lambda_0$) and the mutual coupling measured; λ_0 is the free-space wavelength at the centre frequency of 6.85 GHz. It is noted from that, for a minimum spacing of 15 mm ($0.34\lambda_0$) between diversity branch antennas, the mutual coupling remained below -15 dB across the whole UWB band. This indicates that the antennas are suitably decoupled. The differences observed in the mutual coupling for the five on-body channels are mainly attributed to variation in the effective permittivity surrounding the antenna elements, due to changes in the tissue properties in the chosen on-body positions. However, for all measured on-body channels, the mutual coupling remained below -15 dB. Therefore, for the following measurement campaign, $0.34\lambda_0$ spacing between the branches was applied.

Diversity Combining and Diversity Gain Calculation

Three commonly-used diversity combining techniques are used in this study: selection combining (SC), equal-gain combining (EGC) and maximum-ratio combining (MRC). The channel responses for the two diversity branches are captured by the PNA in the frequency domain and converted to the time domain using an inverse fast Fourier transform (IFFT). Diversity combining is achieved by using the expressions given in [3] for combining the time domain signal:

$$\mathrm{SC}(t) = \max(r_1(t), r_2(t)) \tag{3}$$

$$\mathrm{EGC}(t) = \frac{r_1(t) + r_2(t)}{2} \tag{4}$$

$$\mathrm{MRC}(t) = \sqrt{r_1^2(t) + r_2^2(t)} \tag{5}$$

where $r_1(t)$ and $r_2(t)$ are the two received branch signal envelopes. The DG was calculated by plotting the cumulative distribution functions (CDFs) of the two branch signals and the diversity-combined signal. The DG is the difference between the strongest of the two branch signals and the diversity-combined signal at some specified outage probability [3, 4]. In this thesis, the outage probability is assumed to be 10 % for the DG calculation. For MRC and EGC, co-phasing of the two branch signals was achieved by shifting the phase of one signal with respect to other signal using the simple procedure taken from [2]. Figure 4 shows the CDF plot for the head-to-waist channel for the indoor environment (at location 1).

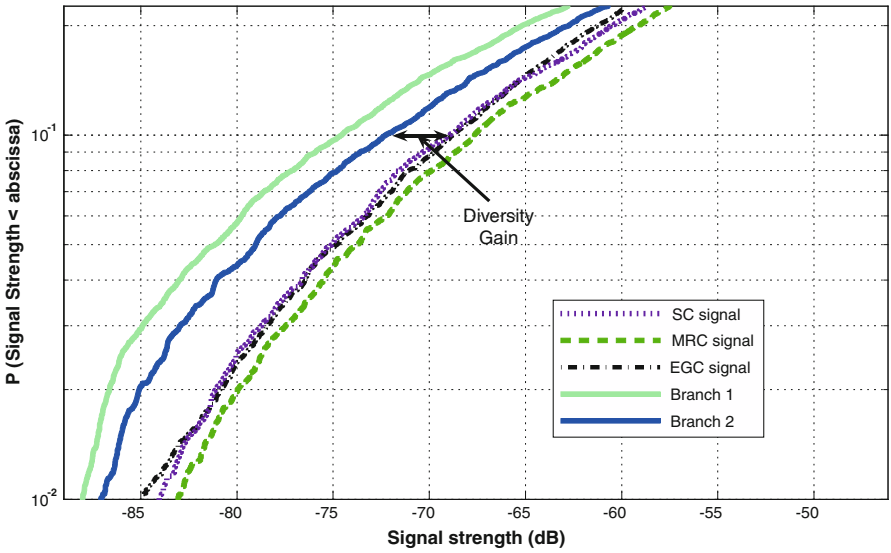

Fig. 4 Cumulative distribution function (CDF) plot for on-body diversity gain (DG) calculation for head-to-waist channel, when receiver (Rx) is at position 1 and the subject is at location 1

Ultra-Wideband On-Body Diversity Radio Channel Characterisation

Impact of Branch Spacing on Diversity Parameters

Table 1 lists the DG values (for all three combining techniques), $\boldsymbol{\rho_e}$ and the power imbalance between the two branches for the five on-body channels, for different spacings between diversity branch antennas, at location 2. In Table 1, power imbalance is calculated by using the ratio of the mean power of the two branch signal envelopes. From Table 1, it can be seen that, for almost all channels, the correlation between the diversity branch signals is lower at $0.48\lambda_0$ than at $0.34\lambda_0$, but power imbalance for $0.48\lambda_0$ case is increased, that reduces the DG slightly. Thus, $0.34\lambda_0$ spacing is a good choice, due to the compactness of the diversity antennas and the relatively high DG. This spacing gives similar performance to the highest possible spacing; as described in "Mutual Coupling Between Diversity Branch Antennas", the mutual coupling remains below − 15 dB for all links at this spacing. From the MRC DG against the antenna spacing for the five channels tested in an indoor environment, it can be seen that the DG tends to increase slightly with increased antenna spacing. There are a few exceptions, however, in which either the power imbalance is larger or the correlation is high, hence reducing overall DG. From the Table 1 it can be seen that power imbalance seems to be increasing for most of the cases because of the change in distance between Tx and Rx: one Rx antenna is closer to the Tx than the other. The variation of MRC-DG with inter-spacing is above 50 %

Table 1 Diversity parameters for five different links at location 1 with different spacings in an indoor environment

Links	Results	Antenna spacing (in terms of λ_0)					
		0.116	0.23	0.34	0.48	0.58	0.73
Chest–waist	MRC (dB)	4.03	2.85	2.98	2.32	2.59	1.22
	EGC (dB)	2.91	2.10	2.45	2.09	1.71	0.5
	SC (dB)	1.92	2.04	1.38	1.21	0.83	0.25
	ρ_e	0.625	0.684	0.686	0.630	0.668	0.711
	Imbalance (dB)	2.37	1.13	2.13	3.14	3.87	3.04
Head–waist	MRC (dB)	3.45	3.34	5.02	4.33	2.17	2.16
	EGC (dB)	2.73	1.02	4.93	3.42	0.79	1.90
	SC (dB)	1.96	0.48	4.19	2.14	0.49	1.17
	ρ_e	0.631	0.675	0.645	0.638	0.686	0.677
	Imbalance (dB)	3.99	2.47	1.11	1.34	1.92	2.22
Wrist–waist	MRC (dB)	1.65	2.23	2.98	2.99	3.22	3.44
	EGC (dB)	0.68	1.49	2.09	1.81	1.40	2.93
	SC (dB)	0.57	0.90	0.92	1.01	0.98	2.45
	ρ_e	0.691	0.730	0.697	0.736	0.734	0.755
	lmbalance (dB)	2.55	3.83	2.75	3.53	3.20	4.47
Ankle–waist	MRC (dB)	3.24	3.70	4.02	2.56	3.96	3.03
	EGC (dB)	2.1	2.35	2.79	2.32	2.73	2.14
	SC (dB)	1.54	1.28	2.11	1.40	2.65	1.01
	ρ_e	0.613	0.621	0.637	0.626	0.649	0.733
	lmbalance (dB)	3.77	4.84	4.95	6.56	6.0	4.63
Back–waist	MRC (dB)	4.10	6.75	6.97	6.03	6.69	5.94
	EGC (dB)	3.56	6.38	5.76	5.53	6.21	4.88
	SC (dB)	1.33	4.90	4.11	3.97	4.15	3.72
	ρ_e	0.604	0.614	0.618	0.627	0.630	0.626
	Imbalance (dB)	3.83	0.28	0.63	0.95	0.31	0.67

EGC equal-gain combining, *MRC* maximum-ratio combining, *SC* selection combining

for the channels that have a line of sight (LOS), or partial LOS, link with Tx; this percentage is calculated by taking the difference between maximum and minimum DG for each link. The exception is the ankle case, where reflections from the ground make the DG process more stable.

Reliability of Diversity Measurements with Respect to Small On-Body Position Changes

In order to ensure that all measurements are reliable, a small grid incorporating the Rx antenna was made, to see how small variations in the position of the diversity antenna affect the measurement of DG. For specific cases, such as the chest and the back (see Fig. 2), a 2 × 2 grid was applied with an approximate spacing of 5 mm; in the case of the ankle and the head, a one dimensional grid was used, with a similar spacing. These grids were adopted in this work to investigate the correlation coefficient between the received signals on different branches and to highlight the stability of the channel within a small window of positions in on-body measurements.

Table 2 shows that the lowest value of DG is obtained in the chest-to-waist link, when there is a LOS link between Tx and Rx. This lowest value is due to the higher imbalance with antenna spacing for different positions of Rx with respect to Tx on the waist in an indoor environment at location 1.

Power imbalance and higher correlation, which results from dominant direct rays, compared to multi-path components. The highest value of DG is obtained in the back-to-waist channel, which is a NLOS channel. The higher value of DG and low power imbalance suggest that signals are reasonably uncorrelated and also the movements of body parts result in higher decorrelation between the two branch signals. For all other partial LOS channels (i.e. the wrist-to-waist, ankle-to-waist and head-to-waist cases), the DG lies between the chest-to-waist and back-to-waist channels. This is due to the fact that the multi-path components are slightly dominating in these cases, because of the scattering from different parts of the human body and the rich scattering environment.

Table 3 shows the DG using different combining techniques and diversity parameters in an anechoic chamber, at $0.34\lambda_0$ spacing between diversity branch antennas. Very low values of the DG for all cases, compared to those found in the indoor environment, confirms the expectation that there are no reflections from the surrounding environment and that the only source of multi-path components in the anechoic chamber was the human body itself. The differences in DG observed between the different on-body channels are due to the same causes described for the indoor environment in the previous paragraph.

Tables 2 and 3 show that, due to the variation in Rx antenna position on the body, the MRC-DG changes from 0.01 to 0.5 dB for the anechoic chamber case and 0.14 to 0.8 dB for the indoor environment. Results therefore show that variation of Rx antenna position will not severely affect the measurement of DG. For the remaining results, only position 2 of diversity antenna (shown in Fig. 2) is used for each Rx location.

Comparison of Diversity Gain for the Free Space and Indoor Environments

A comparison of MRC-DG is shown in Fig. 5 for five different Rx positions (position 2 for each Rx is taken as shown in Fig. 2), in both the anechoic chamber and three different locations in an indoor environment, with Tx on the waist. The results are compared with the measurement results at 2.4 GHz presented in [1] in an indoor environment (this is an approximate comparison; as for both measurement results, subject and indoor environment are different, which contributes to DG). Low values of DG in the chamber are due to less scattering from the surrounding environment, compared to the indoor case, where there are rich multi-path reflections. In the chamber, only reflections from the moving human body parts play a role in acquiring DG; in an indoor environment, both the human body parts and surrounding environment contribute to DG. This shows the fact that diversity is useful only when the human

Table 2 Diversity parameters for different receiver (Rx) positions with respect to transmitter (Tx) on waist in an indoor environment for location 7 at $0.34\lambda_0$ spacing

Link	Chest				Head		Wrist	Ankle			Back			
	1	2	3	4	1	2	1	1	2	3	1	2	3	4
MRC	2.52	2.79	2.74	3.32	4.62	4.76	4.35	4.89	4.38	4.29	5.27	4.85	5.22	4.87
EGC	2.06	2.17	2.28	3.22	3.48	3.28	4.02	4.32	4.12	4.03	4.48	4.22	4.43	4.13
SC	1.11	1.52	1.13	1.63	3.3	1.76	1.42	2.32	2.12	1.98	2.92	3.02	2.54	2.32
ρ_e	0.670	0.667	0.653	0.642	0.694	0.678	0.702	0.701	0.698	0.701	0.646	0.670	0.648	0.671
r_1	−31.74	−33.53	−35.17	−33.01	−36.12	−34.32	−43.61	−36.20	−36.21	−36.48	−47.91	−48.82	−47.16	−48.12
r_2	−35.10	−30.16	−32.66	−29.06	−32.78	−32.83	−41.99	−38.22	−39.12	−33.74	−48.86	−48.34	−49.13	−49.92
I	3.36	3.37	2.51	3.95	3.34	1.49	1.17	2.02	2.91	2.74	0.95	0.48	1.97	1.8

All units are in dB except $\boldsymbol{\rho_e}$, $\boldsymbol{r_1}$ and $\boldsymbol{r_2}$ are mean powers and I is the power imbalance *EGC* equal-gain combining, *MRC* maximum-ratio combining, *SC* selection combining

Table 3 Diversity parameters for different receiver (Rx) positions with respect to transmitter (Tx) on waist in an anechoic chamber at $0.34\lambda_0$ spacing

Link	Chest				Head		Wrist	Ankle			Back			
	1	2	3	4	1	2	1	1	2	3	1	2	3	4
MRC	1.10	1.25	1.5	1	1.28	1.27	1.47	1.52	1.42	1.6	1.93	2.02	1.96	1.92
EGC	0.5	0.6	0.5	0.75	1.22	1.01	1.22	0.64	0.52	0.57	0.53	1.87	1.82	1.76
SC	0.0	0.1	0.0	0.0	0.36	0.34	0.1	0.0	0.0	0.0	0.56	0.54	0.5	0.5
ρ_e	0.640	0.640	0.641	0.640	0.720	0.721	0.730	0.746	0.746	0.745	0.650	0.650	0.651	0.648
r_1	− 29.15	− 29.16	− 29.24	− 29.16	− 39.58	− 39.85	− 44.77	− 39.74	− 39.76	− 39.84	− 47.34	− 47.46	− 47.12	− 47.38
r_2	− 34.66	− 34.68	− 34.52	− 33.99	− 37.85	− 37.55	− 42.53	− 39.65	− 39.72	− 39.52	− 48.14	− 48.24	− 47.98	− 47.02
I	5.51	5.52	5.28	4.83	1.73	2.3	2.24	0.09	0.04	0.32	0.8	0.78	0.86	0.36

All units are in dB except $\boldsymbol{\rho_e}$, $\boldsymbol{r_1}$ and $\boldsymbol{r_2}$ are mean powers and I is the power imbalance *EGC* equal-gain combining, *MRC* maximum-ratio combining, *SC* selection combining

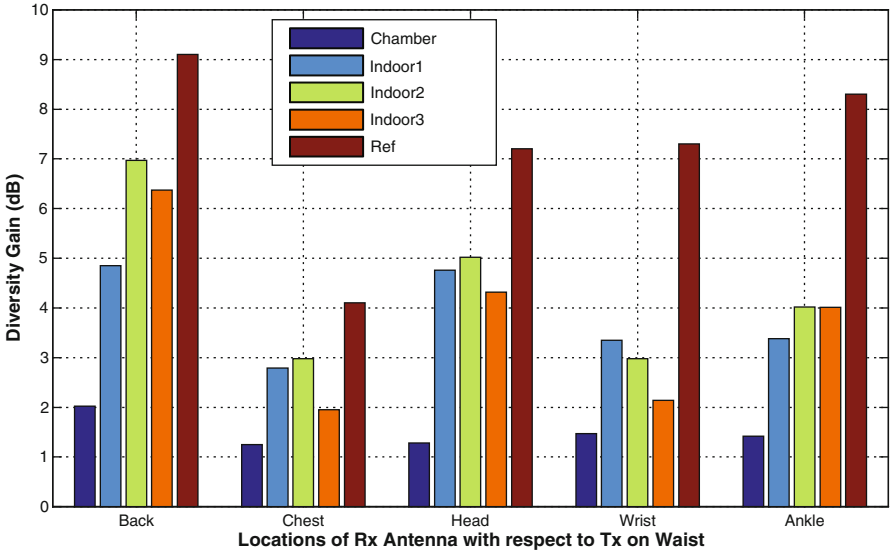

Fig. 5 Comparison of maximum-ratio combining (MRC) diversity gain (DG) for different links for position 1 and three locations at $0.34\lambda_0$ spacing in an indoor environment in comparison with narrow band in an indoor environment presented in [1]

subject is present in rich multi-path environments. Also, moderate values of DG in the anechoic chamber confirms both the presence of multi-path components due to the movement of body parts and the fact that their contribution to DG is not the dominant factor in more realistic environments.

Effect of Indoor Locations on the Ultra-Wideband Diversity Gain

Table 4 shows the diversity parameters for $0.34\lambda_0$ spacing between the diversity branch antennas at three different locations in an indoor environment (Fig. 3; Loc. 1, Loc. 4 and Loc. 7). The highest DG values are obtained for location 1, because the subject is close to the walls and pillar in this case, leading to stronger multi-path reflections. The wrist-to-waist channel is the exception: here, DG is low, compared to other locations, due to the higher power imbalance and higher correlation in this case, as the wrist was very close to the wall.

The highest value of DG (i.e. 6.97 dB using MRC) is obtained for the back-to-waist link (NLOS case), compared to the other links for location 1. The higher value of DG and lower power imbalance (0.63 dB) for the back-to-waist link suggests that signals are reasonably uncorrelated and also that movements of body parts result in a higher decorrelation between the two branch signals. The same reasoning as described in "Reliability of Diversity Measurements with Respect to Small On-Body Position Changes" can be applied to account for DG variation for all other links. The results

Table 4 Diversity parameters for three different locations at $0.34\lambda_0$ spacing between diversity branch receiver (Rx) in an indoor environment

Link	Chest–waist			Head–waist			Wrist–waist			Ankle–waist			Back–waist		
	1	2	3	1	2	3	1	2	3	1	2	3	1	2	3
MRC	2.79	2.98	1.95	4.76	5.02	4.32	3.35	2.98	2.14	3.38	4.02	4.01	4.85	6.97	6.37
EGC	2.17	2.45	1.15	3.28	4.43	3.14	3.02	2.09	2.01	3.12	2.79	2.77	4.22	5.76	5.44
SC	1.11	1.38	0.98	1.76	4.19	3.04	1.42	0.92	1.19	2.12	2.11	2.50	3.02	4.11	3.87
ρ_e	0.670	0.686	0.661	0.678	0.645	0.637	0.702	0.697	0.678	3.698	0.637	0.636	0.670	0.618	0.685
r_1	− 31.74	− 31	− 28.71	− 34.32	− 27.55	− 36.41	− 43.61	− 32.00	− 38.35	− 36.21	− 35.23	− 31.98	− 48.82	− 47.23	− 47.67
r_2	− 35.10	− 33.14	− 26.21	− 32.83	− 26.43	− 32.58	− 41.99	− 35.08	− 40.67	− 39.12	− 30.20	− 28.96	− 48.34	− 46.60	− 48.35
I	3.36	2.13	2.50	3.34	1.11	3.83	1.17	3.08	3.02	2.91	4.95	3.02	0.48	0.63	0.78

All units are in dB except $\boldsymbol{\rho_e}$, $\boldsymbol{r_1}$ and $\boldsymbol{r_2}$, which are mean powers and I is the power imbalance *EGC* equal-gain combining, *L* location number, *MRC* maximum-ratio combining, *SC* selection combining

obtained for UWB on-body diversity at location 1 are compared with the results of Khan et al. at 2.4 GHz presented in [1] in an indoor environment (comparison plot is shown in Fig. 5). This is an approximate comparison; as for both measurement results, human subject and indoor environment were different). Results approximately agree for the chest-to-waist link (where there is direct LOS communication between Tx and Rx). However, there is disagreement for partial LOS cases and NLOS cases (i.e. the head-to-waist, wrist-to-waist and back-to-waist links); this is due to the fact that, for NLOS cases, the reflections and contributions by the environment have a large effect on the quality of the signal and the measurements were done in different environments. In addition, the subject-specific behaviour of the UWB on-body channel (see, for example, the work of Sani et al. [30]) will also play a role in explaining the disagreement between the results.

Concluding Remarks on On-Body UWB Diversity

Spatial diversity techniques for UWB on-body radio channels have been investigated and analysed. Various scenarios, including changes in antenna on-body positions, the location of subject in the indoor environment and also variation in the inter-spacing between antenna element branches, have been considered. Results showed that, for dense multi-path environments, the benefits of applying diversity techniques were significant for the NLOS cases, where there are low power imbalances due to uncorrelated signals, in comparison to the LOS scenarios.

Maximum variations of 0.5 and 0.8 dB, for the anechoic chamber and the indoor environment cases, respectively, have been observed in response to slight changes in the on-body antenna position. This demonstrated the potentially negligible effect of accidental and inherited on-body element location shift, due to the subject's sudden movement. The results presented here gave indications of the beneficial applications of diversity antenna techniques for potential performance enhancement of UWB body-centric wireless communications as experienced in narrowband technologies. This will be increasingly appreciated for off-body communications, due to the variation in the spatial and angular parameters of the multi-path components that will contribute to enhanced DG. Hence, in the next section UWB off-body spatial diversity is being investigated.

Ultra-Wideband Off-Body Diversity Performance Analysis

Reliability of Diversity Measurements Versus Small Variations in On-Body Diversity Receiver Position

In order to ensure that all measurements are reliable, for each channel a small grid incorporating in the Rx antenna was made to see how the small variation in position of diversity antenna will affect the measurement of DG. For specific cases, such as the

chest and the back (see Fig. 3), a 2 × 2 grid was applied with approximate spacing of 5 mm and in the case for the ankle and the head a one dimensional grid was used with similar spacing. Table 5 shows DG values based on different combining techniques, envelope correlation (ρ_e) and power imbalance between two branches for Loc. 2 in an indoor environment (as shown in Fig. 3) at $0.34\lambda_0$ spacing between diversity branch antennas (whereas, power imbalance is calculated by using the ratio of mean power of two branch signal envelopes).

Results show that the values of DG are lower, when Rx is placed at chest and ankle as compared to other links, because there is a direct LOS link between Tx and Rx. Higher power imbalance and relatively higher value of correlation are the factors that plays a role in reducing DG. The highest value of DG is obtained in NLOS channel, i.e. when Rx is placed at the back. Higher value of DG and low power imbalance suggests that movements of body parts result in higher decorrelation between the two branch signals. For other partial LOS Rx locations, i.e. wrist and head cases, DG lies between the LOS and NLOS channels (i.e. chest and back). This is due to the fact that for partial LOS cases, branch signals are less uncorrelated, as for the case of NLOS scenario. From the Table 5, it is obvious that the variations of DG with slight changes in Rx locations for each position is very small (varies from 0.2 to 1.46 dB). It leads to the conclusion that accidental variations in receiver locations on the body have negligible effects on the DG for the UWB off-body diversity as well like for the on-body case. In the rest of off-body diversity discussion, only position 2 for each Rx location is considered(except for wrist case where position 1 is considered).

Ultra-Wideband Diversity Gain Variations Versus Different Locations in an Indoor Environment

Table 6 shows the DG (using different combining techniques) and different diversity parameters for $0.34\lambda_0$ spacing between the diversity branch antennas at eight different locations in an indoor environment (marked as Loc. 1–Loc. 8, each location is at spacing of 0.5 m from the every other location, as shown in Fig. 3). Compared to all other channels, highest DG is obtained as expected, for the back channel (i.e. NLOS scenario), and due to highly uncorrelated signals and very low power imbalance. Same reasoning can be applied for DG variation for all other links as described earlier in "Reliability of Diversity Measurements Versus Small Variations in On-Body Diversity Receiver Position". For all channels due to the change of subject position (from Loc. 1 to Loc. 8 as shown in Fig. 3), there are slight variations in DG and other diversity parameters (i.e. power imbalance and correlation). The maximum DG variations among different subject locations for Rx on chest (with respect to off-body Tx) are only 1.58 dB. For all other Rx locations (i.e. head, wrist, ankle and back), the maximum DG variations with respect to subject position are below 1.5 dB. These lesser variations in DG are due to the fact that for off-body diversity case, there is very small change in power imbalance and correlation coefficient with respect to the change of locations. From the results it is obvious that off-body diversity is independent of subject location, carrying diversity branch antennas in an indoor environment.

Table 5 Diversity parameters for different receiver (Rx) positions with respect to transmitter (Tx) on wall. At Loc. 2 in an indoor environment as shown in Fig. 3) at $0.34\lambda_0$ spacing

Link	Chest				Head		Wrist	Ankle			Back			
	1	2	3	4	1	2	1	1	2	3	1	2	3	4
MRC	9.9	9.11	10.01	10.31	10.94	12.42	11.90	9.74	10.04	9.45	13.46	14.39	14.93	14.28
EGC	9.72	9.39	9.78	10.05	10.44	10.96	11.03	9.36	9.77	8.83	11.24	11.91	12.41	13.09
SC	9.33	9.65	9.35	9.54	9.86	10.04	10.39	8.11	9.23	9.59	10.01	10.78	12.41	13.09
ρ_e	0.094	0.074	0.061	0.064	0.059	0.033	0.085	0.090	0.099	0.053	0.012	0.033	0.030	0.032
I	4.16	4.39	5.08	5.57	4.57	3.33	4.03	5.92	4.53	6.85	1.57	1.93	0.30	0.24

All units are in dB except $\boldsymbol{\rho_{e,}}$ where I is the power imbalance *EGC* equal-gain combining, *MRC* maximum-ratio combining, *SC* selection combining

Table 6 Diversity parameters for five different links at eight different locations in an indoor environment with a spacing of $0.34\lambda_0$ between receiver (Rx) antenna

Links	Results	Location number in an indoor environment							
		1	2	3	4	5	6	7	8
Chest	MRC (dB)	11.92	12	12.16	12.04	12.29	13.28	13.5	12.58
	EGC (dB)	10.63	10.79	10.56	10.83	11.23	12.14	12.29	11.44
	SC (dB)	9.79	9.93	9.78	10.05	10.47	11.28	11.27	10.76
	ρ_e	0.065	0.061	0.070	0.054	0.029	0.031	0.040	
	Imbalance (dB)	3.09	3.08	2.98	2.96	2.59	2.29	2.24	2.36
Head	MRC (dB)	13.08	12.67	12.94	12.26	13.1	12.69	12.18	13.22
	EGC (dB)	11.97	11.61	11.93	11.33	12.49	12.24	11.66	11.93
	SC (dB)	11.12	10.9	11.23	10.57	11.89	11.5	10.62	11.25
	ρ_e	0.071	0.067	0.065	0.056	0.057	0.073	0.072	0.057
	Imbalance (dB)	2.39	2.51	2.51	2.53	2.06	2.23	2.41	1.65
Wrist	MRC (dB)	11.12	11.90	11.47	11.36	11.60	11.11	11.38	10.87
	EGC (dB)	10.23	11.03	10.51	10.66	10.56	10.21	10.7	10.08
	SC (dB)	9.64	10.39	10.02	10.03	9.90	9.45	9.96	9.48
	ρ_e	0.080	0.085	0.078	0.082	0.081	0.082	0.082	0.097
	Imbalance (dB)	4.03	4.03	4.03	4.06	4.01	4.03	3.99	3.93
Ankle	MRC (dB)	11.23	11	10.81	11.13	10.83	12.27	11.58	10.97
	EGC (dB)	10.22	10.44	10.15	10.89	10.35	11.98	11.02	10.48
	SC (dB)	9.79	10.04	9.72	10.49	10.03	11.38	10.89	10.21
	ρ_e	0.121	0.114	0.114	0.120	0.113	0.123	0.147	0.134
	Imbalance (dB)	4.34	4.63	4.56	4.57	4.43	4.13	3.86	4.49
Back	MRC (dB)	14.28	14.42	14.25	14.4	14.13	13.28	13.76	13.58
	EGC (dB)	12.63	12.70	12.95	12.86	11.80	12.39	12.44	11.23
	SC (dB)	11.72	11.85	12.12	12.10	11.86	11.65	11.59	11.23
	ρ_e	0.033	0.030	0.0356	0.039	0.0357	0.0359	0.041	0.048
	Imbalance (dB)	1.60	1.54	1.48	1.84	1.68	2.03	1.99	1.88

EGC equal-gain combining, *MRC* maximum-ratio combining, *SC* selection combining

Diversity Branch Spacing Versus Diversity Parameters

Table 7 lists the DG values using different combining techniques, envelope correlation coefficient ($\boldsymbol{\rho_e}$) and the power imbalance between the two branches for the five on-body channels for different spacing between diversity branch antennas in the indoor environment at location 2 (location 2 is shown in Fig. 3). It can be noticed from the Table 7 that almost for all the channels the correlation between the diversity branch signals is lower at $0.48\lambda_0$ as compared to $0.34\lambda_0$, as is the case for on-body and this is due to an increase in the power imbalance for $0.48\lambda_0$ case that reduces the DG slightly. Thus, $0.34\lambda_0$ spacing is a good choice due to compactness of diversity antennas and relatively high DG. This spacing gives similar performance as the highest spacing possible and also as described in "Mutual Coupling Between Diversity Branch Antennas", the mutual coupling remains below − 15 dB for all links at this spacing.

Table 7 Diversity parameters for five different links at Loc. 2 (as shown in Fig. 3) with different spacings between diversity antennas in an indoor environment

Links	Results	Antenna spacing (in terms of λ_0)			
		0.23	0.34	0.48	0.58
Chest	MRC (dB)	9.98	11.22	11.20	11.98
	EGC (dB)	8.26	10.63	10.64	10.92
	SC (dB)	8.01	9.79	9.65	10.01
	ρ_e	0.098	0.065	0.064	0.058
	Imbalance (dB)	4.98	3.09	3.13	3.02
Head	MRC (dB)	11.12	13.08	13.06	14.24
	EGC (dB)	9.89	11.97	11.90	13.01
	SC (dB)	9.48	11.12	11.01	11.98
	ρ_e	0.112	0.071	0.070	0.078
	Imbalance (dB)	3.34	2.39	2.39	2.01
Wrist	MRC (dB)	10.42	11.90	12.04	13.14
	EGC (dB)	10.01	11.33	11.36	12.02
	SC (dB)	9.46	10.39	10.68	11.18
	ρ_e	0.164	0.085	0.073	0.051
	Imbalance (dB)	5.02	4.03	4.01	3.98
Ankle	MRC(dB)	9.92	11	10.98	11.58
	EGC (dB)	9.07	10.44	10.34	10.92
	SC (dB)	8.24	10.04	10.01	10.58
	ρ_e	0.186	0.114	0.112	0.098
	Imbalance (dB)	5.32	4.63	4.68	4.13
Back	MRC (dB)	13.01	14.28	14.13	14.98
	EGC (dB)	11.84	12.62	12.61	13.04
	SC (dB)	10.12	11.72	11.68	12.52
	ρ_e	0.089	0.033	0.029	0.030
	Imbalance (dB)	1.96	1.60	1.63	1.12

EGC equal-gain combining, *MRC* maximum-ratio combining, *SC* selection combining

Figure 6 shows the relationship between correlation coefficient, power imbalance, DG using MRC and spacing between diversity branch antennas (when Rx is placed at wrist). From the Fig. 6, it is obvious that DG is linked to spacing between diversity branch antennas and it also depends on correlation and power imbalance. Results show that DG is approximately directly proportional to spacing between diversity branch antennas and inversely proportional to power imbalance and correlation coefficient.

Uplink and Downlink Diversity Comparison

Uplink and downlink diversity performance has been compared by swapping Tx and Rx antennas. For uplink diversity, Tx was off-body and diversity branch antennas were on the body. For downlink diversity, the branch antennas were placed away from the body and Tx was placed on the body at the same five locations as Rx antennas for uplink diversity case. Table 8 shows MRC DG, ρ, power imbalance and

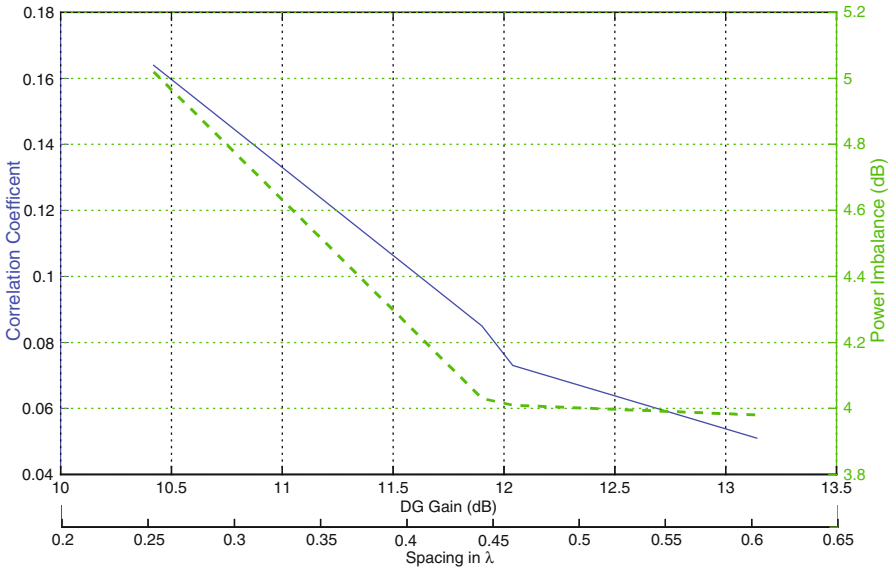

Fig. 6 Variations of maximum ratio combined (MRC) diversity gain (DG), power imbalance and correlation coefficient with respect to variation in spacing between on-body diversity branch antennas (when diversity branch antenna is on wrist)

Table 8 Off-body downlink diversity at Loc. 2 (at 1 m distance between transmitter (Tx) and receiver (Rx), Loc. 2 is shown in Fig. 3) at $0.34\lambda_0$ spacing between diversity branch Rx in an indoor environment

Links	Uplink			Downlink			Difference		
MRC	ρ_e	I	MRC	ρ_e	I	MRC	ρ_e	I	
Chest	12	0.061	3.08	9.53	0.10	6.31	2.47	0.039	3.23
Head	12.67	0.067	2.51	11.31	0.101	5.13	1.36	0.168	2.62
Wrist	11.90	0.085	4.03	9	0.136	5.74	2.90	0.051	1.71
Ankle	11	0.114	4.63	9.11	0.163	4.11	1.89	0.049	0.52
Back	14.42	0.030	1.54	13.49	0.024	2.34	0.93	0.006	0.8

MRC and I are in dB units *I* power imbalance, *MRC* maximum-ratio combining

there difference for both uplink and downlink diversity, when subject was at Loc. 2 (Loc. 2 is shown in Fig. 3), for five on-body Rx locations. By swapping the Tx and Rx antennas, the scattering environment surrounding the diversity branch antenna changes and this leads to difference in results shown in the table.

There may be some repeatability errors in DG and power imbalance as well. DG is always higher when diversity branch antennas are on the body (uplink diversity). This is due the fact that reflections from human body parts are also playing role in improving DG. Hence, uplink diversity seems to be more useful than the downlink diversity.

Comparison Between Off-Body and On-Body Diversity

Off-body diversity results obtained here are compared with the on-body diversity results presented earlier in this chapter. In both measurements, the same subject, Rx locations and the NLOS cases where there is low power imbalance due to highly uncorrelated signals in comparison to the LOS scenarios. Maximum variation of 1 dB has been observed due to slight changes in the on-body antenna position. This demonstrates the potentially negligible effect of accidental and inherited on-body element location shift due to sudden movement of the subject. Higher DG were obtained as inter-spacing between diversity antenna branches increased with a few exceptions where either the power imbalance or the correlation is high. Small variations in DG due to changes in subject location within the indoor environment and orientation between AP and on-body diversity receiver shows that off-body diversity is independent of subject location and orientation in an indoor environment. Results also demonstrate that off-body diversity is almost 50 % more efficient than on-body diversity and off-body diversity is more useful when it is considered as an uplink (i.e. diversity branch antennas are on-body with respect to off-body Tx) as compared to downlink diversity.

Summary

Diversity for UWB body area networks is analysed, using various measurements scenarios. The DG is calculated for five different on/off-body channels by plotting cumulative distribution functions and it is found that DG value is very low for chamber due to no reflections from surroundings as compared to indoor environment. Also, in indoor environment and chamber, DG is lowest for LOS cases. There are significant benefits of diversity techniques for NLOS cases as compared to LOS cases due to low power imbalance and low correlation coefficient between the branch signals. Comparison of on-body and off-body diversity shows a significant improvement for the off-body case. It also reveals that the on-body diversity has almost similar impact for both uplink and downlink diversity, whereas uplink is preferable over downlink diversity for the off-body diversity case.

Analysis also shows that DG is independent of subject-specific behaviour. The results presented in this chapter give indications of the beneficial applications of diversity antenna techniques for potential performance enhancement of the ultra-wideband body-centric wireless communications.

References

1. I. Khan, P.S. Hall, A.A. Serra, A.R. Guraliuc, P. Nepa, Diversity performance analysis for on-body communication channels at 2.45 GHz. IEEE Trans. Antenna Propag. **57**(4), 956–963 (April 2009)
2. W.C. Jakes, *Microwave Mobile Communications*. (Wiley, New York, 1974)
3. I. Khan, P.S. Hall, Multiple antenna reception at 5.8 and 10 GHz for body-centric wireless communication channels. IEEE Transac. Antenna Propag. **57**(1), 248–255 (Jan 2009)

4. L.M. Correia, *Mobile Broadband Multimedia Networks Techniques, Models and Tools for 4G*. (Elsevier, London, 2006)
5. C.B.J. Dietrich, K. Dietze, J.R. Nealy, W.L. Stutzman, Spatial, polarization, and pattern diversity for wireless handheld terminals. IEEE Transac. Antennas Propag. **49**(9), 1271–1281 (September 2001)
6. M. Karaboikis, C. Soras, G. Tsachtsiris, V. Makios, Three-branch antenna diversity systems on wireless devices using various printed monopoles. IEEE Int. Symp. Electromagn. Compat. (11–16 May 2003).
7. J.S. Colburn, Y. Rahmat-Samii, M.A. Jensen, G.J. Pottie, Evaluation of personal communications dual-antenna handset diversity performance. IEEE Transac. Veh. Technol. **47**(3), 737–746 (August 1998)
8. R.G. Vaughan, J.B. Andersen, Antenna diversity in mobile communications. IEEE Transac. Veh. Technol. **VT-36**(4), 149–172 (May Nov. 1987)
9. T.M.K Ogawa, K. Monma, An analysis of the performance of a handset diversity antenna influenced by head, hand, and shoulder effects at 900 MHz: part II correlation characteristics. IEEE Transac. Veh. Technol. **50**(3), 845–853 (May 2001)
10. A.A. Serra, P. Nepa, G. Manara, P. Hall, Diversity measurements for on-body communication systems. IEEE Antennas Wirel. Propag. Lett. **6**(1), 361–363 (Jan 2007)
11. I. Khan, M.R. Kamarudin, L. Yu, Y.I. Nechayev, P.S. Hall, Comparison of space and pattern diversity for on-body channels. 5th Eur. Workshop Conformal Antennas, Bristol, U.K., (10–11 Sep. 2007), pp. 47–50
12. M.R. Kamarudin, Y.I. Nechayev, P.S. Hall, Performance of antenna in on-body environment. IEEE Antenna Propag. Soc. Int. Symp. **3A**, 475–478 (3–8 Jul. 2009)
13. S.L. Cotton, W.G. Scanlon, Channel characterization for single and multiple antenna wearable systems used for indoor body-to-body communications. IEEE Transac. Antenna Propag. **57**(4), 980–990 (Jan. 2009)
14. L. Cotton, G. Scanlon, Characterization and modelling of on-body spatial diversity within indoor environments at 868 MHz. IEEE Transac Wirel. Commun. **8**(1), 176–185 (Jan. 2009)
15. S. Cotton, W. Scanlon, Spatial diversity and correlation for off-body communications in indoor environments at 868 MHz. IEEE 65th, Vehicular Technology Conference, VTC2007-Spring., 2007, pp. 372–376
16. A.J. Ali, S. Cotton, W. Scanlon, Spatial diversity for off-body communications in an indoor populated environment at 5.8 GHz. Loughborough Antennas & Propagation Conference, LAPC 2009, Loughborough, UK, 16–17 Nov. 2009, pp. 641–644
17. P. Van Torre, L. Vallozzi, H. Rogier, J. Verhaevert, Diversity textile antenna systems for firefighters. *Proceedings of the Fourth European Conference on Antennas and Propagation* (*EuCAP*, Barcelona, Spain, 12–16 April 2010), pp. 1–5
18. T. Kaiser, F. Zheng, *Ultra Wideband Systems With MIMO*. (Wiley, Chichester, 2010)
19. W.J. Chang, J.H. Tarng, S.Y. Peng, Frequency-space-polarization on UWB MIMO performance for body area network applications. IEEE Antennas Wirel. Propag. Lett. **7**, 577–580 (Jan. 2009)
20. A. Sibille, S. Bories, Spatial diversity for UWB communications. 5th European (Conf. Publ. No. 492) Personal Mobile Communications Conference, 2003, pp. 367–370
21. R. D'Errico, A. Sibille, A. Giorgetti, M. Chiani, Antenna diversity in UWB indoor channel. IEEE International Conference on Ultra-Wideband ICUWB, 2008, pp. 13–16
22. R. D'Errico, A. Sibille, Multiple antennas effect in UWB spatial multiplexing. European Conference on Antennas and Propagation EUCAP, Berlin, Germany, 23–27 March 2009
23. A. Sibille, Diversity combining for enhanced multi-user throughput in pulse based UWB communications. 11th European Wireless conference, Nicosia, Cyprus, 10–13 April 2005
24. C. Yifan, T. Jianqi, J. Lai, E. Gunawan, S.L. Kay, B.S. Cheong, P. Rapajic, Cooperative communications in ultra-wideband wireless body area networks: channel modeling and system diversity analysis. IEEE J. Sel. Areas Commun. **27**(1), 5–16 (Jan. 2009)
25. M.G. Benedetto, T. Kaiser, A. Molisch, I. Oppermann, D. Porcino, *UWB Communication Systems: A Comprehensive Overview*. (Hindawi Publishing Corporation, New York, 2006)

26. V. Roy, S. Oestges, C. Horlin, F. Doncker, P. Opera, Ultra-wideband spatial channel characterization for body area networks. European Conference on Antennas and Propagation, EuCAP 2007, Edinburgh, U.K., 11–16 Nov. 2007
27. S. Van Roy, C. Oestges, F. Horlin, P. De Doncker, A comprehensive channel model for UWB multisensor multiantenna body area networks. IEEE Transac. Antennas Propag. **58**(1), 163–170 (Jan. 2010)
28. T.S. Rappaport, *Wireless Communications Principles and Practice*. (Prentice Hall, New Jersey, 1996)
29. A.M.D. Turkmani, A.A. Arowojolu, P.A. Jefford, C.J. Kellett, An experimental evaluation of the performance of two-branch space and polarization diversity schemes at 1800 MHz. IEEE Transac. Veh. Technol. **44**(2), 318–326 (May 1995)
30. A. Sani, Y. Hao, Y. Zhao, S.L. Lee, G.Z. Yang, A subject-specific numerical study in UWB body-centric wireless communications. *Proceedings of the Fourth European Conference on Antennas and Propagation*, (*EuCAP*, Barcelona, Spain, 12–16 April 2010)
31. Q.H. Abbasi, Radio channel characterisation and system-level modelling for ultra wideband body-centric wireless communications. PhD Thesis, Queen Mary University of London (December 2011)
32. Q.H. Abbasi, M.M. Khan, S. Liaqat, M. Kamran, A. Alomainy, Y. Hao, Experimental investigation of ultra wideband diversity techniques for on–body radio communications. Prog. Electromag. Res. **C34**, 165–181 (2013)
33. Q. H. Abbasi, A. Sani, A. Alomainy, Y. Hao, Experimental characterisation and statistical analysis of the pseudo–dynamic ultra wideband on–body radio channel. IEEE Antenna Wireless Propag. Lett. **10**, 748–751 (August 2011)
34. Q.H. Abbasi, A. Alomainy, Y. Hao, Ultra wideband antenna diversity techniques for on/off–body radio channel characterisation. IEEE International Workshop on Antenna Technology (iWAT), Tucson, Arizona (5–7 March 2012)

System-on-a-Chip Radio Transceivers for 60-GHz Wireless Body-Centric Communications

Domenico Zito and Domenico Pepe

Abstract The 60-GHz band, previously forgotten because of the attenuation due to the resonance of the oxygen molecule, was recently reconsidered for building very short range wireless communication systems, including wireless body-centric networks. The 60-GHz radio channel has the potential to overcome some of the main limitations encountered in the implementation of body-centric communication systems in the industrial, scientific and medical (ISM) bands at lower frequency in the radio frequency spectrum. In particular, compared to the systems operating at lower frequencies, the 60-GHz radio channel offers the potential for supporting multi-gigabit per second communication rates, security, and low interference with adjacent wireless body-centric networks, and high level of miniaturization of the antennas.

Keywords 60 GHz · Body-centric · On-body · Off-body · Wireless communication · System-on-chip · Transceiver · CMOS · Phased array

The 60-GHz band, previously forgotten because of the attenuation due to the resonance of the oxygen molecule, was recently reconsidered for building very short range wireless communication systems, including wireless body-centric networks. The 60-GHz radio channel has the potential to overcome some of the main limitations encountered in the implementation of body-centric communication systems in the industrial, scientific and medical (ISM) bands at lower frequency in the radio frequency spectrum. In particular, compared to the systems operating at lower frequencies, the 60-GHz radio channel offers the potential for supporting multi-gigabit per second communication rates, security, and low interference with adjacent wireless body-centric networks, and high level of miniaturization of the antennas.

In this frame, the opportunity to realize such systems is directly dependent on the possibility to implement system-on-a-chip (SoC) radio transceivers. This chapter reports some of the main design challenges and perspective for the implementation of

D. Zito (✉)
Department of Electrical and Electronic Engineering,
University College Cork, Cork, Ireland
email: domenico.zito@tyndall.ie

D. Zito · D. Pepe
Tyndall National Institute, Lee Maltings, Dyke Parade, Cork, Ireland

M. R.Yuce (ed.), *Ultra-Wideband and 60 GHz Communications for Biomedical Applications,* DOI 10.1007/978-1-4614-8896-5_9,

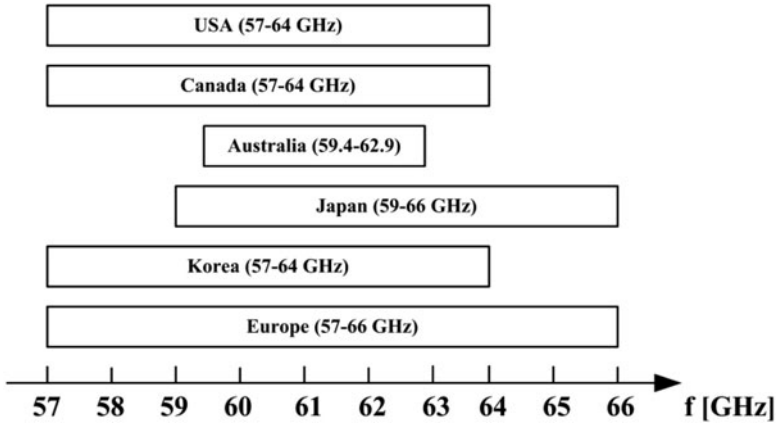

Fig. 1 Worldwide allocations of 60-GHz unlicensed bands

SoC radio transceivers enabling wireless body-centric communications. In detail, it focuses on the feasibility of SoC transceivers in nano-scale complementary metal oxide semiconductor (CMOS) technology. Section 1 reports an introduction to 60-GHz band and its applications. Section 2 introduces wireless body-centric communications, technology challenges, and opportunities. Section 3 reports a preliminary feasibility study of SoC transceivers by taking into account the main characteristics of the radio channel and the main limitations of the nano-scale CMOS technology. The co-integration with wearable millimeter-wave antennas for on- and off-body communications (integration with textile, miniaturized flexible antennas, etc.) will be considered as well. Finally, the conclusions are drawn in Section 4.

Introduction

In 2001, the Federal Communications Commission (FCC) allocated an unlicensed 7-GHz wide band in the radio-frequency (RF) spectrum from 57 to 64 GHz for wireless communications [1]. This is the widest portion of RF spectrum ever allocated in an exclusive way for wireless unlicensed applications, allowing multi-gigabit-per-second wireless communications. Other countries worldwide have allocated the 60-GHz band for unlicensed wireless communications [2–5], allowing in principle a universal compatibility for the systems operating in that band. Figure 1 shows the 60-GHz frequency band allocations in USA, Canada, Japan, Australia, Korea, and Europe.

The 60-GHz band is very attractive for its reduced coverage range, which is limited to a few meters as a result of the dramatic attenuation of the signal propagation. This is primarily due to the high path loss at 60 GHz. This reduced coverage range allows several wireless personal area networks (WPANs) to operate closely with low interference.

Moreover, at the millimeter-waves (mm-waves) it is possible to implement very directional antennas, thus allowing the implementations of highly directional communication links. Line-Of-Sight (LOS) communication may help in alleviating the design challenges of the wireless transceivers. All together, these characteristics of the 60-GHz radio channel have attracted the interests of both industry and academy.

One of the most promising applications that will benefit from the huge amount of bandwidth available in the 60-GHz range is the uncompressed High-Definition (HD) video communication [6]. The reasons that make the uncompressed video streaming attractive are that the compression and decompression (codec) in transmitters and receivers, respectively, exhibit some drawbacks such as latency which is unacceptable in real time applications (e.g., videogames), and compatibility issues between devices that use different codec techniques. To date, this research has reached a considerable level of maturity, and the first commercial products are appearing on the market [7].

In addition to the previous mass-market applications, it is also interesting to consider the potential opportunity offered by wireless body-centric networks [8, 9]. These emerging applications have attracted the interests of several research groups worldwide. To date, most of the research efforts have been limited to antennas and propagation, and addressed to scenarios for military applications [10].

The feasibility of 60-GHz SoC transceivers for wireless body-centric communications is still not addressed. The feasibility for wireless uncompressed video communications has reached an advanced level of development, mainly limited to fixed communication infrastructures (e.g., home video, etc.), demonstrating the feasibility in advanced microelectronic technologies. In spite of all this, the idea of translating these developments directly into wireless body-centric communications could be unsatisfactory, since these last applications require ad hoc developments characterized by high mobility (i.e., wearable devices), and thereby very low power consumptions that can be supported by light batteries.

Moreover, despite the development of military applications which can rely on large investments, the opportunity to justify the development and fabrication costs of SoC implementations in advanced microelectronic technologies would require a potential market of several million units. With this in mind, it is interesting considering the hypothesis that this emerging technology, currently explored for military applications, could be extended also to a number of civil applications, allowing a justification of costs and advancing of technology for the benefits of humanity. In particular, for the increasing needs of communication, sensing, and networking for biomedical and environmental applications. Despite it could be not easy to figure out the details of the possible future civil applications, it is still possible to envisage application scenarios for the future challenges of the information and communication society, such as smart cities [11], augmented reality [12], personalized health [13], sport and fitness [14], emergency operators [15], and any other potential needs of interfacing electronic systems, communication, and data infrastructures (e.g., wireless local area networks, cellular phone networks, satellite networks, cloud computing networks, etc.) with the biological and environmental systems, supporting mobility, continuity, and diversity of services in a variety of scenarios including urban (i.e., hospitals [16]) and rural environments.

Therefore, considering that the feasibility of wireless body-centric communications is dependent on the feasibility of SoC transceivers, currently not addressed by the research community, our objective in this chapter is to introduce and then accelerate the research and development of this interesting frontier of the emerging wireless applications. In particular, on the basis of the latest advances of the microelectronic CMOS technology [17–19]—today superior to all the other commercial technologies and capable of providing transistors with maximum cut-off in excess of 300 GHz and low noise figure (NF) (e.g., lower than 2 dB at 60 GHz)—we report hereinafter a preliminary feasibility of SoC transceivers in nano-scale CMOS technology in support of the needs of 60-GHz wireless body-centric communications.

Wireless Body-Centric Communications

The continuing miniaturization of electronic devices, together with the development of wearable computing technologies, leads toward the realization of a series of devices that can be carried on the human body [8]. Before stepping into the details of the specific design challenges for the SoC implementations of radio transceivers in nano-scale CMOS technology, it is worth summarizing in short the typical scenarios of the body-centric wireless communications.

In particular, the concept of wireless body area networks (WBANs) consists in a network of several sensors placed around the human body that can communicate information via wireless link. These sensors can monitor several vital parameters (ECG, EEG, glucose level, etc.) and transmit the information through a wireless link to a central node. In some cases, the sensor itself may use RF contactless sensing technologies [16], which remove the need of contact, reduce the encumbrance, and improve the wearability [20–23]. As mentioned earlier, the main advantages of exploiting the 60 GHz wireless link are the very high data rates of multi-Gb/s for short range applications, covertness, high frequency reuse, reduced interference, narrow antenna beam width, and small antenna size [10, 24]. We can distinguish three levels of communication [8] (see Fig. 2):

- *In-body* wireless transceivers are implanted in the body and most of channel is inside the body (for example a sensor placed on a broken bone to monitor its recovering). In Fig. 2a, the in-body sensor is represented with an orange spots, the central node with blue spots, and the wireless link between them with orange arrows.
- *On-body* wireless transceivers are placed on the surface of the body or on a wearable garment. This can be the case of external sensors as respiratory and heart-rate monitors [25, 26], EEG, motion detectors, etc. In this case most of the channel is on the surface of the body. In 2 and 2b, the sensors are represented by the green spots, while the central nodes by the blue spots. The on-body wireless link is represented by the green arrows.
- *Off-body* wireless transceivers are placed on the surface of the body, but they communicate outside the body, to a central node worn by other persons (e.g., as

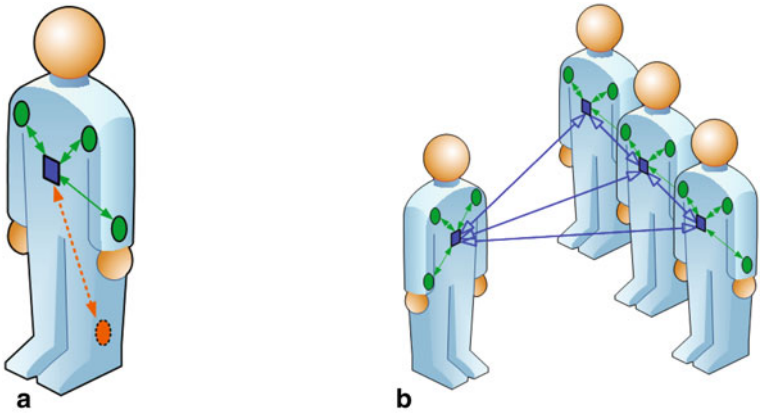

Fig. 2 **a** Scenario for in-body (*orange link*, *dashed circle* and *line*) and on-body (*green links*, *solid circles* and *lines* with *filled arrows*) wireless communications. **b** Scenario for on-body (*green links*) and off-body (*blue links*, *solid squares* and *lines* with *empty arrows*) wireless communication. Here, the devices in *blue* operate as coordinators

in [10], therein limited to military applications), or to an external communication infrastructure of the surrounding environment (not shown). In Fig. 2b, central nodes and their off-body wireless links are represented by the blue spots, while on-body sensors and their on-body wireless links are in green.

Preliminary Feasibility Analysis of 60-Ghz System-on-a-Chip Transceivers for Wireless Body-Centric Networks

In this Section we report the link budget analyses for 60-GHz wireless transceivers for wireless body-centric communications (see Fig. 2), compliant to the millimeter-wave High Rate Wireless Personal Area Networks standard IEEE 802.15.3c-2009 [27]. The results of the link budget analyses are exploited to carry out some preliminary evaluations on the feasibility of SoC transceivers by taking into account the capabilities and limitations of the modern nano-scale CMOS technologies and the latest advances in wearable textile antennas.

The IEEE 802.15 WPAN Task Group 3c (TG3c) [27] provides a reference for systems operating in the RF spectrum 57–66 GHz in United States (57–64 GHz), Canada (57–64 GHz), Australia (59.4–62.9 GHz), and Europe (57–66 GHz). This standard specifies that the RF spectrum 57–66 GHz is divided in four channels of 2.16 GHz, as shown in Table 1 (not available in all countries, depending on the RF spectrum allocation for 60 GHz unlicensed wireless communication by the regulatory agencies).

The standard supports a variety of modulation and coding schemes, that support up to 5 Gb/s. For the high-data rate physical layer (HRP), the modulation parameters

Table 1 Millimetre-wave physical layer channelization

Channel number.	Start frequency	Stop frequency
1	57.240	59.400
2	59.400	61.560
3	61.560	63.720
4	63.720	65.880

Table 2 High-data rate physical layer (HRP) modulation parameters

Parameter	Value
Bandwidth	1.76 GHz
Reference sampling rate	2.538 GS/s
Number of subcarriers	512
FFT period	Ref. sampling rate/number of subcarriers
Guard interval	64/reference sampling rate
Symbol duration	FFT period + guard interval
Number of data subcarriers	336
Modulation	16QAM-OFDM

are specified as in Table 2. Convolutional channel coding may be employed to attain the desired Bit Error Rate (BER). For instance, let us assume that we are interested in achieving a quasi-error free communication (BER $> 10^{-11}$) between two on-body transceivers. For a system employing the modulation parameters as shown in Table 2, with forward error correction made by Reed–Solomon (216/224) block code and inner convolutional code (2/3), a signal-to-noise ratio (SNR) at the input of the receiver equal to 17 dB is required [28].

For the low-data rate physical layer (LRP), the modulation parameters are specified as in Table 3. The LRP supports largely lower data rates than the HRP, up to a maximum of 10.2 Mb/s.

In the United States the maximum effective isotropic radiated power (EIRP) limits imposed by the Federal Communication Commission (FCC) [1] are 27 dBm for indoor applications and 40 dBm for outdoor applications [27], while in Japan and Australia those limits are set equal to 57 and 51.8 dBm [27]. In Europe those limits are set to 25 dBm and 40 dBm for indoor and outdoor applications, respectively [29].

Table 3 Low-data rate physical layer (LRP) modulation parameters

Parameter	Value
Bandwidth	92 MHz
Reference sampling rate	317.25 MS/s
Number of subcarriers	128
FFT period	Ref. sampling rate/number of subcarriers
Guard interval	28/reference sampling rate
Symbol duration	FFT period + Guard interval
Number of data subcarriers	30
Modulation	BPSK-OFDM

On-Body High Rate Line-of-Sight Communication

Let us consider the scenario shown in Fig. 2a. The radio communication occurs within a maximum of 2 m (i.e., a reasonable maximum distance between devices) around the human body.

The literature reports 60-GHz wearable textile antennas with antenna gain (G_{ANT}) of 12 dB [30].

As for the achievable performance of millimetre-wave CMOS transceiver, Chen and Niknejad [31] report a 60 GHz power amplifier with 1-dB output, compression point higher than 15 dBm, and Mitomo et al. [32] report a complete receiver with a total NF of 14 dB.

Thus, consider a CMOS transceiver with the following performance, achievable with modern nano-scale CMOS technologies:

- transmitted power P_{TX} equal to 15 dBm
- receiver NF equal to 14 dB
- signal bandwidth equal to 1.76 GHz centered at 60 GHz.

Then, the receiver sensitivity (S) amounts to:

$$S = -174\ \mathrm{dBm/Hz} + \mathrm{NF} + 10 \times \log_{10}(BW) + \mathrm{SNR} = -50\ \mathrm{dBm} \tag{1}$$

The free space path loss (PL) amounts to:

$$PL = 20 \times \log_{10}\left(\lambda / (4\pi d)\right) = 74\ \mathrm{dB} \tag{2}$$

where $\lambda = f/c = 5$ mm ($f = 60$ GHz, $c = 3 \times 10^8$ m/s) and $d = 2$ m.

In the case of LOS communication, the received power (P_{RX}) is equal to:

$$P_{\mathrm{RX}} = P_{\mathrm{TX}} + 2 \times G_{\mathrm{ANT}} - PL = -35\ \mathrm{dBm} \tag{3}$$

Thus, the loss margin (LM) left for shadowing, body loss, polarization mismatch, and other losses, is equal to:

$$LM = P_{\mathrm{RX}} - S = 15\ \mathrm{dB} \tag{4}$$

On-Body High Rate Nonline-of-Sight Communication

In the previous section, we considered on-body LOS communication. In spite of this, the case offers an opportunity to derive some considerations, this communication scenario is quite unrealistic since the position of each on-body transceiver relative to the others varies as a consequence of the human body movements. Therefore, a more appropriate scenario would be to consider the case in which omni-directional

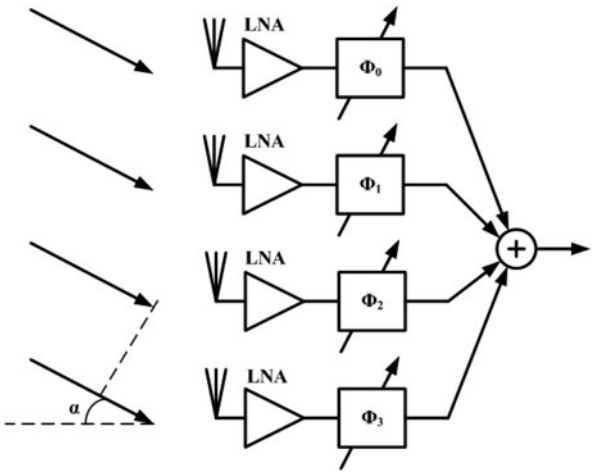

Fig. 3 A four-element phased array receiver. Φ_i are the phase shifters, α is the angle of incidence of the EM radiation with respect to the receiver

antennas ($G_{ANT} = 1$) [33] are employed in order to allow a non-LOS communication. Moreover, the considerations that could be derived for this communication scenario could be extended in part also to the case of off-body communication (see Fig. 2b).

In the case of on-body non-LOS communication, we can easily verify that we are not able to match the desired specifications anymore, and that a minimum P_{TX} of 24 dBm ($P_{TX} = S - PL = -50 + 74 = 24$ dBm) is required in order to have the desired SNR at a distance of 2 m from the transmitter, without any loss margin left.

In order to meet the initial requirements also by employing omni-directional antennas, a phased array approach could be adopted. The overall transceiver can be implemented on silicon by integrating multiple parallel transceivers on the same silicon die, connected to an array of antennas (see Fig. 3). In this way, not only the antenna beam-form can be steered (by selecting appropriately the value of the phase shifting Φ of each path) in order to improve the link between transmitter and receiver, but also the specifications of transmitters and receivers are more relaxed, since the power delivered will be N times that delivered by a unit element and the receiver NF is reduced of $10 \times \log_{10} N$ dB (N is the number of transceivers in parallel). For instance, a number of more than ten independent antennas and partial radio chains have been employed in this; the first solution recently appeared in the literature [34].

Let us suppose to have a SoC phased array transceiver made by N transmitters and N receivers in parallel, with $N = 10$. In this case, the total transmitted power is equal to:

$$P_{TX} = 15 \text{ dBm} + 10 \times \log_{10}(N) = 25 \text{ dBm} \tag{5}$$

The equivalent receiver NF is equal to:

$$\text{NF} = 14 \text{ dB} - 10 \times \log_{10}(N) = 4 \text{ dB} \tag{6}$$

The total receiver sensitivity amounts to:

$$S = 174 \text{ dBm/Hz} + \text{NF} + 10 \times \log_{10}(BW) + \text{SNR} = -60 \text{ dBm} \tag{7}$$

The received power is equal to:

$$P_{RX} = P_{TX} - PL = -49 \text{ dBm} \tag{8}$$

Thus, in this case, we have again a *LM* left for shadowing, body loss, polarization mismatch, and other losses, that is equal to:

$$LM = P_{RX} - S = 11 \text{ dB} \tag{9}$$

On-Body and Off-Body Low Rate Communication

Let us consider now the case in which a high data rate is not required, and thus the 60 GHz transceivers can communicate by exploiting the LRP. Let us suppose that the transceivers are equipped with omni-directional antennas. Therefore, the following considerations apply to both on-body and off-body communication scenarios. Let us suppose also that SNR requirements are the same as for the HRP case (this is a worsening condition: the use of a simpler modulation scheme in LRP with respect to HRP relaxes largely SNR requirements to achieve a certain BER). In this case it is possible to realize the wireless communication even by means of single transceivers, because of the reduced minimum sensitivity due to the smaller communication bandwidth ($BW = 92$ MHz) of the LRP with respect to the HRP (and hence less noise floor).

$$S = -174 \text{ dBm/Hz} + \text{NF} + 10 \times \log_{10}(BW) + \text{SNR} = -63 \text{ dBm} \tag{10}$$

The received power is

$$P_{RX} = P_{TX} - PL = -59 \text{ dBm} \tag{11}$$

Thus, even with a single transmitter and receiver, in this case we could still have a *LM* left, equal to:

$$LM = P_{RX} - S = 4 \text{ dB} \tag{12}$$

Conclusions

In this chapter we presented the opportunity offered by the emerging wireless body-centric networks, envisaging their applications to a number of possible future civil applications, beyond the current interests limited to military applications. In particular, we addressed the opportunities of implementing SoC transceivers in support of the needs required by the wireless body-centric networks, be they for on-body or off-body communication scenarios. In detail, we focused on the feasibility through preliminary analyses considering the characteristics of the 60-GHz radio channel,

international standard regulations, current performance and limitations of nano-scale CMOS technology, and integrated circuits designs, as well as the performance of wearable antenna designs.

From the preliminary feasibility analyses reported herein it is possible to derive that the performance available at the state of the art for CMOS millimeter-wave wireless transceivers and millimeter-wave wearable antennas may offer concrete opportunities to realize wireless body-centric networks by exploiting the 60-GHz frequency band. However, the results of these preliminary considerations on feasibility should be revised in the light of the on-field experimental validations and observations in presence of shadowing, body loss, and other nonidealities, which may have a significant impact on the operation of the wireless body-centric communications.

Acknowledgement This work was supported in part by the Science Foundation Ireland (SFI) and in part by Irish Research Council (IRC).

References

1. Federal Communications Commission. Code of Federal Regulation, title 47 Telecommunication, Chapter 1, part 15.255, 2001.
2. MIC, Frequency Assignment Plan, March 2008. http://www.tele.soumu.go.jp/e/adm/freq/search/share/plan.htm. Regulation for enforcement of the radio law 6-2-4 specified low power radio station (11) 59–66 GHz band. Accessed 16 March 2013.
3. ACMA. Radio communications (low interference potential devices) Class License Variation 2005 (no. 1), August 2005.
4. Ministry of Information Communication of Korea. Frequency Allocation Comment of 60 GHz band, April 2006.
5. ETSI DTR/ERM-RM-049. Electromagnetic compatibility and radio spectrum matters (ERM). System reference document. Technical characteristics of multiple gigabit wireless systems in the 60 GHz range, March 2006.
6. WirelessHD. http://www.wirelesshd.org. Accessed 16 March 2013.
7. Silicon Image. http://www.siliconimage.com/solutions/wireless/. Accessed 16 March 2013.
8. Hall PS, Hao Y. Antennas and propagation for body-centric wireless communications. Norwood, MA: Artech House; 2006.
9. Hall PS, Hao Y. Antennas and propagation for body centric communications. in European Space Agency, (Special Publication) ESA SP, vol. 626 SP, Oct 2006.
10. Cotton SL, Scanlon WG, Madahar BK. Millimeter-wave soldier-to-soldier communications for covert battlefield operations. IEEE Comm Magazine. 2009;47(10):72–9.
11. Welcome to the Smarter City. http://www-03.ibm.com/innovation/us/thesmartercity. Accessed 16 March 2013.
12. Sutherland I. Augmented reality: "The Ultimate Display". Proceedings of IFIP Congress, pp. 506–8, 1965
13. Personalized Health Care. http://www.hhs.gov/myhealthcare. Accessed 16 March 2013.
14. Patel M, Wang J. Applications, challenges, and prospective in emerging body area networking technologies. IEEE Wireless Commun. 2010 Feb;17(1):80–8.
15. Curone D, Secco EL, Tognetti A, Loriga G, Dudnik G, Risatti M, Whyte R, Bonfiglio A, Magenes G. Smart garments for emergency operators: The ProeTEX project. IEEE Trans Inf Technol Biomed. 2010 May;14(3):694–701.
16. Kyro M, Takizawa K, Haneda K, Vainikainen P. Validation of statistical channel models for 60 GHz radio systems in hospital environments. IEEE Trans Biomed Eng. 2013 May;60(5): 1458–62.

17. Niknejad A. 0–60 GHz in four years: 60 GHz RF in digital CMOS. IEEE Solid-State Circuits Newslett. 2007 Spring;12(2):5–9.
18. Marcu C, et al. A 90 nm CMOS low-power 60 GHz transceiver with integrated baseband circuitry. IEEE J Solid-State Circuits. 2009 Dec;44(12):3434–47.
19. Yao T, et al. Algorithmic design of CMOS LNAs and PAs for 60-GHz radio. IEEE J Solid-State Circuits. 2007 May;42(5):1044–57.
20. Mincica M, Pepe D, Tognetti A, Lanata A, De Rossi D, Zito D. Enabling technology for heart health wireless assistance. IEEE International Conference on e-Health Networking Applications and Services (HealthCom) 2010, Aug. 2010, pp. 36–41.
21. Zito D, et al. Wearable system-on-a-chip radiometer for remote temperature sensing and its application to the safeguard of emergency operators. IEEE International Conference of IEEE Engineering in Medicine and Biology Society, Lyon, Aug. 2007, pp. 5751–4.
22. Zito D, et al. Wearable system-on-a-chip UWB radar for health care and its application to the safety improvement of emergency operators. IEEE Proceedings of International Conference of the IEEE Engineering in Medicine and Biology Society, Lyon, Aug. 2007, pp. 2651–4.
23. Bonfiglio A, De Rossi D, Editors. Wearable monitoring systems. New York: Springer; 2011. ISBN 978-1-4419-7384-9.
24. Park C, Rappaport TS. Short-range wireless communications for next-generation networks: UWB, 60 GHz millimeter-wave WPAN, and ZigBee. IEEE Commun Mag. 2007 Aug;14(4): 70–8.
25. Zito D, Pepe D, Mincica M, Zito F. A 90 nm CMOS SoC UWB pulse radar for respiratory rate monitoring. 2011 IEEE International Solid-State Circuits Conference, Digest of Technical Papers (ISSCC), pp. 40–1, 20–24 Feb. 2011.
26. Zito D, Pepe D, Mincica M, Zito F, Tognetti A, Lanatà A, De Rossi D. SoC CMOS UWB pulse radar sensor for contactless respiratory rate monitoring. IEEE Transac Biomed Circuits Systems. 2011 Dec;5(6):503–10. (Special Issue on ISSCC 2011).
27. IEEE 802.15 WPAN Task Group 3c (TG3c) Millimeter Wave Alternative PHY. http://ieee802.org/15/pub/TG3c.html. Accessed 16 March 2013.
28. Pepe D, Zito D. System-level simulations investigating the system-on-chip implementation of 60-GHz transceivers for wireless uncompressed HD video communications. In: Michalowski T, Editor. Applications of MATLAB in Science and Engineering. Intech Open-Access Publisher, Aug. 2011
29. Final draft ETSI EN 302 567 V1.1.0 (2009–01). Broadband Radio Access Networks (BRAN); 60 GHz Multiple-Gigabit WAS/RLAN systems, harmonized EN covering the essential requirements of article 3.2 of the R & TTE Directive, 2009.
30. Chahat N, Zhadobov M, Le Coq L, Sauleau R. Wearable endfire textile antenna for on-body communications at 60 GHz. IEEE Antennas Wireless Prop Lett. 2012;11:799–802.
31. Chen J., Niknejad AM. A compact 1 V 18.6 dBm 60 GHz power amplifier in 65 nm CMOS. ISSCC Dig. Tech. Papers, pp. 432–3, Feb 2011.
32. Mitomo T, et al. A 2-Gb/s throughput CMOS transceiver chipset with in-package antenna for 60-GHz short-range wireless communication. IEEE J Solid-State Circuits. 2012 Dec;47(12): 3160–71.
33. Ranvier S, et al. Low-cost planar omnidirectional antenna for mm-wave applications. IEEE Antennas Wireless Prop Lett. 2008;7:521–3.
34. Gilbert JM, Doan CH, Emami S, Shung CB. A 4-Gbps uncompressed wireless HD A/V transceiver chipset. IEEE Micro. 2008 Mar-Apr;28(2):56–64.

Low-Power 60-GHz CMOS Radios for Miniature Wireless Sensor Network Applications

Kuo-Ken Huang and David D. Wentzloff

Abstract This chapter discusses several design considerations for low-power 60-GHz complementary metal-oxide semiconductor (CMOS) radios for wireless sensor network applications at the cubic-mm scale. A background study is provided first, followed by a discussion of challenges to provide a practical scope of the hardware design for the readers. Finally, a compact 60-GHz CMOS transmitter with on-chip frequency-locked loop is presented as an example. This transmitter utilizes the on-chip patch antenna as both a radiator and a frequency reference. This eliminates the bulky off-chip crystal, is FCC compliant, and ensures the node transmits at the antenna's peak efficiency point, making this a cost-effective 60-GHz radio for mm-scale sensor nodes.

Keywords Wireless sensor networks · CMOS · Transmitter · 60 GHz · Low-power · Crystal replacement · Frequency reference · Integrated antenna

Introduction

The continual evolution of computing devices has significantly changed daily life over the past several decades. In the 1950s, mainframe computers occupied large rooms because of their substantial size and provided the basic data computation for hundreds of employees in a company. Nowadays, smartphones have become the platform of personal computing, as predicted by Bell's Law [1]. Emerging applications such as wireless sensing, smart health care, unobtrusive surveillance, etc. will demand ubiquitous computing, which will continue to drive the computing platform down to the mm scale, while also driving production volume of these devices up to 100s to 1,000s per person. According to Bell's Law, a new class of computers will dominate the market approximately every decade [1]. Gordon Bell defines a computer class as a set of computers with similar cost, programming environment, network, and user interface. He postulates that each class undergoes a standard product life

D. D. Wentzloff (✉) · K.-K. Huang
Electrical Engineering and Computer Science,
University of Michigan, Ann Arbor, USA
e-mail: wentzlof@umich.edu

M. R. Yuce (ed.), *Ultra-Wideband and 60 GHz Communications for Biomedical Applications,* DOI 10.1007/978-1-4614-8896-5_10,

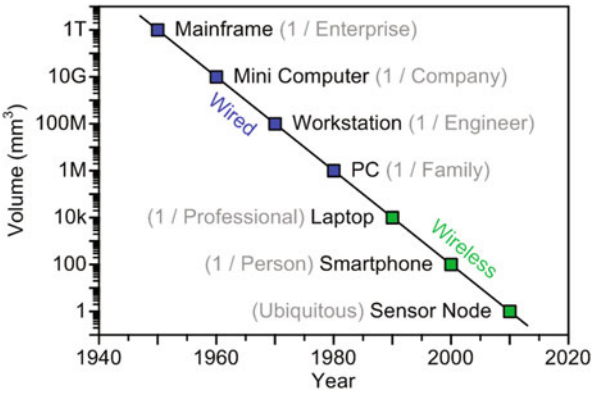

Fig. 1 Scaling and production trend of computing devices over several decades [1]

cycle of growth and decline. Based on prior market trends, a new computer class has come into existence approximately every decade, and each successive class has resulted in a 100-fold reduction in volume. Figure 1 shows the scaling and production trend of computing devices over several decades. Computers progressed from the mainframe in the early 1950s, through minicomputers, workstations, personal computers (PCs), and laptops, to the class of smartphones in the 2000s. Based on the trends, a new computer class has in fact emerged approximately every decade, each class resulting in both a reduction in unit cost and a 100-fold increase in production volume [2].

The next computer class is expected to be even smaller and more pervasive—the class of cubic-mm-scale devices. Ubiquitous sensing is projected to reach volumes of 1,000 sensors per person by 2017 [3]. Considering that today we are surrounded by about 100 sensors while at work, in the car, and at home, this target does not seem that far off. At the mm scale, there is a growing demand for "smaller and smarter" devices in applications such as biomedical implants and unobtrusive monitoring. Wireless sensor networks (WSNs) are perceived as the next big step in the decades-long trend toward smaller, more ubiquitous computing. A WSN consists of distributed autonomous sensor nodes to monitor the environmental conditions around them, such as temperature, vibration, imaging, and sound, etc. Each node is made up of components to process, sense, and communicate with other nodes in the network, and to cooperatively pass their data through the network to a main location [4–8]. WSNs eliminate the need for costly and obtrusive wiring between sensors, allowing sensors to be deployed in almost any location, which is promising for many emerging applications (Fig. 2).

Cubic-mm Wireless Sensor Nodes

The requirements on a WSN can vary widely depending on the application. The hardware design plays an important role for many of these applications. Compact hardware, wireless connectivity, and local processing, along with long node lifetime

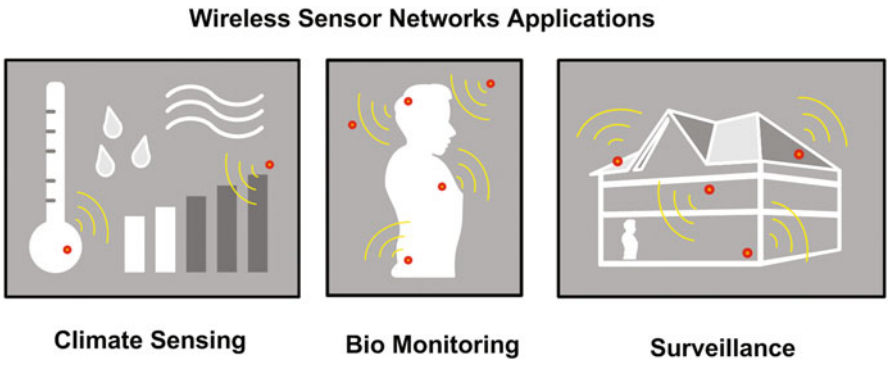

Fig. 2 Wireless sensor network applications

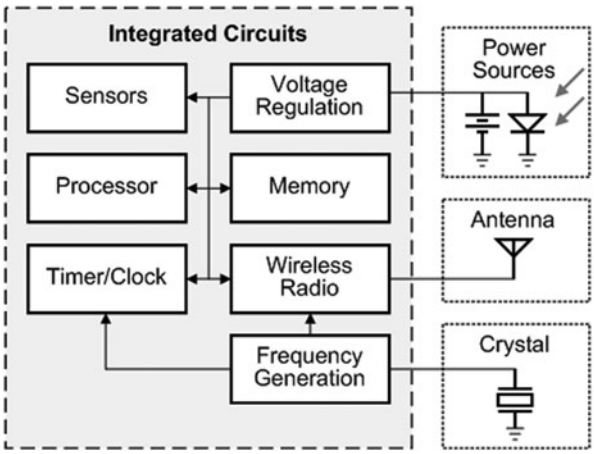

Fig. 3 Block diagram for a typical wireless sensor network (WSN) node

are generally desirable, nonetheless, quite challenging. In this section, we will start with the conventional WSN node and then explain the difficulties of realizing a low-power mm-scale WSN radio.

Conventional Wireless Sensor Node

Figure 3 shows the block diagram of a typical integrated WSN node. Each node generally has one to five sensors (e.g., temperature, pressure, accelerometer), a digital signal processor (DSP), voltage regulation and power management controller, a radio frequency (RF) front end and antennas for wireless communication, a battery as the energy source, and a crystal for a frequency reference. Among the building blocks, the power source, antenna, and the crystal are the hardest components to integrate in silicon [4], which is desirable for lowering cost and miniaturization of

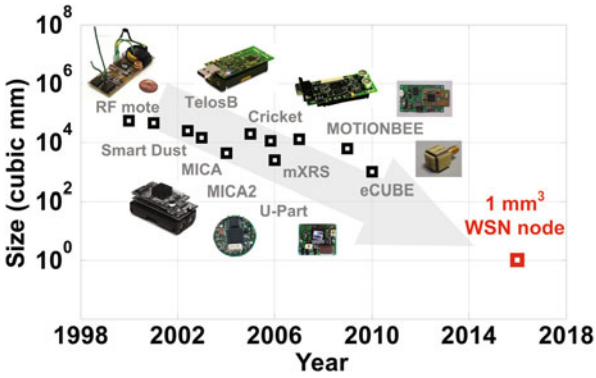

Fig. 4 Size reduction trend of integrated wireless sensor network (WSN) nodes over years

the node. Figure 4 summarizes commercially available integrated WSN nodes over the past decade. We can see there is a clear trend of size reduction for the WSN nodes [9]. In the late 1990s, WSN nodes were composed of multiple components on a printed circuit board (PCB) as shown in Fig. 4. These nodes consistently use commercial-off-the-shelf (COTS) components, and as a result, their sizes are in the tens of cubic centimeters. Higher levels of integration and better system-level node design are pushing this to the mm scale. Nonetheless, there are few bottlenecks in cubic-mm WSN system integration that need to be solved to achieve long lifetimes and small volumes.

mm-Scale Energy Storage: Microbatteries

Rechargeable batteries are being manufactured today at the mm scale, termed microbatteries, by using solid-state lithium technology. These batteries are manufactured on wafers with a planar process and with connections on the top side, similar to integrated circuits (ICs), and they can be diced with sub-mm dimensions. Also like ICs, no special packaging is required once the batteries are fabricated; therefore, they are amenable to die stacking and integrating with other silicon ICs in a stack. However, these microbatteries have limited capacity and small peak current due to the direct relationship between capacity and volume [10–17]. For a $1.38 \times 0.85 \times 0.15$ mm custom lithium-ion (Li-ion) battery from Cymbet Corporation, the capacity is only 1 μAh (Fig. 5) and the maximum discharge current is only 10 μA [11]. This presents direct challenges on the radio circuits, which typically consume > 100 μW when active. As a result, for a node to survive longer, it must be duty-cycled heavily and energy must be harvested from other sources to supplement battery power. From a circuit design point of view, energy usage must be reduced by clever circuit techniques. The radio and oscillators easily dominate system energy usage if they are operated continuously to maintain synchronization for WSN nodes to communicate at the same frequency band [18]. A phase-locked loop (PLL) with a crystal reference

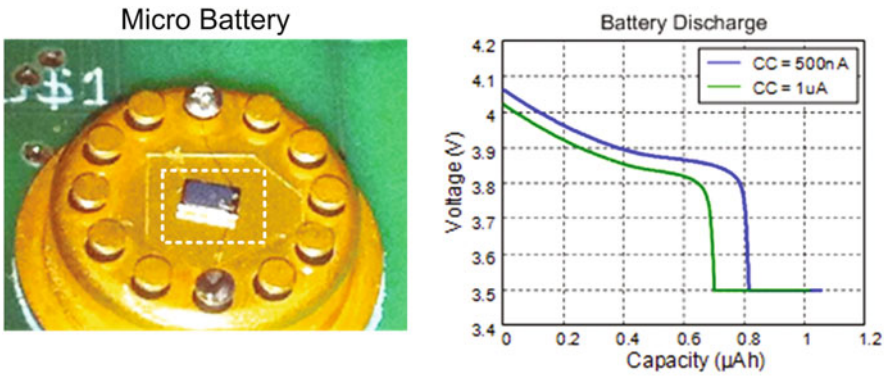

Fig. 5 Micrograph of the Cymbet microbattery and its discharge curves

is typically used to accurately set the center frequency of the radio [19]. Reducing the RF synchronization power consumption can greatly improve the WSN node lifetime and alleviate the burden of cubic-mm-scale microbatteries.

mm-Scale Frequency References

A frequency reference provides a stable frequency over process, voltage, and temperature (PVT) variations for synchronization of a communication system. The accuracy requirement depends on the system specifications (e.g., frequency allocations, modulation type, etc.) [18], and can be achieved through different ways. A quartz crystal is the most common source for a frequency reference. It provides excellent stability with PVT variations. However, its size has not scaled down significantly with processes or frequency. Furthermore, crystals require a piezoelectric process and special packaging, which are incompatible with monolithic integration for ICs. In order to achieve stable oscillation out of crystals, a certain amount of driving power is still necessary [20]. Figure 6 shows a COTS WSN node, the TelosB [24]. The 32 kHz crystal is highlighted with a red square, illustrating the volume and packaging of these references. Therefore, bulky size and power become the bottlenecks for using crystals at the mm scale. Recently, microelectromechanical systems (MEMS) and complementary metal-oxide semiconductor (CMOS) references have been demonstrated with near-crystal accuracies [20–23]. Table 1 shows a comparison of compact frequency references made of crystal, MEMS and CMOS. These frequency accuracies are acceptable for typical WSN node specifications; however, powers are high and none of their sizes are below 1 mm^3. A compromise must therefore be made on the frequency accuracy, in order to allow a stable frequency reference to be integrated in CMOS at the mm scale, along with other WSN circuits, with a power consumption that better matches what can be supported by a microbattery.

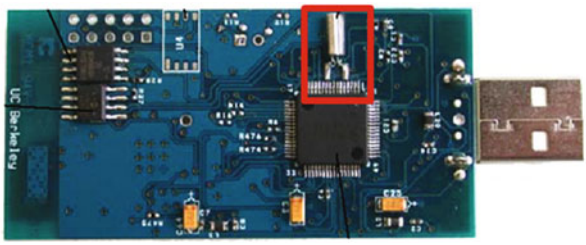

Fig. 6 A 32-kHz crystal on wireless sensor network (WSN) node, TelosB [24]

Table 1 Comparison of compact frequency references

	Crystal [21]	MEMS [22]	CMOS [23]
Manufacturer	Vectron International	SiTime	Silicon Labs
Volume	9.6 mm^3	4.5 mm^3	11.5 mm^3
Accuracy	25 ppm	50 ppm	150 ppm
Power	82.5 mW	72.6 mW	26.4 mW

MEMS microelectromechanical systems, *CMOS* complementary metal-oxide semiconductor

mm-Scale Antennas

Among the building blocks in a WSN node, the antenna plays a critical role because it is traditionally off-chip for better performance, and its size dominates at least one dimension of the node. Antennas integrated in a CMOS process have a size advantage over external packaged antennas; however, reducing antenna size at a fixed frequency, in general, results in reduced performance [25]. Antennas can be integrated directly on-chip, but at the mm scale, the operating frequencies need to be at least 10 GHz for good radiation efficiency [9]. However, operating at higher frequency has other disadvantages. First, the path loss in the wireless channel increases [25]. As a result, more signal power is lost for a fixed communication distance. Second, RF front end circuits that operate at these higher frequencies will consume more power. On-chip antennas seem to be a good candidate to meet the mm^3 volume requirement of future sensor nodes, but there are several design trade-offs to consider.

CMOS technology is preferable nowadays of ICs because of its low cost, decent performance, and ease of integration [32]. Nevertheless, there are several challenges for on-chip antenna integration. First, the area occupied by the antenna and the space for isolating the crosstalk between antenna and active circuits should be considered. Additionally, the lossy silicon P-substrate ($\sim$10 Ω cm) in a CMOS process degrades the antenna performance significantly because energy dissipates in the substrate instead of radiating into the air. Moreover, the design rules in CMOS technology such as metal slotting and density requirements also impact the antenna design. Figure 7 shows the cross section of an on-chip CMOS patch antenna [32]. In this example, the patch radiator is in top metal, with the patch ground plane in an intermediate metal layer, and metal layers below the ground plane are used for routing circuits under the patch (e.g., DSP and memory). This approach suffers from reduced antenna

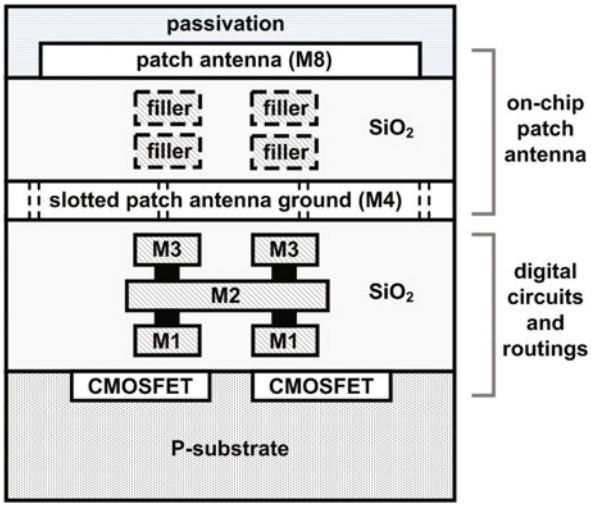

Fig. 7 Layout cross section of an on-chip patch antenna integrated in complementary metal-oxide semiconductor (CMOS) technology

efficiency due to the higher ground plane, but allows for reusing the area below the patch for circuits and routing in a system-on-a-chip (SoC) application. For example, conventional digital circuits typically use four to six metal layers for wire routing; fewer metal layers is feasible, but at the cost of lower circuit density. Consequently, the patch antenna is a good candidate for system integration in CMOS technology because of the better performance (ground shielding) and reusable area beneath the patch ground plane.

A 60-GHz Transmitter for WSNs

The 60-GHz band is an emerging field for miniature radio design because the sizes of the antenna and passive components are at or below mm scale. Recently, several highly integrated CMOS radio systems with on-chip antennas operating at the mm-wave range have been reported [26–29], showing promising opportunities for complete SoC integration. In this section, we will discuss the 60-GHz band allocation and show a design example of a low-power 60-GHz frequency-locked loop (FLL) that can serve as a fully integrated transmitter for WSNs. The transmitter described in this section was designed in a 130-nm CMOS process with eight metal layers, including a thick top metal for RF routing.

60-GHz Wireless Communication

The industrial, science, and medical (ISM) band approved by Federal Communications Commission (FCC) has 7 GHz of bandwidth from 57 to 64 GHz [30]. At 60

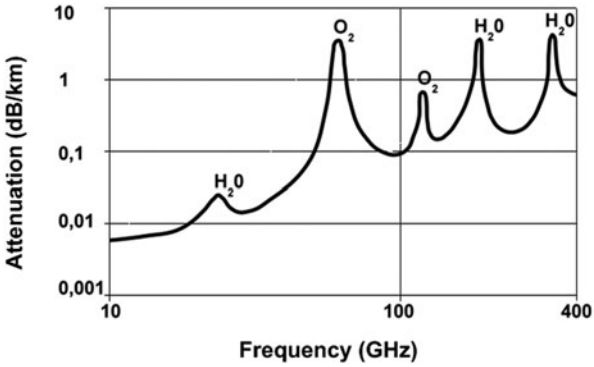

Fig. 8 Atmosphere attenuation of electromagnetic wave versus frequency

GHz, the guided wave length λ in silicon is about 2.5 mm; which is on the same scale as the active circuit blocks implemented in CMOS (e.g., processor, memory, and radio circuits). Furthermore, the elimination of expensive off-chip antennas, path loss, crystal references, and the total size reduction makes 60-GHz operation more appealing for wireless system integration. Sixty gigahertz is also referred to as the oxygen absorption band [31]. As shown in Fig. 8, the oxygen molecule (O_2) absorbs electromagnetic energy due to resonance at different frequencies. The excessive attenuation causes high path loss at 60 GHz. Despite this increased attenuation, the 60-GHz band can still be beneficial for short-range applications like WSNs and wireless personal area networks (WPAN).

60-GHz Antenna-Referenced Frequency-Locked Loop

In order to eliminate the bulky off-chip components and further reduce the size of a fully integrated WSN node, we will discuss a solution of using a 60-GHz on-chip patch antenna as both the radiator and frequency reference in this section. The natural resonant frequency of the patch antenna serves as the frequency reference. The resonant frequency is mainly determined by the physical dimensions of the patch antenna, and the standard deviation due to process variation is around 1,100 ppm. This accuracy level is suitable for, e.g., low-rate communication with a noncoherent energy-detection receiver, commonly used in ultralow power WSN radios. With the antenna as the reference, an FLL circuit to track the reference frequency for RF synchronization is described and implemented. Furthermore, the area beneath the patch antenna ground plane is investigated for containing additional circuits for higher integration. Figure 9 depicts the concept of a complete mm-scale WSN node. By integrating the antenna, frequency reference, RF front end, and digital circuitry onto the same die, a form factor of 1 mm^3 is feasible.

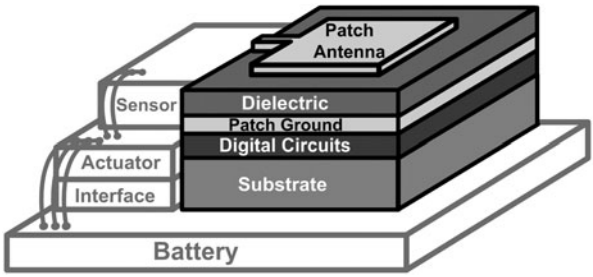

Fig. 9 A miniature fully integrated wireless sensor network (WSN) node system

Patch Antenna Design

As an on-chip radiator, the patch antenna topology is chosen because its ground plane shields the radiating element from the lossy substrate in standard CMOS processes, and thus provides higher radiation efficiency than nonshielded integrated antennas. Moreover, the patch antenna is also a good candidate for system integration because of the reusable area beneath the ground plane for high noise margin digital circuits. The distance between the patch metal layer (top-metal M8) and the ground metal layer determines the height of the patch antenna. The tradeoff between radiation efficiency and height are discussed by Huang and Wentzloff [32]. The analysis suggests that lower antenna height (or implementing the patch ground in a higher metal layer in a CMOS process) results in lower radiation efficiency. In this 130-nm CMOS process, Metal 4 is used as the ground plane, resulting in an antenna height of 14.1 μm. On the basis of simulations, using Metal 4 for the ground plane instead of Metal 1 reduces the radiation efficiency by 15 %, but frees up three metal layers for routing of circuits beneath the antenna. With the center frequency (f_0), dielectric constant of the silicon dioxide (SiO_2) (ε_r), and the height (h), we can calculate the required width (W) of the patch antenna by antenna theory.

$$W = \frac{c}{2f_0\sqrt{\frac{(\varepsilon_r+1)}{2}}}, \tag{1}$$

where c is the speed of light [25]. With the calculated W, we can find the effective dielectric constant ε_{eff}.

$$\varepsilon_{eff} = \frac{\varepsilon_r + 1}{2} + \frac{\varepsilon_r - 1}{2}\left(1 + 12\frac{h}{W}\right)^{\frac{-1}{2}}. \tag{2}$$

It follows that the length of the patch antenna (L) is

$$L = \frac{c}{2f_0\sqrt{\varepsilon_{reff}}} - 0.824h\frac{(\varepsilon_{eff} + 0.3)\left(\frac{W}{h} + 0.264\right)}{(\varepsilon_{eff} - 0.258)\left(\frac{W}{h} + 0.8\right)}. \tag{3}$$

Note that the size of the ground plane layer is greater than the patch dimensions by approximately six times the height all around the periphery to achieve results similar

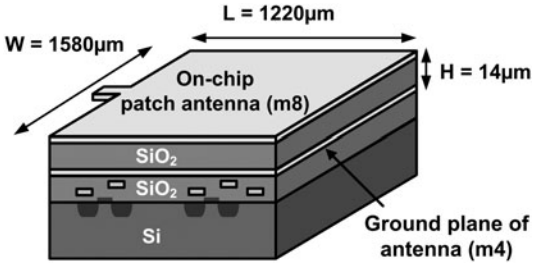

Fig. 10 The dimensions of the 60-GHz patch antenna

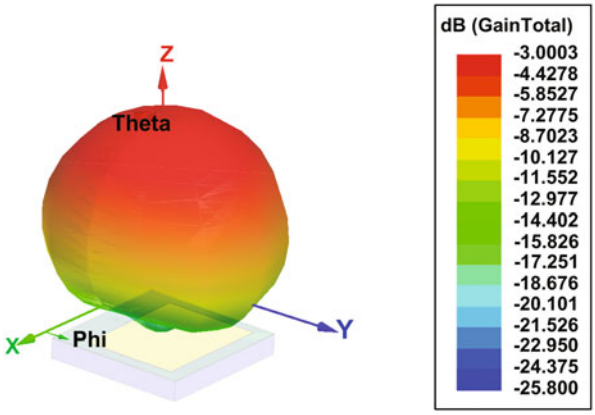

Fig. 11 Radiation pattern of the 60-GHz on-chip patch antenna

to that of an infinite ground plane [25]. Figure 10 illustrates the final dimensions of the patch antenna. The resonant frequency is mainly determined by the width and length that can be verified by back calculating for f_0 from Eqs. 1–3 when W and L are known. The 3σ process variation parameters on length and width of the top metal layer are on the order of 400 ppm, resulting in the same order of accuracy of the resonant frequency of the patch antenna, determined by the first-order antenna theory. The simulated antenna radiation pattern is shown in Fig. 11. The simulation results include the effects of required dummy filling for meeting local metal density requirements, and show that the center frequency is 60.54 GHz with a bandwidth of 920 MHz. The peak antenna gain is -3 dB while the efficiency at resonance is 15.6 %.

Resonant Frequency Detection

Another advantage of the integrated patch antenna at 60 GHz is the ability to design circuits that monitor the standing wave pattern along the edge of the radiator. This allows for detecting the resonant frequency of the antenna, and ultimately using it as a replacement for a crystal reference. To detect the resonant frequency, we will need to understand the physical phenomena on the patch antenna when it is resonating.

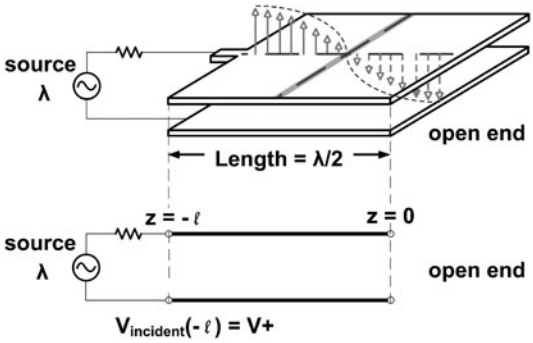

Fig. 12 Simplified lossless transmission line model of the patch antenna

A simplified lossless transmission line model for the antenna is adopted for this analysis. Figure 12 shows the transmission line model corresponding to the patch antenna along the length axis. We can consider the patch antenna as a very wide transmission line, with the feed point being the source terminal, while the other edge behaves as the open end. When the source frequency is exactly at the resonant frequency, the length of the transmission line is equal to λ/2, and a standing wave pattern is generated by the superposition of the incident wave from the source and the reflected wave from the load. At this frequency and under these conditions, the patch antenna radiates at its peak efficiency value. The source end and open end have the strongest electric fields, and those are the radiation edges. Note that there is an electrical null located in the center of the length axis (e.g., $z = -l/2$, where l is the length of the patch), shown as the solid shaded area in Fig. 12. The amplitude of the standing wave on the transmission line as a function of the length can be written in the general form [33]:

$$V(z) = V^{+}(e^{-j\beta z} + \Gamma e^{j\beta z}), \tag{4}$$

where V^{+} is the incident wave magnitude at $z = -l$, β is the propagation constant $2\pi/\lambda$, and Γ is the voltage reflection coefficient. When the load is open, $\Gamma = 1$, thus the magnitude of the standing wave reduces to

$$|V(z)| = \left|V^{+}\right| \sqrt{[2 + \cos(2\beta z)]} \tag{5}$$

Figure 13a shows the magnitude plot of three standing wave patterns corresponding to three different source frequencies. The standing wave pattern according to Eq. 5 changes with frequency, and the corresponding location of the electrical null will move along the transmission line length as frequency changes. When the source frequency is lower than the resonant frequency, the electrical null moves toward the source end. On the other hand, the electrical null will move toward the open end if the source frequency is higher than the resonant frequency. Consider two taps, Z_A and Z_B (Fig. 13a), placed along the edge but at equal distances from the center of the patch, that monitor the magnitude of the standing wave. By monitoring the

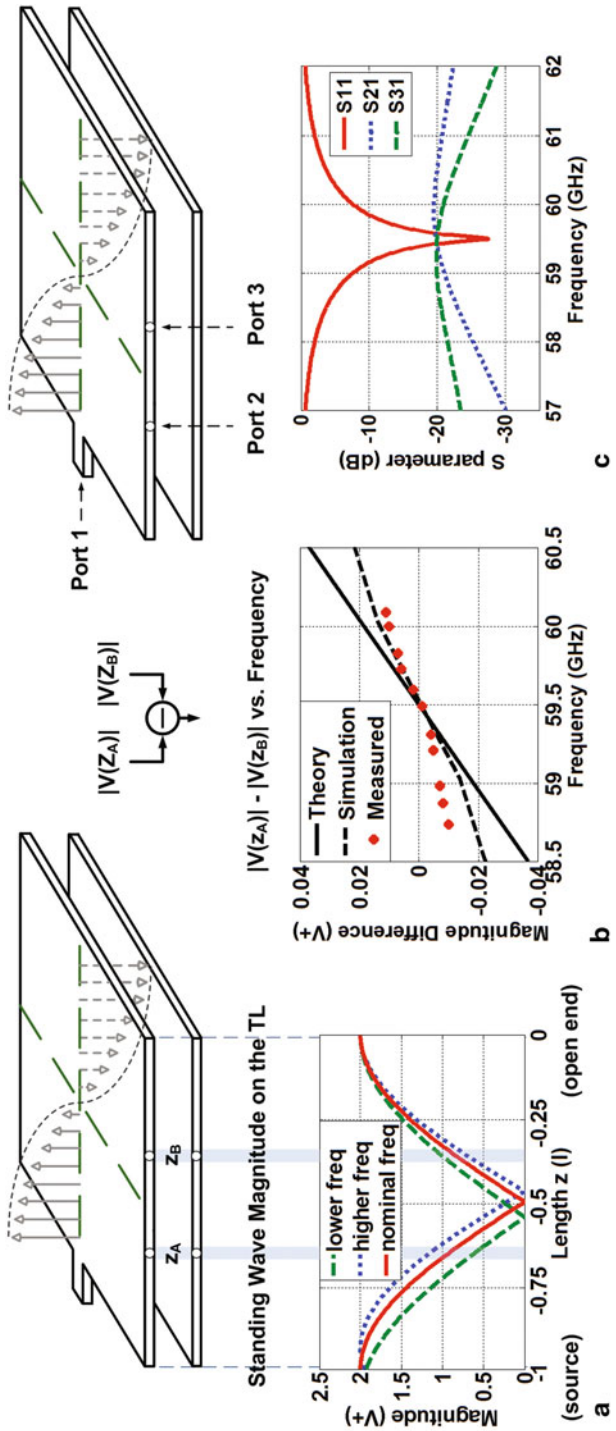

Fig. 13 Center frequency detection of the antenna reference. **a** Standing wave magnitude along the length for three frequencies at source. **b** The difference in magnitude of two taps Z_A and Z_B versus frequency. **c** S-parameter analysis of the three-port antenna reference. TL = Transmission Line

difference in voltage magnitudes at these two taps as frequency changes, a monotonic curve passing through zero will be traced out, with the zero-crossing occurring at the resonant frequency. Figure 13b shows three monotonic curves plotting the difference in magnitude measured at these two taps. The solid line is derived from the lossless transmission line model, assuming perfect matching over the frequency band. The dashed line is obtained from Ansoft HFSS full-Electro-Magnetic (EM) simulations of the three-port antenna reference setup in Fig. 13c, showing the discrepancy due to the limited bandwidth of the patch antenna. Measured results from a 60-GHz patch antenna fabricated in 130-nm CMOS are shown as dots in Fig. 13b, which follow the same trend as the simulation. Figure 13c also shows the S-parameter analysis. S21 and S31 represent the ratio of power delivered onto Z_A and Z_B, respectively, from the antenna feed point at Port 1. The two tap nodes are designed to be high-impedance nodes, so that they do not load the patch antenna significantly, but provide enough voltage swing for envelope detector circuits below the patch to measure the standing wave magnitude. Simulation results show that only 2 % of the power delivered onto the patch antenna is lost on the two tap nodes.

The locations of the two taps along the edge of the antenna depend on several factors. A wider separation between the two taps provides a larger slope of the monotonic curve, thus a larger controller gain in the FLL and more accurate resonant frequency detection. However, the frequency locking range over which the sensed voltage magnitude difference remains monotonic is inversely proportional to the separation between taps. Therefore, if the separation is too wide for a target frequency range, the monotonic characteristic no longer applies, which could result in instability in the FLL. Furthermore, the two envelope detectors would be placed far away from each other on the chip, causing mismatch from separation within the single IC [34], and thus affecting the accuracy of tracking the resonant frequency. In the final layout of the antenna reference, the two taps are equally spaced, 110 μm away from the length center, resulting in a calculated locking range of 8.5 GHz. Another factor that will affect the locking range of the antenna reference is the antenna bandwidth. A larger bandwidth implies a wider locking range. In this case, the antenna bandwidth is around 1 GHz, which provides sufficient range for covering process variation of the patch antennas.

In order to test the antenna resonant frequency and bandwidth, the patch antenna design with the same dimensions as the one in the FLL was fabricated in 130-nm CMOS. Twenty of the patch antennas were tested, all from the same wafer. Figure 14 shows the distribution on measured resonant frequency and bandwidth over 20 replica patch antennas. The mean and standard deviation of the center frequency is 59.7 GHz and 65.1 MHz, respectively. The mean and standard deviation of the bandwidth is 1.03 GHz and 67.9 MHz, respectively. This results in a 3σ variation in center frequency of 3,270 ppm, which is enough to ensure the transmitter is FCC compliant (i.e., it remains in the 60-GHz ISM band). In order for the transmitter to reliably communicate with, e.g., an energy-detection receiver with an identical patch antenna (not included in this work), process variation should not cause the transmitter frequency to fall outside the bandwidth of the receiving antenna. Assuming a worst-case 3σ variation on all parameters from process variation, the 3,270 ppm variation is

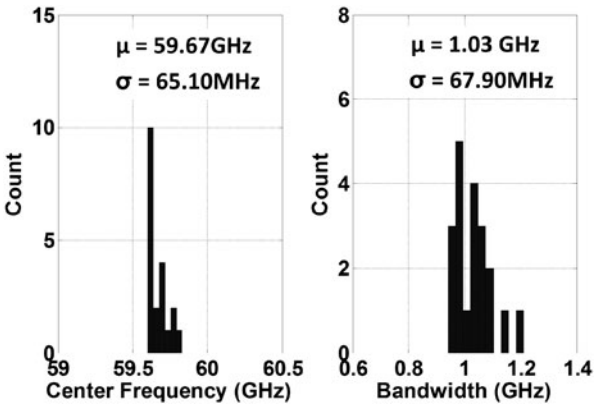

Fig. 14 Measured antenna resonant frequency and bandwidth distribution over 20 replicas

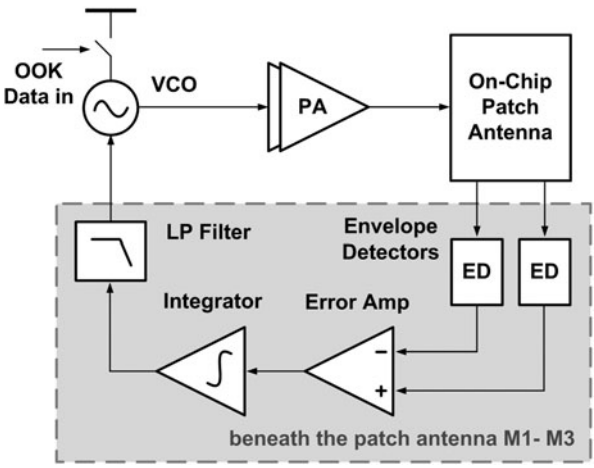

Fig. 15 Block diagram of the 60-GHz FLL. *OOK* on–off keying, *VCO* voltage-controlled oscillator, *PA* power amplifier, *LP* low pass

not enough to prevent two patch antennas from overlapping in frequency responses. On the basis of the measured S11 of 20 dies from a single wafer, no missed alignment between two antennas was observed.

Frequency-Locked Loop

Figure 15 shows the block diagram of the 60-GHz FLL. The FLL mainly consists of two parts: a feed-forward RF part and a feedback baseband part. The RF part comprises a differential voltage-controlled oscillator (VCO), a buffered output of the VCO, a power amplifier (PA), and the on-chip patch antenna reference. The baseband part functions as a Proportional Integral (PI) controller, and has two envelope detectors, an error amplifier, an integrator, and a loop filter. The VCO signal is amplified by the PA and radiated through the antenna. The frequency of the VCO is

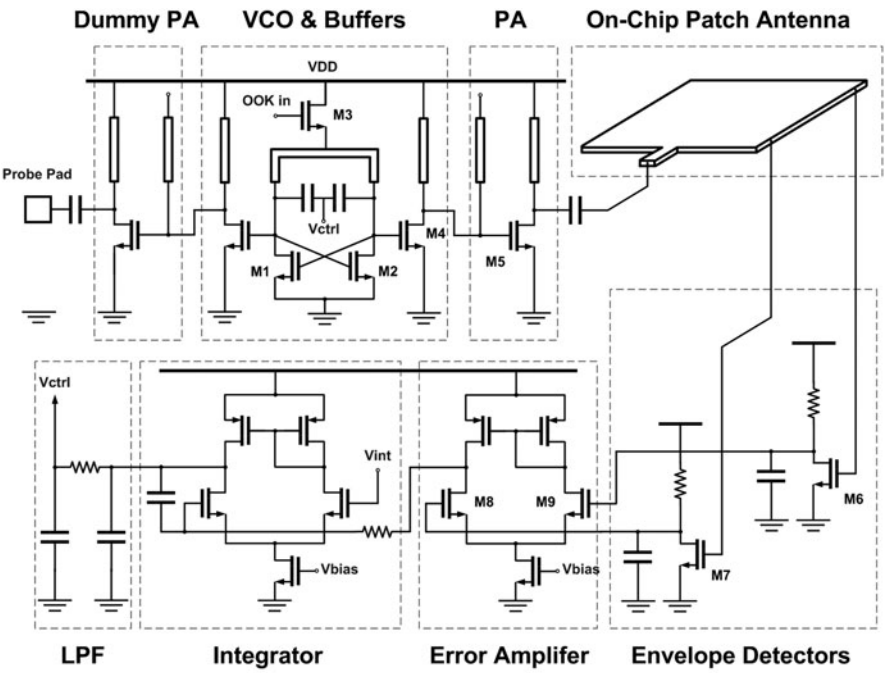

M1	M2	M3	M4	M5	M6	M7	M8	M9
12.8	12.8	50.0	6.4	26.0	50.0	50.0	18.0	18.0
0.12	0.12	0.12	0.12	0.12	0.48	0.48	1.00	1.00

Fig. 16 Schematic of the 60-GHz frequency-locked loop (FLL). *VCO* voltage-controlled oscillator, *PA* power amplifier, *LPF* low-pass filter

regulated by the feedback baseband part. The VCO is designed to be on–off keying (OOK) modulated by power gating with a PMOS header device, so that the FLL can serve as a simple low-rate OOK transmitter. Note that the baseband circuits highlighted in Fig. 15 are placed beneath the patch antenna ground plane using Metal 1 to Metal 3 routing layers.

Figure 16 shows the schematic of the 60-GHz FLL. The VCO uses a cross-coupled pair topology with an LC resonator. The resonator is realized by a half-wavelength transmission line at the top metal layer, and the simulated Q-factor of the resonator is 15 at 60 GHz. The frequency tuning is achieved by a pair of thin oxide negative-channel metal-oxide semiconductor (NMOS) varactors. One of the differential VCO outputs feeds the signal onto the patch antenna through a common source stage buffer and a PA. The PA is designed for maximum power delivery, using the top metal layer for high-Q transmission lines for matching. Ideally, we want to probe the signal at the antenna input, where the FLL output is. However, the pad and probing might destroy the matching condition between the PA and the antenna, so the secondary output of the differential VCO is used for testing and is connected to an RF probe

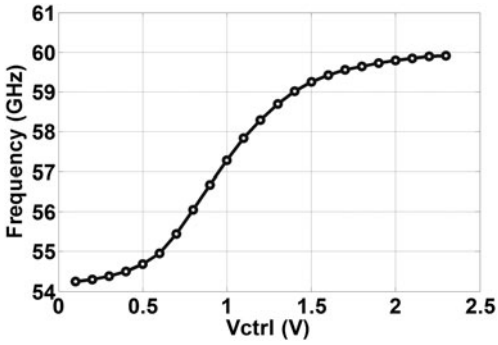

Fig. 17 Tuning range of the voltage-controlled oscillator (VCO) in the frequency-locked loop (FLL)

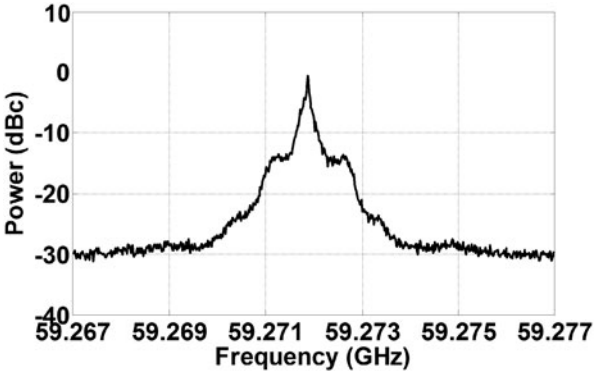

Fig. 18 Output spectrum of the frequency-locked loop (FLL) in 10-MHz span

pad through a dummy PA. In this way, we can monitor the FLL output frequency. However, the absolute output power is not available through direct measurement because of an extra 500 μm routing that is necessary for the on-chip probing pads setup. The simulated FLL output frequency and power are 60.12 GHz and − 3.6 dBm, respectively. The measured power consumption of the VCO core, buffers, and PA are 8.8, 2.6, and 16.0 mW, respectively.

The envelope detectors sense the magnitude of the standing wave on the antenna, and down-convert the signal from 60 GHz to direct current (DC). An active envelope detector topology is used for larger output voltage levels, which is a class-AB biased amplifier with parallel resistor–capacitor (RC) load at the output [35]. The bias of the two envelope detectors is critical, and the connection through the patch antenna ensures the DC voltage at both gates of the envelope detectors are the same. The setup also makes sure that the patch antenna is not DC floating when it is operating. Moreover, large devices are used and they are laid out in close proximity to lower the mismatch between the two envelope detectors [34]. The simulated offset voltage of the envelope detector inputs due to process variation is 190 μV, corresponding to a frequency offset of roughly 6 MHz (100 ppm). By changing the bias gate voltage and the drain current, the input node of the envelope detectors can be designed as high-impedance nodes, so that the two taps on the edge of the patch antenna do not significantly affect the standing wave pattern. The measured power consumption of one envelope detector is 670 μW.

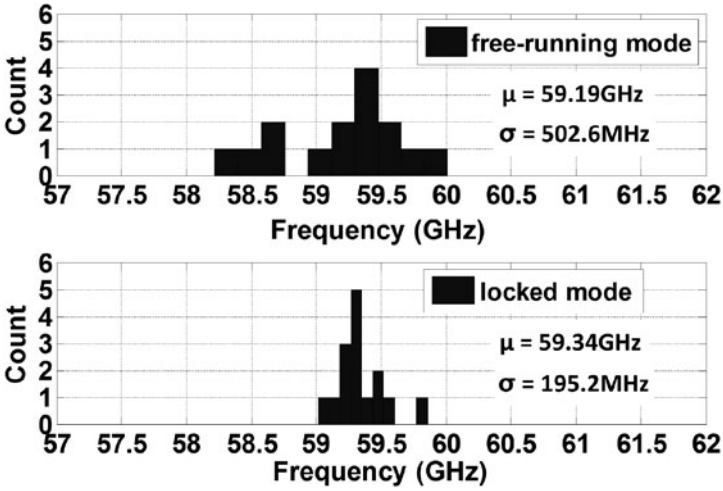

Fig. 19 Frequency distribution of the frequency-locked loop (FLL) in different modes

The error amplifier provides the difference and controller gain for the FLL. It is an amplifier with a differential input and an active load for single-ended output. Gain of 20 dB and bandwidth of 300-MHz bandwidth is obtained from this stage. The simulated offset voltage at the input of the error amplifier is 52 μV, corresponding to a frequency offset of roughly 11 MHz. The integrator introduces a pole at DC, minimizing the steady state error between the FLL output and the natural resonant frequency of the patch antenna. Bias conditions of the error amplifier, envelope detectors, and the integrator must be considered together for the proper input voltage range and gain margin. The loop filter stabilizes the FLL and is realized by a distributed resistive transmission line with metal comb capacitor units with a self-resonant frequency above 60 GHz. The cutoff frequency of the loop filter is designed to be 100 MHz.

Measurement Results and Summary

The FLL is fabricated in a 130-nm CMOS process and the power consumption (excluding the dummy PA to test pads) is 29.6 mW. Figure 17 shows the tuning range of the VCO in the FLL, which covers $\pm 3\sigma$ of the patch antenna resonant frequency.

The output spectrum measured with a 10-MHz span while the FLL is locked is shown in Fig. 18. The locked frequency is at 59.27 GHz, which is within the variation of the replica antenna. There are no reference spurs in the output spectrum, which would typically appear in a frequency synthesizer with a crystal reference multiplied by a PLL [36]. Fifteen FLLs from a single wafer were tested, and Fig. 19 compares

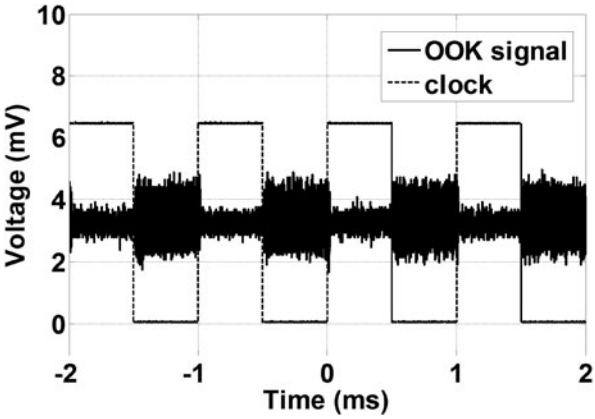

Fig. 20 On–off keying (OOK) modulating the voltage-controlled oscillator (VCO) at 1 kbps

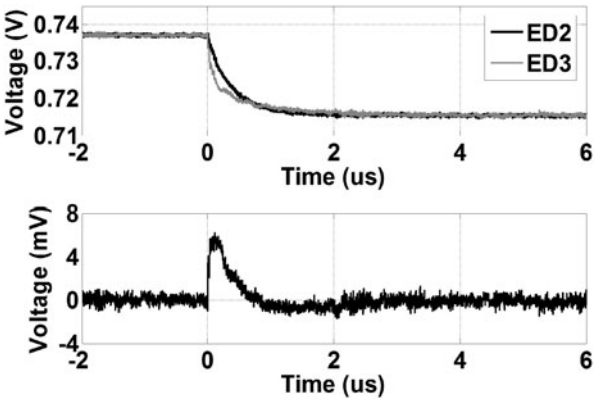

Fig. 21 Transient response of the two envelope detector outputs when turning the frequency-locked loop (FLL) on and the envelope outputs difference for settling time characterization

the frequency distribution of the free-running VCO when the feedback loop is off and when operating in locked mode. The mean center frequency is 59.34 GHz, with a standard deviation of 195 MHz. Compared with the 503-MHz standard deviation of the free-running VCO, the FLL provides an improvement in frequency variation, while eliminating the need for an external reference and tracking the peak-efficiency frequency of the integrated antenna.

Figure 20 shows the FLL Tx signal when the VCO is being OOK modulated at 1 kbps. The signal amplitude is small because it is down-converted through a passive harmonic mixer which has an uncalibrated attenuation; therefore, this plot simply verifies the OOK functionality. Figure 21 shows the two envelope detector output signals when the FLL is OOK modulated and the difference of the two envelope detector outputs as the error signal. The settling time is around 3 μs once the loop is turned on; therefore, the VCO can be powered on and FLL locked during every bit transmission for data rates less than around 200 kbps. The measured results of the FLL are summarized in Table 2 and compared with a state-of-the-art PLL, frequency synthesizer, and OOK transmitter. While a frequency synthesizer requires a crystal

Table 2 FLL performance summary

Study	[37]	[38]	[39]	This work
Type	PLL	Frequency synthesizer	OOK Tx	FLL
Technology	90-nm CMOS	90-nm CMOS	90-nm CMOS	0.13-μm CMOS
Power	80.0 mW	80.0 mW	183.0 mW	29.6 mW
Frequency	75 GHz	60 GHz	60 GHz	60 GHz
Antenna	N/A	N/A	Off-chip	On-chip
Area	0.80 mm^2	0.95 mm^2	0.43 mm^2	2.85 mm^2
Active circuit area	0.80 mm^2	0.95 mm^2	0.43 mm^2	0.64 mm^2

N/A not applicable, *PLL* phase-locked loop, *OOK* on–off keying, *FLL* frequency-locked loop, *CMOS* complementary metal-oxide semiconductor

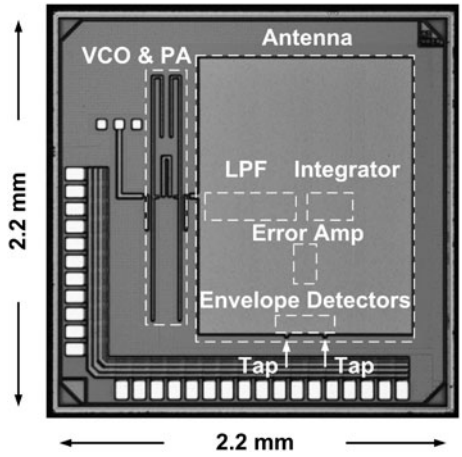

Fig. 22 Die micrograph of the 60-GHz frequency-locked loop (FLL). *VCO* voltage-controlled oscillator, *PA* power amplifier, *LPF* low-pass filter

reference, this antenna-referenced FLL performs closed-loop frequency regulation without any off-chip components. A die micrograph of the FLL is shown in Fig. 22. The FLL including antenna occupies 1.60 × 1.78 mm^2 without pads.

References

1. G. Bell, Bell's Law for the birth and death of computer classes. Commun. ACM. **51**(1), 86–94 (Jan 2008)
2. T. Nakagawa et al., 1-cc computer: cross-layer integration with UWB-IR communication and locationing. IEEE J. Solid-State Circuits **43**(4), 964–973 (Apr 2008)
3. J. Bryzek, *Emergence of a $Trillion MEMS Sensor Market* (SensorsCon, Santa Clara, CA, Mar 2012)
4. I.F. Akyildiz et al., A Survey on sensor networks. IEEE Commun. Mag. pp. 102–114 (Aug 2002)
5. K. Romer, F. Mattern, The design space of wireless sensor networks. IEEE Wireless Commun. **11**(6), 54–61 (Dec 2004)

6. D. Puccinelli, M. Haenggi, Wireless sensor networks: applications and challenges of ubiquitous sensing. IEEE Circ. Syst. Mag. **5**(3), 19–31 (2005)
7. J. Yick, B. Mukherjee, D. Ghosal, Wireless sensor networks survey. J. Comput. **52**(12), 2292–2330 (Apr 2008)
8. P. Corke et al., Environmental wireless sensor networks. Proc. IEEE **98**(11), 1903–1917 (Nov 2010)
9. K.-K. Huang, D.D. Wentzloff, A 60 GHz antenna-referenced frequency-locked loop in 0.13μm CMOS for wireless sensor networks. IEEE J. Solid-State Circuits **46**(12), 2956–2965 (Dec 2011)
10. G. Chen et al., Millimeter-scale nearly perpetual sensor system with stacked battery and solar cells. ISSCC Dig. Tech. Papers pp. 288–289 (Feb 2010)
11. Cymbet Corp., EnerChip smart solid state batteries. http://www.cymbet.com/products/enerchip-solid-state-batteries.php. Accessed 6 Feb 2012
12. S.D.I. Samsung, Prismatic rechargeable battery. http://samsungsdi.com/battery/prismatic-rechargeable-battery.jsp. Accessed 6 Feb 2012
13. Y. Nishi, Lithium ion secondary batteries; past 10 years and the future. J. Power Sources **100**(1–2), 101–106 (Nov 2001)
14. A.H. Zimmermann, M.V. Quinzio, *Tech. Rep. TR-2010(8550)-5. Performance of SONY 18650-HC Lithium-Ion Cells for Various Cycling Rates* (Aerospace Corp., El Segundo, CA, Jan 2010)
15. S. Hossain et al., Lithium-ion cells for aerospace applications. Proc. 32nd Intersociety Energy Conversion Eng. Conf. **1**, 35–38 (Aug 1997)
16. CGR18650D: cylindrical model. Panasonic Corp., Product Spec., CGR18650D (Jun 2005)
17. Panasonic batteries energy catalog. Panasonic Corp., Rolling Meadows, IL, Product Spec., PIC-PanBat-FY11-PanaEnergyCatalog (2011)
18. S. Hanson, M. Seok, Y.-S. Lin, Z. Foo, D. Kim, Y. Lee, N. Liu, D. Sylvester, D. Blaauw, A low-voltage processor for sensing applications with picowatt standby mode. IEEE J. Solid-State Circuits **44**(4), 1145–1155 (Apr 2009)
19. H.-J. Lee, A.M. Kerns, S. Hyvonen, I.A. Young, A scalable Sub-1.2 mW 300 MHz-to-1.5 GHz host-clock PLL for system-on-chip in 32 nm CMOS. ISSCC Dig. Tech. Papers pp. 96–97 (Feb 2011)
20. K. Sundaresan, G.K. Ho, S. Pourkamali, F. Ayazi, Electronically temperature compensated silicon bulk acoustic resonator reference oscillators. IEEE J. Solid-State Circuits **42**(6), 1425–1434 (June 2007)
21. Temperature compensated crystal oscillators (TCXO). Vectron Corp., Product Spec., VT820 Series (2009)
22. Standard frequency high performance MEMs VCTCXO. SiTime, Product Spec., SiT5000 (2012)
23. Single-ended output silicon oscillator. Silicon Labs, Product Spec., Si500S (2011)
24. TELOS-B user's manual. Crossbow Technology Inc., San Jose, CA (2004)
25. C.A. Balanis, *Antenna Theory: Analysis and Design*, Ch. 4, 2nd edn. (Wiley, New York, 1997)
26. A. Babakhani, X. Guan, A. Komijani, A. Natarajan, A. Hajimiri, A 77-GHz phased-array transceiver with on-chip antennas in silicon: receiver and antennas. IEEE J. Solid-State Circuits **41**(12), 2795–2806 (Dec 2006)
27. T. Yao, L. Tchoketch-Kebir, O. Yuryevich, M.Q. Gordon, S.P. Voinigescu, 65 GHz doppler sensor with on-chip antenna in 0.18 μm SiGe BiCMOS. IEEE MTT-S Int. Microwave Symp. Dig. pp. 1493–1496 (2006)
28. C. Wang, Y. Cho, C. Lin, H. Wang, C. Chen, D. Niu, J. Yeh, C. Lee, J. Chern, A 60 GHz transmitter with integrated antenna in 0.18 μm SiGe BiCMOS technology. ISSCC Dig. Tech. Papers pp. 186–187 (2006)
29. C.-M. Hung, D. Bravo, T.O. Dickson, G. Xiaoling, L. Ran, N. Trichy, J. Caserta, W.R. Bomstad, J. Branch, Y. Dong-Jun, J. Bohorquez, E. Seok, G. Li, A. Sugavanam, J.J. Lin, C. Jie, J.E. Brewer, On-chip antennas in silicon ICs and their application. IEEE Trans. Electron Devices **52**(7), 1312–1323 (July 2005)

30. Federal Communications Commission, FCC part 15, sec. 15
31. C.H. Doan, S. Emami, D.A. Sobel, A.M. Niknejad, R.W. Broadersen, Design considerations for 60 GHz radios. lEEE Comm. Mag. pp. 132–140 (Dec 2004)
32. K.-K. Huang, D.D. Wentzloff, 60 GHz on-chip patch antenna integration in a 0.13-um CMOS technology. IEEE International Conference on Ultra-Wideband (ICUWB) (Sep 2010)
33. D.M. Pozar, *Microwave Engineering*, 3rd edn. (Wiley, New York, 2005)
34. M. Pelgrom, A. Duinmaijer, A. Welbers, A.P.G. Welbers, Matching properties of MOS transistors. IEEE J. Solid-State Circuits **24**, 1433–1440 (Oct 1989)
35. J. Lee, Y. Huang, Y. Chen, H. Lu, C. Chang, A low-power fully integrated 60 GHz transceiver system with OOK modulation and on-board antenna assembly. ISSCC Dig. Tech. Papers pp. 315–316 (Feb 2009)
36. Y. Lee, G. Chen, S. Hanson, D. Sylvester, D. Blaauw, Ultra-low power circuit techniques for a new class of sub-mm3 sensor nodes. IEEE CICC 2010 (Nov 2010)
37. J. Lee, S. Cho, 10 MHz 80μW 67 ppm/°C CMOS reference clock oscillator with a temperature compensated feedback loop in 0.18 μm CMOS. Symposium on VLSI Circuits pp. 226–227 (Jun 2009)
38. J. He, Y.P. Zhang, Design of SPST/SPDT switches in 65 nm CMOS for 60-GHz applications. IEEE Asia Pacific Microwave Conf. pp. 1–4 (Dec 2008)
39. S.-F. Chao, H. Wang, C.-Y. Su, J.G.J. Chern, A 50–94 GHz CMOS SPDT switch using traveling-wave concept. IEEE Microwave Wireless Compon. Lett. **17**(2), 130–132 (Feb 2007)

60-GHz LTCC Antenna Arrays

Yong-Xin Guo and Lei Wang

Abstract The wide unlicensed frequency band around 60-GHz for wireless short-range communications are receiving a lot of attention in recent years. As one of the key components in wireless communication systems, the antenna technology affects radio propagation channels, transceiver designs, and choice of digital modulation schemes in establishing a reliable 60-GHz link. In this connection, the 60-GHz antennas for wireless communications, especially antenna-in-package (AiP), have received considerable attention and become a hot research topic. In this chapter, wideband antenna arrays based on the multilayer low temperature co-fired ceramic (LTCC) technology are presented and discussed for 60-GHz wireless short-range communications applications.

Keywords Antenna design · 60 GHz ISM band · 60 GHz radio · IEEE 802.15.3c · LTCC technology · Antenna array

Introduction

The wide unlicensed frequency band around 60 GHz with high data rate characteristic for wireless short-range communications are receiving a lot of attention. For this wireless communication, the data rate of short distance between electronic devices can be realized in multiGbps which is 40–100 times faster than the current WLAN technologies. Communications at the 60-GHz band have lots of advantages such as the possibility of frequency reuse over small distances because of the high attenuation by walls, and the possible miniaturization of the analog components and antennas as the corresponding wavelength in free space is only 5 mm. 60-GHz band wireless short-range communications have a number of applications such as uncompressed high definition video streaming, mobile distributed computing, wireless gaming, fast bulky file transfer, sensing and radar applications, virtually instantaneous access to massive libraries of information, etc. [1].

Y.-X. Guo (✉) · L. Wang
Department of Electrical and Computer Engineering,
National University of Singapore, Singapore, Republic of Singapore
e-mail: eleguoyx@nus.edu.sg

M. R. Yuce (ed.), *Ultra-Wideband and 60 GHz Communications for Biomedical Applications,* DOI 10.1007/978-1-4614-8896-5_11,

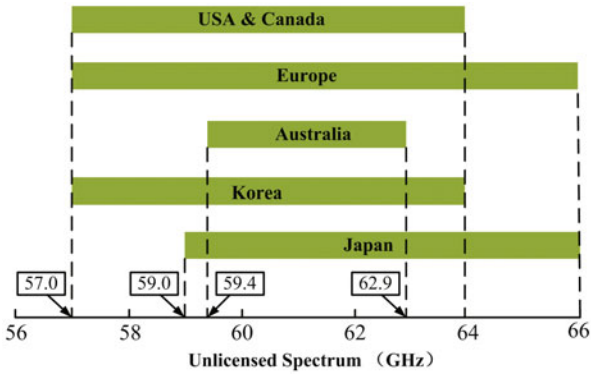

Fig. 1 The spectrum allocation around the 60-GHz band for some countries and regions [3–5]

The IEEE 802.15.3c task group was formed to standardize 60-GHz radios in March 2005, and the IEEE 802.15.3c standard was published in September 2009 to define available and unlicensed frequencies band from 57 to 66 GHz as the 60-GHz band radios applications [2]. The standard divides nearly 9 GHz frequency bandwidth into four 2.16-GHz channels. The Nyquist bandwidth of the standard is 1.632 GHz with a guard bandwidth of 264 MHz on each side to limit spectral leakage. The standard also enforces basic transmission modes: common mode, single-carrier (SC) mode and orthogonal frequency division multiplexing (OFDM) mode. Significant progress has been made in regulations, standards, and solutions. According to the actual situation of countries and regions, different countries and regions have established the 60-GHz regulations for unlicensed utilization, as is shown in Fig. 1. Japan first issued the 60-GHz regulation for unlicensed band from 59 to 66 GHz in the year 2000. The maximum allowable antenna gain of 47 dBi and maximum transmission bandwidth of 2.5 GHz. In 2004, the United States allocated 7 GHz from 57 to 64 GHz for unlicensed use and specified a total maximum transmit power of 500 mW for an emission bandwidth greater than 100 MHz. The 60-GHz regulation in Australia is a narrower 3.5 GHz bandwidth from 59.4 to 62.9 GHz than 7 GHz bandwidth in Japan and USA. The maximum transmit power is limited to 10 mW. A wider 9 GHz bandwidth from 57 to 66 GHz is recommended in Europe. The maximum transmit power of 20 mW, maximum allowable antenna gain of 37 dBi, and minimum transmission bandwidth of 500 MHz are established. Therefore, antennas with wide operating bandwidth to cover more than 9 GHz of the whole 60-GHz bandwidth for different countries and regions applications are desired.

The atmospheric absorption property of sub-terahertz radio spectrum is shown in the Fig. 2. The 60-GHz band is located at the peak point of the oxygen absorption with high attenuation and large propagation loss. The dramatic attenuation at the 60-GHz band is suitable for “whisper radio” short-range wireless communication, where weak signals do not propagate more than a few meters before dropping below the thermal noise level. For 60-GHz wireless communications, the link budget is constrained due to low transmit power (10 mW), large propagation loss (68 dB at 1 m), and high data rate ($\geq$ 1.5 Gb/s). Assuming the 10-mW value for the average

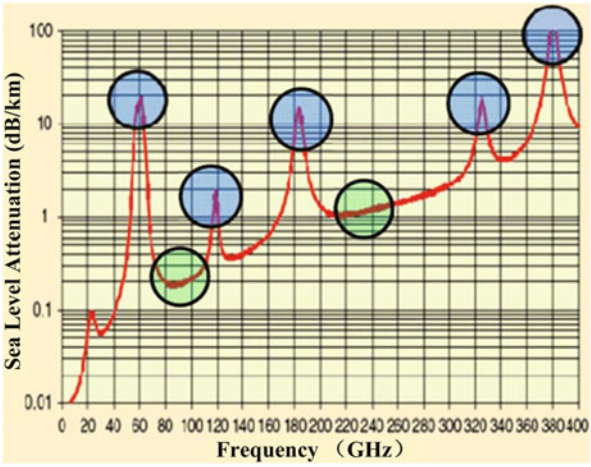

Fig. 2 The properties of atmospheric absorption of electromagnetic waves [4]

transmitter power for portable devices, a gain of ∼ 15 dBi is usually required for 60-GHz indoor WLAN applications. Hence, the use of antenna arrays with high-gain is anticipated.

Low-temperature co-fired ceramic (LTCC) multilayer technology enables integration of passive components including antennas in a single package. Compared with the multilayer print circuit board (PCB) technology, the LTCC technology is capable of realizing blind, buried and through vias and air cavities in the substrate easily [6]. The LTCC technology is also allowed to mount active devices or integrated circuit on/in them to achieve a new option to integrate an antenna array in a chip package. Several LTCC materials can be selected. Ferro A6 is one kind of LTCC material suitable for 60-GHz antenna array design, due to its excellent high frequency characteristic. Based on the Ferro A6 material, LTCC technologies can realize functional packages and antennas for applications in the 60-GHz band. The LTCC process has been regarded the promising technology of achieving light weight, compactness, easy integration, and excellent high frequency performance for 60-GHz wireless communication applications.

Considering the wide 15 % bandwidth (for 9 GHz world wide band coverage) and more than 15 dBi gain requirements, the antenna arrays based on LTCC technology have many challenges for 60-GHz wireless short-range communications. Due to the high permittivity of the LTCC substrate, the bandwidth of antenna arrays is limited. Hence, the choice of the array element becomes more significant for 60-GHz antenna array design. A variety of array elements, such as patch, dipole, slot, and others have been used as the element in the 60-GHz LTCC antenna array designs. Also some methods about broadening bandwidth of the LTCC antennas have been reported, such as using aperture coupled patch, U-slot patch, L-probe patch, stacked patch, and off-center dipole, etc. [7–13]. For the antenna arrays, the feeding network is crucial to develop the antenna arrays. A parallel, series, or combined feed is used to produce the necessary amplitude and phase distribution for an array element.

Compared with a series feed, a parallel feed can offer a wider bandwidth. Several types of transmission line can be used as the feeding network, such as microstrip line, stripline (SL), coplanar waveguide (CPW), substrate-integrated waveguide (SIW), or hybrid structures. However, the gain of the antenna array is limited by the loss caused by its feeding network, such as a microstrip line, especially at the 60-GHz band applications. Stripline and SIW with lower transmission loss and better isolation than microstrip line have been widely employed at the 60-GHz LTCC antenna array designs.

Furthermore, due to the higher permittivity of LTCC substrate, the surface wave could introduce significant loss in LTCC antenna array design at millimeter-wave 60-GHz bands. Enhancing the gain performance of the 60-GHz antenna array based on LTCC technology becomes much more challenging. The strong surface wave propagation is the primary reason of producing the mutual coupling between the elements. Some methods of suppressing the surface-wave loss to reduce the mutual coupling and enhance the gain of the LTCC antenna have been reported, such as embedding an air cavity inside the substrate, removing the partially substrate around the radiating elements, loading the uniplanar-compact electromagnetic band-gap (UC-EBG), loading the artificial soft-surface structure, using open-ended SIW cavity structure, and using metal-top via fence structure, etc. [14–18].

In this chapter, the antenna arrays based on LTCC technology for 60-GHz short-range wireless communication applications are presented. The antenna elements and compact feeding networks for achieving different polarization performances of the antenna arrays are studied. For measurement, the transition of the grounded coplanar waveguide (GCPW) to the SL is designed based on LTCC multilayer structure. Also, for suppressing the surface wave propagation in the array, the soft-surface structure, and open-ended SIW cavities are used to improve the radiation performance of antenna arrays with different polarization characteristic. The antenna arrays with compact structure and good performance, including a wideband linearly polarized L-probe feed patch antenna array with soft-surface structure, and a dual-polarized L-probe feed patch antenna array with open-ended SIW cavities structure are presented and studied.

60-GHz LTCC Linearly Polarized Antenna array

A 4×4 L-probe patch linearly polarized antenna array with a soft-surface structure using multilayer LTCC technology is presented for 60-GHz band applications. The technique of employing an L-shaped probe to feed a thick patch antenna for achieving a wideband antenna of bandwidth $> 30\,\%$ has been widely reported [19–21]. However, all these antennas were designed on traditional substrate materials, and the operating frequency bands were below 10 GHz. The L-probe feed patch antenna as an element is designed and fabricated using LTCC technology at 60-GHz band. On the other hand, the artificially soft-surface structure was employed to improve antenna performance as it can force the field intensity for any polarization to be

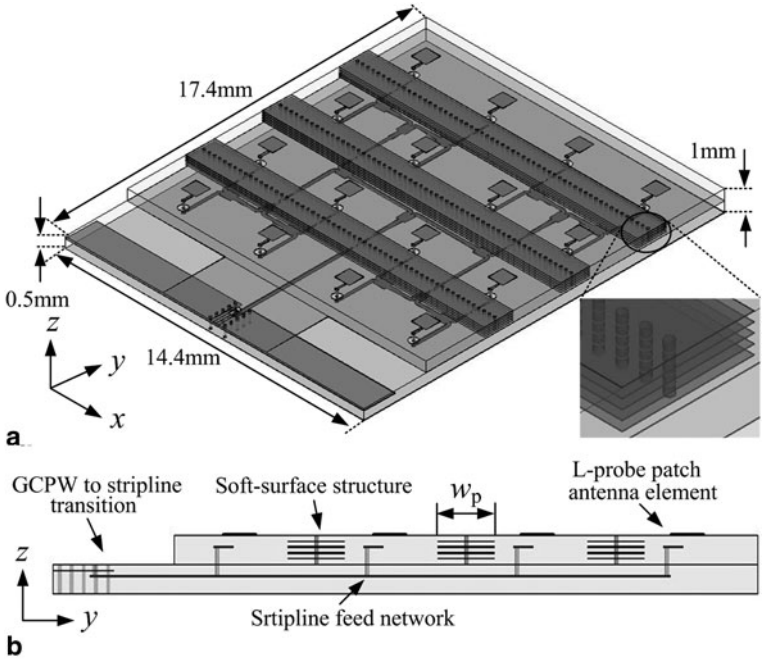

Fig. 3 Geometry of the proposed low temperature co-fired ceramic (LTCC) based L-probe patch array with novel soft-surface structures. **a** 3D view, **b** *side* view (from [10], reprinted with permission from IEEE)

zero on the surface for wave propagating along the surface [22–24]. A novel soft-surface structure is introduced in the LTCC L-probe antenna array to suppress the substrate surface wave and thus enhance the antenna array radiation performance without increasing the overall size and requiring additional process. The proposed antenna array is fed by a SL feed network to separate from the radiation elements. The effects of the soft-surface structure on the performance of antenna array are numerically and experimentally investigated by comparing with the conventional L-probe patch linearly polarized array without the soft-surface structure.

Overview of the Antenna Array

A planar array of 4 × 4 L-probe patch antenna elements with a novel soft-surface structure was designed. The proposed antenna array is composed of 16 L-probe fed patch antenna elements; T-junction feeding network, and GCPW to SL transition for probe station testing as shown in Fig. 3. Three novel soft-surface structures constituted of metal strips on each layer and via fences were inserted in the middle of the antenna array along the x-axis. The value of w_p is the metal strip width of the proposed soft-surface structure. The via fences are composed of a row of vias.

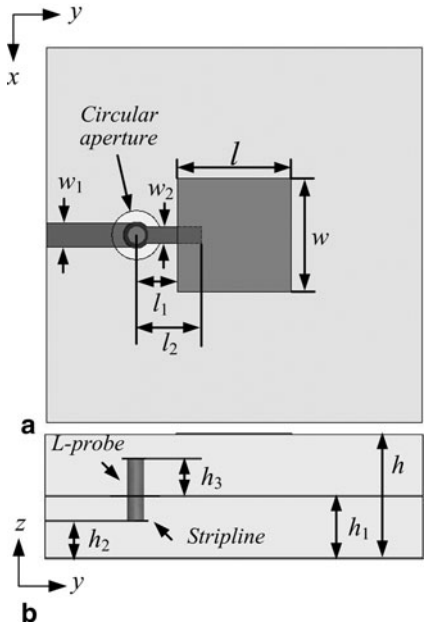

Fig. 4 Geometry of the LTCC L-probe patch element. **a** *Top* view, **b** *Side* view (from [10], reprinted with permission from IEEE)

Following the fabrication process requirement, the diameter of each via is 0.1 mm, and the distance between the centers of two adjacent vias is 0.25 mm. In this work, the element spacing of $d = 3.7$ mm ($0.75\lambda_0$) was chosen. The total size of the proposed antenna array excluding the measurement transition is $14.4 \times 14.4 \times 1\ \text{mm}^3$.

Single L-probe Patch Radiating Element

The single L-probe patch antenna element is shown in Fig. 4. The multilayer LTCC substrate used is Ferro A6-M with dielectric permittivity $\varepsilon_r = 5.9$ and loss tangent $\tan\delta = 0.001$. The conductor thickness is $t = 0.01$ mm. The L-probe is constituted by a vertical via and a horizontal microstrip line. The proposed antenna element is fed by a SL to suppress the radiation from the feeding line. The detailed dimensions are shown in Table 1. The total thickness h is 1 mm (10 LTCC layers) including five LTCC layers (0.5 mm) as the SL feeding part and five LTCC layers (0.5 mm) as the antenna part. The width w_1 of the feed SL was chosen to be 0.15 mm, which corresponds to the characteristic impedance of 50 Ω. The via diameter is 0.1 mm.

Figure 5 shows the simulated impedance bandwidth and gain of the proposed antenna element by HFSS. The simulated impedance bandwidth is about 50.4 % with respect to the center frequency of 61.5 GHz from 46 to 77 GHz for $|S_{11}| \leq -10$ dB. The simulated gain is 5.7 dBi at 60 GHz.

Table 1 Detailed L-probe patch antenna element dimensions

Parameters	Dimensions (mm)	Parameters	Dimensions (mm)	Parameters	Dimensions (mm)
w	0.7	w_1	0.15	l	0.7
w_2	0.1	l_1	0.25	l_2	0.4
h	1	h_1	0.5	h_2	0.3
h_3	0.3				

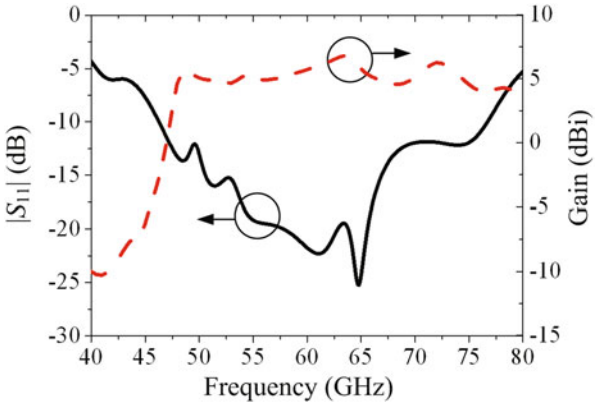

Fig. 5 Simulated $|S_{11}|$ and gain of the single element (from [10], reprinted with permission from IEEE)

Feeding Network and GCPW-SL Transition

A quarter-wave T-junction power divider was used as a feed network to split the power equally. From 48 to 70 GHz, the simulated insertion loss of the T-junction is less than 0.3 dB and simulated $|S_{11}|$ is better than -20 dB.

A (GCPW to SL transition was designed on LTCC so that the antenna array can be measured with the probe station measurement as illustrated in Fig. 6. A partial middle ground which is lower than the upper ground by 0.1 mm to facilitate the probe pitch touching. The simulated $|S_{11}|$ is below -18 dB and $|S_{21}|$ is less than -0.15 dB from 40 to 70 GHz.

Investigation of Antenna Array with Soft-surface

The Effect of the Soft-surface Structure Metal Strips Width

The antenna array with different metal strip width of the soft-surface structure: $w_p =$ 0.4, 0.8, 1.4, and 2.0 mm are simulated to study its influence on the performance of the antenna array. The comparisons of the simulated $|S_{11}|$ and gain with different w_p are shown in the Fig. 7. It is seen that both the impedance and radiation performance are related to the width of the soft-surface structure obviously. When w_p is smaller than 0.4 mm, the impedance matching of the antenna array is poor and the gain is

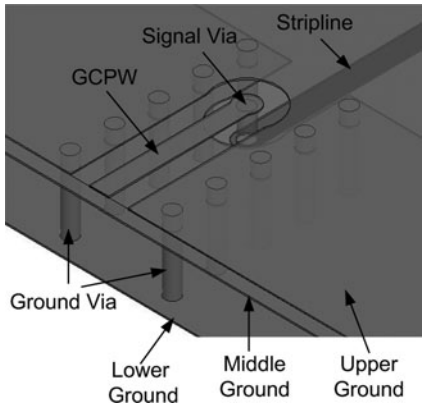

Fig. 6 Geometry of the grounded co-planar waveguide (GCPW) to SL transition (from [10], reprinted with permission from IEEE)

not improved. The antenna is well matched and the antenna gain can be improved significantly when $w_p = 0.8$ and 1.4 mm. But, when the width of the soft-surface structure is big enough to affect the antenna radiation, the impedance becomes worse again. After optimization, considering the simulated $|S_{11}|$ and gain, the value of w_p is chosen to be 1.4 mm.

The Effect of the Soft-Surface Structure Location

To understand the effectiveness of the soft-surface structure location, we simulated the $|S_{11}|$ and gain of the antenna array for three different types of the soft-surface structure locations: along x-axial as the Fig. 8a, along y-axial as the Fig. 8b, and along both x-axial and y-axial as the Fig. 8c, respectively.

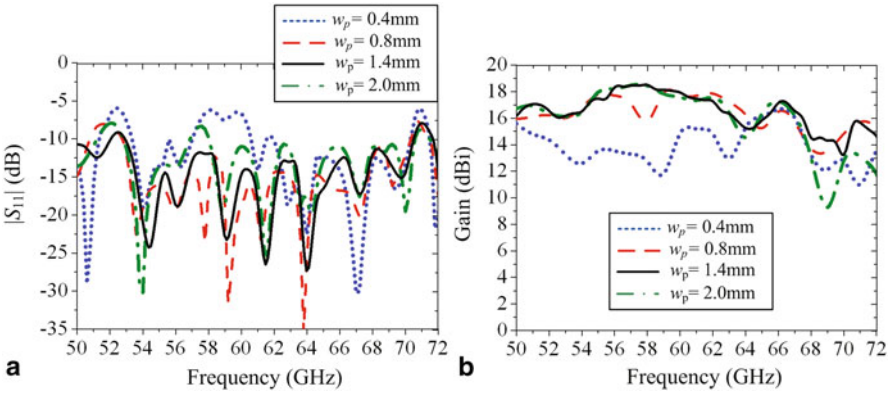

Fig. 7 Comparison of simulated $|S_{11}|$ and gain with different w_p. **a** Simulated $|S_{11}|$, **b** Simulated gain (from [10], reprinted with permission from IEEE)

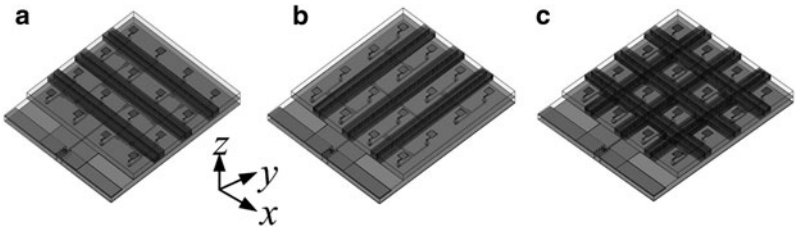

Fig. 8 Geometry of three antenna arrays with different locations of the soft-surface structure, **a** Along *x*-axial, **b** Along *y*-axial, **c** Along both *x*-axial and *y*-axial(from [10], reprinted with permission from IEEE)

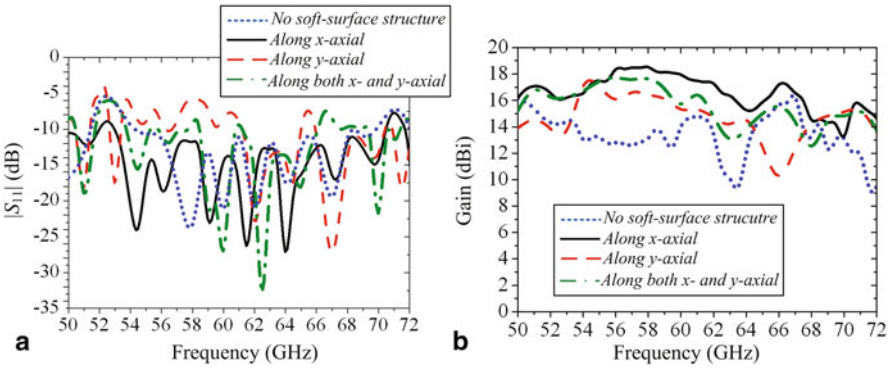

Fig. 9 Comparison of simulated $|S_{11}|$ and gain with different locations. **a** Simulated $|S_{11}|$, **b** Simulated gain (from [10], reprinted with permission from IEEE)

The simulated $|S_{11}|$ and gain of the soft-surface structure at different locations are compared in Fig. 9. The simulated results of the conventional L-probe patch antenna array without any soft-surface structure are also shown as a reference. If the soft-surface structure is changed to be along the *y*-axis as in Fig. 8b, the impedance is mismatched seriously, and the gain is not improved as significantly as the case with soft-surface structure along the *x*-axis as in Fig. 8a. The reason is that the coupling along *y*-axis between antenna elements are stronger than that along *x*-axis. For the case with soft-surface structures along both *x*-axis and *y*-axis, as in Fig. 8c, the impedance matching becomes worse to result in lower gain than that for the case with soft-surface structures only along *x*-axis. Both good impedance and radiation performance of the antenna array can be achieved by placing the soft-surface structure just along the *x*-axis.

Antenna Arrays With or Without the Soft-surface Structure

Figure 1 shows the 3D view and side view geometry figures of the three different types of antenna arrays with or without the novel soft-surface structure, respectively. Design I shown in Fig. 10a is the L-probe patch antenna array without any soft-surface structure. Design II shown in Fig. 10b is the L-probe patch antenna array with

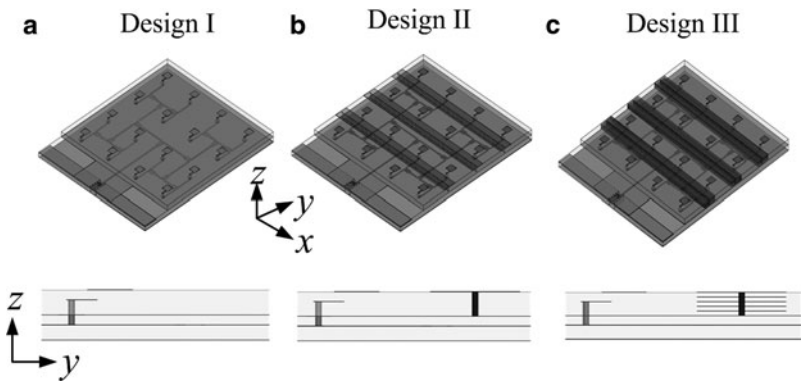

Fig. 10 Geometry of three different L-probe patch antenna arrays with or without the soft-surface structure. **a** Array without the soft-surface structure, **b** Array with the soft-surface structure of one layer, **c** Array with the soft-surface structure of each layer (from [10], reprinted with permission from IEEE)

the soft-surface structure of the metal strip only on the top layer. Design III shown in Fig. 10c is the L-probe patch antenna array with the proposed soft-surface structure of the metal strips on each layer to guarantee the good connection of the vias at different layers. To simplify the simulation, all the metal strips have the identical width of $w_p = 1.4$ mm on each layer. To demonstrate the effectiveness of the proposed novel soft-surface structure inserted in the antenna array for the impedance and radiation performance improvement, simulated results for the above three cases were presented for comparison.

The simulated results show that the impedance and radiation performance are almost the same for Designs II and III, which indicates that only the top metal strip has the primary influence on the performance. The metal strips at the other layers which are used to guarantee the good connection of the vias have little effect as long as the width of those strips are not bigger than that of the top metal strip (w_p).

Figure 11a compares the simulated $|S_{11}|$ of the antenna arrays with or without the soft-surface structure. The bandwidths of the arrays without and with the soft-surface structure for $|S_{11}| < 10$ dB are 27 % (Design I) and 29 % (Design III), respectively. The impedance bandwidth of the antenna array seems not sensitive to the soft-surface structure, and the bandwidth is improved for the array with the soft-surface structure slightly. From Fig. 11b, the simulated peak gain around 60 GHz of the antenna array with the soft-surface structure (Design III) is near 18 dBi, which is about 4 dBi higher than that of the array without the soft-surface structure (Design I). Also, compared with the antenna array without the soft-surface structure (Design I), a more stable peak gain is achieved by adding the soft-surface structure in the operation band.

The radiation patterns of different antenna arrays with or without the soft-surface structure in two principal planes at 60 GHz are compared in Fig. 12. It is seen that the antenna array without the soft-surface structure (Design I) has a worse sidelobe radiation due to the contribution from the surface wave diffraction. As we know, the L-probe patch antenna has a poor cross polarization at the H-plane. By introducing the

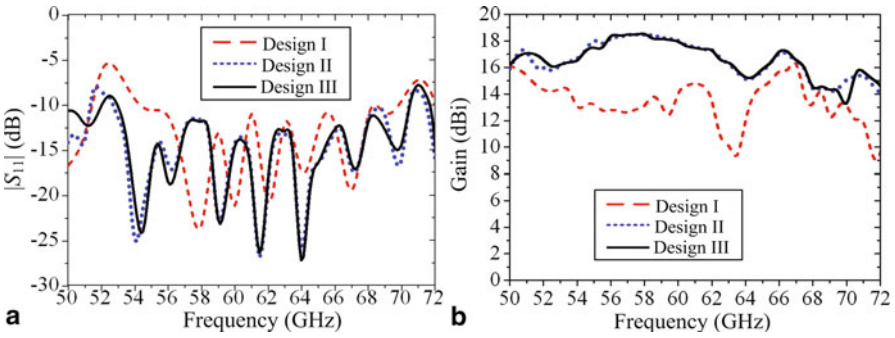

Fig. 11 Comparison of simulated $|S_{11}|$ and gain among three cases, **a** Simulated $|S_{11}|$, **b** Simulated gain (from [10], reprinted with permission from IEEE)

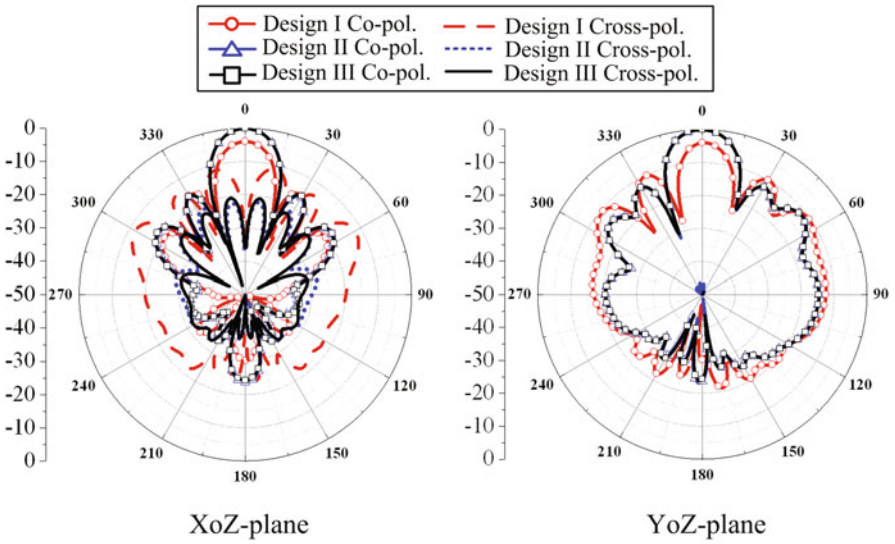

Fig. 12 Comparison of simulated radiation patterns between three different arrays at 60 GHz (from [10], reprinted with permission from IEEE)

soft-surface structure, the radiation performance is significantly improved, including enhanced radiation field in the maximum radiation direction, lower cross polarization of the H-plane, and reduced sidelobe radiation.

Mechanism for Performance Enhancement of Antenna Array by the Soft-surface Structure

In order to investigate the mechanism for the novel soft-surface structures placed in the antenna array, the electric field distributions on the top surface of the substrate for the middle two-row eight elements of the antenna array simulated by HFSS are shown in Fig. 13.

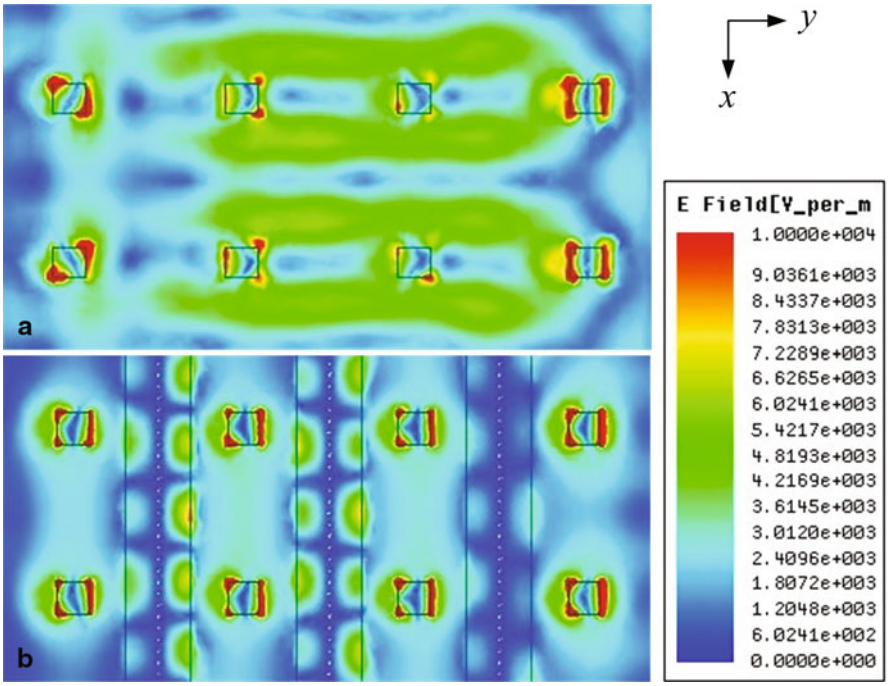

Fig. 13 Simulated electric field distributions on the *top* surface of the substrate for the *middle* two-row eight elements of the antenna array with and without the soft-surface structure. **a** Without the soft-surface structure, **b** With the soft-surface structure (from [10], reprinted with permission from IEEE)

When the antenna is fabricated on a large-size substrate with higher dielectric constant, the radiation performance will be much affected by the diffraction of surface waves. As Fig. 13a shows, there is a strong electric field from the surface waves in the area between the antenna elements, in particular along the *y*-axis. As the intrinsic electric field of the L-probe patch antenna element is heavily affected by the strong surface waves, the radiation performance of antenna array is deteriorated. The proposed soft-surface structure with the shorted metal strip and via fence blocks the surface wave propagates. As a result, the surface waves can be substantially suppressed; hence, the radiation performance of antenna array is improved. To confirm this finding by checking the field distribution in the substrate shown in Fig. 13b, we can see that the surface waves is suppressed in the substrate and the field distribution of the L-probe radiation patch is improved obviously.

The other factor contributing to the radiation performance improvement is the fringing field along the metal strips of the proposed soft-surface structure. As Fig. 13b shows, the fringing field along the metal strips forms a radiation array. The formed array acts as a broadside array. Although the magnitude of the fringing field along the soft-surface structure is much lower than radiating edge of the L-probe patch antenna, the size of the soft-surface structure is much larger than the patch. As a result, the contribution from the soft-surface structure to improve the performance of antenna array is significant.

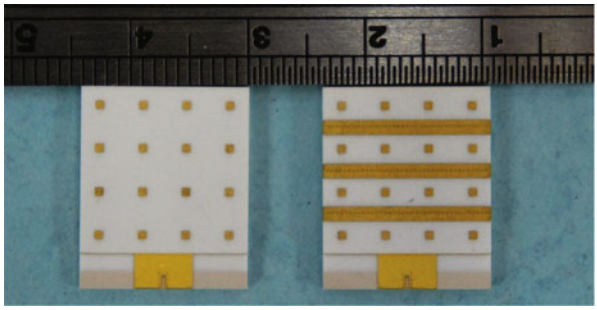

Fig. 14 Photographs of the proposed antenna arrays. *Left* without the soft-surface structure. *Right* with the soft-surface structure (from [10], reprinted with permission from IEEE)

Experimental Results

Figure 14 exhibits the photographs of the fabricated L-probe patch antenna arrays without and with the novel soft surface using LTCC process, respectively.

Figures 15 and 16 compare the measured and simulated $|S_{11}|$ and gain of the antenna array without and with the soft-surface structures, respectively. The measured frequency band ranged from 50 to 67 GHz is limited by the test cable and adapter. The measured and simulated results are in good agreement. The simulated impedance bandwidth for $|S_{11}| < -10$ dB are as follows: 26.7 % with respect to the center frequency of 61.7 GHz (from 53.5 to 70 GHz) for the antenna array without the soft-surface structure, and 29 % with respect to the center frequency of 62 GHz (from 53 to 71 GHz) for the array with the soft-surface structure, respectively. The measured $|S_{11}|$ of the frequency ranges from 51 to 67 GHz for the array without the soft-surface structure and from 51.5 to 67 GHz for the array with the soft-surface structure are all below −10 dB.

The simulated and measured gain values are 14 and 13.4 dBi for the antenna array without the soft-surface structure, and 18 and 17.5 dBi for the array with the soft-surface structure at 60 GHz, respectively. The measured 3-dB gain bandwidth

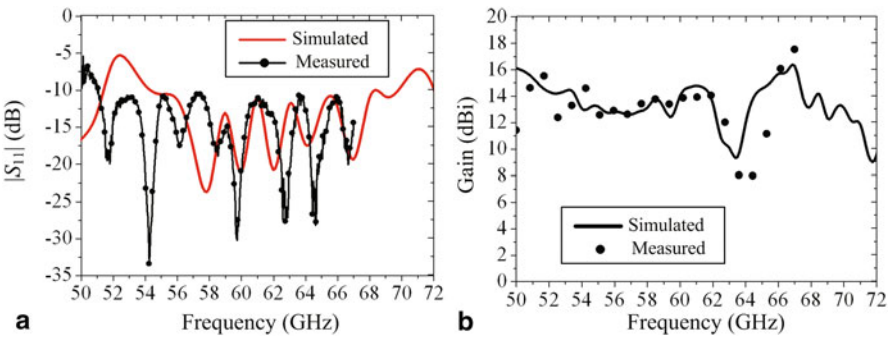

Fig. 15 Measured and simulated $|S_{11}|$ and gain of the antenna array without the soft-surface structure. **a** $|S_{11}|$, **b** Gain (from [10], reprinted with permission from IEEE)

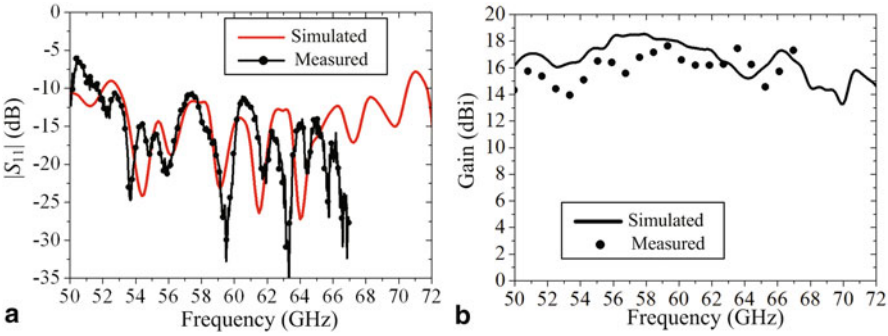

Fig. 16 Measured and simulated $|S_{11}|$ and gain of the antenna array with the soft-surface structure. **a** $|S_{11}|$, **b** Gain and efficiency (from [10], reprinted with permission from IEEE)

of the array with the soft-surface structure is from 54.5 to 65.5 GHz. The gain of the array with the soft-surface structure is about 4 dB higher than that of the array without the soft-surface structure at 60 GHz. This is because stronger surface wave introduced by the thicker substrate and high dielectric constant makes the radiation in the broadside worse for the case without the soft-surface structure. By adding the soft-surface structure in this design, the surface wave is suppressed significantly.

The measured and simulated co-pol and cross-pol radiation patterns of the L-probe patch antenna array with the soft-surface structure in two principal planes (XoZ-plane and YoZ-plane) at the frequencies of 55, 60, and 65 GHz are shown in Fig. 17, respectively. The measured HPBW is about 20° in two principal planes at 60 GHz. The measured cross-polarization level is almost 20 dB below the corresponding co-polarization at 60 GHz. Slight discrepancies between the simulated and measured results are mainly caused by the fabrication tolerance and possible effect of the test setup.

A 4 × 4 LTCC L-probe patch linearly polarized antenna array with a novel soft-surface structure is presented and tested for 60-GHz wireless communication applications. The introduced soft-surface structure has suppressed the surface wave significantly. The proposed antenna array features wide impedance bandwidth, high gain and stable gain bandwidth.

60-GHz LTCC Dual-Polarized Antenna array

A 60-GHz dual-polarized 4 × 4 L-probe patch antenna array based on LTCC technology is presented. Few efforts have been made for a polarization diversity antenna which is an important issue in a mobile or portable wireless communication system. A dual-polarized antenna can provide polarization diversity to reduce the multipath fading of the received signals or furnish frequency reuse to double the capacities [25–29]. A "differential feed" approach is adopted to realize the dual polarization in this work. The L-probe feed patch antenna is designed and fabricated using LTCC technology at the 60-GHz band to achieve wideband impedance bandwidth. A compact multilayer SL feeding network structure is employed to realize the dual

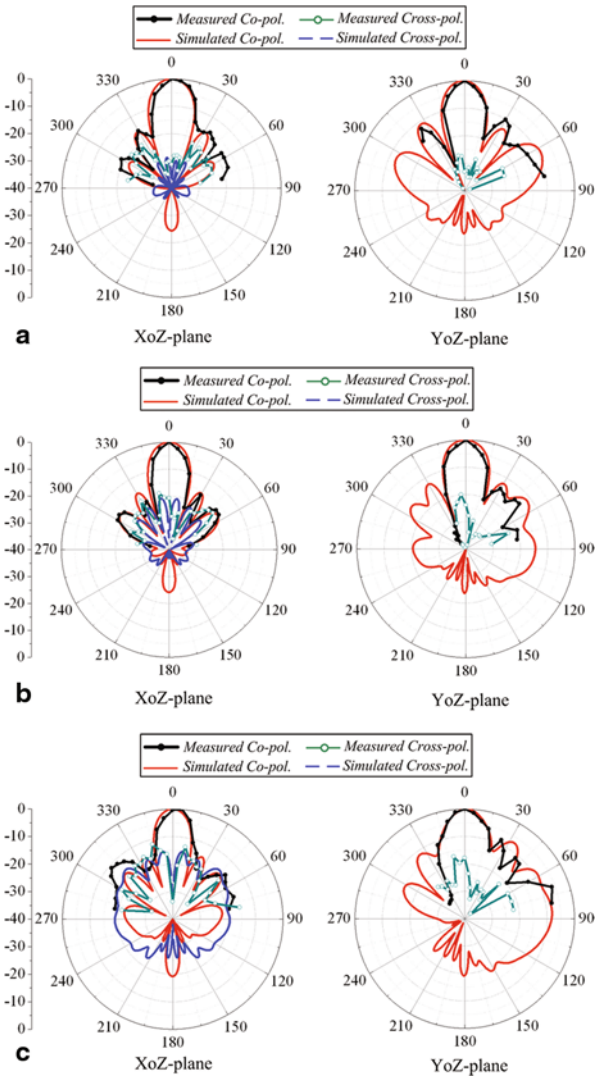

Fig. 17 Measured and simulated radiation patterns of the antenna array with the soft-surface structure. **a** 55 GHz, **b** 60 GHz, **c** 65 GHz

polarization characteristic of the array. The open-ended substrate integrated cavities (SICs) structure is embedded in the antenna array without increasing the overall size and requiring additional process to suppress the substrate surface wave and enhance the gain. A 4 × 4 dual-polarized L-probe patch antenna array in LTCC technology with the open-ended SICs is built and demonstrated for 60-GHz wireless communication applications.

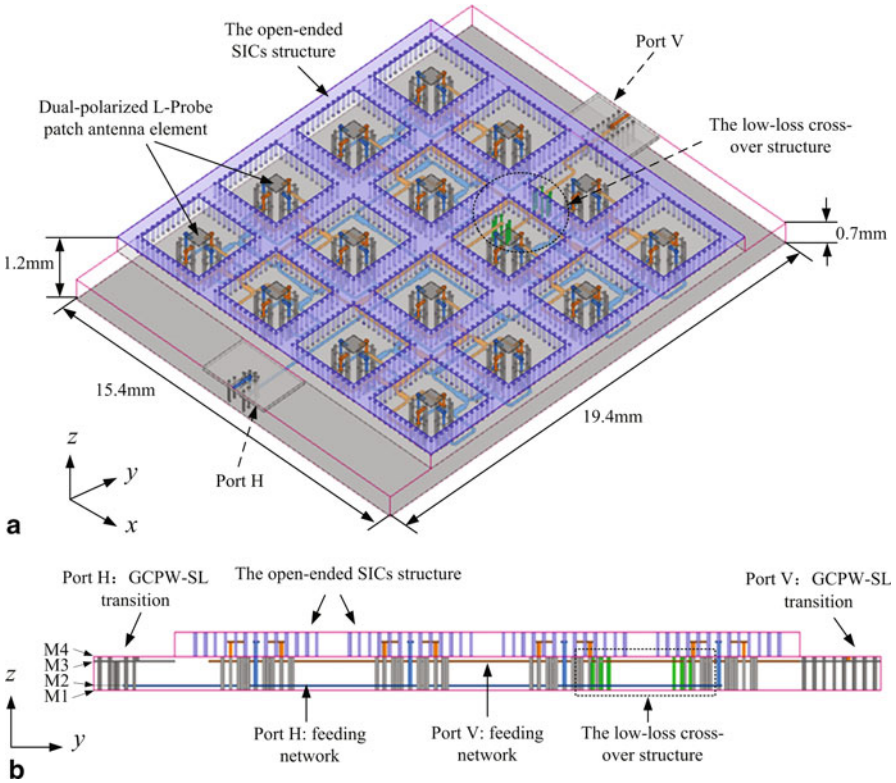

Fig. 18 Geometry of the proposed dual-polarized L-probe patch array with the open-ended SICs. **a** 3D view, **b** *Side* view

Overview of the Antenna Array

A 4 × 4 dual-polarized L-probe patch antenna array using "differential feed" approach with the open-ended SICs is designed and implemented for 60-GHz applications. The configuration of the proposed antenna array is shown in Fig. 18. The proposed antenna array is composed of 16 "differential feed" L-probe antenna elements, compact dual polarization SL feeding network, the open-ended SICs, and two GCPW to SL transitions for probe station testing. The element spacing of two adjacent patches is 3.8 mm (0.76 λ_0). The total size of the proposed antenna array excluding the measurement transitions is 15.4 × 15.4 × 1.2 mm^3.

Antenna Element Design and Investigation

Investigation of "Differential Feed" Approach for Isolation Enhancement

Figure 19 shows the geometry of the two antenna elements with different feeding approaches. Element A, as shown in Fig. 19a, uses the conventional "single feed"

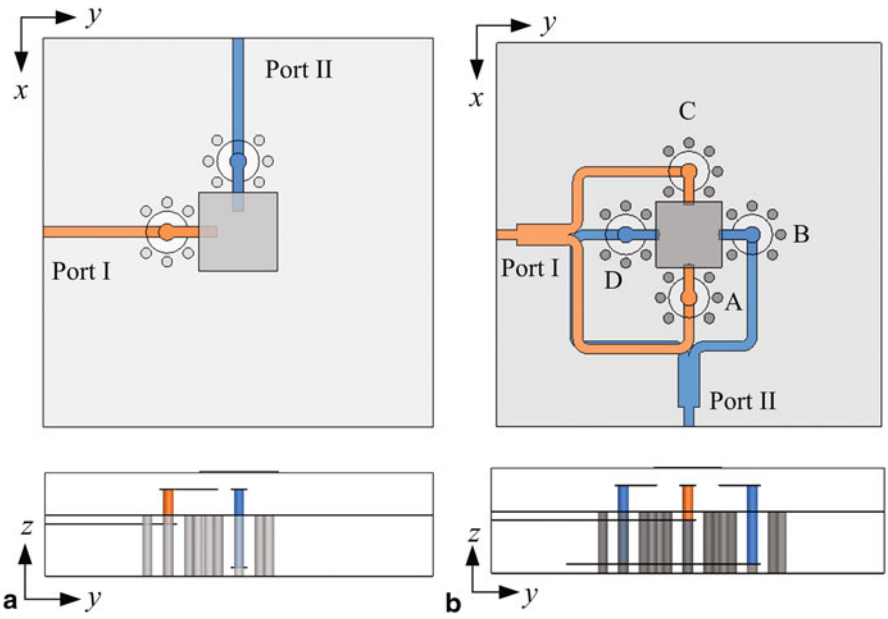

Fig. 19 Geometry of two antenna elements with different feeding technology. **a** Element A: "single feed" approach, **b** Element B: "differential feed" approach

approach. Two orthogonal L-probes as two input ports excite the patch to achieve dual polarization characteristic. In Fig. 19b, Element B illustrates the "differential feed" approach. Four mutual orthogonal L-probes are employed to excite the patch. Probes A and C along x-axis connected to the balun with 180° phase difference of two outputs as Port I are used to excite horizontal polarization, and Probes B and D along y-axis connected to the balun with 180° phase difference of two outputs as Port II are used to excite vertical polarization. Here, we define that horizontal polarization is the polarized direction along the x-axis and vertical polarization is the polarized direction along the y-axis. The signal via of the L-probe is surround by a circle of shielding vias which are composed of six vias connected the top and bottom ground of the SL structure. The shielding vias positioned around the apertures can achieve an optimum coaxial effect to ensure a low transmission loss of the signal via [30, 31].

Figure 20 shows the simulated S parameters of the proposed two antenna elements. For the element A, as Fig. 20a shows, the simulated impedance bandwidth in the frequency range is from 51.5 to 70 GHz for Port I ($|S_{11}| < -10$ dB) and from 53.5 GHz to simulation upper limit frequency 75 GHz for Port II ($|S_{22}| < -10$ dB). For Element B, as Fig. 20b shows, the simulated 10-dB bandwidth is about 25.4 % with respect to the center frequency of 60.5 GHz from 52.5 to 68.5 GHz for Port I ($|S_{11}|$) and about 30.2 % with respect to the center frequency of 63 GHz from 53.5 to 72.5 GHz for Port II ($|S_{22}|$), respectively.

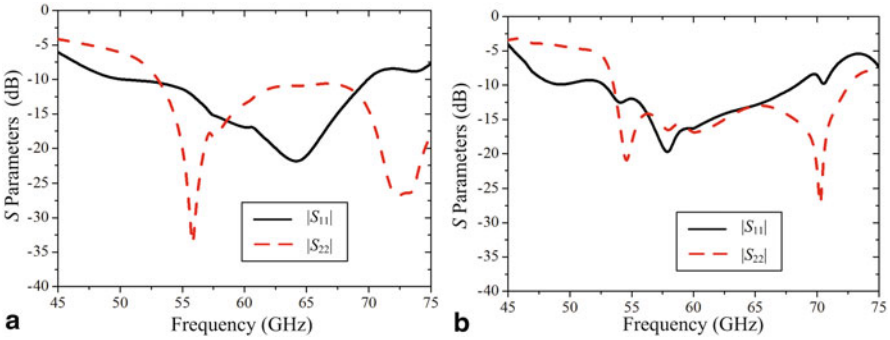

Fig. 20 Simulated *S*parameters with different feed technologies. **a** Simulated $|S_{11}|$ and $|S_{22}|$ for Element A, **b** Simulated $|S_{11}|$ and $|S_{22}|$ for Element B

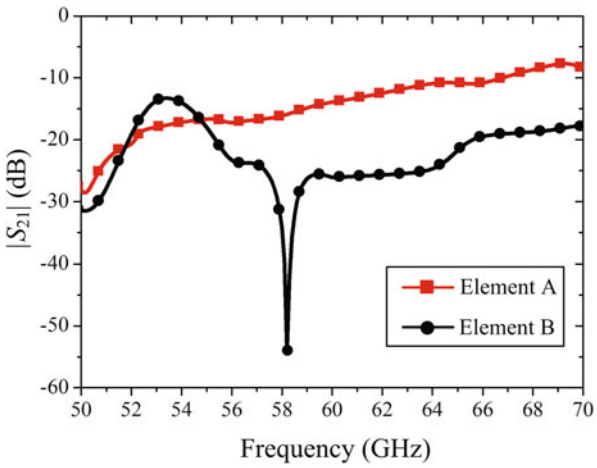

Fig. 21 Simulated isolation against frequency for Element A and Element B

Figure 21 shows the simulated $|S_{21}|$ for Element A and Element B. It is clearly seen that the $|S_{21}|$ of Element A is about −15 dB around 60 GHz, and the corresponding $|S_{21}|$ of Element B is less than −25 dB form 55 to 65 GHz. The 10 dB improvement of the isolation is contributed by the "differential feed" approach obviously. It is because that the poor isolation in Element A is mainly due to the strong coupling between two vertical via portions of the L-probes. However, for Element B which employs the "differential feed" approach, the probes A and C are excited with 180° phase difference, while the probes B and D are also excited with 180° phase difference. The coupling between the probes A and B can be cancelled by the coupling between the probes A and D. Similarly, the coupling between the probes C and B can be cancelled by the coupling between the probes C and D with equal magnitude but 180° out of phase. For this reason, applying the "differential feed" approach can improve the isolation significantly.

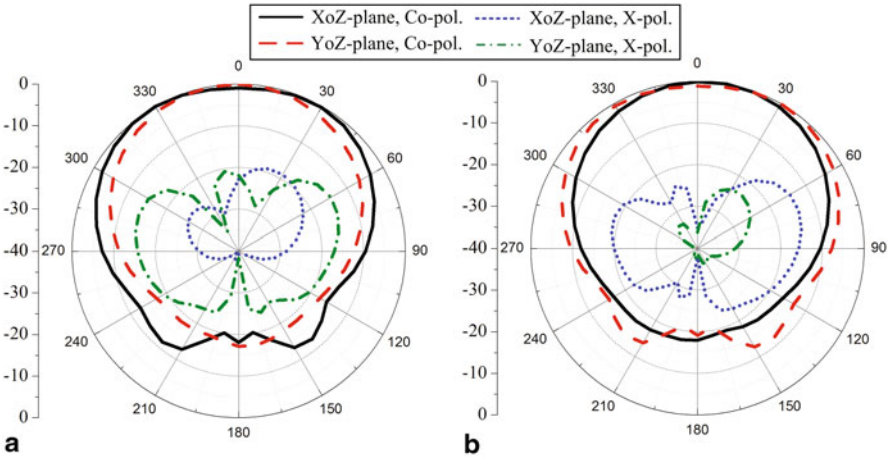

Fig. 22 Simulated radiation pattern for Element B at 60 GHz. **a** Port I: *horizontal* polarization, **b** Port II: *vertical* polarization

The simulated radiation pattern at 60 GHz for Element B is shown in Fig. 22. For Port I, the 3-dB beamwidths are 110 and 90° in XoZ- and YoZ-plane, respectively. The corresponding values for Port II are 80 and 120°. The back-lobe levels for both the horizontal and vertical polarizations are about −18 dB. The simulated gain of Element B are 5.3 dBi for Port I and 5.15 dBi for Port II at 60 GHz, respectively.

The Effect of the Open-Ended SICs on the Antenna Element

The proposed dual-polarized L-probe patch antenna element with the open-ended SIC is shown in Fig. 23. The distance between the power divider feeding network as the Port I and the bottom metal ground of SL structure is h_2. Whereas the distance between the power divider feeding network as the Port II and the bottom metal ground of SL structure is h_3. The multilayer SL as the feeding network structure can be of compact size and suppress the radiation from the feeding line. The open-ended SIC structure is loaded around the L-probe feed dual-polarized antenna element. It is composed of topped metal strip and metal vias fence constituted by a circle of vias. The distance *cd* between the centers of two adjacent vias is 0.25 mm. The width of the feed SL was chosen to be 0.1 mm, which corresponds to the characteristic impedance of 50 Ω. The detailed dimensions of the proposed dual-polarized antenna element are shown in Table 2.

The simulated *S* parameters of the antenna element with the open-ended SIC are shown in Fig. 24 compared with the performances of the antenna element without the open-ended SIC (Element B). For the antenna element with the open-ended SIC, as the Fig. 24a shown, the simulated impedance bandwidth is about 27.5 % with respect to the center frequency of 63.25 GHz from 54.5 to 72 GHz for Port I ($|S_{11}| < -10$ dB) and about 32.2 % with respect to the center frequency of 63.75 GHz from 53.5

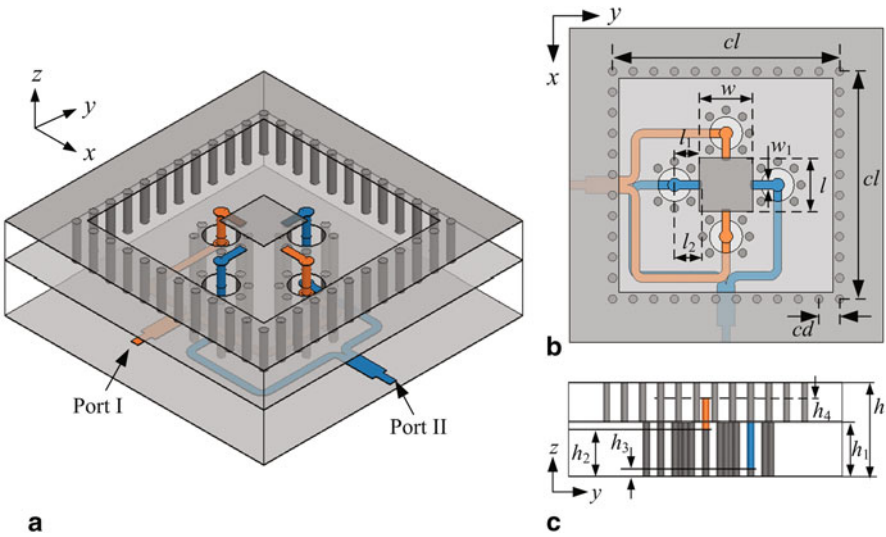

Fig. 23 Geometry of the proposed LTCC dual-polarized L-probe patch antenna element. **a** 3D view, **b** *Top* view, **c** *Side* view

Table 2 Detailed dual-polarized antenna element dimensions

Parameters	Dimensions (mm)	Parameters	Dimensions (mm)	Parameters	Dimensions (mm)
w	0.7	w_1	0.1	l	0.7
l_1	0.25	l_2	0.3	cl	2.7
cd	0.25	h	1.2	h_1	0.7
h_2	0.6	h_3	0.1	h_4	0.3

to 74 GHz for Port II ($|S_{22}| < -10$ dB), respectively. Compared with the element without the open-ended SIC, the impedance bandwidth of the antenna element with the open-ended SIC is improved slightly. The simulated $|S_{21}|$ of the proposed antenna element with the open-ended SICs is less than −25 dB form 56 to 65 GHz.

Figure 25 shows the simulated radiation pattern at 60 GHz for the proposed antenna element with the open-ended SIC. For Port I, the 3-dB beamwidths are 95 and 75° in XoZ-plane and YoZ-plane, respectively. The corresponding values for Port II are 70 and 100°. The back-lobe levels for both the horizontal and vertical polarizations are about −22 dB. Compared with the antenna element without the open-ended SIC, the 3-dB beamwidths are more narrow, the back-lobe levels and cross polarization levels are improved. The simulated gain of the antenna element with the open-ended SICs are 7.3 dBi for Port I and 7.15 dBi for Port II, about 2 dBi higher the gain values of the element without the open-ended SIC.

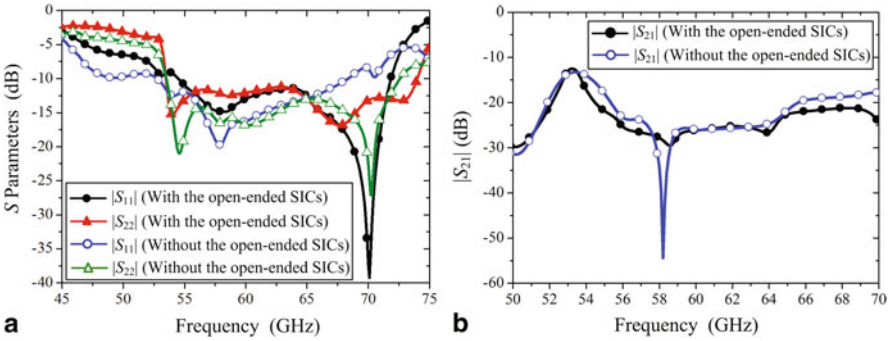

Fig. 24 Simulated S parameters of the proposed antenna element with or without the open-ended SIC. **a** $|S_{11}|$ and $|S_{22}|$, **b** $|S_{21}|$

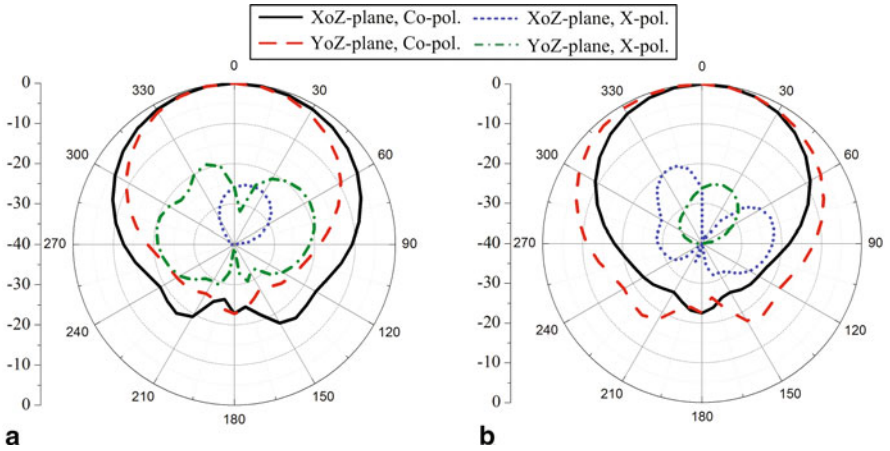

Fig. 25 Simulated radiation pattern for the proposed antenna element with the open-ended SIC at 60 GHz. **a** Port I: horizontal polarization, **b** Port II: vertical polarization

Feeding Network and GCPW-SL Transition

A compact multilayer SL feeding network consisted of two 1-to-32 power dividers is employed to achieve dual polarization characteristic of the antenna array, as Fig. 18 shows. One 1-to-32 power divider located at M2 layer is used to excite the horizontal polarization and connected to Port H. The distance between the Port H feeding network and the bottom ground (M1 layer) is 0.1 mm. The other 1-to-32 power divider located at M3 layer is used to excite the vertical polarization and connected to Port V. The distance between the Port V feeding network and the bottom ground (M1 layer) is 0.6 mm.

To make the loss from the transmission line of the feeding network, as far as possible to shorten the transmission line length is considered, a low-loss cross-over structure is used in the Port V feeding network to shorten the transmission line length

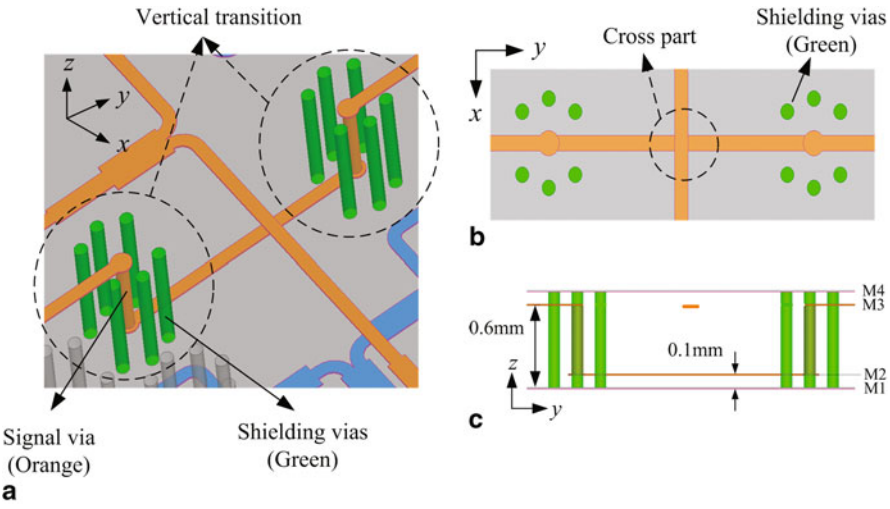

Fig. 26 Configuration of the proposed low-loss cross-over structure. **a** 3D view, **b** *Top* view, **c** *Side* view

and solve the overlap cross of the transmission line. The configuration of the low-loss cross-over structure is shown in Fig. 26. The low-loss cross-over structure consists of two vertical coaxial-like type transmission structures. The signal via connect the signal line at M2 layer and M3 layer. Surrounding the signal via, six shielding vias connected the top (M4 layer) and bottom grounds (M1 layer) are used to achieve an optimum coaxial effect and less low transmission. Figure 27 shows the simulated S parameters of the proposed cross-over structure. The simulated $|S_{11}|$ and $|S_{22}|$ are below -20 dB and $|S_{21}|$ is less than -0.4 dB from 55 to 65 GHz.

The SL fed antenna array is almost impossible to test directly. Therefore, two GCPW-SL transitions were designed as the Port H and Port V of the proposed dual-polarized antenna array, so that the antenna array can be measured with the probe station measurement as illustrated in Fig. 28. For both two different types of GCPW-SL transitions, a partial middle ground is added lower than the upper ground by 0.1 mm (1 LTCC layer) to facilitate probe pitch touching. For the Port H GCPW-SL transition, the simulated $|S_{11}|$ is below -15 dB and $|S_{21}|$ is less than -0.3 dB from 50 to 70 GHz. While, the simulated performance of the Port V GCPW-SL transition is $|S_{11}| < -18$ dB and $|S_{21}| > -0.25$ dB from 50 to 70 GHz.

The Mechanism for Performance Enhancement of Antenna Array by Loading the Open-ended SICs Structure

The electric distributions on the top surface of antenna array for Port H and Port V are simulated by HFSS software are shown in Figs. 29 and 30, so as to investigate the mechanism for performance enhancement of the antenna array loaded by the open-ended SICs structure. When the antenna is fabricated on a large size substrate

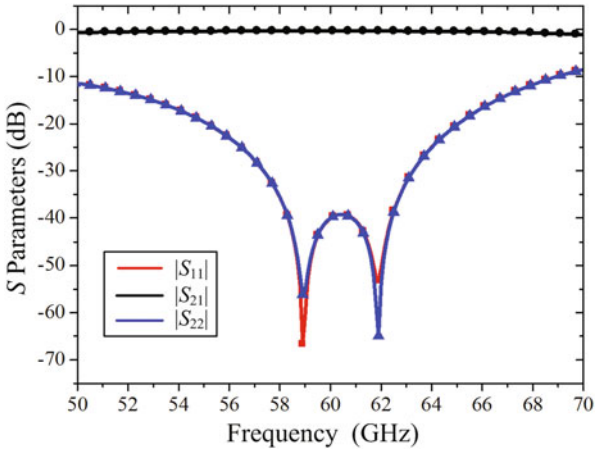

Fig. 27 Simulated *S* parameters of the proposed low-loss cross-over structure

with higher dielectric constant and thicker thickness, the strong surface waves will propagate along the substrate to weaken the radiation performance of the antenna. For Port H exciting, as Fig. 29a shows, there is strong electric field from the surface waves in the area between the antenna elements, in particular along the *y*-axis. Due to the surface wave, the original phase of each element has been changed. Therefore, the radiation performance of antenna array is deteriorated. The proposed open-ended SICs structure like an electric wall around the antenna element blocks the surface wave propagating. As Fig. 29b shows, because of the surface wave substantially suppressed, the field distribution of the radiation patch elements is improved obviously. On the other hand, the loss of the surface wave is reduced by the open-ended SICs structure, more power as the effective radiation to enhance the gain of the antenna array.

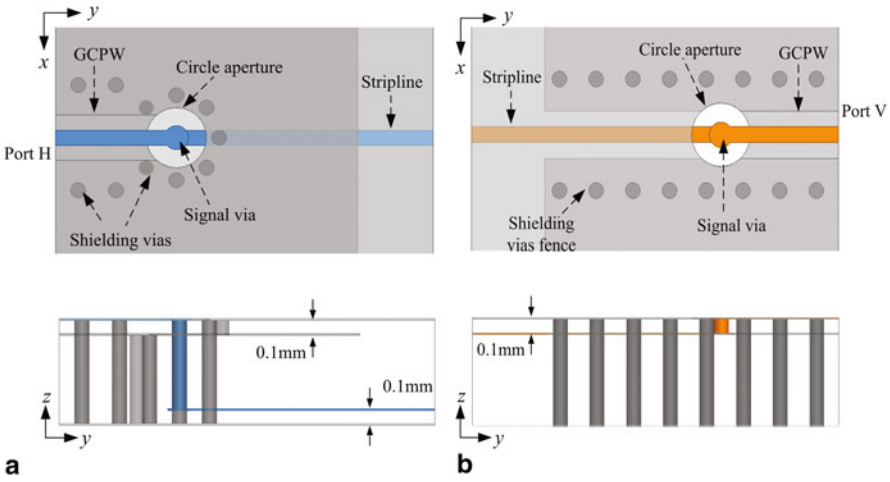

Fig. 28 Geometry of two GCPW-SL transitions. **a** Port H, **b** Port V

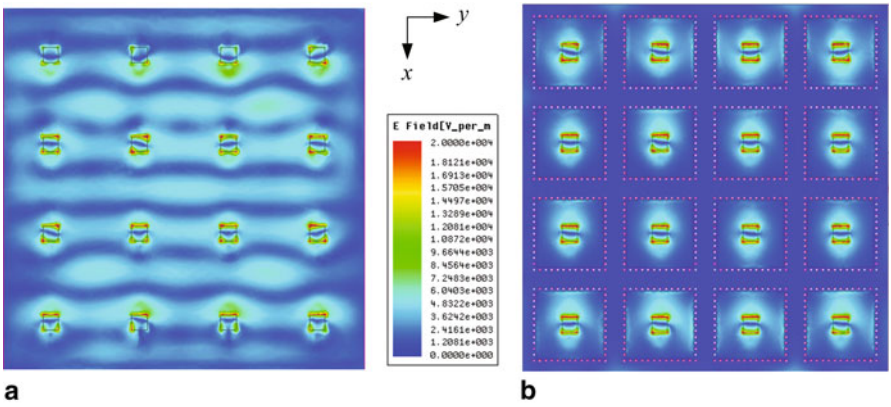

Fig. 29 Simulated electric field distributions on the *top* substrate surface of two cases arrays for Port H. **a** Without the open-ended SICs structure, **b** With the open-ended SICs structure

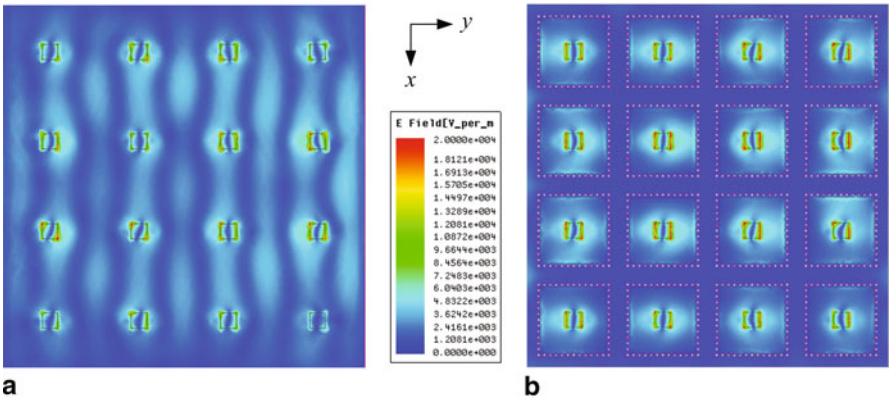

Fig. 30 Simulated electric field distributions on the *top* substrate surface of two cases arrays for Port V. **a** Without the open-ended SICs structure, **b** With the open-ended SICs structure

Similarly, for Port V exciting, strong electric field from the surface waves existing in the area between the antenna elements in Fig. 30a, in particular along the x-axis, disturb the original phase of each element. For this reason, the radiation performances of antenna array are deteriorated. After employing the open-ended SICs structure, as Fig. 30b shows, the surface wave is substantially suppressed to result in the gain enhancement of the antenna array.

Simulated and Measured Results

Figure 31 shows the photograph of the fabricated antenna array with the open-ended SICs and two GCPW-SL transitions.

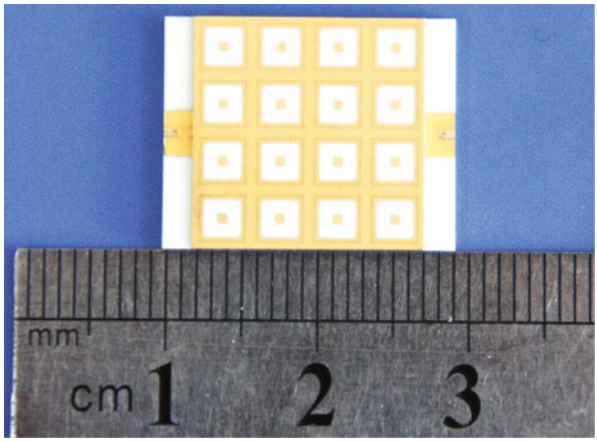

Fig. 31 Photograph of the proposed fabricated dual-polarized antenna array with open-end SICs

The measured and simulated *S* parameters of the proposed antenna array are illustrated in Fig. 32. The simulated 10-dB impedance bandwidths are ∼19.1 % with respect to 60.25 GHz from 54.5 to 66 GHz for Port H, and ∼24.4 % with respect to 61.5 GHz from 54 to 69 GHz for Port V, respectively. The measured reflection coefficients of antenna array is slightly worse than the simulated values. The discrepancy could come from the LTCC fabrication tolerance and substrate shrink, the inaccuracy of the dielectric permittivity, and even from the touching position of the Ground-Signal-Ground (GSG) probe influence.

Figure 33 shows the measured and simulated input ports isolation of the proposed dual-polarized antenna array. It can be seen that, the simulated $|S_{21}|$ of the antenna array is less than −25 dB from 58.5 to 65 GHz. Whereas, the measured isolation $|S_{21}|$ is below −20 dB over the frequency range from 58.5 to 65 GHz.

The measured gain of the proposed antenna array for Port H and Port V are plotted in Fig. 34, and compared with the simulated results. Considering the metal chuck and the different calibrations needed for this setup (standard horn antenna, waveguide

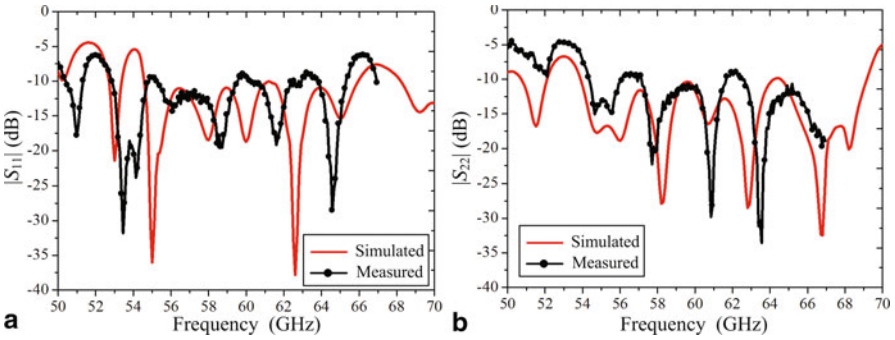

Fig. 32 Measured and simulated *S* parameters of the antenna array, **a** Port H ($|S_{11}|$), **b** Port V ($|S_{22}|$)

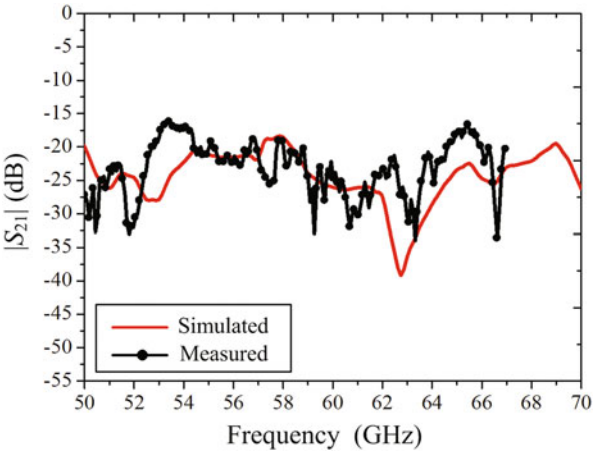

Fig. 33 Measured and simulated ports isolation ($|S_{21}|$) of the antenna array

to coaxial adapter, GSG probes, and misalignment), the accuracy of the measured gain is estimated to be 1 dB in the frequency band. The simulated and measured gain results are 18.5 and 17.1 dBi for Port H, respectively. The measured 3-dB gain bandwidth of the proposed array for Port H is from 56 to 67 GHz. As Fig. 22b shows, the simulated and measured gain results are 17.8 and 16.6 dBi for Port V, respectively. The measured 3-dB gain bandwidth of the proposed array for Port V is from 55 to 66 GHz. compared with the simulated results, the gain is dropped about 1.4 dB. It is mainly caused by three following reasons: (1) the deterioration of impedance matching; (2) the deviation of the LTCC substrate dielectric and the conductivity of the metallization material; (3) The shrinking of LTCC fabrication.

The measured and simulated co-pol and cross-pol radiation patterns of the proposed dual-polarized antenna array in two principal planes (XoZ-plane and YoZ-plane) at 60 GHz for Port H and Port V are shown in Fig. 35, respectively. For Port H horizontal polarization, as Fig. 35a shows, the simulated and measured

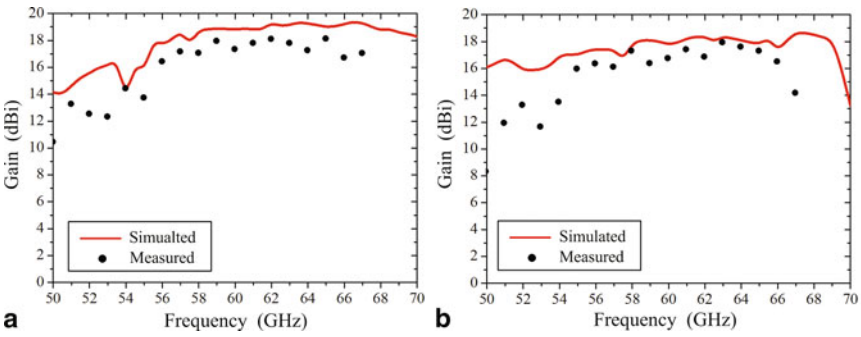

Fig. 34 Measured and simulated gain of the antenna array, **a** Port H: *horizontal* polarization, **b** Port V: *vertical* polarization

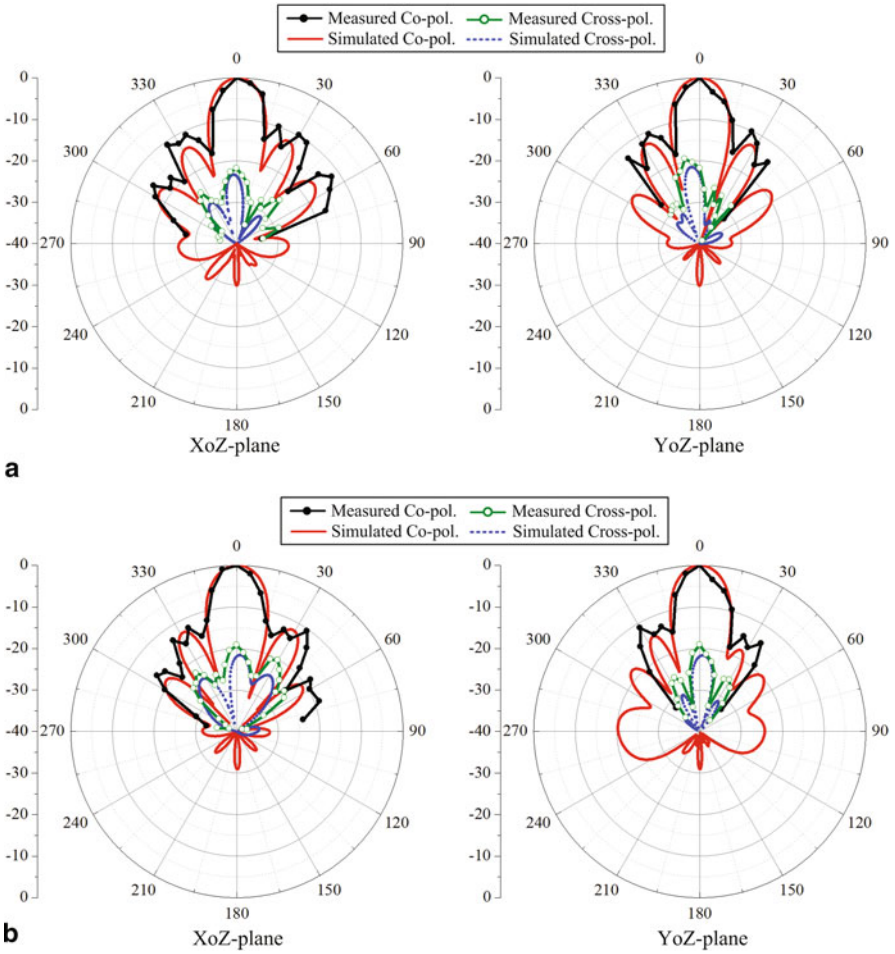

Fig. 35 Measured and simulated radiation patterns of the proposed antenna array at 60 GHz, **a** Port H for *horizontal* polarization, **b** Port V for *vertical* polarization

cross-polarization levels are almost −22.3 and −19.1 dB in two principal planes. For Port V vertical polarization, as Fig. 35b shows, the simulated and measured cross-polarization levels are about −21.6 and −19.5 dB in two principal planes, respectively.

A 4 × 4 LTCC dual-polarized L-probe patch antenna array with the open-ended SICs structure for 60 GHz wireless communication applications has been designed and tested. The proposed 60-GHz dual-polarized antenna array has compact size, wide bandwidth, good isolation, high gain and wide 3-dB gain bandwidth by employed the multilayer SL feeding network, "differential feed" L-probe approach, and open-ended SICs.

References

1. P. Smulders, Exploring the 60 GHz band for local wireless multimedia access: prospects and future directions. IEEE. Commun. Mag. **40**(1), 40–147 (Jan. 2002)
2. A. Sadri, 802.15.3c usage model document. IEEE 802.15-06-0055-14-003c (May 2006)
3. Y.P. Zhang, D. Liu, Antenna-on-chip and antenna-in-package solutions to highly integrated millimeter-wave devices for wireless communications. IEEE. Trans. Antennas Propag. **57**(10), 2830–2841 (Oct. 2009)
4. T.S. Rappaport, J.N. Murdck, F. Gutierrez, State of the art in 60-GHz integrated circuits and systems for wireless communications. Proc. IEEE. **99**(8), 1390–1436 (Aug. 2011)
5. D. Liu, Y.P. Zhang, Integration of antenna arrays in chip package for 60-GHz radios. Proc. IEEE. **100**(7), 2364–2371 (Jul. 2012)
6. R.R. Tummala, M. Swaminathan, M.M. Tentzeris, J. Laskar, G.-K. Chang, S. Sitaraman, D. Keezer, D. Guidotti, Z.R. Huang, K. Lim, L.X. Wan, S.K. Bhattacharya, V. Sundaram, F.H. Liu, P.M. Raj, The SOP for miniaturized, mixed-signal computing, communication, and consumer systems of the next decade. IEEE Trans. Adv. Packag. **27**(2), 250–267 (May 2004)
7. Y.P. Zhang, M. Sun, D. Liu, Y. Lu, Dual grid antenna arrays in a thin-profile package for flip-chip interconnection to highly integrated 60-GHz radios. IEEE Trans. Antennas Propag. **59**(4), 1191–1199 (Apr. 2011)
8. H. Chu, Y.-X. Guo, Z. Wang, 60-GHz LTCC wideband vertical Off-Center dipole antenna and arrays. IEEE. Trans. Antennas Propag. **61**(1), 153–161 (Jan. 2013)
9. J. Xu, Z.N. Chen, X. Qing, W. Hong, Bandwidth enhancement for a 60 GHz substrate integrated waveguide fed cavity antenna array on LTCC. IEEE. Trans. Antennas Propag. **59**(3), 826–832 (Mar. 2012)
10. L. Wang, Y.-X. Guo, W.X. Sheng, Wideband high-gain 60-GHz LTCC L-probe patch antenna array with a soft surface. IEEE. Trans. Antennas Propag. **61**(4) 1802–1809 (Apr. 2013)
11. H. Sun, Y.-X. Guo, Z. Wang, 60-GHz circularly polarized U-slot patch antenna array on LTCC. IEEE. Trans. Antennas Propag. **61**(1), 430–435, (Jan. 2013)
12. M. Sun, Y.Q. Zhang, Y.-X. Guo, M.F. Karim, L.C. Ong, M.S. Leong, Integration of circular polarized array and LNA in LTCC as a 60-GHz active receiving antenna. IEEE. Trans. Antennas Propag. **59**(8), 3083–3089 (Aug. 2011)
13. C. Liu, Y.-X. Guo, X. Bao, S.Q. Xiao, 60-GHz LTCC integrated circularly polarized helical antenna array. IEEE. Trans. Antennas Propag. **60**(3), 1329–1335 (Mar. 2012)
14. A.E.I. Lamminen, J. Säily, A.R. Vimpari, 60-GHz patch antennas and arrays on LTCC with embedded-cavity substrates. IEEE. Trans. Antennas Propag. **56**(9), 2865–2874 (Sep. 2008)
15. I. K. Kim, N. Kidera, S. Pinel, J. Papapolymerou, J. Laskar, J.-G. Yook, M.M. Tentzeris, Linear tapered cavity-backed slot antenna for millimeter-wave LTCC modules. IEEE. Antennas Wireless. Propag. Lett. **5**, 175–178 (2006)
16. S.B. Yeap, Z.N. Chen, X. Qing, Gain-enhanced 60-GHz LTCC antenna array with open air cavities. IEEE. Trans. Antennas Propag. **59**(9), 3470–3473 (Sep. 2011)
17. A.E.I. Lamminen, A.R. Vimpari. J. Säily, UC-EBG on LTCC for 60-GHz frequency band antenna applications. IEEE. Trans. Antennas Propag. **57**(10), 2904–2912 (Oct. 2009)
18. Y. Li, Z.N. Chen, X. Qing, Z. Zhang, J. Xu, Z. Feng, Axial ratio bandwidth enhancement of 60-GHz substrate integrated waveguide-fed circularly polarized LTCC antenna array. IEEE. Trans. Antennas Propag. **60**(10), 4619–4626 (Oct. 2012)
19. K.M. Luk, C.L. Mak, Y.L. Chow, K.F. Lee, Broadband microstrip patch antenna. Electron. Lett. **34**, 1442–1443 (July 1998)
20. C.L. Mak, K.M. Luk, K.F. Lee, Y.L. Chow, Experimental study of a microstrip antenna with an L-shaped probe. IEEE. Trans. Antennas Propag. **48**, 777–783 (May 2000)
21. Y.-X. Guo, C.L. Mak, K.M. Luk, K.F. Lee, Analysis and design of L-probe proximity fed patch antenna. IEEE. Trans. Antennas Propag. **49**(2), 145–149 (Feb. 2001)
22. P.-S. Kildal, Artificially soft and hard surfaces in electromagnetic. IEEE. Trans. Antennas Propag. **38**(10), 1537–1544 (Oct. 1990)

23. Z. Ying, P.-S. Kildal, Study of different realizations and calculation models for soft-surfaces by using vertical monopole on soft disk as test bed. IEEE. Trans. Antennas Propag. **44**(11), 1474–1481 (Nov. 1996)
24. R. Li, G. DeJean, M.M. Tentzeris, J. Papapolymerou, J. Laskar, Radiation-pattern improvement of patch antenna on a large-size substrate using a compact soft-surface structure and Its realization on LTCC multilayer technology. IEEE. Trans. Antennas Propag. **53**(1), 200–208 (Jan. 2005)
25. Y.-X. Guo, K.M. Luk, K.F. Lee, Broadband dual polarization patch element for cellular-phone base stations. IEEE. Trans. Antennas Propag. **50**(2), 251–253 (Feb 2002)
26. L. Bian, Y.-X. Guo, L.C. Ong, X.Q. Shi, Wideband circularly-polarized patch antenna. IEEE. Trans. Antennas Propag. **54**(9), 2682–2686 (Sep. 2006)
27. H. Wong, K.-L. Lau, K.-M. Luk, Design of dual-polarized L-probe patch antenna arrays with high isolation. IEEE. Trans. Antennas Propag. **52**(1), 45–52 (Jan. 2004)
28. Y.-X, Guo, K.-W. Khoo, L.C. Ong, Wideband dual-polarized patch antenna with broadband baluns. IEEE. Trans. Antennas Propag. **55**(1), 78–83 (Jan. 2004)
29. K.L. Lau, K.M. Luk, A. wideband dual-polarized L-Probe stacked patch antenna array. IEEE. Lett. **6**, 529–532 (2007)
30. J. Heyen, A. Gordiyenko, P. Heide, A.F. Jacob, Vertical feedthroughs for millimeter-wave LTCC modules. In IEEE Eur. Microw. Conf., Munich, Germany, pp. 411–414 (Oct. 2003)
31. C.-C. Tsai, T.-S. Chen, T.-Y. Huang, Y.A. Hsu, R.-B. Wu, Design of microstrip-to-microstrip via transition in multilayered LTCC for frequencies up to 67 GHz. IEEE Trans. Compon. Packag. Manufactur. Tech. **1**(4), 595–600 (April. 2011)

Frequency Domain Breast Lesion Classification Using Ultra-Wideband Lesion Response

Arash Maskooki, Cheong Boon Soh, Aye Chan, Erry Gunawan and Kay Soon Low

Abstract Shape of an object has been shown to affect the backscattered ultra-wideband (UWB) pulse in frequency domain. Frequency-domain response of the backscattered signal is the sum of damping harmonics where each harmonic is associated with a specific scatterer and the damping factor is a function of the shape of the corresponding scatterer. Backscattered signals from benign and malignant breast tumors are obtained through numerical analysis. The damping factors were extracted from frequency response of the backscattered signal and neural networks were used to classify breast lesions into benign and malignant tumors. Different architectures of neural networks were investigated and cascaded Kolmogorov network was found to be most accurate classifier. Results show that the cascaded Kolmogorov network classifier can increase the accuracy of diagnosis up to 75.2 %, which is higher than existing methods.

Keywords Ultra-wideband · Breast cancer detection · Lesion classification · Neural networks · Numerical lesion model · Kolmogorov architecture · Finite-difference time-domain (FDTD) · Geometrical theory of diffraction (GTD) · Frequency domain analysis · Scattering · Diffraction

Introduction

Breast cancer is the second most prevalent type of cancer and the second leading cause of death by cancer in women in the USA according to the Center for Disease Control and Prevention (CDC) [1]. Lifetime risk of breast cancer among women in the USA is very close to one in eight and it is estimated that it has claimed 40,676 lives in the USA in 2009.

C. B. Soh (✉) · A. Maskooki · A. Chan · E. Gunawan · K. S. Low
School of Electrical and Electronic Engineering,
Nanyang Technological University, 50 Nanyang Drive,
Singapore, 637553 Republic of Singapore
e-mail: ecbsoh@ntu.edu.sg

M. R. Yuce (ed.), *Ultra-Wideband and 60 GHz Communications for Biomedical Applications,* DOI 10.1007/978-1-4614-8896-5_12,

Early detection of breast cancer and timely medical intervention will ensure long-term survival and an improved quality of life of breast-cancer victims. Early breast cancers with a higher statistical chance of cure are those which are below 15 mm in size and found at stage I, when the cancer is confined to the breast. The gold-standard method of breast imaging is film-screen mammography, which provides very high-resolution (50 μm) X-ray images of compressed breasts. This technology can detect micro-calcifications of pre-invasive cancer (ductal carcinoma in situ) and both masses and distortion of parenchyma in small breast cancers with high sensitivity. It has been used routinely for detecting and characterizing breast disease for 3 decades. However, X-ray mammography has significant limitations, which include high false-positive and -negative rates, difficulty in imaging women with dense breasts and inconclusive results. The callback rate of standard screening mammography in community practice is approximately 8–20 % depending on the screening scenario used. The false-negative rate with mammography is also significant and ranges from 4 to 34 %, depending on the clinical context. The relatively poor specificity of mammography is due to huge overlap in the appearances of a benign disease and early breast cancer. Lack of sensitivity of mammography is largely due to obscuration of pathology by glandular tissue. As a result, mammography is less sensitive for breast cancer detection in women with radiographically dense breast tissue. This is of particular concern because there is a significant proportion of dense breasts in both younger and older women receiving exogenous estrogen. Furthermore, in Asian women, particularly of Chinese, Korean and Japanese ethnicity, there is a higher incidence of diffusely dense glandular parenchyma than that in Western, Indian or Malay women of equivalent age. Other drawbacks of mammography include examinee tolerance of compression, variability in radiological interpretation and radiation-dose considerations. As a result, there is a clear motivation for the development of alternative or complementary breast-imaging tools to assist in detection and diagnosis. Other well-established imaging modalities, such as magnetic resonance imaging (MRI), positron emission tomography (PET) and ultrasound, are in various stages of use in diagnosis. However, each of these imaging modalities has its limitations. MRI exhibits highly variable specificity, ranging from 65 to 90 %, depending on the interpretation technique used and the patient population. Moreover, the cost of MRI scanners is high and the availability of the technique and the expertise required for interpretation is very limited. PET scans are even more expensive and scarce; they are also even more insensitive for both ductal carcinoma in situ and very small cancers. Ultrasound has difficulty seeing the micro-calcifications produced in early cancers and is also highly nonspecific for nodules smaller than 1 cm in size. Many small breast nodules are found in normal women, with a wide range of mostly benign pathology and neither ultrasound nor mammography is able to distinguish between these and small cancers with great reliability.

Ultra-wideband (UWB) imaging offers many of the desirable characteristics as an ideal breast cancer evaluation tool. The method is attractive to patients because both ionizing radiation and breast compression are avoided, potentially leading to safer and more comfortable exams. It also has the potential to be both sensitive and specific, to detect small tumors and to be much cheaper than methods such as MRI

and PET. UWB screening and diagnosis of breast cancer has been investigated by researchers for over a decade [2–21]. Low-cost equipments and harmless radiation make UWB imaging a promising modality in early detection of breast cancer. UWB pulse could be used for both detection and classification of the breast lesion. The feasibility of using UWB pulse to detect breast lesions is studied in [2, 3, 7, 10, 20, 22]. In this approach, a breast is illuminated by a UWB pulse and the backscattered signal is collected by an array of antennae. The UWB beam is synthetically focused spatially to yield a map of dielectric variations within the breast medium. Breast lesions normally exhibit irregularly high dielectric constant and thus appear brighter in the synthetic beamformer images. In addition to localization of the lesion, UWB could also be used to determine malignancy of the lesion [4, 6, 8, 9, 15, 21]. In [15], the authors have investigated the feasibility of using UWB pulse in characterizing the lesion based on its size and shape. In this study, two basis selection methods, local discriminant basis and principal component analysis, are employed to construct and evaluate a UWB lesion classifier. The effect of lesion morphology on temporal response of the backscattered UWB pulse is studied in [6]. It is shown that the lesion morphology affects the complex natural resonances in the late-time backscatter response of UWB pulse and hence, the potential use of this method for discriminating between benign and malignant masses. The use of contrast agent for lesion classification is studied in [5]. In this study, the damping factors of the differentiated backscatter responses are compared before and after infusion of the contrast agent to detect anomalies. In [8], support vector machine (SVM) classifier is suggested and compared with linear discriminant analysis (LDA) and quadratic discriminant analysis (QDA) classifiers. Multi-input multi-output (MIMO) radar techniques are used in [4] to enhance resonance scattering based lesion classification. In [21], the early time portion of the backscattered breast response is passed through a correlator to quantify the degree of lesion ruggedness and hence, the malignancy of the lesion is determined.

The main objective of this chapter is to investigate the feasibility of classifying breast lesions using their frequency-domain UWB backscatter responses. A UWB breast lesion classifier is introduced based on the frequency-domain signature of the lesion. Complex harmonics are extracted from the frequency response and combined to form an input vector to a neural network classifier. The classifier is then trained using a training subgroup of vectors obtained from numerical analysis of the lesion responses. Different architectures of neural networks and their performances in characterizing lesions are evaluated and discussed.

This chapter is organized as follows: The state-of-the-art UWB breast lesion detection and classification is given in “Introduction”. Details on the numerical analysis of the lesion backscattered signal are given in the section, “Numerical Breast Model”. “Complex Harmonic Estimation” discusses the frequency-domain processing of the backscatter signal followed by “Lesion Classifier”,which provides the frequency-domain classifier design and architecture. “Results” evaluates the performance of different architectures of neural networks. Finally, “Conclusion” concludes this chapter.

Numerical Breast Model

Finite difference time domain (FDTD) TE_z mode (E_x, E_y and E_z) with spatial resolution of 0.5 mm square was used to obtain the backscatter signals. The computational space consists of 401 cells along the direction of propagation and the direction of electric field source arranged to form a square box. Uniaxial perfectly matched layer (UPML) is used beyond the computational space to ensure perfect absorption at the boundaries. Details of the update equations used for the FDTD simulation are discussed in [23].

Permittivity for average breast medium, clutter sources and lesion target at different frequencies is obtained through Debye model,

$$\epsilon(\omega) = \epsilon_\infty + \frac{\epsilon_s - \epsilon_\infty}{1 + j\omega\tau_p} - j\frac{\sigma}{\omega\epsilon_0}, \tag{1}$$

where $\omega = 2\pi f$ is the angular frequency, ϵ_s the static permittivity, ϵ_∞ the infinite permittivity, ϵ_0 the permittivity of free space, σ the conductivity of the medium and T_p is the relaxation constant. The nominal values used for the breast and lesion tissue are given in Table 1. The clutter sources of varying dielectric constants between 8.1 and 9.9 are introduced to mimic a realistic breast tissue.

The breast is modeled as a 5 cm radius cylinder with some regions containing clutter sources as in [6]. A directed field point source transceiver and four additional point receivers are placed at a radius of 6.5 cm away from the center at 15-degree intervals. Figure 1 shows the configuration of simulation space. Two types of lesions, smooth and spiculated, were used in this study to represent benign and malignant lesions, respectively. Figure 2 shows a sample of each type of lesion.

Five hundred and forty backscatter responses from the respective environments, each consisting of 3,201 temporal points, are obtained through numerical methods. Out of the 540 responses, 270 responses correspond to benign lesions, which have been modeled as non-spiculated lesions and the rest are malignant lesions which are highly spiculated. As an antenna array of nine antennae has been modeled, nine backscatter signals are collected from each lesion realization. Total realization number of the lesions is 30 lesions from each of the benign and malignant type.

Further details of the configuration, simulation steps and lesion characteristics are discussed in [21].

Complex Harmonic Estimation

According to the geometrical theory of diffraction (GTD) [24, 25], backscattered signal from a number of scattering points has a pattern in frequency domain. As described in [26], each scatterer in the view of the antenna will create a harmonic term in the frequency-domain response of a UWB pulse. This means that the frequency response of the backscattered signal is a combination of some complex harmonic

Table 1 Nominal values of the model parameters

	ϵ_S	ϵ_∞	σ (S/m)	T_p
Normal breast tissue	10	7	0.15	7
Lesion	54	4	0.7	7

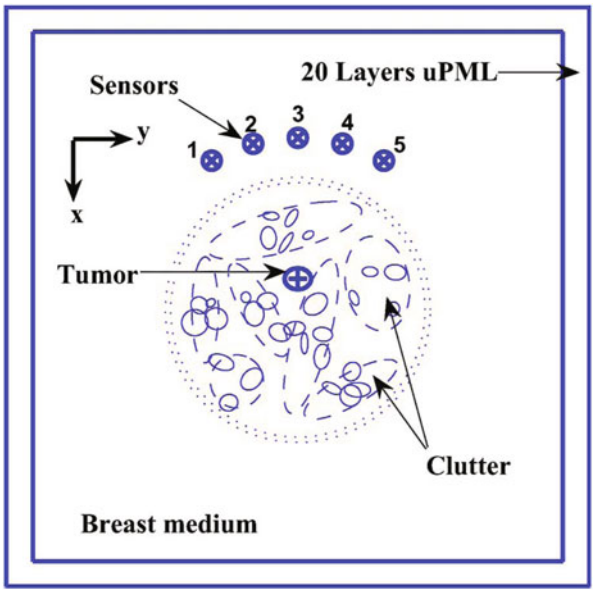

Fig. 1 Configuration of simulation space. The transmitter is placed at the center of the array. Receivers equidistant from the lesion at regular intervals

terms with different attenuation coefficients and frequencies (poles). As predicted by GTD, the attenuation coefficient is a function of the shape of the object while its frequency is determined by the distance between the scatterer and the receiver. This representation has interesting applications in UWB microwave radars. Fitting an

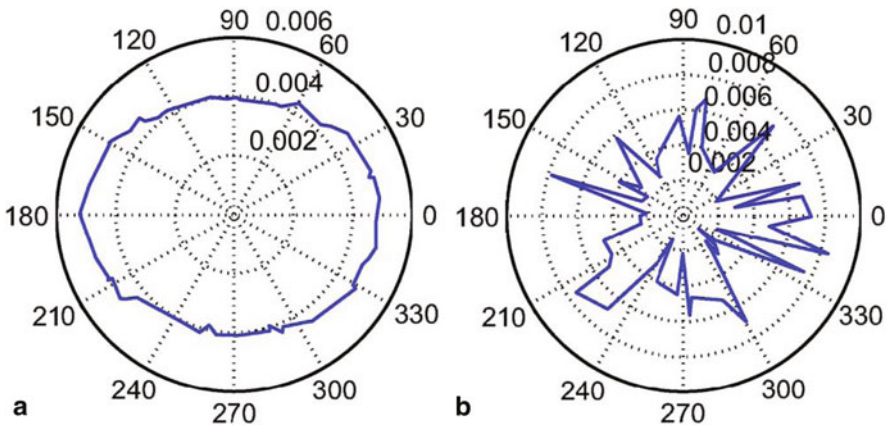

Fig. 2 **a** Sample of smooth lesion. **b** Sample of rough lesion

appropriate model to this pattern helps to reconstruct the signal beyond the bandwidth of the system and thus leads to a higher image resolution without additional hardware cost. Cumo et al. [26] have used this bandwidth extrapolation method to estimate the frequency response of the backscattered signal in the gap between two different incoherent sub-bands.

The number of harmonics in frequency domain is the same as the number of the scattering points in the view of the antenna and multiple scattering effect [27]. Mathematical model of the frequency-domain signal is [28]

$$y(f) = \sum_{i=1}^{N} A_i(f) e^{\left(j\frac{4\pi}{c}R_i\right)f}, \tag{2}$$

where f is the frequency, c the speed of light, N the number of scattering points and R_i is the range of the i^{th} scattering point. $A_i(f)$ is the frequency dependence function corresponding to the i^{th} scattering point. This frequency dependence function is of the form f^{α}, where the exponent α is known for some common scattering mechanisms. For example, a flat plate has $\alpha = 1$ while a spherical object will have $\alpha = 0$ [27]. As stated by Cumo et al. [26], f^{α} scattering behavior can accurately be estimated by exponential functions over a finite bandwidth interval. Hence, the following discrete model can represent the frequency behavior of the reflected signal given in Eq. 2 above:

$$y(k) = \sum_{i=1}^{N} a_i e^{-\left(\alpha_i + j\frac{4\pi}{c}R_i\right)k\Delta f}, \tag{3}$$

where a_i are the constant coefficients of the sinusoids, α_i and R_i refer to the frequency decay/growth factor and the range of the i^{th} scatterer, respectively and Δf is the sampling frequency. In the rest of this section, we provide the formulation to estimate model parameters in Eq. 3. More details and derivations are available in [28].

From system theory, we know that the following state-space equations hold for input–output relation in a linear system:

$$\begin{aligned} \mathbf{x}(k+1) &= \mathbf{A}\mathbf{x}(k) + \mathbf{B}\mathbf{w}(k) \\ \mathbf{y}(k) &= \mathbf{C}\mathbf{x}(k) + \mathbf{w}(k), \end{aligned} \tag{4}$$

where $\mathbf{x}(k)$ is the state vector, $\mathbf{w}(k)$ the input vector and $\mathbf{y}(k)$ is the output of the system. $\mathbf{A}$, $\mathbf{B}$ and $\mathbf{C}$ are matrices characterizing the system and define its state-space behavior. The transfer function of the system described in Eq. 4 is given in Eq. 5:

$$\mathbf{T}(z) = \frac{\mathbf{Y}(z)}{\mathbf{X}(z)} = \mathbf{C}(z\mathbf{I} - \mathbf{A})^{-1}\mathbf{B} + 1. \tag{5}$$

The impulse response of such a system in general comprises a number of complex sinusoids or poles of the system which are the roots of the denominator or as seen

in Eq. 5 are the eigenvalues of **A**, the open-loop matrix of the system. Hence, the output signal of the system $y(k)$ can be written as

$$y(k) = \sum_{i=1}^{M} a_i e^{-(\alpha_i + j\beta_i)k\Delta t}. \tag{6}$$

In Eq. 6, M is the number of the poles of the system or the eigenvalues of **A**, a_i are the constant coefficients of each complex sinusoid and α_i and β_i are the damping factor and frequency of the i^{th} harmonic, respectively. Δt is the sampling time interval.

Comparing Eqs. 6 and 3 reveals that the frequency response of the backscattered signal and the impulse response of a linear system have a similar mathematical structure. Thus, we can use the mathematics of linear system identification to estimate the parameters of the frequency model for the backscattered data.

Suppose that the frequency response of the backscattered signal is the impulse response of a hypothetical linear system. Here we try to extract the system matrices and consequently, a model for the impulse response based on the eigenvalues or poles of this hypothetical system. As mentioned before, we can derive the desired frequency model parameters from this impulse response model.

The process of finding the hypothetical system matrices involves forming forward prediction or a Hankel matrix from the sample data of the frequency response of the backscattered signal and deriving **A** through singular value decomposition of **H**, the Hankel matrix which is defined as follows:

$$\mathbf{H} = \begin{pmatrix} y(1) & \cdots & y(L) \\ \vdots & \ddots & \vdots \\ y(N-L+1) & \cdots & y(N) \end{pmatrix}, \tag{7}$$

where $y(i)$ are the samples of frequency-domain response of the backscattered data, N is the number of data samples and L is chosen as $N/3$ [25]. By singular value decomposition, **H** is decomposed into three matrices,

$$\mathbf{H} = \mathbf{U}\,\mathbf{\Sigma}\,\mathbf{V}^*, \tag{8}$$

where **U** is the left unitary matrix, $\mathbf{V}^*$ is the right unitary matrix and $\mathbf{\Sigma}$ is a diagonal matrix containing singular values of **H** in descending order.* denotes the complex conjugate and transpose.

Singular values of **H** could be separated into two subspaces, the signal-plus-noise subspace and the noise-only subspace. If the signal-to-noise ratio (SNR) value is high enough there would be a sharp transition between singular values of the signal and those of the noise. The criterion for separating the two parts is described in [29]. Hence, **U**, $\mathbf{\Sigma}$ and $\mathbf{V}^*$ could be divided into two different subspaces as follows:

$$\mathbf{H} = \begin{pmatrix} \mathbf{U_{sn}} & \mathbf{U_n} \end{pmatrix} \begin{pmatrix} \mathbf{\Sigma_{sn}} & 0 \\ 0 & \mathbf{\Sigma_n} \end{pmatrix} \begin{pmatrix} \mathbf{V^*_{sn}} \\ \mathbf{V^*_n} \end{pmatrix}, \tag{9}$$

in which the subscripts '*sn*' and '*n* ' refer to the signal-noise and noise subspaces, respectively. Removing the noise part, $\tilde{\mathbf{H}}$ can be formed as follows:

$$\tilde{\mathbf{H}} = \mathbf{U_{sn}}\,\mathbf{\Sigma}_{\mathbf{sn}}\mathbf{V}^{*}_{\mathbf{sn}}. \tag{10}$$

Using the balanced coordinate method [28], $\tilde{\mathbf{H}}$ could further be factorized as

$$\tilde{\mathbf{H}} = \mathbf{\Omega}\ \mathbf{\Gamma}, \tag{11}$$

where

$$\mathbf{\Omega} = \mathbf{U_{sn}}\,\mathbf{\Sigma}_{\mathbf{sn}}{}^{1/2} \text{ and } \mathbf{\Gamma} = \mathbf{\Sigma}_{\mathbf{sn}}{}^{1/2}\mathbf{V}^{*}_{\mathbf{sn}}, \tag{12}$$

where $\mathbf{\Omega}$ and $\mathbf{\Gamma}$ are the observability and controllability matrices, respectively.

A could be derived from both the observability or the controllability matrices; here $\mathbf{\Omega}$ is used to derive **A**.

$$\mathbf{A} = (\mathbf{\Omega}^{*}_{\mathbf{-rl}}\,\mathbf{\Omega}_{\mathbf{-rl}})^{-1}(\mathbf{\Omega}_{\mathbf{-rl}}\,\mathbf{\Omega}_{\mathbf{-rf}}), \tag{13}$$

where $\mathbf{\Omega}_{\mathbf{-rl}}$ and $\mathbf{\Omega}_{\mathbf{-rf}}$ are obtained by removing the last and first rows of $\mathbf{\Omega}$, respectively. Now α_i and R_i are related to the eigenvalues of **A** by

$$\alpha_i = \frac{-\log|\lambda_i|}{\Delta f} \text{ and } R_i = -c\frac{\Phi_i}{4\pi\,\Delta f}, \tag{14}$$

where R_i is the range and α_i is the damping factor of the sinusoid related to the i^{th} scattering point. Φ_i is the phase of λ_i, the i^{th} eigenvalue of **A**. To find the constant coefficients a_i, we use the following equation:

$$a_i = \frac{(\mathbf{Cm_i})(\mathbf{v_iB})}{\lambda_i^{f_1/\Delta f}}, \tag{15}$$

where $\mathbf{m_i}$ are eigenvectors of **A** and $\mathbf{v_i}$ are defined as

$$\mathbf{V} = [\mathbf{m_1}\cdots\mathbf{m_p}]^{-1} = \begin{bmatrix} \mathbf{v_1} \\ \vdots \\ \mathbf{v_p} \end{bmatrix}. \tag{16}$$

In Eq. 15, **C** is the first row of $\mathbf{\Omega}$, f_1 is the carrier frequency of the pulse and the k^{th} element of frequency vector is related to carrier frequency by

$$f_k = f_1 + (k-1)\Delta f. \tag{17}$$

To derive $\mathbf{B}$, $\mathbf{\Omega_N}$ is defined as

$$\mathbf{\Omega_N} = \begin{bmatrix} \mathbf{C} \\ \mathbf{CA} \\ \vdots \\ \mathbf{CA}^{N-1} \end{bmatrix} \tag{18}$$

and $\mathbf{B}$ is obtained by

$$\mathbf{B} = (\mathbf{\Omega_N^*}\,\mathbf{\Omega_N})^{-1}(\mathbf{\Omega_N^*}\mathbf{y^T}), \tag{19}$$

where $\mathbf{y}$ is the vector of the frequency samples of the backscattered data. Thus, a_i could be derived from Eq. 15. Now that all the parameters of the model in Eq. 3 are derived, the frequency response of the system could be reconstructed.

Lesion Classifier

Decay rate and oscillation frequency of complex harmonics extracted from frequency-domain data are determined by α and R in Eq. 3, respectively. As discussed in the previous section, the decay factors or poles of the harmonics are dependent on the shape of the scattering point while phase factors R are determined by the distance of the scatterer. A sample of time-domain backscattered signal and its frequency response is shown in Fig. 3. In this study, we investigate the feasibility of using shape parameter α to distinguish benign and malignant lesions. In fact, as mentioned before, benign lesions tend to be more regular and spherical while malignant lesions are usually irregular and highly spiculated. This will affect the poles in the backscattered signal. The classifier captures the changes in poles of the frequency-domain signals from benign and malignant lesions and hence, classifies the lesion type. MATLAB (matrix laboratory) environment was used to build neural network classifiers. Algorithms written for the processing of the data set and the computation of the results are thus in MATLAB's native language. In this study, a total of 25 harmonics were extracted from each response initially which is the number of singular values of the Hankel matrix. Optimizing the number of the poles will be discussed later in this chapter.

Neural networks constructed were trained at least 30 times with the initial weights and biases of the networks re-initialized before each trial. Only the trial with the highest accuracy among others with the same network structure has been chosen for discussion to be compared with other networks that likewise have been chosen for highest accuracy from their respective network structures.

A pattern recognition network, typically a feed-forward back-propagation network with tan-sigmoid transfer functions in both hidden layers and output layer, is used in this application.

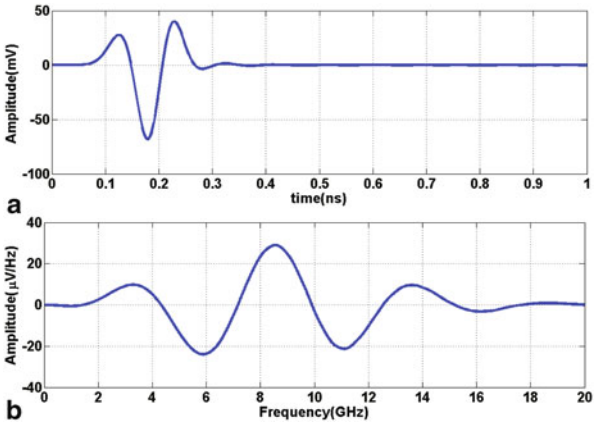

Fig. 3 A sample of the transmitted pulse. **a** Time domain. **b** Frequency domain

Two main architectures of networks with this characteristic are explored. As there are only two classes of output, the network should perform as a binary classifier. Consequentially, either architectures will require that the output layer of the network has two neurons regardless of the number of hidden layers and neuron types, as the networks will be required to classify between the two groups—benign and malignant. The number of hidden neurons used in this study is based on extensive simulations and emulation of other related clinical studies.

Kolmogorov Architecture

Kolmogorov argued that the correct and efficient number of hidden layers required to solve a classification problem is either one or two [30]. In addition, it is shown that additional hidden layers beyond the second one are superfluous and only serve to slow down the network.

In light of this hypothesis, Kolmogorov network 1 (K1) has been constructed. It has 50 tangent-sigmoid neurons in the hidden layer and 2 tangent-sigmoid neurons in the output layer. The network is illustrated in Fig. 4. In the figure, 'W' represents the weights matrix by which the input vector is multiplied and 'b' is the bias vector. An extension of K1 is also constructed with an additional hidden layer also constituting of 50 tangent-sigmoid neurons (Fig. 5).

9-5-5-2 Architecture

This architecture is made up of four hidden layers containing 9, 5, 5 and 2 tangent-sigmoid neurons, respectively in the order of distance from the input. The network

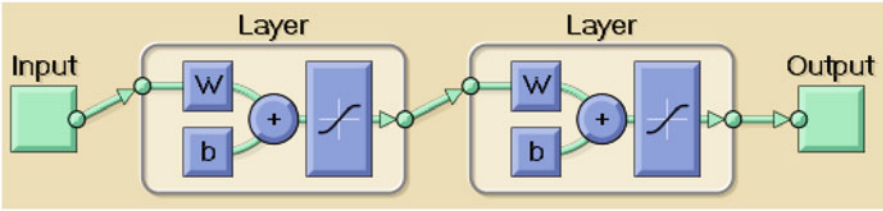

Fig. 4 Kolmogorov network 1 (K1)

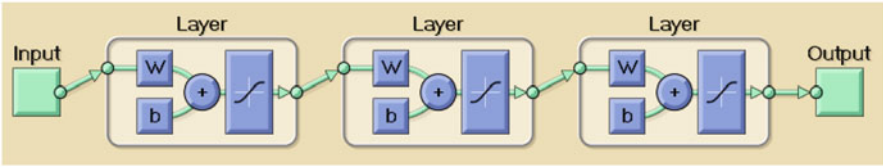

Fig. 5 Kolmogorov network 2 (K2)

structure is derived from that of a benchmark test of classifying tumors based on cell descriptions gathered by microscopic examination [31].

The structure of the network (C1) is given in Fig. 6:

Training

In light of the relatively small sizes of the networks considered in this work and consequentially, the small number of weights, the Levenberg–Marquardt (LM) algorithm is chosen as training function. Resilient back propagation was also considered in simulations. In the resilient back-propagation training, only the sign of the derivatives of the training function is used to update the weights. The size of the weight update is determined by another value. This significantly improves the training speed but simulations showed that its performance was not ideal for the small error tolerance desired.

The ratio of input data to be used for training, validation and testing has also been left at the default of 0.6, 0.2 and 0.2, respectively.

Results

The accuracy (ACC) of a test is the proportion of the true positives (TP) and true negatives (TN) to the number of estimated positives (P) and negatives (N). This can be expressed as $ACC = (TP + TN)/(P + N)$ where P and N are the total numbers of positives and negatives classified by the binary classifier.

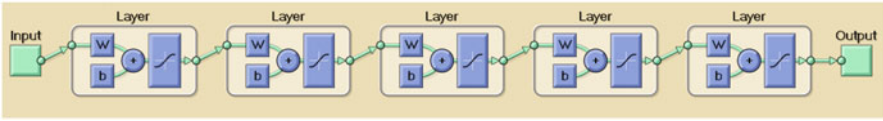

Fig. 6 9-5-5-2 network (C1)

True positive rate (*TPR*) is computed as TPR $= TP/P$. It indicates the accuracy of the network in classifying malignant lesions. The complement of TPR is the false positive rate (FPR) which may also be labeled as the false alarm rate. This value is of interest to doctors as a false positive result may cause the patient undue stress.

False negative rate (FNR) is of higher concern than the aforementioned TPR and FPR in this project. The FPR is known to be found as FNR $= 1-$TNR $= 1-(TN/N)$.

This is because a high FNR means too many cases of the cancer will be left undetected which is highly undesirable.

Table 2 details the networks' four main performance indicators for homogenous environment (no clutter).

From Table 2, the FNR values of the networks are unsatisfactory. However, because these preliminary networks are fairly accurate (except for network C1, which not only has an unsatisfactory accuracy of 65.74 % but also a high false alarm rate of 40.37 %), the results obtained in the homogeneous environment still prove that the lesions are classifiable with the technique proposed.

The same networks were trained with the backscatter signal obtained from a heterogeneous environment (with clutter) to observe their performances in more realistic heterogeneous environment.

The results of this application for the same networks in the heterogeneous environment are presented in Table 3.

The general trend of the performance is similar to that shown in Table 2. K2 is still the network with the highest accuracy although its performance is degraded in noisy environment.

On the other hand, performance of C1, unlike Kolmogorov networks, has lost only 5 % of its accuracy. This suggests that the binary classification problem is indeed more complex in the heterogeneous environment and the Kolmogorov networks may be underfitting the problem.

To improve the results in heterogeneous environment, dimension reduction of the input vectors is investigated. From the results found earlier, the current networks are clearly underfitting the problem. From Table 3, a significant decrease in accuracies of the networks can be observed when compared to the results obtained for Table 2. Classifiers were not able to perform as well in the heterogeneous environment because the responses from the other tissue present are also detected and the number of neurons in the networks may not be sufficient, thus causing underfitting.

Principal component analysis (PCA) was used to reduce the number of poles extracted from frequency response of each lesion. Based on PCA results, only a few number of poles significantly contribute to the total variations in different lesion

Table 2 Network performances in homogeneous environment

Network	ACC (%)	TPR (%)	FNR (%)	FPR (%)
K1	77.78	87.04	31.48	12.96
K2	79.07	82.96	24.81	17.04
C1	65.74	59.63	28.15	40.37

ACC accuracy *TPR* true positive rate, *FNR* false negative rate, *FPR* false positive rate, *K1* Kolmogorov network 1, *K2* Kolmogorov network 2, *C1* 9-5-5-2 network

Table 3 Network performances in heterogeneous environment

Network	ACC (%)	TPR (%)	FNR (%)	FPR (%)
K1	62.59	64.44	39.26	35.56
K2	62.78	57.78	32.22	42.23
C1	60.74	56.67	35.19	43.33

ACC accuracy *TPR* true positive rate, *FNR* false negative rate, *FPR* false positive rate, *K1* Kolmogorov network 1, *K2* Kolmogorov network 2, *C1* 9-5-5-2 network

responses. Hence, input vectors can be constructed using these highly variable poles and fed to the neural network for classification.

Table 4 shows the results after reducing the number of poles by PCA.

Comparing the results in Table 4 to that obtained in Table 3, the increase in the accuracy of Kolmogorov network is evident. K1 is more accurate by 2.78 % when the 18-pole inputs were used instead of the 25-pole inputs before PCA. At its best, K1 is found to be 6.11 % more accurate with the 12-pole inputs. K2 also follows a similar trend as K1 with its accuracy peaking at the 12-pole inputs scenario. C1 on the other hand did not perform better after pole reduction except for the 7-pole inputs case, where it fared marginally better by only 2.22 %.

To further increase the performance of the classifier, a cascaded form of the feed-forward back-propagation network is proposed. This structure will guarantee more updates of the biases and weights while they will also be propagated back as shown in Fig. 7.

As K1 has the highest accuracy, only the cascaded form of K1 (K1c) was developed for discussion. The result of the accuracy of K1c in the various scenarios is presented below (Table 5).

The accuracy of K1c is noticeably higher than the previously attained with any network in the heterogeneous environment.

It is worth noting that PCA results in some loss of detail in the input signals but this trade-off has allowed for the development of a significantly accurate network that coupled with the benefits of a cascaded network, is able to attain a performance comparable to other studies that have achieved an accuracy of more than 70 % [32].

From the figure and table above, it is clear that K1c with 12-pole vector inputs is the most accurate network.

Specificity is mathematically defined as $TN/(TN + FP)$. In practice, a positive result in a high specificity test is used to confirm a disease. Specificity of 73.9 % obtained through this classifier which indicates that should this test be administered

Table 4 Accuracy of K1, K2 and C1 with PCA

Network	ACC			
	7 Poles (%)	8 Poles (%)	12 Poles (%)	18 Poles (%)
K1	66.30	67.04	68.70	65.37
K2	64.81	62.22	65.37	63.89
C1	62.96	56.48	50.93	60.19

ACC accuracy *K1* Kolmogorov network 1, *K2* Kolmogorov network 2, *C1* 9-5-5-2 network

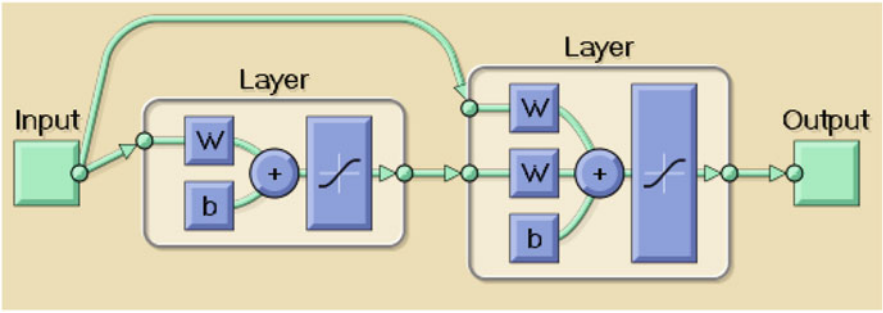

Fig. 7 Cascaded Kolmogorov network 1 (K1c) architecture

Table 5 Accuracy of K1c with PCA

Network	ACC			
	7 Poles (%)	8 Poles (%)	12 Poles (%)	18 Poles (%)
K1c	70.37	71.11	75.19	68.33

ACC accuracy *K1c* cascaded form of K1 (Kolmogorov network 1)

as an screening tool, it can reject up to 74 % of suspicious lesions as non-cancerous correctly.

Sensitivity is a measure of how efficiently the classifier can detect cancerous lesions and is defined mathematically as $TP/(TP + FN)$. Sensitivity obtained through this classifier is about 76.6 % which is higher than that in similar studies.

Conclusion

In this chapter, the feasibility of classifying breast lesions using their frequency-domain signature is investigated. Time-domain signature of the lesions is obtained through FDTD numerical analysis and converted into frequency domain using fast Fourier transform. Frequency-domain signature of the lesion is decomposed into complex harmonics associated with scattering points in the view of the receiver antenna. Attenuation coefficients of these harmonics are used to form a vector assigned to each lesion response. Different structures of neural network classifiers are trained

using these vectors. The performance of the neural network classifiers is evaluated and compared. Results show that cascade Kolmogrov architecture has the best performance among the network architectures compared. To improve the accuracy of the classifier, PCA is used to reduce the vector dimension. The resulting classifier achieves lesion classification accuracy of 75.19 % which is higher than similar existing methods [21, 32].

References

1. Center for Disease Control and Prevention (CDC). Statistics (2013), http://www.cdc.gov/cancer/breast/statistics
2. E.J. Bond, X. Li, S.C. Hagness, B.D. Van Veen, Microwave imaging via space–time beamforming for early detection of breast cancer. IEEE Trans. Antennas Propag. **51**(8), 1690–1705 (2003)
3. D. Byrne, M. O'Halloran, M. Glavin, E. Jones, Data independent radar beamforming algorithms for 2 cancer detection. PIER. **107**, 331–348 (2010)
4. Y. Chen, I.J. Craddock, P. Kosmas, M. Ghavami, P. Rapajic, Multiple-input multiple-output radar for lesion classification in ultra-wideband breast imaging. IEEE J. Selected Topics Signal Processing. **4**(1), 187–201 (2010)
5. Y. Chen, I.J. Craddock, P. Kosmas, Feasibility study of lesion classification via contrast-agent-aided UWB breast imaging. IEEE Trans. Biomed. Eng. **57**(5), 1003–1007 (2010)
6. Y. Chen, E. Gunawan, K.S. Low, S.-C. Wang, C.B. Soh, T.C. Putti, Effect of lesion morphology on microwave signature in 2-d ultra-wideband breast imaging. IEEE Trans. Biomed. Eng. **55**(8), 2011–2021 (2008)
7. Y. Chen, E. Gunawan, K.S. Low, S.-C. Wang, C.B. Soh, L.L. Thi, Time of arrival data fusion method for two-dimensional ultra-wideband breast cancer detection. IEEE Trans. Antennas Propag. **55**(10), 2852–2865 (2007)
8. R.C. Conceicao, M. O'Halloran, M. Glavin, E. Jones, Support vector machines for the classification of early-stage breast cancer based on radar target signatures. PIER B. **23**, 311–327 (2010)
9. R.C. Conceicao, M. O'Halloran, E. Jones, M. Glavin, Investigation of classifiers for early-stage breast cancer based on 2 target signatures. PIER. **105**, 295–311 (2010)
10. S.K. Davis, H. Tandradinata, S.C. Hagness, B.D. Van Veen, Ultra-wideband microwave breast cancer detection: a detection-theoretic approach using the generalized likelihood ratio test. IEEE Trans. Biomed. Eng. **52**(7), 1237–1250 (2005)
11. S.C. Hagness, A. Taflove, J.E. Bridges, in *Antennas and Propagation Society International Symposium*. FDTD modeling of a coherent-addition antenna array for early-stage detection of breast cancer, vol. 2 (IEEE, Atlanta, 1998), pp. 1220–1223
12. S.C. Hagness, A. Taflove, J.E. Bridges, Three-dimensional FDTD analysis of a pulsed microwave confocal system for breast cancer detection: design of an antenna-array element. IEEE Trans. Antennas Propag. **47**(5), 783–791 (1999)
13. S.C. Hagness, A. Taflove, J.E. Bridges, in *Engineering in Medicine and Biology Society*. FDTD analysis of a pulsed microwave confocal system for breast cancer detection. Proceedings of the 19th Annual International Conference of the IEEE, vol. 6, (IEEE, Chicago, 1997), pp. 2506–2508
14. H. Kanj, M. Popovic, A novel ultra-compact broadband antenna for microwave 2 tumor detection. PIER. **86**, 169–198 (2008)
15. M. Klemm, I.J. Craddock, J.A. Leendertz, A. Preece, R. Benjamin, Radar-based breast cancer detection using a hemispherical antenna array—experimental results. IEEE Trans. Antennas Propag. **57**(6), 1692–1704 (2009)

16. A. Lazaro, D. Girbau, R. Villarino, Simulated and experimental investigation of microwave imaging using UWB. PIER. **94**, 263–280 (2009)
17. A. Lazaro, D. Girbau, R. Villarino, Wavelet-based breast tumor localization technique using a UWB radar. PIER. **98**, 75–95 (2009)
18. H.B. Lim, N.T.T. Nhung, E.-P. Li, N.D. Thang, Confocal microwave imaging for breast cancer detection: delay-multiply-and-sum image reconstruction algorithm. IEEE Trans. Biomed Eng. **55**(6), 1697–1704 (2008)
19. X. Li, E.J. Bond, B.D. Van Veen, S.C. Hagness. An overview of ultra-wideband microwave imaging via space-time beamforming for early-stage breast-cancer detection. IEEE Antennas Propag. Mag. **47**(1), 19–34 (2005)
20. X. Li, S.K. Davis, S.C. Hagness, D.W. Van Der Weide, B.D. Van Veen, Microwave imaging via space-time beamforming: experimental investigation of tumor detection in multilayer breast phantoms. IEEE Trans. Microw. Theory Tech. **52**(8), 1856–1865 (2004)
21. J. Teo, Y. Chen, C.B. Soh, E. Gunawan, K.S. Low, T.C. Putti, S.-C. Wang, Breast lesion classification using ultra-wideband early time breast lesion response. IEEE Trans. Antennas Propag. **58**(8), 2604–2613 (2010)
22. D.W. Winters, E.J. Bond, B.D. Van Veen, S.C. Hagness, Estimation of the frequency-dependent average dielectric properties of breast tissue using a time-domain inverse scattering technique. IEEE Trans. Antennas Propag. **54**(11), 3517–3528 (2006)
23. Y. Huo, R. Bansal, Q. Zhu, Modeling of noninvasive microwave characterization of breast tumors. IEEE Trans. Biomed. Eng. **51**(7), 1089–1094 (2004)
24. J.B. Keller, Geometrical Theory of Diffraction. J. Opt. Soc. Am. (1917–1983), **52**, 116 (1962)
25. K. Naishadham, J.E. Piou, A super-resolution method for extraction of modal responses 2 wideband data. IEEE Antennas Propag. (Society International Symposium). **4**, 4168–4171 (2004)
26. K.M. Cuomo, J.E. Piou, J.T. Mayhan, Ultra-wideband coherent processing. IEEE Microw. Mag. **47**(6), 1094–1107 (1999)
27. T.G. Moore, B.W. Zuerndorfer, E.C. Burt, Enhanced imagery using spectral-estimation-based techniques. Linc. Lab. J. **10**(2), 171–186 (1997)
28. J.E. Piou, A state identification method for 1-d measurements with gaps. Proceedings of American Institute of Aeronautics and Astronautics Guidance Navigation and Control Conference, Aug. 2005
29. K. Naishadham, J.E. Piou, State-space spectral estimation of characteristic electromagnetic responses in wideband data. IEEE Antennas Wirel. Propag. Lett. **4**, 406–409 (2005)
30. J.-N. Lin, R. Unbehauen, On the realization of a Kolmogorov network. Neural Comput. **5**(1), 18–20 (1993)
31. H. Demuth, M. Beale, M. Hagan, Neural network toolbox™ 6, User's guide ©, 2008 (1992)
32. S.K. Davis, B.D. Van Veen, S.C. Hagness, F. Kelcz, Breast tumor characterization based on ultra-wideband microwave backscatter. IEEE Trans. Biomed. Eng. **55**(1), 237–246 (2008)

Index

M. R. Yuce (ed.), *Ultra-Wideband and 60 GHz Communications for Biomedical Applications,* DOI 10.1007/978-1-4614-8896-5,